MODELING OF MULTIPHASE FLOW

IN THE NEAR-WELLBORE REGION OF THE RESERVOIR

UNDER TRANSIENT CONDITIONS

A Dissertation

by

HE ZHANG

Submitted to the Office of Graduate Studies of
Texas A&M University
in partial fulfillment of the requirements for the degree of

DOCTOR OF PHILOSOPHY

May 2010

Major Subject: Petroleum Engineering

MODELING OF MULTIPHASE FLOW

IN THE NEAR-WELLBORE REGION OF THE RESERVOIR

UNDER TRANSIENT CONDITIONS

A Dissertation

by

HE ZHANG

Submitted to the Office of Graduate Studies of
Texas A&M University
in partial fulfillment of the requirements for the degree of

DOCTOR OF PHILOSOPHY

Approved by:

Chair of Committee,	Gioia Falcone
Committee Members,	Peter P. Valkó
	Catalin Teodoriu
	Yuefeng Sun
Head of Department,	Stephen A. Holditch

May 2010

Major Subject: Petroleum Engineering

ABSTRACT

Modeling of Multiphase Flow in the Near-Wellbore Region
of the Reservoir under Transient Conditions. (May 2010)
He Zhang, B.En.; B. S., University of Science and Technology of China;
M.S., University of New Orleans
Chair of Advisory Committee: Dr. Gioia Falcone

In oil and gas field operations, the dynamic interactions between reservoir and wellbore cannot be ignored, especially during transient flow in the near-wellbore region. As gas hydrocarbons are produced from underground reservoirs to the surface, liquids can come from condensate dropout, water break-through from the reservoir, or vapor condensation in the wellbore. In all three cases, the higher density liquid needs to be transported to the surface by the gas. If the gas phase does not provide sufficient energy to lift the liquid out of the well, the liquid will accumulate in the wellbore. The accumulation of liquid will impose an additional backpressure on the formation that can significantly affect the productivity of the well. The additional backpressure appears to result in a "U-shaped" pressure distribution along the radius in the near-wellbore region that explains the physics of the backflow scenario. However, current modeling approaches cannot capture this U-shaped pressure distribution, and the conventional pressure profile cannot explain the physics of the reinjection.

In particular, current steady-state models to predict the arrival of liquid loading, diagnose its impact on production, and screen remedial options are inadequate, including Turner's criterion and Nodal Analysis. However, the dynamic interactions between the reservoir and the wellbore present a fully transient scenario, therefore none of the above solutions captures the complexity of flow transients associated with liquid loading in gas wells. The most satisfactory solution would be to couple a transient reservoir model to a transient well model, which will provide reliable predictive models to link the well

dynamics with the intermittent response of a reservoir that is typical of liquid loading in gas wells. The modeling work presented here can be applied to investigate liquid loading mechanisms, and evaluate any other situation where the transient flow behavior of the near-wellbore region of the reservoir cannot be ignored, including system start-up and shut-down.

ACKNOWLEDGEMENTS

I would like to thank my committee chair, Dr. Gioia Falcone, and my committee members, Dr. Peter Valko, Dr. Catalin Teodoriu, and Dr. Yuefeng Sun, for their guidance and kindest support throughout the course of this research. My appreciation also goes to Dr. Jader Barbosa and Tobias Gessner (currently a PhD student) at UFSC in Brazil who helped build the transient wellbore model. I also want to thank Ms. Darla-Jeans Weatherford for her greatest patience to formalize this dissertation. Thanks also go to the department faculty, staff, all my research group members, and friends for making my time at Texas A&M University a great experience. I sincerely appreciate that Dr. Falcone allowed her start-up funds to initialize this work, and extend my gratitude to the RWE, PetroBras, and Shell US, which sponsored this work as part of the JIP project later of this study.

Finally, thanks to my father, mother, and sister for their consistent encouragement and to my wife for her greatest support and love.

NOMENCLATURE

B	FVF
c	user-defined coefficient
c_t	total compressibility, psi^{-1}
C_{op}	coefficient of $\Delta_t p_o$ in the expansion of oil accumulation, STB/(D-psia)
C_{wp}	coefficient of $\Delta_t p_o$ in the expansion of water accumulation, STB/(D-psia)
C_{gp}	coefficient of $\Delta_t p_o$ in the expansion of gas accumulation, STB/(D-psia)
f	frequency of the sine function, D^{-1}
k	permeability, md
$m(p)$	pseudopressure, $psia^2/cp$
p	pressure, psia
P	period of the sine function, D
p_{cow}	oil/water capillary pressure, psia
p_{cgo}	gas/oil capillary pressure, psia
q_{fgsc}	free gas production rate at standard conditions, scf/D
q_{gsc}	gas production rate at standard conditions, scf/D
q_{osc}	oil production rate at standard conditions, STB/D
q_{wsc}	water production rate at standard conditions, STB/D
r	size of the gridblock in radial model
r_e	reservoir drainage, ft
r_w	wellbore radius, ft
R_s	solution GOR, scf/STB
S	saturation, percentage
T	transmissibility, STB/(D-psia) or scf/(D-psia) *or* temperature, ^oF
Δt	timestep, D

Δx	size of gridblock along the x direction, ft
Δy	size of gridblock along the y direction, ft
Δz	size of gridblock along the z direction, ft
Z	elevation referred to datum (positive downward), ft
γ	gravity, psi/ft
ϕ	porosity
μ	viscosity, cp
θ	angle, degree

Subscripts

c	condensate
g	gas
m	neighboring gridblock to gridblock n
n	gridblock
o	oil
r	relative
sg	solution gas
w	water

Superscripts

n	old timestep
n+1	current timestep

TABLE OF CONTENTS

CHAPTER Page

LIST OF FIGURES

Page

Page

Page

Page

LIST OF TABLES

Page

CHAPTER I

INTRODUCTION

Objectives

The goal of this work is to develop representative solutions for transient flow in the near-wellbore region, later use this modeling solution to investigate phase redistribution in the near-wellbore region, and apply it to suggest novel methods for liquid-loading problems in gas reservoirs as well as many other applications.

The Importance of Research

In oil and gas field operations, the effects of the dynamic interactions between reservoir and wellbore is important, especially during transient flow in the near-wellbore region.

A particular instance of transient flow in the near-wellbore region is the intermittent response of a reservoir that is typical of liquid loading in gas wells. This particular instance relates to the transient flow in both the wellbore and the near-wellbore region. Liquid loading occurs when the reservoir pressure decreases in mature gas fields and the liquid content of the well and its particular distribution at a given instant in time creates a backpressure that restricts, and in some cases even stops, the flow of gas from the reservoir. Liquid loading is an all too common problem in mature gas fields around the world. In the USA alone at least 90% of the producing gas wells encounter such problems, at least occasionally.

Such is the importance of liquid loading that the industry has devoted a lot of attention to the alleviation of the problem using various measures. However, the fundamental understanding of the associated phenomena is still surprisingly weak. This applies not

---

This dissertation follows the format of *Society of Petroleum Engineers Journal*.

those in the reservoir. The classical way of dealing with these interactions is through inflow performance relationships (IPRs) where the inflow from the reservoir is related to the pressure at the bottom of the well, which is related to the multiphase flow behavior in the well (and in the rest of the production system, if appropriate). The latter is also usually calculated from steady-state relationships (though these often lack a fundamental basis). However, a transition from an acceptable liquid loading regime to an unacceptable one may occur over a relatively short time. Flow at the surface will remain in mist or annular flow regime till the conditions change sufficiently to exhibit characteristics of transitional flow. At this point, the well production becomes somewhat erratic, progressing to slug and churn flow, while following an overall decreasing trend. As a result, the liquids start to dynamically accumulate in the wellbore, causing downhole pressure fluctuations. The increasing liquid holdup augments the backpressure on the formation, which ultimately accounts for the well's death.

The conventional pressure profile in the near-wellbore region of a flowing reservoir (**Fig. 1.1a**) is not suitable to characterize the transient phenomena that take place during liquid loading. The wellbore phase redistribution that occurs during liquid loading causes the bottomhole pressure to change with time. The frequency and amplitude of these changes vary with the magnitude of the liquid loading occurrence. If the reservoir were capable of providing an instantaneous response to the bottomhole pressure fluctuations, the pressure profile in the near-wellbore region would quickly readjust to the new wellbore conditions (**Fig. 1.1b**). However, because of the combination of inertia and compressibility effects, the reservoir response is not instantaneous and can be particularly slow for tight formations. A sequence of conventional pressure profiles (from **a** to **b** in **Fig. 1**) could be assumed, but this would imply a temporary discontinuity of the pressure function at the wellbore, which is unphysical. Thus, this dissertation proposes a U-shaped pressure profile (**Fig. 1.1c**), which could also explain the possibility of reinjection of the heavier phase into the reservoir.

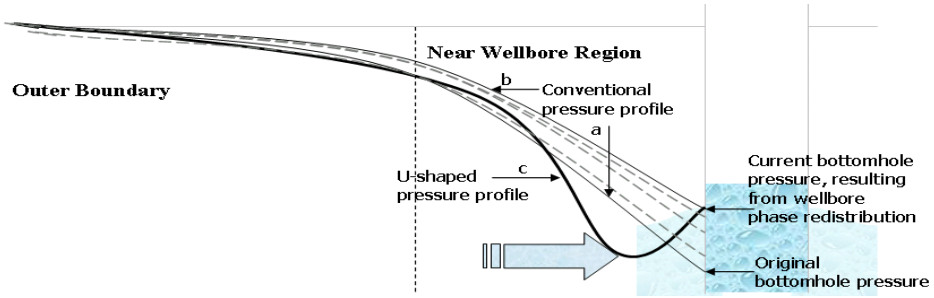

Fig. 1.1—As the well starts to load up with liquid, a backpressure will occur. The fat arrow points to the minimum pressure existing in the near-wellbore region, where the pressure profile is actually a U-shaped curve (Zhang *et al.*, 2009*).*

An integrated model for the multiphase flow in wellbore and reservoir under fully transient conditions is highly desired by the industry. It can not only apply to the investigation of liquid loading problems in gas fields, but also to that of disturbed pressure profiles due to well shut-ins, transient flow in fractures, optimum choice of injection spots for gas lift operations, and serve other transient conditions due to the dynamic interactions between wellbore and reservoir.

Structure of the Dissertation

Chapter II gives a detailed state-of-the-art of current modeling approaches adopted by the industry for the investigation of liquid loading in gas wells, and highlights the limits of such methods. Then it also reviews past wellbore/reservoir coupling attempts, and the objective of this work. Finally it presents an overview of the Joint Industry Project (JIP) on "Liquid Loading in the Operation of Gas Fields: Mechanisms, Prediction and Reservoir Response," and explains the role of this work as part of the JIP's objectives.

Chapter III describes the classical Implicit Pressure Explicit Saturation (IMPES) method for the numerical simulation of multiphase flow in reservoir systems.

Chapter IV re-derives the linear equations for the IMPES method under different boundary conditions.

Chapter V presents the blackoil, IMPES reservoir simulator that was developed in FORTRAN as part of this study, and that was compared with the Eclipse, commercial software.

Chapter VI presents the results of a numerical modeling effort focused on the identification of the transient pressure profile in the near-wellbore region under fully transient conditions. A "U-shaped" pressure profile along the reservoir radius has been reproduced, whereas the commercial software failed to do so under the same imposed conditions. The existence of a similar pressure profile can explain the reinjection of the heavier phase into the reservoir during liquid loading in gas wells.

Chapter VII presents a study on relative permeability hysteresis effects. It is shown that, as the fluid flowing direction changes at high frequency, the hysteresis effects are negligible.

Chapter VIII presents the results of the simulations aiming at investigating counter-current flow in the near-wellbore region by coupling a pseudo-wellbore model in slug flow regime. The observed counter-current flow indicates that gas flows into the wellbore, while the liquid is reinjected into the formation, even at the same reservoir depth.

Chapter IX presents the basic theory to couple a mechanistic wellbore model with a transient reservoir model (modified after Falcone, 2006), and suggests the need for integrating a transient wellbore model with the transient near-wellbore simulator developed as part of this study.

Chapter X proposes an explicit wellbore/reservoir coupling method.

CHAPTER II

LITERATURE REVIEW

To investigate the multiphase flow in the near-wellbore region, the dynamic interaction between the wellbore and reservoir is important. Besides modeling other transient scenarios mentioned before, this work is primarily applied for modeling the liquid loading problem, so the literature review will be carried out in two parts.

The first part is about current simulation methods currently used in the industry to identify or predict the onset of liquid loading, including the so-called "droplet model" and Nodal Analysis. Both of them are based on steady-state flow assumptions and therefore do not capture the complexity of flow transients associated with liquid loading in gas wells. The implied shortages suggest the strong need for an integrated modeling of the wellbore and reservoir under transient flow conditions.

The second part introduces the past efforts to couple wellbore and reservoir models in literature. An integrated wellbore/reservoir model would assist in studying transient flow in the near-wellbore region. However, none of the coupled models in public domain suggest the U-shaped pressure profile introduced in the previous chapter.

Current Models to Predict the Onset of Liquid Loading

Liquid loading is a very popular problem. The understanding of the multiphase flows associated with liquid loading is still weak. Although major efforts have been made to predict the flowing conditions at which the well remains out of the liquid loading region, using the so-called "Turner's criteria" (droplet model), these do not capture the dynamics of the loading sequence following its onset. Turner's criteria are used by operators to design a production system in such a way that it will flow at gas rates

capable of lifting all liquids out of the well, but they cannot be used to understand how serious the loading occurrence is or how quickly it will impair production. Another conventional approach to characterize the dynamic interaction between reservoir and wellbore is to combine a steady-state or pseudosteady-state reservoir performance model with a steady-state or pseudosteady-sate wellbore performance model and to determine the point of stable operating conditions for the integrated system by solving the models together (Nodal Analysis). However, the realistic transient boundary conditions at the interface between reservoir and wellbore is not defined appropriately. The following discussions investigate the disadvantages of the above two conventional methods.

Turner Model (also called "droplet model")

It is generally believed that liquids are lifted in the gas flow velocity regimes by the shear stress at the interface between the gas and the liquid before the onset of severe liquid loading. Turner et al. (1969) analyzed all the upwards and downwards force on a droplet and developed the concept of "critical velocity." As the drag force from the gas upward movement is equal to the weight, the gas velocity is at "critical" (**Fig. 2.1**).

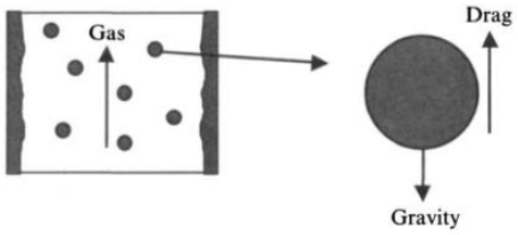

Fig. 2.1—Illustrations of concepts investigated for defining "critical velocity" (Lea *et al.*, 2003).

The empirical equations for condensate and water are:

$$v_{t,c} = \frac{4.043(45 - 0.0031p)^{1/4}}{(0.0031p)^{1/2}} \quad \text{..... (2.1)}$$

$$v_{t,w} = \frac{5.321(67 - 0.0031p)^{1/4}}{(0.0031p)^{1/2}} \quad \text{..... (2.2)}$$

where p is the flowing wellhead pressure, psi, and v is the velocity, ft/sec.

Converting the unit to MMscf/D,

$$q_g = \frac{3.06PAv_t}{(T + 460)z} \quad \text{..... (2.3)}$$

Introducing $A = \frac{\pi\ d_{ti}^2}{4 \cdot 144}$ where d_{ti} is the tubing ID in inches, we have

$$q_{t,c} = \frac{0.0676pd_{ti}^2}{(T + 460)z} \frac{(45 - 0.0031p)^{1/4}}{(0.0031p)^{1/2}} \quad \text{..... (2.4)}$$

$$q_{t,w} = \frac{0.0890pd_{ti}^2}{(T + 460)z} \frac{(67 - 0.0031p)^{1/4}}{(0.0031p)^{1/2}} \quad \text{..... (2.5)}$$

The Turner droplet model is only accurate in the case of surface flowing pressure higher than 1000 psia. In addition, Coleman et al. (1991) developed a similar relationship for the minimum critical flow rate for both water and liquid without employing the 1.2 multiplier to fit Turner's data.

$$v_{t,c} = \frac{3.369(45 - 0.0031p)^{1/4}}{(0.0031p)^{1/2}} \quad \text{..... (2.6)}$$

$$v_{t,w} = \frac{4.434(67 - 0.0031p)^{1/4}}{(0.0031p)^{1/2}} \quad \text{..... (2.7)}$$

The relative critical gas flow rates for condensate and water are respectively:

$$q_{t,c} = \frac{0.0563pd_{ti}^2}{(T+460)z}\frac{(45 - 0.0031p)^{1/4}}{(0.0031p)^{1/2}} \quad \text{..... (2.8)}$$

$$q_{t,w} = \frac{0.0742pd_{ti}^2}{(T+460)z}\frac{(67 - 0.0031p)^{1/4}}{(0.0031p)^{1/2}} \quad \text{..... (2.9)}$$

The reverse calculation of Eq. 2.3, the critical tubing diameter can be obtained in inches by Eq. 2.10,

$$q_g = \frac{3.06P\dfrac{\pi d_{ti}^2}{4\cdot 144}v_t}{(T+460)z} \Rightarrow d_{ti} = \sqrt{\frac{59.94q_g(T+460)z}{Pv_t}} \quad \text{..... (2.10)}$$

Nodal Analysis

Nodal Analysis (Mach et al., 1979 and Economides et al. 1994) divides the total well system into two subsystems at a specific spot called “nodal point”. One subsystem considers the inflow from the reservoir, through possible pressure drop components; while the other one considers the outflow system from the surface pressure down to the nodal point. The Nodal point pressure is calculated and plotted as two independent pressure-rate curves (**Fig. 2.2**).

The “backpressure” (Eq. 2.11) is one of the most widely used inflow expressions for gas well.

$$q_G = C(\bar{p}_r^2 - p_{wf}^2)^n \quad \text{..... (2.11)}$$

where C is the inflow coefficient, Mscf/(D-psi^n), and n is the inflow exponent in the range of 0.5 to 1.

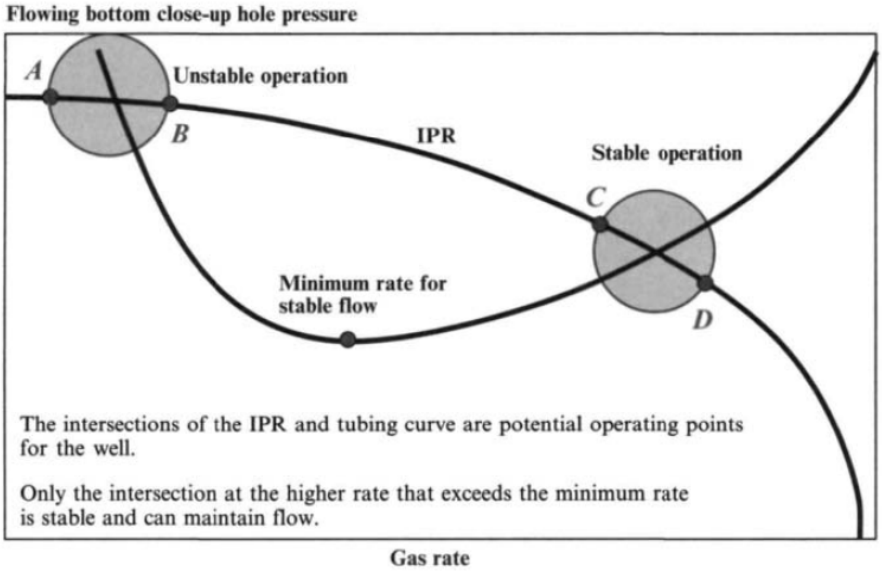

Fig. 2.2—Tubing performance curve in relation to well deliverability curve (Lea *et al.*, 2003).

Values for C and n are usually determined by a minimum of four data pairs (q_g - p_{wf}). However, all the inflow curves are based on the steady- or pseudosteady-state equations. Nodal Analysis is used to examine the controllable variables, like number of perforations, surface pressure, tubing size and so on. It can help design the proper gas flow rate for a tight gas reservoir in order to keep it above the critical velocity and avoid the liquid loading problem.

Summary

As illustrated above, both the Turner model and the Nodal Analysis approach assume steady-state or pseudosteady-state conditions to predict the onset of liquid loading, and therefore do not capture the complexity of flow transients associated with liquid loading in gas wells. An integrated model is required to link the well dynamics with the intermittent response of a reservoir. The shared boundary at bottomhole needs to be defined dynamically to describe the latter life of the liquid loaded well and accurately, estimate the productivity loss of liquid loaded gas wells.

The Past Efforts on Integrating Wellbore and Reservoir Models

Several coupled reservoir/wellbore models are capable of handling flow contributions from different feedzones (Bjornsson and Bodvarsson, 1987; Freeston and Hadgu, 1987; Hadgu and Freeston, 1990; Aunzo et al., 1991). These models typically ignore the details of flow in the wellbore or treat it in a very simplified manner.

Hadgu, Zimmerman, and Bodvarsson (1995) published their results with a new module, COUPLE, which was written to serve as an interface between the reservoir simulator TOUGH and wellbore simulator WFSA. TOUGH is designed to simulate the coupled transport of fluid, heat and chemical species for multiphase flow in porous as well as fractured media. The model is based on the conservation of mass and Darcy's law. This 3D code can solve the equations of motion by discretizing them in space and time in a fully implicit manner. It has been widely used for geothermal applications. Also, it has a deliverability option to evaluate well output based on a specified bottomhole pressure and productivity index. The wellbore simulator WFSA was developed at Auckland University, New Zealand (1990). It is a multipurpose geothermal simulator with features

such as presence of dissolved solids, multiple feedzones, and fluid/rock heat exchange. However, it can model the flow with the presence of gases. The main assumptions were made that the flow is steady-state and 1D, the phases are in thermodynamic equilibrium, fluid properties are constant within a selected depth interval, etc. Further it is essentially a mechanistic geothermal wellbore model. COUPLE is the interface that makes the communications between the TOUGH and WFSA modules. The main evaluated and iterated parameters are mass flow rate and bottomhole pressure. It starts with trial values of these two parameters and calculates flow parameters up the wellbore through several feedzones. Once the mass flow rate and the thermodynamic conditions at the wellhead are reached, the computations are repeated with a new trial bottomhole pressure till the difference between the specified and calculated wellhead pressures is within an acceptable limit. The results showed the outputs between the new coupling model and TOUGH's deliverability method are quite different, which means the coupled reservoir/wellbore simulations are generally required. Users need to define the feedzones in the wellbore, which are not generally used for liquid loading problem.

Cazenave and Dickstein (1996) published a linearized model of well/reservoir coupling for a monophasic flow with boundary conditions corresponding to oil production at either a given pressure or at a given flow rate. The rigorously coupled system is a hybrid of parabolic and hyperbolic nonlinear partial differential equations (PDEs), and its solution is provided by numerical methods. The coupling requirements are satisfied by preserving the continuity of pressure and conservation of mass at the sandface. This model is for monophasic flow, not appropriate to the liquid loading problem as condensate drops out.

Vicente, Sarica, and Ertekin (2000) developed a fully implicit 3D simulator with local refinement around the wellbore to solve reservoir and horizontal well flow equations simultaneously for single-phase liquid or gas cases. The model consists of conservation of mass, Darcy's law in the reservoir, and mass and momentum conservation in the

wellbore for isothermal conditions. This model can be used to simulate the transient pressure and flow rate behavior of both the reservoir and the horizontal wellbore. Further, this model is also capable of predicting the horizontal wellbore storage and unloading, as well as the flow pattern determination verified by the transient well testing using pressure derivative curves. Again, this single phase horizontal well/reservoir simulator is not generally used for liquid loading investigation.

Ali et al. (2005) and Al-Darmaki et al. (2008) experimentally verified the occurrence of phase redistribution in the wellbore under transient flowing conditions, which leads to downhole pressure fluctuations that could trigger transient flow in the near wellbore. Attempts have recently been made to characterize the dynamic interaction between reservoir and wellbore under transient flow conditions. This experimental work is used to validate the dynamic interaction at the shared boundary.

Sturm et al. (2004) presented an investigation of unstable production from a vertical, gas-lifted well tapping into segregated black oil and gas layers. For their study, they described the two-phase flow in the tubing by means of a drift-flux model, and modeled single-phase gas flow in the annulus. They characterized the gas and liquid reservoir inflow by applying the radial Darcy equation to the liquid flow, and the radial Forcheimer equation to the gas flow. The authors also investigated the reservoir inflow response to sinusoidal variations of the drawdown and obtained an ellipsis on a plot of drawdown vs. liquid production. This model simplified the reservoir side.

Dousi et al. (2005) defined metastable gas flow in a liquid-loaded well as the flow that occurs when a dynamic equilibrium is attained between liquid produced out of the well and liquid falling downward and being reinjected into the reservoir. This results in a stable liquid column at the bottom of the well. To mimic the gas metastable flow, they assumed a reservoir made of two layers, with the top layer producing gas and the bottom one taking in liquid from the wellbore. They used steady-state relationships to

characterize both the reservoir and the wellbore. This model assumes steady-state conditions.

Nennie et al. (2007) simulated the flow from a horizontal well with three inflow sections located in a thin oil rim, each individually regulated by an inflow control valve (ICV's). They used a commercial transient wellbore simulator to mimic the well's response, and a full-field numerical reservoir simulator to model the reservoir, including the near wellbore. Nennie et al. integrated the two simulators by explicit coupling, assuming no capillary effects in the reservoir. Among their case studies, they included a sinusoidal ICV setting variation and obtained an ellipsis on a plot of bottomhole pressure vs. mass rate. This explicit coupling can be the source of diverging problems; for example, it is hard to make the PVT properties consistent in both reservoir and wellbore software.
Chupin et al. (2007) and Sagen et al. (2007) investigated liquid loading in gas wells by implicit coupling of a commercial transient wellbore simulator and a near-wellbore model based on the mass conservation equations and Darcy's law written for the liquid and gas phases. However, they did not provide details of the model and solution procedure. For the coupling, they suggested using "sensitivity coefficients" to be determined from the size of the near-wellbore region, estimated a priori as a user input. In fact, it is impractical for field engineers to anticipate the near-wellbore region size.

Through the modeling efforts and related discussions in the previous chapters, an explicitly integrated model was highly demanded to accurately describe the transient interaction between the wellbore and reservoir in the near-wellbore region. A preliminary method was proposed by Falcone (2006) in five steps. The model is based on the integration between wellbore and reservoir equations via a shared boundary condition and a well-defined solution procedure that should allow for fully transient pressure changes in the near-wellbore region. This model was not validated.

Summary

This literature review shows the efforts that have been made towards a more detailed characterization of the dynamic interactions between reservoir and wellbore under transient flow conditions. However, further development and validation is still required, as none of the past solutions is specifically designed for liquid loading investigation.

The reservoir simulator built as part of this work focuses on multiphase flow in the near-wellbore region as liquid loading occurs; it captures the transient, U-shaped pressure profile that responds to bottomhole pressure oscillations due to wellbore phase redistribution effects. This simulator also describes the possible counter-current flow rates in the near-wellbore region, with capillary pressure identified to be responsible for this phenomenon. This simulator will require coupling with a transient wellbore model in the future.

CHAPTER III

MULTIPHASE RESERVOIR MODEL

In a multiphase-flow system, multiple equations with multiple unknowns exist for each gridblock. The final equations set needs to be formulated in several ways, depending on which unknowns are solved directly from the constraint equations. This formulation includes combining mass-conservation equations (differential mass balance, or the continuity equation), equations of state (EOS), and a transport equation. Darcy's law is conventionally used with multiphase flow systems to derive the partial differential equation (PDE). Once it is formulated, several solution methods can be applied to generate the coefficient matrix and the linear equations. In this work, we used the implicit pressure explicit saturation (IMPES) method.

The objective of this reservoir simulator is to work under fully transient conditions and be able to capture the backflow rates as well as the transient pressure distribution along the radius in the near-wellbore region. The IMPES method obtains a single pressure equation for each grid block by combining all flow equations for different phases, and explicitly iterates the saturation, capillary pressure, and transmissibility by Newton-Raphson algorithm.

Conservation Equation

With the purpose of deriving a general mass-conservation equation, the gas component is split fictitiously into a free-gas component and a solution-gas component. The material-balance equation for Component *c*, written over a finite control volume of the porous reservoir over a time interval Δt is:

$$(m_i)_c - (m_o)_c + s_c = (m_a)_c \quad \text{..... (3.1)}$$

where

$$(m_i)_c = \left[\left(\dot{m}_{cx}A_x\right)_{x-\Delta x/2} + \left(\dot{m}_{cy}A_y\right)_{y-\Delta y/2} + \left(\dot{m}_{cz}A_z\right)_{z-\Delta z/2}\right]\Delta t$$

$$(m_o)_c = \left[\left(\dot{m}_{cx}A_x\right)_{x+\Delta x/2} + \left(\dot{m}_{cy}A_y\right)_{y+\Delta y/2} + \left(\dot{m}_{cz}A_z\right)_{z+\Delta z/2}\right]\Delta t$$

$$s_c = \left(q_{mt_c} + q_{m_c}\right)\Delta t$$

$$(m_a)_c = V_b\left[\left(m_{vc}\right)_{t+\Delta t} - \left(m_{vc}\right)_t\right]$$

Bring these definitions into the Eq. 3.1, we have

$$\left[\left(\dot{m}_{cx}A_x\right)_{x-\Delta x/2} + \left(\dot{m}_{cy}A_y\right)_{y-\Delta y/2} + \left(\dot{m}_{cz}A_z\right)_{z-\Delta z/2}\right]\Delta t - \left[\left(\dot{m}_{cx}A_x\right)_{x+\Delta x/2} + \left(\dot{m}_{cy}A_y\right)_{y+\Delta y/2} + \left(\dot{m}_{cz}A_z\right)_{z+\Delta z/2}\right]\ \Delta t$$
$$+\left(q_{mt_c} + q_{m_c}\right)\Delta t = V_b\left[\left(m_{vc}\right)_{t+\Delta t} - \left(m_{vc}\right)_t\right]$$
$$-\left[\left(\dot{m}_{cx}A_x\right)_{x+\Delta x/2} - \left(\dot{m}_{cx}A_x\right)_{x-\Delta x/2}\right] - \left[\left(\dot{m}_{cy}A_y\right)_{y+\Delta y/2} - \left(\dot{m}_{cy}A_y\right)_{y-\Delta y/2}\right] - \left[\left(\dot{m}_{cz}A_z\right)_{z+\Delta z/2} - \left(\dot{m}_{cz}A_z\right)_{z-\Delta z/2}\right]$$
$$= \frac{V_b}{\Delta t}\left[\left(m_{vc}\right)_{t+\Delta t} - \left(m_{vc}\right)_t\right] - \left(q_{mt_c} + q_{m_c}\right)$$
$$-\left[\frac{\left(\dot{m}_{cx}A_x\right)_{x+\Delta x/2} - \left(\dot{m}_{cx}A_x\right)_{x-\Delta x/2}}{\Delta x}\right]\Delta x - \left[\frac{\left(\dot{m}_{cy}A_y\right)_{y+\Delta y/2} - \left(\dot{m}_{cy}A_y\right)_{y-\Delta y/2}}{\Delta y}\right]\Delta y$$
$$-\left[\frac{\left(\dot{m}_{cz}A_z\right)_{z+\Delta z/2} - \left(\dot{m}_{cz}A_z\right)_{z-\Delta z/2}}{\Delta z}\right]\Delta z = \frac{V_b}{\Delta t}\left[\left(m_{vc}\right)_{t+\Delta t} - \left(m_{vc}\right)_t\right] - \left(q_{mt_c} + q_{m_c}\right)$$

…….. (3.2)

In differential expression,

$$-\frac{\partial}{\partial x}\left(\dot{m}_{cx}A_x\right)\Delta x - \frac{\partial}{\partial y}\left(\dot{m}_{cy}A_y\right)\Delta y - \frac{\partial}{\partial z}\left(\dot{m}_{cz}A_z\right)\Delta z = V_b\frac{\partial}{\partial t}\left(m_{v_c}\right) - \left(q_{mt_c} + q_{m_c}\right)\ldots\ldots\ldots \quad (3.3)$$

where c means component (= o, w, g)

Because $B_c = \frac{\rho_{\mathrm{csc}}}{\rho_c} = \frac{q_c}{q_{sc}}$, $m_{vc} = \frac{\phi \cdot S_c}{B_c}$ and $\dot{m}_c = \alpha_c \rho_c u_c$, for different phases, the mass balance conservation equation is derived as,

Oil: $$-\frac{\partial}{\partial x}\left(\frac{A_x}{B_o}u_{ox}\right)\Delta x-\frac{\partial}{\partial y}\left(\frac{A_y}{B_o}u_{oy}\right)\Delta y-\frac{\partial}{\partial z}\left(\frac{A_z}{B_o}u_{oz}\right)\Delta z=\frac{V_b}{\alpha_c}\frac{\partial}{\partial t}\left(\frac{\phi S_o}{B_o}\right)-q_{osc}$$

…….. (3.4)

Water: $$-\frac{\partial}{\partial x}\left(\frac{A_x}{B_w}u_{wx}\right)\Delta x-\frac{\partial}{\partial y}\left(\frac{A_y}{B_w}u_{wy}\right)\Delta y-\frac{\partial}{\partial z}\left(\frac{A_z}{B_w}u_{wz}\right)\Delta z=\frac{V_b}{\alpha_c}\frac{\partial}{\partial t}\left(\frac{\phi S_w}{B_w}\right)-q_{wsc}$$

…….. (3.5)

Gas: $$-\frac{\partial}{\partial x}\left(\frac{A_x}{B_g}u_{fgx}+\frac{A_xR_s}{B_o}u_{ox}\right)\Delta x-\frac{\partial}{\partial y}\left(\frac{A_y}{B_g}u_{fgy}+\frac{A_yR_s}{B_o}u_{oy}\right)\Delta y-\frac{\partial}{\partial z}\left(\frac{A_z}{B_g}u_{fgz}+\frac{A_zR_s}{B_o}u_{oz}\right)\Delta z$$
$$=\frac{V_b}{\alpha_c}\frac{\partial}{\partial t}\left(\frac{\phi S_g}{B_g}+\frac{\phi R_sS_o}{B_o}\right)-\left(q_{fgsc}+R_sq_{osc}\right)$$

…….. (3.6)

Taking Darcy's Law into the above three equations for each phase, and replace the velocity term,

Darcy's Law: $$\vec{u}_c=-\beta_c\frac{kk_{rc}}{\mu_c}\left(\vec{\nabla}p_c-\gamma_c\vec{\nabla}Z\right)$$ …….. (3.7)

Oil: $$\frac{\partial}{\partial x}\left(\beta_c\frac{A_x}{B_o}\frac{k_xk_{ro}}{\mu_o}\left(\frac{\partial p_o}{\partial x}-\gamma_o\frac{\partial Z}{\partial x}\right)\right)\Delta x+\frac{\partial}{\partial y}\left(\beta_c\frac{A_y}{B_o}\frac{k_yk_{ro}}{\mu_o}\left(\frac{\partial p_o}{\partial y}-\gamma_o\frac{\partial Z}{\partial y}\right)\right)\Delta y$$
$$+\frac{\partial}{\partial z}\left(\beta_c\frac{A_z}{B_o}\frac{k_zk_{ro}}{\mu_o}\left(\frac{\partial p_o}{\partial z}-\gamma_o\frac{\partial Z}{\partial z}\right)\right)\Delta z=\frac{V_b}{\alpha_c}\frac{\partial}{\partial t}\left(\frac{\phi S_o}{B_o}\right)-q_{osc}$$

…….. (3.8)

Water:
$$\frac{\partial}{\partial x}\left(\beta_c \frac{A_x}{B_w}\frac{k_x k_{rw}}{\mu_w}\left(\frac{\partial p_w}{\partial x}-\gamma_w\frac{\partial Z}{\partial x}\right)\right)\Delta x+\frac{\partial}{\partial y}\left(\beta_c \frac{A_y}{B_w}\frac{k_y k_{rw}}{\mu_w}\left(\frac{\partial p_w}{\partial y}-\gamma_w\frac{\partial Z}{\partial y}\right)\right)\Delta y$$
$$+\frac{\partial}{\partial z}\left(\beta_c \frac{A_z}{B_w}\frac{k_z k_{rw}}{\mu_w}\left(\frac{\partial p_w}{\partial z}-\gamma_w\frac{\partial Z}{\partial z}\right)\right)\Delta z=\frac{V_b}{\alpha_c}\frac{\partial}{\partial t}\left(\frac{\phi S_w}{B_w}\right)-q_{wsc}$$

…….. (3.9)

Gas:
$$\frac{\partial}{\partial x}\left(\beta_c \frac{A_x}{B_g}\frac{k_x k_{rg}}{\mu_g}\left(\frac{\partial p_g}{\partial x}-\gamma_g\frac{\partial Z}{\partial x}\right)+R_s\beta_c \frac{A_x}{B_o}\frac{k_x k_{ro}}{\mu_o}\left(\frac{\partial p_o}{\partial x}-\gamma_o\frac{\partial Z}{\partial x}\right)\right)\Delta x$$
$$+\frac{\partial}{\partial y}\left(\beta_c \frac{A_y}{B_g}\frac{k_y k_{rg}}{\mu_g}\left(\frac{\partial p_g}{\partial y}-\gamma_g\frac{\partial Z}{\partial y}\right)+R_s\beta_c \frac{A_y}{B_o}\frac{k_y k_{ro}}{\mu_o}\left(\frac{\partial p_o}{\partial y}-\gamma_o\frac{\partial Z}{\partial y}\right)\right)\Delta y$$
$$+\frac{\partial}{\partial z}\left(\beta_c \frac{A_z}{B_g}\frac{k_z k_{rg}}{\mu_g}\left(\frac{\partial p_g}{\partial z}-\gamma_g\frac{\partial Z}{\partial z}\right)+R_s\beta_c \frac{A_z}{B_o}\frac{k_z k_{ro}}{\mu_o}\left(\frac{\partial p_o}{\partial z}-\gamma_o\frac{\partial Z}{\partial z}\right)\right)\Delta z$$
$$=\frac{V_b}{\alpha_c}\frac{\partial}{\partial t}\left(\frac{\phi S_g}{B_g}+\frac{\phi R_s S_o}{B_o}\right)-\left(q_{fgsc}+R_s q_{osc}\right)$$

…….. (3.10)

The set of the above three equations has six unknowns: p_o, p_w, p_g, S_o, S_w, and S_g.

We apply the two constraints:

1. Phase-saturation constraint

   $S_o + S_w + S_g = 1$

2. Capillary effects lead to a pressure difference among different phases

   $p_w = p_o - P_{cow}(S_o)$

   $p_g = p_o + P_{cgo}(S_o)$

   Usually, water is the wetting phase, oil is the intermediate-wetting phase, and gas is the nonwetting phase.

Bringing these two constraints into the previous Eq. 3.8 to 3.10; the unknown variables are reduced from six to three,

Oil:
$$\frac{\partial}{\partial x}\left(\beta_c \frac{A_x}{B_o}\frac{k_x k_{ro}}{\mu_o}\left(\frac{\partial p_o}{\partial x}-\gamma_o\frac{\partial Z}{\partial x}\right)\right)\Delta x+\frac{\partial}{\partial y}\left(\beta_c \frac{A_y}{B_o}\frac{k_y k_{ro}}{\mu_o}\left(\frac{\partial p_o}{\partial y}-\gamma_o\frac{\partial Z}{\partial y}\right)\right)\Delta y$$
$$+\frac{\partial}{\partial z}\left(\beta_c \frac{A_z}{B_o}\frac{k_z k_{ro}}{\mu_o}\left(\frac{\partial p_o}{\partial z}-\gamma_o\frac{\partial Z}{\partial z}\right)\right)\Delta z=\frac{V_b}{\alpha_c}\frac{\partial}{\partial t}\left(\frac{\phi\left(1-S_w-S_g\right)}{B_o}\right)-q_{osc}$$

…….. (3.11)

Water:
$$\frac{\partial}{\partial x}\left(\beta_c \frac{A_x}{B_w}\frac{k_x k_{rw}}{\mu_w}\left(\frac{\partial p_o}{\partial x}-\frac{\partial P_{cow}}{\partial x}-\gamma_w\frac{\partial Z}{\partial x}\right)\right)\Delta x$$
$$+\frac{\partial}{\partial y}\left(\beta_c \frac{A_y}{B_w}\frac{k_y k_{rw}}{\mu_w}\left(\frac{\partial p_o}{\partial y}-\frac{\partial P_{cow}}{\partial y}-\gamma_w\frac{\partial Z}{\partial y}\right)\right)\Delta y$$
$$+\frac{\partial}{\partial z}\left(\beta_c \frac{A_z}{B_w}\frac{k_z k_{rw}}{\mu_w}\left(\frac{\partial p_o}{\partial z}-\frac{\partial P_{cow}}{\partial z}-\gamma_w\frac{\partial Z}{\partial z}\right)\right)\Delta z=\frac{V_b}{\alpha_c}\frac{\partial}{\partial t}\left(\frac{\phi S_w}{B_w}\right)-q_{wsc}$$

…….. (3.12)

Gas:
$$\frac{\partial}{\partial x}\left(\beta_c \frac{A_x}{B_g}\frac{k_x k_{rg}}{\mu_g}\left(\frac{\partial p_o}{\partial x}+\frac{\partial P_{cgo}}{\partial x}-\gamma_g\frac{\partial Z}{\partial x}\right)+R_s\beta_c \frac{A_x}{B_o}\frac{k_x k_{ro}}{\mu_o}\left(\frac{\partial p_o}{\partial x}+\frac{\partial P_{cgo}}{\partial x}-\gamma_g\frac{\partial Z}{\partial x}\right)\right)\Delta x$$
$$+\frac{\partial}{\partial y}\left(\beta_c \frac{A_y}{B_g}\frac{k_y k_{rg}}{\mu_g}\left(\frac{\partial p_o}{\partial y}+\frac{\partial P_{cgo}}{\partial y}-\gamma_g\frac{\partial Z}{\partial y}\right)+R_s\beta_c \frac{A_y}{B_o}\frac{k_y k_{ro}}{\mu_o}\left(\frac{\partial p_o}{\partial y}+\frac{\partial P_{cgo}}{\partial y}-\gamma_g\frac{\partial Z}{\partial y}\right)\right)\Delta y$$
$$+\frac{\partial}{\partial z}\left(\beta_c \frac{A_z}{B_g}\frac{k_z k_{rg}}{\mu_g}\left(\frac{\partial p_o}{\partial z}+\frac{\partial P_{cgo}}{\partial z}-\gamma_g\frac{\partial Z}{\partial z}\right)+R_s\beta_c \frac{A_z}{B_o}\frac{k_z k_{ro}}{\mu_o}\left(\frac{\partial p_o}{\partial z}+\frac{\partial P_{cgo}}{\partial z}-\gamma_g\frac{\partial Z}{\partial z}\right)\right)\Delta z$$
$$=\frac{V_b}{\alpha_c}\frac{\partial}{\partial t}\left(\frac{\phi S_g}{B_g}+\frac{\phi R_s S_o}{B_o}\right)-\left(q_{fgsc}+R_s q_{osc}\right)$$

…….. (3.13)

So far, for any basic flow models, the equations can be expressed in terms of oil pressure and fluid saturations in the $\left(p_o - S_w - S_g\right)$ relationships.

Now we discretize the multiphase flow equations by a set of Finite Difference Equations (FDE) with defining the transmissibility, *T* at different directions *x, y,* and *z*.

$$T_{cx} = \beta_c \frac{k_x A_x}{\Delta x} \frac{k_{rc}}{\mu_c B_c} \quad T_{cy} = \beta_c \frac{k_y A_y}{\Delta y} \frac{k_{rc}}{\mu_c B_c} \quad T_{cz} = \beta_c \frac{k_z A_z}{\Delta z} \frac{k_{rc}}{\mu_c B_c}$$

…….. (3.14)

Meanwhile, the finite-difference approximation of the second-order partial derivatives in the x, y, and z directions are:

$$\frac{\partial f}{\partial x}\Delta x \approx \Delta_x f \qquad \frac{\partial f}{\partial y}\Delta y \approx \Delta_y f \qquad \frac{\partial f}{\partial z}\Delta z \approx \Delta_z f$$

The above three equations can be simplified for each gridblock (*i,j,k*) as

Oil: $$\Delta\left[T_o\left(\Delta p_o - \gamma_o \Delta Z\right)\right] = \frac{V_b}{\alpha_c \Delta t}\Delta_t\left(\frac{\phi\left(1 - S_w - S_g\right)}{B_o}\right) - q_{osc}$$ ……... (3.15)

Water: $$\Delta\left[T_w\left(\Delta p_w - \Delta P_{cow} - \gamma_w \Delta Z\right)\right] = \frac{V_b}{\alpha_c \Delta t}\Delta_t\left(\frac{\phi S_w}{B_w}\right) - q_{wsc}$$ …… (3.16)

Gas: $$\Delta\left[T_g\left(\Delta p_g + \Delta P_{cgo} - \gamma_g \Delta Z\right)\right] + \Delta\left[R_s \cdot T_o\left(\Delta p_o - \gamma_o \Delta Z\right)\right] = \frac{V_b}{\alpha_c \Delta t}\Delta_t\left(\frac{\phi S_g}{B_g} + \frac{R_s \cdot \phi\left(1 - S_g - S_w\right)}{B_o}\right) - q_{gsc}$$ ……..(3.17)

Discretizing the equations in time, the explicit finite-difference equations for all components in the black-oil model may be written in a compact form:

Oil: $$\Delta\left[T_o\left(\Delta p_o - \gamma_o \Delta Z\right)\right]^n = \frac{V_b}{\alpha_c \Delta t}\left(\left[\frac{\phi\left(1 - S_w - S_g\right)}{B_o}\right]^{n+1} - \left[\frac{\phi\left(1 - S_w - S_g\right)}{B_o}\right]^n\right) - q_{osc}^n$$

…….... (3.18)

Water: $$\Delta\left[T_w\left(\Delta p_w - \Delta P_{cow} - \gamma_w \Delta Z\right)\right]^n = \frac{V_b}{\alpha_c \Delta t}\left(\left[\frac{\phi S_w}{B_w}\right]^{n+1} - \left[\frac{\phi S_w}{B_w}\right]^n\right) - q_{wsc}^n$$

…….... (3.19)

Gas: $$\begin{aligned}&\Delta\left[T_g\left(\Delta p_g + \Delta P_{cgo} - \gamma_g \Delta Z\right)\right]^n + \Delta\left[R_s \cdot T_o\left(\Delta p_o - \gamma_o \Delta Z\right)\right]^n \\ &= \frac{V_b}{\alpha_c \Delta t}\left(\left[\frac{\phi S_g}{B_g} + \frac{R_s \cdot \phi\left(1 - S_g - S_w\right)}{B_o}\right]^{n+1} - \left[\frac{\phi S_g}{B_g} + \frac{R_s \cdot \phi\left(1 - S_g - S_w\right)}{B_o}\right]^n\right) \\ &- \left(q_{fgsc} + R_s q_{osc}\right)^n\end{aligned}$$

…….... (3.20)

In comparison, the implicit finite-difference equations for all components in the black-oil model may be written in a compact form:

Oil: $$\Delta\left[T_o\left(\Delta p_o - \gamma_o \Delta Z\right)\right]^{n+1} = \frac{V_b}{\alpha_c \Delta t}\left(\left[\frac{\phi\left(1 - S_w - S_g\right)}{B_o}\right]^{n+1} - \left[\frac{\phi\left(1 - S_w - S_g\right)}{B_o}\right]^n\right) - q_{osc}^{n+1}$$

…….... (3.21)

Water: $$\Delta\left[T_w\left(\Delta p_w - \Delta P_{cow} - \gamma_w \Delta Z\right)\right]^{n+1} = \frac{V_b}{\alpha_c \Delta t}\left(\left[\frac{\phi S_w}{B_w}\right]^{n+1} - \left[\frac{\phi S_w}{B_w}\right]^n\right) - q_{wsc}^{n+1}$$

…….... (3.22)

Gas: $$\begin{aligned}&\Delta\left[T_g\left(\Delta p_g + \Delta P_{cgo} - \gamma_g \Delta Z\right)\right]^{n+1} + \Delta\left[R_s \cdot T_o\left(\Delta p_o - \gamma_o \Delta Z\right)\right]^{n+1} \\ &= \frac{V_b}{\alpha_c \Delta t}\left(\left[\frac{\phi S_g}{B_g} + \frac{R_s \cdot \phi\left(1 - S_g - S_w\right)}{B_o}\right]^{n+1} - \left[\frac{\phi S_g}{B_g} + \frac{R_s \cdot \phi\left(1 - S_g - S_w\right)}{B_o}\right]^n\right) \\ &- \left(q_{fgsc} + R_s q_{osc}\right)^{n+1}\end{aligned}$$

…….... (3.23)

The implicit FDEs are unconditionally stable. Hence the implicit, backward-in-time discretization is used almost exclusively in modeling black-oil reservoirs.

In the expansion approach of the accumulation terms (Ertekin, 2001),

$$\Delta_t f = f^{n+1} - f^n \quad \text{..... (3.24)}$$

where f is the time accumulation term.

Converting it into the form of

$$\Delta_t (UVXY) = (UVXY)^{n+1} - (UVXY)^n \quad \text{..... (3.25)}$$

where $U \equiv \phi$, $V \equiv \dfrac{1}{B_l}$, $X \equiv R_s$, and $Y \equiv S_l$.

Continuing the derivation for the conservative expansion formula,

$$\Delta_t (UVXY) = (VXY)^n \Delta_t U + U^{n+1} (XY)^n \Delta_t V + (UV)^{n+1} Y^n \Delta_t X + (UVX)^{n+1} \Delta_t Y$$

..... (3.26)

$$\Delta_t U = \Delta_t \phi = \phi' \Delta_t p_o \quad \text{..... (3.27)}$$

$$\Delta_t V = \Delta_t \left(\frac{1}{B_l} \right) = \left(\frac{1}{B_l} \right)' \Delta_t p_o \quad \text{..... (3.28)}$$

$$\Delta_t X = \Delta_t R_s = R_s' \Delta_t p_o \quad \text{..... (3.29)}$$

$$\Delta_t Y = \Delta_t S_l = S_l' \Delta_t p_o \quad \text{..... (3.30)}$$

For a three-variable function,

$$\Delta_t \left[\frac{\phi S_l}{B_l} \right] = (UY)^n \Delta_t U + U^{n+1} (Y)^n \Delta_t V + (UV)^{n+1} \Delta_t Y$$

$$= \left(\frac{1}{B_l} S_l \right)^n \Delta_t \phi + \phi^{n+1} (S_l)^n \Delta_t \left(\frac{1}{B_l} \right) + \left(\phi \frac{1}{B_l} \right)^{n+1} \Delta_t S_l$$

$$= \left(\frac{1}{B_l} S_l\right)^n \phi' \Delta_t p_o + \phi^{n+1} (S_l)^n \left(\frac{1}{B_l}\right)' \Delta_t p_o + \left(\frac{\phi}{B_l}\right)^{n+1} \Delta_t S_l$$

$$= \left[\frac{\phi'}{B_l^n} + \phi^{n+1} \left(\frac{1}{B_l}\right)'\right] S_l{}^n \Delta_t p_o + \left(\frac{\phi}{B_l}\right)^{n+1} \Delta_t S_l$$

…….....…….....……..... (3.31)

For a four-variable function,

$$\Delta_t \left[\frac{\phi R_s S_l}{B_l}\right] = (VXY)^n \Delta_t U + U^{n+1} (XY)^n \Delta_t V + (UV)^{n+1} Y^n \Delta_t X + (UVX)^{n+1} \Delta_t Y$$

$$= \left(\frac{1}{B_l} R_s S_l\right)^n \Delta_t \phi + \phi^{n+1} (R_s S_l)^n \Delta_t \left(\frac{1}{B_l}\right) + \left(\phi \frac{1}{B_l}\right)^{n+1} S_l{}^n \Delta_t R_s + \left(\phi \frac{1}{B_l} R_s\right)^{n+1} \Delta_t S_l$$

$$= \left(\frac{1}{B_l} R_s S_l\right)^n \phi' \Delta_t p_o + \phi^{n+1} (R_s S_l)^n \Delta_t \left(\frac{1}{B_l}\right)' \Delta_t p_o + \left(\phi \frac{1}{B_l}\right)^{n+1} S_l{}^n R_s' \Delta_t p_o + \left(\phi \frac{1}{B_l} R_s\right)^{n+1} \Delta_t S_l$$

$$= \left[S_l^n R_s^n \left(\frac{1}{B_l}\right)^n \phi' + S_s^n R_s^n \phi^{n+1} \left(\frac{1}{B_l}\right)' + S_l{}^n \left(\frac{\phi}{B_l}\right)^{n+1} R_s'\right] \Delta_t p_o + \left(\frac{\phi}{B_l} R_s\right)^{n+1} \Delta_t S_l$$

$$= \left[S_l^n \left(R_s^n \left(\left(\frac{1}{B_l}\right)^n \phi' + \phi^{n+1} \left(\frac{1}{B_l}\right)'\right) + \left(\frac{\phi}{B_l}\right)^{n+1} R_s'\right)\right] \Delta_t p_o + \left(\frac{\phi}{B_l} R_s\right)^{n+1} \Delta_t S_l$$

…….....…….....……..... (3.32)

Now the implicit (backward) finite-difference equations can be in the new form of,

Oil: $$\Delta\left[T_o \left(\Delta p_o - \gamma_o \Delta Z\right)\right]^{n+1} = \frac{V_b}{\alpha_c \Delta t} \left(\left[\frac{\phi\left(1 - S_w - S_g\right)}{B_o}\right]^{n+1} - \left[\frac{\phi\left(1 - S_w - S_g\right)}{B_o}\right]^n\right) - q_{osc}^{n+1}$$

$$\Delta\left[T_o \left(\Delta p_o - \gamma_o \Delta Z\right)\right]^{n+1}$$

$$= \frac{V_b}{\alpha_c \Delta t} \left(\left[\frac{\phi'}{B_o^n} + \phi^{n+1} \left(\frac{1}{B_o}\right)'\right] \left(1 - S_w{}^n - S_g{}^n\right) \Delta_t p_o + \left(\frac{\phi}{B_o}\right)^{n+1} \Delta_t \left(1 - S_w - S_g\right)\right) - q_{osc}^{n+1}$$

$$\Delta\left[T_o\left(\Delta p_o-\gamma_o\Delta Z\right)\right]^{n+1}$$
$$=\frac{V_b}{\alpha_c\Delta t}\left(\left[\frac{\phi'}{B_o^n}+\phi^{n+1}\left(\frac{1}{B_o}\right)'\right]\left(1-S_w{}^n-S_g{}^n\right)\Delta_t p_o-\left(\frac{\phi}{B_o}\right)^{n+1}\Delta_t S_w-\left(\frac{\phi}{B_o}\right)^{n+1}\Delta_t S_g\right)-q_{osc}^{n+1}$$

$$\Delta\left[T_o\left(\Delta p_o-\gamma_o\Delta Z\right)\right]^{n+1}=\frac{V_b}{\alpha_c\Delta t}\left[\frac{\phi'}{B_o^n}+\phi^{n+1}\left(\frac{1}{B_o}\right)'\right]\left(1-S_w{}^n-S_g{}^n\right)\Delta_t p_o$$
$$-\frac{V_b}{\alpha_c\Delta t}\left(\frac{\phi}{B_o}\right)^{n+1}\Delta_t S_w-\frac{V_b}{\alpha_c\Delta t}\left(\frac{\phi}{B_o}\right)^{n+1}\Delta_t S_g-q_{osc}^{n+1}$$

…….…….…….... (3.33)

A compact form is given as:

$$\Delta\left[T_o\left(\Delta p_o-\gamma_o\Delta Z\right)\right]^{n+1}=C_{op}\Delta_t p_o+C_{ow}\Delta_t S_w+C_{og}\Delta_t S_g-q_{osc}^{n+1}$$

…….…….…….... (3.34)

where,
$$C_{op}=\frac{V_b}{\alpha_c\Delta t}\left[\frac{\phi'}{B_o^n}+\phi^{n+1}\left(\frac{1}{B_o}\right)'\right]\left(1-S_w{}^n-S_g{}^n\right)$$

$$C_{ow}=-\frac{V_b}{\alpha_c\Delta t}\left(\frac{\phi}{B_o}\right)^{n+1}$$

$$C_{og}=-\frac{V_b}{\alpha_c\Delta t}\left(\frac{\phi}{B_o}\right)^{n+1}$$

In the same way, the compact forms for water and gas phase are derived.

Water:

$$\Delta\left[T_w\left(\Delta p_o-\Delta P_{cow}-\gamma_o\Delta Z\right)\right]^{n+1}=\frac{V_b}{\alpha_c\Delta t}\left(\left[\frac{\phi'}{B_w^n}+\phi^{n+1}\left(\frac{1}{B_w}\right)'\right]S_w{}^n\Delta_t p_o+\left(\frac{\phi}{B_w}\right)^{n+1}\Delta_t S_w\right)-q_{wsc}^{n+1}$$

$$\Delta\left[T_w\left(\Delta p_o-\Delta P_{cow}-\gamma_o\Delta Z\right)\right]^{n+1}=\frac{V_b}{\alpha_c\Delta t}\left[\frac{\phi'}{B_w^n}+\phi^{n+1}\left(\frac{1}{B_w}\right)'\right]S_w{}^n\Delta_t p_o+\frac{V_b}{\alpha_c\Delta t}\left(\frac{\phi}{B_w}\right)^{n+1}\Delta_t S_w-q_{wsc}^{n+1}$$

$$\Delta\left[T_w\left(\Delta p_o - \Delta P_{cow} - \gamma_o \Delta Z\right)\right]^{n+1} = C_{wp}\Delta_t p_o + C_{ww}\Delta_t S_w + C_{wg}\Delta_t S_g - q_{osc}^{n+1}$$

…….…….…….... (3.35)

where $C_{wp} = \dfrac{V_b}{\alpha_c \Delta t}\left[\dfrac{\phi'}{B_w^n} + \phi^{n+1}\left(\dfrac{1}{B_w}\right)'\right] S_w{}^n$

$$C_{ww} = \frac{V_b}{\alpha_c \Delta t}\left(\frac{\phi}{B_w}\right)^{n+1}$$

$$C_{wg} = 0$$

Gas:

$$\Delta\left[T_g\left(\Delta p_o + \Delta P_{cgo} - \gamma_g \Delta Z\right)\right]^{n+1} + \Delta\left[R_s \cdot T_o\left(\Delta p_o - \gamma_o \Delta Z\right)\right]^{n+1}$$

$$= \frac{V_b}{\alpha_c \Delta t}\left(\left[\frac{\phi S_g}{B_g} + \frac{R_s \cdot \phi\left(1 - S_g - S_w\right)}{B_o}\right]^{n+1} - \left[\frac{\phi S_g}{B_g} + \frac{R_s \cdot \phi\left(1 - S_g - S_w\right)}{B_o}\right]^{n}\right) - \left(q_{fgsc} + R_s q_{osc}\right)^{n+1}$$

$$\Delta\left[T_g\left(\Delta p_o + \Delta P_{cgo} - \gamma_g \Delta Z\right)\right]^{n+1} + \Delta\left[R_s \cdot T_o\left(\Delta p_o - \gamma_o \Delta Z\right)\right]^{n+1}$$

$$= \frac{V_b}{\alpha_c \Delta t}\left(\left[S_o^n\left(R_s^n\left[\frac{\phi'}{B_o^n} + \phi^{n+1}\left(\frac{1}{B_o}\right)'\right] + \left(\frac{\phi}{B_o}\right)^{n+1} R_s'\right)\right]\Delta_t p_o + \left(\frac{\phi}{B_o} R_s\right)^{n+1}\Delta_t S_o + \frac{\phi}{B_g}\Delta_t S_g\right)$$

$$- \left(q_{fgsc} + R_s q_{osc}\right)^{n+1}$$

$$\Delta\left[T_g\left(\Delta p_o + \Delta P_{cgo} - \gamma_g \Delta Z\right)\right]^{n+1} + \Delta\left[R_s \cdot T_o\left(\Delta p_o - \gamma_o \Delta Z\right)\right]^{n+1}$$

$$= \frac{V_b}{\alpha_c \Delta t}\left(\left\{R_s^n\left[\frac{\phi'}{B_o^n} + \phi^{n+1}\left(\frac{1}{B_o}\right)'\right] + \left(\frac{\phi}{B_o}\right)^{n+1} R_s'\right\} S_o^n \Delta_t p_o + \left(\frac{\phi}{B_o} R_s\right)^{n+1}\Delta_t S_o + \frac{\phi}{B_g}\Delta_t S_g\right)$$

$$- \left(q_{fgsc} + R_s q_{osc}\right)^{n+1}$$

$$\Delta\left[T_g\left(\Delta p_o + \Delta P_{cgo} - \gamma_g \Delta Z\right)\right]^{n+1} + \Delta\left[R_s \cdot T_o\left(\Delta p_o - \gamma_o \Delta Z\right)\right]^{n+1}$$

$$= \frac{V_b}{\alpha_c \Delta t}\left\{ R_s^n \left[\frac{\phi'}{B_o^n} + \phi^{n+1}\left(\frac{1}{B_o}\right)' \right] + \left(\frac{\phi}{B_o}\right)^{n+1} R_s' \right\}\left(1 - S_w^n - S_g^n\right)\Delta_t p_o$$

$$+ \frac{V_b}{\alpha_c \Delta t}\left(\frac{\phi}{B_o} R_s\right)^{n+1} \Delta_t\left(1 - S_w - S_g\right) + \frac{V_b}{\alpha_c \Delta t}\frac{\phi}{B_g}\Delta_t S_g - \left(q_{fgsc} + R_s q_{osc}\right)^{n+1}$$

$$\Delta\left[T_g\left(\Delta p_o + \Delta P_{cgo} - \gamma_g \Delta Z\right)\right]^{n+1} + \Delta\left[R_s \cdot T_o\left(\Delta p_o - \gamma_o \Delta Z\right)\right]^{n+1}$$

$$= \frac{V_b}{\alpha_c \Delta t}\left\{ R_s^n \left[\frac{\phi'}{B_o^n} + \phi^{n+1}\left(\frac{1}{B_o}\right)' \right] + \left(\frac{\phi}{B_o}\right)^{n+1} R_s' \right\}\left(1 - S_w^n - S_g^n\right)\Delta_t p_o$$

$$- \frac{V_b}{\alpha_c \Delta t}\left(\frac{\phi}{B_o} R_s\right)^{n+1} \Delta_t S_w + \frac{V_b}{\alpha_c \Delta t}\left(\frac{\phi}{B_g} - \left(\frac{\phi}{B_o} R_s\right)^{n+1}\right)\Delta_t S_g - \left(q_{fgsc} + R_s q_{osc}\right)^{n+1}$$

$$\Delta\left[T_g\left(\Delta p_o + \Delta P_{cgo} - \gamma_g \Delta Z\right)\right]^{n+1} + \Delta\left[R_s \cdot T_o\left(\Delta p_o - \gamma_o \Delta Z\right)\right]^{n+1}$$

$$= C_{gp}\Delta_t p_o - C_{gw}\Delta_t S_w - C_{gg}\Delta_t S_g - q_{gsc}^{n+1} \quad \text{..... (3.36)}$$

where $C_{gp} = \dfrac{V_b}{\alpha_c \Delta t}\left\{ \left[\dfrac{\phi'}{B_o^n} + \phi^{n+1}\left(\dfrac{1}{B_o}\right)' \right] R_s^n + \left(\dfrac{\phi}{B_o}\right)^{n+1} R_s' \right\}\left(1 - S_w^n - S_g^n\right)$

$$C_{gw} = -\frac{V_b}{\alpha_c \Delta t}\left(\frac{\phi}{B_o} R_s\right)^{n+1}$$

$$C_{gg} = \frac{V_b}{\alpha_c \Delta t}\left(\frac{\phi}{B_g} - \frac{\phi}{B_o} R_s\right)^{n+1}$$

$$q_{gsc}^{n+1} = \left(q_{fgsc} + R_s q_{osc}\right)^{n+1}$$

IMPES Model

The objective of the IMPES method is to obtain a single pressure equation for each grid block by combining all flow equations to eliminate the saturation unknowns, which means capillary pressure and transmissibilities are evaluated explicitly (at time level *n*).

IMPES Method for Three-Phase Black-Oil Model

Summarizing the explicit transmissibilities, flow rates, and capillary pressures, these equations for gridblock *n* are:

Oil: $$\Delta\left[T_o\left(\Delta p_o - \gamma_o \Delta Z\right)\right]^{n+1} = C_{op}\Delta_t p_o + C_{ow}\Delta_t S_w + C_{og}\Delta_t S_g - q_{osc}^{n+1}$$

…….. (3.37)

Water: $$\Delta\left[T_w\left(\Delta p_w - \Delta P_{cow} - \gamma_o \Delta Z\right)\right]^{n+1} = C_{wp}\Delta_t p_o + C_{ww}\Delta_t S_w + C_{wg}\Delta_t S_g - q_{osc}^{n+1}$$

…….. (3.38)

Gas: $$\Delta\left[T_g\left(\Delta p_g + \Delta P_{cgo} - \gamma_g \Delta Z\right)\right]^{n+1} + \Delta\left[R_s \cdot T_o\left(\Delta p_o - \gamma_o \Delta Z\right)\right]^{n+1} = C_{gp}\Delta_t p_o + C_{gw}\Delta_t S_w + C_{gg}\Delta_t S_g - q_{gsc}^{n+1}$$

…….. (3.39)

We determine the multipliers *A* and *B* for water and gas equations respectively,

$$A = \frac{B_{w_n}^{n+1}}{\left(B_o - R_s B_g\right)_n^{n+1}}$$ ……. (3.40)

$$B = \frac{B_{g_n}^{n+1}}{\left(B_o - R_s B_g\right)_n^{n+1}}$$ ……. (3.41)

The new material balance equations for water and gas phases are,

$$A\left[\Delta\left[T_w\left(\Delta p_w - \Delta P_{cow} - \gamma_o \Delta Z\right)\right]^{n+1}\right] = A\left(C_{wp}\Delta_t p_o + C_{ww}\Delta_t S_w + C_{wg}\Delta_t S_g - q_{osc}^{n+1}\right)$$

…….... (3.42)

Gas:
$$B\left[\Delta\left[T_g\left(\Delta p_g + \Delta P_{cgo} - \gamma_g \Delta Z\right)\right]^{n+1} + \Delta\left[R_s \cdot T_o\left(\Delta p_o - \gamma_o \Delta Z\right)\right]^{n+1}\right]$$
$$= B\left(C_{gp}\Delta_t p_o - C_{gw}\Delta_t S_w - C_{gg}\Delta_t S_g - q_{gsc}^{n+1}\right)$$

…….... (3.43)

After summing the Eq. 4.44 to 4.46 and multiplying the term $\left(B_o - R_s B_g\right)_n^{n+1}$,

Oil:
$$\Delta\left[T_o\left(\Delta p_o - \gamma_o \Delta Z\right)\right]^{n+1} = C_{op}\Delta_t p_o + C_{ow}\Delta_t S_w + C_{og}\Delta_t S_g - q_{osc}^{n+1}$$

…….... (3.44)

Water:
$$\frac{B_{w_n}^{n+1}}{\left(B_o - R_s B_g\right)_n^{n+1}}\left(\Delta\left[T_w\left(\Delta p_w - \Delta P_{cow} - \gamma_o \Delta Z\right)\right]^{n+1}\right)$$
$$= \frac{B_{w_n}^{n+1}}{\left(B_o - R_s B_g\right)_n^{n+1}}\left(C_{wp}\Delta_t p_o + C_{ww}\Delta_t S_w + C_{wg}\Delta_t S_g - q_{osc}^{n+1}\right)$$

…….... (3.45)

Gas:
$$\frac{B_{g_n}^{n+1}}{\left(B_o - R_s B_g\right)_n^{n+1}}\left(\Delta\left[T_g\left(\Delta p_g + \Delta P_{cgo} - \gamma_g \Delta Z\right)\right]^{n+1} + \Delta\left[R_s \cdot T_o\left(\Delta p_o - \gamma_o \Delta Z\right)\right]^{n+1}\right)$$
$$= \frac{B_{g_n}^{n+1}}{\left(B_o - R_s B_g\right)_n^{n+1}}\left(C_{gp}\Delta_t p_o - C_{gw}\Delta_t S_w - C_{gg}\Delta_t S_g - q_{gsc}^{n+1}\right)$$

…….... (3.46)

Left-Hand-Side:

$$\left(B_o - R_s B_g\right)_n^{n+1}\Delta\left[T_o\left(\Delta p_o - \gamma_o \Delta Z\right)\right]^{n+1} + B_{w_n}^{n+1}\left(\Delta\left[T_w\left(\Delta p_w - \Delta P_{cow} - \gamma_o \Delta Z\right)\right]^{n+1}\right)$$
$$+ B_{g_n}^{n+1}\left(\Delta\left[T_g\left(\Delta p_g + \Delta P_{cgo} - \gamma_g \Delta Z\right)\right]^{n+1} + \Delta\left[R_s \cdot T_o\left(\Delta p_o - \gamma_o \Delta Z\right)\right]^{n+1}\right)$$

Right-Hand-Side:

$$\left(B_o - R_s B_g\right)_n^{n+1}\left(C_{op}\Delta_t p_o + C_{ow}\Delta_t S_w + C_{og}\Delta_t S_g - q_{osc}^{n+1}\right)$$
$$+ B_{w_n}^{n+1}\left(C_{wp}\Delta_t p_o + C_{ww}\Delta_t S_w + C_{wg}\Delta_t S_g - q_{osc}^{n+1}\right)$$
$$+ B_{g_n}^{n+1}\left(C_{gp}\Delta_t p_o - C_{gw}\Delta_t S_w - C_{gg}\Delta_t S_g - q_{gsc}^{n+1}\right)$$

$$= \left[\left(B_o - R_s B_g\right)_n^{n+1} C_{op} + B_{w_n}^{n+1} C_{wp} + B_{g_n}^{n+1} C_{gp}\right]\Delta_t p_o$$
$$+ \left[\left(B_o - R_s B_g\right)_n^{n+1} C_{ow} + B_{w_n}^{n+1} C_{ww} - B_{g_n}^{n+1} C_{gw}\right]\Delta_t S_w$$
$$+ \left[\left(B_o - R_s B_g\right)_n^{n+1} C_{og} + B_{w_n}^{n+1} C_{wg} - B_{g_n}^{n+1} C_{gg}\right]S_g$$
$$- \left[\left(B_o - R_s B_g\right)_n^{n+1} q_{osc}^{n+1} + B_{w_n}^{n+1} q_{osc}^{n+1} + B_{g_n}^{n+1} q_{gsc}^{n+1}\right]$$

$$= \left[\left(B_o - R_s B_g\right)_n^{n+1} C_{op} + B_{w_n}^{n+1} C_{wp} + B_{g_n}^{n+1} C_{gp}\right]\Delta_t p_o$$
$$- \left[\left(B_o - R_s B_g\right)_n^{n+1} q_{osc}^{n+1} + B_{w_n}^{n+1} q_{osc}^{n+1} + B_{g_n}^{n+1} q_{gsc}^{n+1}\right]$$
$$+ \left[\left(B_o - R_s B_g\right)_n^{n+1} C_{ow} + B_{w_n}^{n+1} C_{ww} - B_{g_n}^{n+1} C_{gw}\right]\Delta_t S_w$$
$$+ \left[\left(B_o - R_s B_g\right)_n^{n+1} C_{og} + B_{w_n}^{n+1} C_{wg} - B_{g_n}^{n+1} C_{gg}\right]S_g$$

$$= \left[\left(B_o - R_s B_g\right)_n^{n+1} C_{op} + B_{w_n}^{n+1} C_{wp} + B_{g_n}^{n+1} C_{gp}\right]\Delta_t p_o$$
$$- \left[\left(B_o - R_s B_g\right)_n^{n+1} q_{osc}^{n+1} + B_{w_n}^{n+1} q_{osc}^{n+1} + B_{g_n}^{n+1} q_{gsc}^{n+1}\right]$$
$$+ \left[\left(B_o - R_s B_g\right)_n^{n+1} C_{ow} + B_{w_n}^{n+1} C_{ww} - B_{g_n}^{n+1} C_{gw}\right]\Delta_t S_w$$
$$+ \left[\left(B_o - R_s B_g\right)_n^{n+1} C_{og} + B_{w_n}^{n+1} C_{wg} - B_{g_n}^{n+1} C_{gg}\right]S_g$$

$$= \left[\left(B_o - R_s B_g\right)_n^{n+1} C_{op} + B_{w_n}^{n+1} C_{wp} + B_{g_n}^{n+1} C_{gp}\right]\Delta_t p_o$$
$$- \left[\left(B_o - R_s B_g\right)_n^{n+1} q_{osc}^{n+1} + B_{w_n}^{n+1} q_{osc}^{n+1} + B_{g_n}^{n+1} q_{gsc}^{n+1}\right]$$

So the final form is,

$$\left(B_o - R_s B_g\right)_n^{n+1} \Delta\left[T_o\left(\Delta p_o - \gamma_o \Delta Z\right)\right]^{n+1} + B_{w_n}^{n+1}\left(\Delta\left[T_w\left(\Delta p_w - \Delta P_{cow} - \gamma_o \Delta Z\right)\right]^{n+1}\right)$$
$$+ B_{g_n}^{n+1}\left(\Delta\left[T_g\left(\Delta p_g + \Delta P_{cgo} - \gamma_g \Delta Z\right)\right]^{n+1} + \Delta\left[R_s \cdot T_o\left(\Delta p_o - \gamma_o \Delta Z\right)\right]^{n+1}\right)$$
$$= \left[\left(B_o - R_s B_g\right)_n^{n+1} C_{op} + B_{w_n}^{n+1} C_{wp} + B_{g_n}^{n+1} C_{gp}\right]\Delta_t p_o - \left[\left(B_o - R_s B_g\right)_n^{n+1} q_{osc}^{n+1} + B_{w_n}^{n+1} q_{osc}^{n+1} + B_{g_n}^{n+1} q_{gsc}^{n+1}\right]$$

……..……..... (3.46)

Applying the control volume finite difference method (CVFD), which is used for the expansion of the spatial-difference operator at a given gridblock-ordering in multidimensional space, the above equation is expressed as,

$$\sum_{m\in\psi_n}\left\{\left(B_o - R_s B_g\right)_n^{n+1} T_{o\,n,m}^{\,n} + B_{w\;n}^{n+1} T_{w\,n,m}^{n} + B_{g\;n}^{n+1}\left[T_{g\,n,m}^{\,n} + \left(T_o R_s\right)_{n,m}^{n}\right]\right\} p_{o\;m}^{n+1}$$
$$-\left(\begin{array}{l}\left(B_o - R_s B_g\right)_n^{n+1} C_{op\,n} + B_{w\;n}^{n+1} C_{wp\,n} + B_{g\;n}^{n+1} C_{gp\,n} \\ + \sum_{m\in\psi_n}\left\{\left(B_o - R_s B_g\right)_n^{n+1} T_{o\,n,m}^{\,n} + B_{w\;n}^{n+1} T_{w\,n,m}^{n} + B_{g\;n}^{n+1}\left[T_{g\,n,m}^{\,n} + \left(T_o R_s\right)_{n,m}^{n}\right]\right\}\end{array}\right) p_{o\;n}^{n+1}$$
$$= -\left[\left(B_o - R_s B_g\right)_n^{n+1} C_{op\,n} + B_{w\;n}^{n+1} C_{wp\,n} + B_{g\;n}^{n+1} C_{gp\,n}\right] p_{o\,n}^{n}$$
$$-\left[\left(B_o - R_s B_g\right)_n^{n+1} q_{osc\,n}^{n} + B_{w\;n}^{n+1} q_{wsc\,n}^{n} + B_{g\;n}^{n+1} q_{gsc\,n}^{n}\right] + \sum_{m\in\psi_n} B_{w\;n}^{n+1} T_{w\,n,m}^{n}\left(P_{cow\,m}^{n} - P_{cow\,n}^{n}\right)$$
$$-\sum_{m\in\psi_n} B_{g\;n}^{n+1} T_{g\,n,m}^{\,n}\left(P_{cgo\,m}^{n} - P_{cgo\,n}^{n}\right) + \sum_{m\in\psi_n}\left\{\begin{array}{l}\left(B_o - R_s B_g\right)_n^{n+1} T_{o\,n,m}^{\,n}\,\bar{\gamma}_{o\,n,m}^{\,n} + B_{w\;n}^{n+1} T_{w\,n,m}^{n}\,\bar{\gamma}_{w\,n,m}^{\,n} \\ + B_{g\;n}^{n+1}\left[T_{g\,n,m}^{\,n}\,\bar{\gamma}_{g\,n,m}^{\,n} + \left(T_o R_s\right)_{n,m}^{n}\,\bar{\gamma}_{o\,n,m}^{\,n}\right]\end{array}\right\}\left(Z_m - Z_n\right)$$

……..……..... (3.47)

where the subscript m is the neighboring gridblock to gridblock n

n is the study gridblock

the superscript n is old timestep

$n+1$ is current timestep

$m \in \psi_n$ is the study matrix, in a simplified case, only x-direction

Eq. 3.47 is the formulated form for the final diffusivity equation.

In a simple example of a water/gas two-phase system:

1. The solution-gas/oil ratio, R_S, is zero for any pressure and timestep;
2. All the terms with subscript of "o"are zero;
3. No gradational variation;
4. P_{cgo} is same as P_{cgw}.

The final formulated equation will be simplified as:

$$\sum_{m\in\psi_n}\left\{B_{w\ n}^{n+1}T_{w\ n,m}^{n}+B_{g\ n}^{n+1}\left[T_{g\ n,m}^{n}\right]\right\}p_{w\ m}^{n+1}$$
$$-\left(B_{w\ n}^{n+1}C_{wp_n}+B_{g\ n}^{n+1}C_{gp_n}+\sum_{m\in\psi_n}\left\{B_{w\ n}^{n+1}T_{w\ n,m}^{n}+B_{g\ n}^{n+1}\left[T_{g\ n,m}^{n}\right]\right\}\right)p_{w\ n}^{n+1}$$
$$=-\left[B_{w\ n}^{n+1}C_{wp_n}+B_{g\ n}^{n+1}C_{gp_n}\right]p_{wn}^{n}-\left[B_{w\ n}^{n+1}q_{wsc\,n}^{n}+B_{g\ n}^{n+1}q_{gsc_n}\right]-\sum_{m\in\psi_n}B_{g\ n}^{n+1}T_{g\ n,m}^{n}\left(P_{cgo\,m}^{n}-P_{cgo_n}^{n}\right)$$
……..…….... (3.48)

Eq. 3.48 is also derived starting the material balance equation in **Appendix A**.

Calculating the flow rates between adjacent gridblocks in the three-phase system:

$$S_{wn}^{n+1}=S_{wn}^{n}+\frac{1}{C_{wwn}}\left\{\sum_{m\in\psi_n}\left[T_{w\ n,m}^{n}\left(\Delta_m p_o^{n+1}-\Delta_m P_{cow}^{n}-\bar{\gamma}_{w\,n,m}^{n}\Delta_m Z\right)\right]-C_{wp_n}\left(p_{o\ n}^{n+1}-p_{o\,n}^{n}\right)+q_{wsc\,n}^{n}\right\}$$
……..…….... (3.49)

$$S_{gn}^{n+1}=S_{gn}^{n}+\frac{1}{C_{og_n}}\left\{\sum_{m\in\psi_n}\left[T_{o\ n,m}^{n}\left(\Delta_m p_o^{n+1}-\bar{\gamma}_{wn,m}^{n}\Delta_m Z\right)\right]-C_{op_n}\left(p_{o\ n}^{n+1}-p_{o\,n}^{n}\right)-C_{ow_n}\left(S_{w\ n}^{n+1}-S_{wn}^{n}\right)+q_{osc\,n}^{n}\right\}$$
……..…….... (3.50)

Calculating the flow rates between adjacent gridblocks in the two-phase system:

$$S_{w\ n}^{n+1} = S_{wn}^{n} + \frac{1}{C_{wwn}}\left\{\Delta\left[T_w\left(\Delta p_w - \gamma_w \Delta Z\right)\right]^{n+1} - C_{wp}\Delta_t p_w + q_{wsc}^{n+1}\right\}$$

…….... (3.51)

$$S_{g\ n}^{n+1} = S_{g\ n}^{n} + \frac{1}{C_{gg\ n}}\left\{\Delta\left[T_g\left(\Delta p_w + \Delta P_{cgo} - \gamma_g \Delta Z\right)\right]^{n+1} - C_{gp}\Delta_t p_w + q_{gsc}^{n+1}\right\}$$

or $S_{g\ n}^{n+1} = 1 - S_{w\ n}^{n+1}$

…….... (3.52)

Calculating the flow rates between adjacent gridblocks in the three-phase system:

Oil: $$q_o^{n+1} = q_{osc}^{n+1} B_o^{n+1} = C_{op}\Delta_t p_o + C_{ow}\Delta_t S_w + C_{og}\Delta_t S_g - \Delta\left[T_o\left(\Delta p_o - \gamma_o \Delta Z\right)\right]^{n+1}$$

…….... (3.53)

Water: $$q_w^{n+1} = q_{wsc}^{n+1} B_w^{n+1} = C_{wp}\Delta_t p_o + C_{ww}\Delta_t S_w + C_{wg}\Delta_t S_g - \Delta\left[T_w\left(\Delta p_w - \Delta P_{cow} - \gamma_o \Delta Z\right)\right]^{n+1}$$

…….... (3.54)

Gas: $$q_g^{n+1} = q_{gsc}^{n+1} B_g^{n+1} = C_{gp}\Delta_t p_o + C_{gw}\Delta_t S_w + C_{gg}\Delta_t S_g$$
$$-\left(\Delta\left[T_g\left(\Delta p_g + \Delta P_{cgo} - \gamma_g \Delta Z\right)\right]^{n+1} + \Delta\left[R_s \cdot T_o\left(\Delta p_o - \gamma_o \Delta Z\right)\right]^{n+1}\right)$$

…….... (3.55)

To calculate the water and gas flowrates in the three-phase system explicitly:

$$q_{wsc}^{n+1} = C_{wp}\Delta_t p_o + C_{ww}\Delta_t S_w - \Delta\left[T_w\left(\Delta p_w - \gamma_w \Delta Z\right)\right]^{n+1}$$

…….... (3.56)

$$q_{gsc}^{n+1} = C_{gp}\Delta_t p_w + C_{gg}\Delta_t S_g - \Delta\left[T_g\left(\Delta p_w + \Delta P_{cgo} - \gamma_g \Delta Z\right)\right]^{n+1}$$

……...……..... (3.57)

We perform Newton-Raphson iterations on $B_{o\ n}^{n+1}$, $B_{w\ n}^{n+1}$, $B_{g\ n}^{n+1}$, $R_{S\ n}^{n+1}$, C_{op_n}, C_{wp_n} and C_{gp_n} during each timestep. At the new timestep, the simulator updates all the PVT data and calculates the maximum relative difference between the new pressure and the iterative pressure distributions. If the maximum relative error is bigger than the valve value, 10^{-6}, the program will go back to re-solve the linear equation according to the new PVT data. After a certain number of iterations, the valve value will be increased to avoid the diverging problem. Then the FORTRAN program solves the saturations explicitly.

CHAPTER IV

CHARACTERIZATION OF BOUNDARY CONDITIONS

In the previous sections, the formulated FDEs were obtained; however, to solve for p_o^{n+1}, the initial conditions, and the inner and outer boundary conditions must be specified. Three possible specifications of boundaries are discussed in this section, including fixed or constant bottomhole pressure, constant influx rate (closed boundary), and constant pressure drop over time. In the discussion of the inner boundary, the outer boundary is specified as constant reservoir pressure; in the discussion of the outer boundary, the inner boundary is specified as constant production rate.

In this section, the subscript *n* represents the furthest gridblock at the outer boundary conditions; and the subscript *1* represents the nearest gridblock at the inner boundary condition. The matrix coefficients are *a*, *b*, *c*, and *d* in the linear equations. The derivation starts from the final formulated equation, Eq. 3.47,

$$
\begin{aligned}
&\sum_{m\in\psi_n}\left\{\left(B_o-R_sB_g\right)_n^{n+1}T_{o\,n,m}^{n}+B_{w\;n}^{n+1}T_{w\,n,m}^{n}+B_{g\;n}^{n+1}\left[T_{g\,n,m}^{n}+\left(T_oR_s\right)_{n,m}^{n}\right]\right\}p_{o\;m}^{n+1}\\
&-\left(\begin{array}{l}\left(B_o-R_sB_g\right)_n^{n+1}C_{op\,n}+B_{w\;n}^{n+1}C_{wp\,n}+B_{g\;n}^{n+1}C_{gp\,n}\\+\sum_{m\in\psi_n}\left\{\left(B_o-R_sB_g\right)_n^{n+1}T_{o\,n,m}^{n}+B_{w\;n}^{n+1}T_{w\,n,m}^{n}+B_{g\;n}^{n+1}\left[T_{g\,n,m}^{n}+\left(T_oR_s\right)_{n,m}^{n}\right]\right\}\end{array}\right)p_{o\;n}^{n+1}\\
&=-\left[\left(B_o-R_sB_g\right)_n^{n+1}C_{op\,n}+B_{w\;n}^{n+1}C_{wp\,n}+B_{g\;n}^{n+1}C_{gp\,n}\right]p_{o\,n}^{n}\\
&-\left[\left(B_o-R_sB_g\right)_n^{n+1}q_{osc\,n}^{n}+B_{w\;n}^{n+1}q_{wsc\,n}^{n}+B_{g\;n}^{n+1}q_{gsc\,n}^{n}\right]+\sum_{m\in\psi_n}B_{w\;n}^{n+1}T_{w\,n,m}^{n}\left(P_{cow\,m}^{n}-P_{cow\,n}^{n}\right)\\
&-\sum_{m\in\psi_n}B_{g\;n}^{n+1}T_{g\,n,m}^{n}\left(P_{cgo\,m}^{n}-P_{cgo\,n}^{n}\right)+\sum_{m\in\psi_n}\left\{\begin{array}{l}\left(B_o-R_sB_g\right)_n^{n+1}T_{o\,n,m}^{n}\bar{\gamma}_{o\,n,m}^{n}+B_{w\;n}^{n+1}T_{w\,n,m}^{n}\bar{\gamma}_{w\,n,m}^{n}\\+B_{g\;n}^{n+1}\left[T_{g\,n,m}^{n}\bar{\gamma}_{g\,n,m}^{n}+\left(T_oR_s\right)_{n,m}^{n}\bar{\gamma}_{o\,n,m}^{n}\right]\end{array}\right\}\left(Z_m-Z_n\right)
\end{aligned}
$$

……..…….... (3.47)

Rearranging,

$$\begin{aligned}
&\left\{\left(B_o - R_s B_g\right)_n^{n+1} T_{o\,n,n-1}^{\,n} + B_{w\;n}^{n+1} T_{w\,n,n-1}^{\,n} + B_{g\;n}^{n+1}\left[T_{g\,n,n-1}^{\,n} + \left(T_o R_s\right)_{n,n-1}^{n}\right]\right\} p_{o\;n-1}^{n+1} \\
&-\left(\begin{array}{l}
\left(B_o - R_s B_g\right)_n^{n+1} C_{op\,n} + B_{w\;n}^{n+1} C_{wp\,n} + B_{g\;n}^{n+1} C_{gp\,n} \\
+\left(B_o - R_s B_g\right)_n^{n+1} T_{o\,n,n-1}^{\,n} + B_{w\;n}^{n+1} T_{w\,n,n-1}^{\,n} + B_{g\;n}^{n+1}\left[T_{g\,n,n-1}^{\,n} + \left(T_o R_s\right)_{n,n-1}^{n}\right] \\
+\left(B_o - R_s B_g\right)_n^{n+1} T_{o\,n+1,n}^{\,n} + B_{w\;n}^{n+1} T_{w\,n+1,n}^{\,n} + B_{g\;n}^{n+1}\left[T_{g\,n+1,n}^{\,n} + \left(T_o R_s\right)_{n+1,n}^{n}\right]
\end{array}\right) p_{o\;n}^{n+1} \\
&+\left\{\left(B_o - R_s B_g\right)_n^{n+1} T_{o\,n+1,n}^{\,n} + B_{w\;n}^{n+1} T_{w\,n+1,n}^{\,n} + B_{g\;n}^{n+1}\left[T_{g\,n+1,n}^{\,n} + \left(T_o R_s\right)_{n+1,n}^{n}\right]\right\} p_{o\;n+1}^{n+1} \\
&= -\left[\left(B_o - R_s B_g\right)_n^{n+1} C_{op\,n} + B_{w\;n}^{n+1} C_{wp\,n} + B_{g\;n}^{n+1} C_{gp\,n}\right] p_{o\,n}^{n} - \left[\left(B_o - R_s B_g\right)_n^{n+1} q_{osc\,n}^{n} + B_{w\;n}^{n+1} q_{wsc\,n}^{n} + B_{g\;n}^{n+1} q_{gsc\,n}^{n}\right] \\
&+ \sum_{m\in\psi_n} B_{w\;n}^{n+1} T_{w\,n,m}^{\,n}\left(P_{cow\,m}^{n} - P_{cow\,n}^{n}\right) - \sum_{m\in\psi_n} B_{g\;n}^{n+1} T_{g\,n,m}^{\,n}\left(P_{cgo\,m}^{n} - P_{cgo\,n}^{n}\right) \\
&+ \sum_{m\in\psi_n} \left\{\left(B_o - R_s B_g\right)_n^{n+1} T_{o\,n,m}^{\,n} \bar{\gamma}_{o\,n,m}^{\,n} + B_{w\;n}^{n+1} T_{w\,n,m}^{\,n} \bar{\gamma}_{w\,n,m}^{\,n} + B_{g\;n}^{n+1}\left[T_{g\,n,m}^{\,n} \bar{\gamma}_{g\,n,m}^{\,n} + \left(T_o R_s\right)_{n,m}^{n} \bar{\gamma}_{o\,n,m}^{\,n}\right]\right\}\left(Z_m - Z_n\right)
\end{aligned}$$

…….....…….…..... (4.1)

So the matrix coefficients are,

$$a_i = \left\{\left(B_o - R_s B_g\right)_n^{n+1} T_{o\,n,n-1}^{\,n} + B_{w\;n}^{n+1} T_{w\,n,n-1}^{\,n} + B_{g\;n}^{n+1}\left[T_{g\,n,n-1}^{\,n} + \left(T_o R_s\right)_{n,n-1}^{n}\right]\right\}$$

…….....…….…..... (4.2)

$$b_i = \left(\begin{array}{l}
\left(B_o - R_s B_g\right)_n^{n+1} C_{op\,n} + B_{w\;n}^{n+1} C_{wp\,n} + B_{g\;n}^{n+1} C_{gp\,n} \\
+\left(B_o - R_s B_g\right)_n^{n+1} T_{o\,n,n-1}^{\,n} + B_{w\;n}^{n+1} T_{w\,n,n-1}^{\,n} + B_{g\;n}^{n+1}\left[T_{g\,n,n-1}^{\,n} + \left(T_o R_s\right)_{n,n-1}^{n}\right] \\
+\left(B_o - R_s B_g\right)_n^{n+1} T_{o\,n+1,n}^{\,n} + B_{w\;n}^{n+1} T_{w\,n+1,n}^{\,n} + B_{g\;n}^{n+1}\left[T_{g\,n+1,n}^{\,n} + \left(T_o R_s\right)_{n+1,n}^{n}\right]
\end{array}\right)$$

…….....…….…..... (4.3)

$$c_i = \left\{\left(B_o - R_s B_g\right)_n^{n+1} T_{o\,n+1,n}^{\,n} + B_{w\;n}^{n+1} T_{w\,n+1,n}^{\,n} + B_{g\;n}^{n+1}\left[T_{g\,n+1,n}^{\,n} + \left(T_o R_s\right)_{n+1,n}^{n}\right]\right\}$$

…….....…….…..... (4.4)

$$
\begin{aligned}
d_i = &-\left[\left(B_o - R_s B_g\right)_n^{n+1} C_{op\,n} + B_{w\;n}^{n+1} C_{wp\,n} + B_{g\;n}^{n+1} C_{gp\,n}\right] p_{o\,n}^{n} \\
&-\left[\left(B_o - R_s B_g\right)_n^{n+1} q_{osc\,n}^{n} + B_{w\;n}^{n+1} q_{wsc\,n}^{n} + B_{g\;n}^{n+1} q_{gsc\,n}^{n}\right] + \sum_{m\in\psi_n} B_{w\;n}^{n+1} T_{w\,n,m}^{n} \left(P_{cow\,m}^{n} - P_{cow\,n}^{n}\right) \\
&- \sum_{m\in\psi_n} B_{g\;n}^{n+1} T_{g\,n,m}^{n} \left(P_{cgo\,m}^{n} - P_{cgo\,n}^{n}\right) \\
&+ \sum_{m\in\psi_n} \left\{ \begin{array}{l} \left(B_o - R_s B_g\right)_n^{n+1} T_{o\,n,m}^{n} \bar{\gamma}_{o\,n,m}^{n} + B_{w\;n}^{n+1} T_{w\,n,m}^{n} \bar{\gamma}_{w\,n,m}^{n} \\ + B_{g\;n}^{n+1} \left[T_{g\,n,m}^{n} \bar{\gamma}_{g\,n,m}^{n} + \left(T_o R_s\right)_{n,m}^{n} \bar{\gamma}_{o\,n,m}^{n} \right] \end{array} \right\} \left(Z_m - Z_n\right)
\end{aligned}
$$

……..……..... (4.5)

Formulated into the matrix form,

$$
\begin{vmatrix} b_1 & c_1 & 0 & 0 & 0 \\ a_2 & b_2 & c_2 & 0 & 0 \\ 0 & ... & ... & ... & 0 \\ 0 & 0 & a_{n-1} & b_{n-1} & c_{n-1} \\ 0 & 0 & 0 & a_n & b_n \end{vmatrix} \begin{vmatrix} p_1^{n+1} \\ p_2^{n+1} \\ ... \\ p_{n-1}^{n+1} \\ p_n^{n+1} \end{vmatrix} = \begin{vmatrix} d_1^n \\ d_2^n \\ ... \\ d_{n-1}^n \\ d_n^n \end{vmatrix}
$$

……..……..... (4.6)

Discussion of the Inner Boundary

Constant rate production

Because p_n is constant at the outer boundary and d_n is constant, the linear equation is not appropriate for the pressure vector in the left. A modification is made,

$$
d_{n-1}^{n(new)} = d_{n-1}^{n} - c_n p_n^{n+1}
$$

$$\begin{vmatrix} b_1 & c_1 & 0 & 0 & 0 \\ a_2 & b_2 & c_2 & 0 & 0 \\ 0 & ... & ... & ... & 0 \\ 0 & 0 & a_{n-2} & b_{n-2} & c_{n-2} \\ 0 & 0 & 0 & a_{n-1} & b_{n-1} \end{vmatrix} \begin{vmatrix} p_1^{n+1} \\ p_2^{n+1} \\ ... \\ p_{n-2}^{n+1} \\ p_{n-1}^{n+1} \end{vmatrix} = \begin{vmatrix} d_1^n \\ d_2^n \\ ... \\ d_{n-2}^n \\ d_{n-1}^n - c_{n-1} p_n^{n+1} \end{vmatrix}$$

……...……..... ..(4.7)

If the fluid compressibility is assumed to be zero (all *C*'s are zero), no capillary pressure, and the gravity potential is zero, the d_i is reduced to

$$d_i = -\left[\left(B_o - R_s B_g\right)_n^{n+1} q_{osc\,n}^n + B_{w\ n}^{n+1} q_{wsc\,n}^n + B_{g\ n}^{n+1} q_{gsc\,n}^n\right]$$

……...……..... (4.8)

Assuming no gas exists, and the liquid formation volume factor (FVF) is *1*, the above equation to calculate the coefficient *d* is reduced to,

$$d_i = -\left(q_{osc\,n}^n + q_{wsc\,n}^n\right)$$

……...……..... (4.9)

For all the internal gridblocks, d_i is zero. The linear equation is reduced to,

$$\begin{vmatrix} b_1 & c_1 & 0 & 0 & 0 \\ a_2 & b_2 & c_2 & 0 & 0 \\ 0 & ... & ... & ... & 0 \\ 0 & 0 & a_{n-2} & b_{n-2} & c_{n-2} \\ 0 & 0 & 0 & a_{n-1} & b_{n-1} \end{vmatrix} \begin{vmatrix} p_1^{n+1} \\ p_2^{n+1} \\ ... \\ p_{n-2}^{n+1} \\ p_{n-1}^{n+1} \end{vmatrix} = \begin{vmatrix} -q_{osc1}^n \\ 0 \\ ... \\ 0 \\ -c_{n-1} p_n^{n+1} \end{vmatrix}$$

……...……..... (4.10)

The last term in the RHS vector is always a non-zero value, so the pressure through the whole reservoir will change from the initial pressure even at time zero. From the physical point of view, because of the assumptions on the constant fluid FVF and zero fluid compressibility, which implies the fluid compressibility is gone, the whole reservoir appears as a rigid character. In no matter the reservoir drainage area, the outer boundary feels the inner boundary in no time.

Constant or specified BHP production

At this configuration of the boundary conditions, a similar modification as discussed above is needed for the first row in the final matrix form. An example is given to calculate the pressure at time $n+1$ for a n gridblocks of 1D reservoir.

Carrying on the discussion from the previous matrix form,

$$\begin{vmatrix} b_1 & c_1 & 0 & 0 & 0 \\ a_2 & b_2 & c_2 & 0 & 0 \\ 0 & ... & ... & ... & 0 \\ 0 & 0 & a_{n-2} & b_{n-2} & c_{n-2} \\ 0 & 0 & 0 & a_{n-1} & b_{n-1} \end{vmatrix} \begin{vmatrix} p_1^{n+1} \\ p_2^{n+1} \\ ... \\ p_{n-2}^{n+1} \\ p_{n-1}^{n+1} \end{vmatrix} = \begin{vmatrix} d_1^n \\ d_2^n \\ ... \\ d_{n-2}^n \\ d_{n-1}^n - c_{n-1} p_n^{n+1} \end{vmatrix}$$

……...……..... (4.7)

Because we know the pressure at the both boundaries, p_1 is fixed at the inner boundary and d_1 is constant, so this linear equation is not appropriate for the pressure vector. A modification is made,

$$d_2^{n(new)} = d_2^n - a_2 p_1^{n+1} \text{…….…..... ……... (4.11)}$$

$$\begin{vmatrix} b_2 & c_2 & 0 & 0 & 0 \\ a_3 & b_3 & c_3 & 0 & 0 \\ 0 & ... & ... & ... & 0 \\ 0 & 0 & a_{n-2} & b_{n-2} & c_{n-2} \\ 0 & 0 & 0 & a_{n-1} & b_{n-1} \end{vmatrix} \begin{vmatrix} p_2^{n+1} \\ p_3^{n+1} \\ ... \\ p_{n-2}^{n+1} \\ p_{n-1}^{n+1} \end{vmatrix} = \begin{vmatrix} d_2^n - a_2 p_1^{n+1} \\ d_3^n \\ ... \\ d_{n-2}^n \\ d_{n-1}^n - c_{n-1} p_n^{n+1} \end{vmatrix}$$

……...……..... (4.12)

Using the same assumption as for the previous discussion, if the fluid compressibility is assumed to be zero (all *C*'s are zero), no capillary pressure, and the gravity potential is zero, the d_i is reduced to,

$$d_i = -\left[\left(B_o - R_s B_g\right)_n^{n+1} q_{osc\,n}^n + B_{w\ n}^{n+1} q_{wsc\,n}^n + B_{g\ n}^{n+1} q_{gsc\,n}^n\right]$$

……...……..... (4.13)

In this boundary condition configuration, no flow rates are in consideration, so all the d_i's are zero, except at the boundaries. The linear equation is reduced to,

$$\begin{vmatrix} b_2 & c_2 & 0 & 0 & 0 \\ a_3 & b_3 & c_3 & 0 & 0 \\ 0 & ... & ... & ... & 0 \\ 0 & 0 & a_{n-2} & b_{n-2} & c_{n-2} \\ 0 & 0 & 0 & a_{n-1} & b_{n-1} \end{vmatrix} \begin{vmatrix} p_2^{n+1} \\ p_3^{n+1} \\ ... \\ p_{n-2}^{n+1} \\ p_{n-1}^{n+1} \end{vmatrix} = \begin{vmatrix} -a_2 p_1^{n+1} \\ 0 \\ ... \\ 0 \\ -c_{n-1} p_n^{n+1} \end{vmatrix}$$

……...……..... (4.14)

These linear equations calculated the required (or resulting) production or injection flow rates. In the later part of Chapter VI, the simplest case for single gas phase adopted these boundary configurations.

Specified pressure gradient at the inner boundary

At the inner boundary, we assume the pressure gradient is known, which means,

$$\frac{dp^n_{1,2}}{dx_{1,2}} = \frac{p^n_2 - p^n_1}{(x_1 + x_2)/2}$$

Let,

$$d_1 = \frac{dp^n_{1,2}}{dx_{1,2}} = \frac{p^n_2 - p^n_1}{(x_1 + x_2)/2} \quad \text{.....} \quad (4.15)$$

Studying the linear equation at the inner boundary while ignoring the accumulation term at the boundary to make $b_1 = c_1$,

$$\left(B_o - R_s B_g\right)^{n+1}_1 C_{op_1} + B^{n+1}_{w\ 1} C_{wp_1} + B^{n+1}_{g\ 1} C_{gp_1} = 0$$

..... (4.16)

$$\begin{aligned} b_1 &= \left(\begin{array}{l} \left(B_o - R_s B_g\right)^{n+1}_1 C_{op_1} + B^{n+1}_{w\ 1} C_{wp_1} + B^{n+1}_{g\ 1} C_{gp_1} \\ + \left(B_o - R_s B_g\right)^{n+1}_1 T^n_{o\ 2,1} + B^{n+1}_{w\ n} T^n_{w\ 2,1} + B^{n+1}_{g\ 1} \left[T^n_{g\ 2,1} + \left(T_o R_s\right)^n_{2,1} \right] \end{array} \right) \\ &= \left\{ \left(B_o - R_s B_g\right)^{n+1}_1 T^n_{o\ 2,1} + B^{n+1}_{w\ 1} T^n_{w\ 2,1} + B^{n+1}_{g\ 1} \left[T^n_{g\ 2,1} + \left(T_o R_s\right)^n_{2,1} \right] \right\} \\ &= c_1 \end{aligned}$$

..... (4.17)

An example is given to calculate the pressure at time *n*+1 for a *n* gridblocks 1D reservoir ignoring the accumulation term at the inner boundary. Because we know the pressure at the outer boundary, put into matrix form,

$$\begin{vmatrix} -c_1 & c_1 & 0 & 0 & 0 \\ a_2 & b_2 & c_2 & 0 & 0 \\ 0 & ... & ... & ... & 0 \\ 0 & 0 & a_{n-2} & b_{n-2} & c_{n-2} \\ 0 & 0 & 0 & a_{n-1} & b_{n-1} \end{vmatrix} \begin{vmatrix} p_1^{n+1} \\ p_2^{n+1} \\ ... \\ p_{n-2}^{n+1} \\ p_{n-1}^{n+1} \end{vmatrix} = \begin{vmatrix} \frac{dp_{1,2}^n}{dx_{1,2}} \\ d_2^n \\ ... \\ d_{n-2}^n \\ d_{n-1}^n - c_{n-1} p_n^{n+1} \end{vmatrix}$$

……...……..... (4.18)

With the same assumption as the previous discussion, if the fluid compressibility is assumed to be zero (all *C*'s are zero), no capillary pressure, and the gravity potential is zero, the d_i is reduced to,

$$d_i = -\left[\left(B_o - R_s B_g\right)_i^{n+1} q_{osc\,i}^n + B_{w\ \ i}^{n+1} q_{wsc\,i}^n + B_{g\ \ i}^{n+1} q_{gsc_i}^n\right]$$

……...……..... (4.19)

In this boundary condition configuration, no flow rates are cosidered, so all the d_i 's are zero, except at the boundaries. The linear equation is reduced to,

$$\begin{vmatrix} -c_1 & c_1 & 0 & 0 & 0 \\ a_2 & b_2 & c_2 & 0 & 0 \\ 0 & ... & ... & ... & 0 \\ 0 & 0 & a_{n-2} & b_{n-2} & c_{n-2} \\ 0 & 0 & 0 & a_{n-1} & b_{n-1} \end{vmatrix} \begin{vmatrix} p_1^{n+1} \\ p_2^{n+1} \\ ... \\ p_{n-2}^{n+1} \\ p_{n-1}^{n+1} \end{vmatrix} = \begin{vmatrix} \frac{dp_{1,2}^1}{dx_{1,2}} \\ 0 \\ ... \\ 0 \\ -c_{n-1} p_n^{n+1} \end{vmatrix}$$

……...……..... (4.20)

Neglecting the accumulation term at the inner boundary, the final formulated linear equation is derived at these boundary conditions.

Discussion of the Outer Boundary

Constant pressure at the outer boundary

This case is discussed in the previous sections. The final formulated equation for constant production rate at the inner boundary is,

$$d_{n-1}^{n(new)} = d_{n-1}^{n} - c_n p_n^{n+1} \quad \text{..... (4.21)}$$

$$\begin{vmatrix} b_1 & c_1 & 0 & 0 & 0 \\ a_2 & b_2 & c_2 & 0 & 0 \\ 0 & ... & ... & ... & 0 \\ 0 & 0 & a_{n-2} & b_{n-2} & c_{n-2} \\ 0 & 0 & 0 & a_{n-1} & b_{n-1} \end{vmatrix} \begin{vmatrix} p_1^{n+1} \\ p_2^{n+1} \\ ... \\ p_{n-2}^{n+1} \\ p_{n-1}^{n+1} \end{vmatrix} = \begin{vmatrix} d_1^n \\ d_2^n \\ ... \\ d_{n-2}^n \\ d_{n-1}^n - c_{n-1} p_n^{n+1} \end{vmatrix}$$

..... (4.22)

Constant flow influx at the outer boundary

This case can be derived from the original Eq. 3.47,

$$\begin{aligned}
&\sum_{m\in\psi_n} \left\{ \left(B_o - R_s B_g\right)_n^{n+1} T_{o\,n,m}^{n} + B_{w\;n}^{n+1} T_{w\,n,m}^{n} + B_{g\;n}^{n+1} \left[T_{g\,n,m}^{n} + \left(T_o R_s\right)_{n,m}^{n} \right] \right\} p_{o\;m}^{n+1} \\
&- \left(\begin{array}{l} \left(B_o - R_s B_g\right)_n^{n+1} C_{op\,n} + B_{w\;n}^{n+1} C_{wp\,n} + B_{g\;n}^{n+1} C_{gp\,n} \\ + \sum_{m\in\psi_n} \left\{ \left(B_o - R_s B_g\right)_n^{n+1} T_{o\,n,m}^{n} + B_{w\;n}^{n+1} T_{w\,n,m}^{n} + B_{g\;n}^{n+1} \left[T_{g\,n,m}^{n} + \left(T_o R_s\right)_{n,m}^{n} \right] \right\} \end{array} \right) p_{o\;n}^{n+1} \\
&= -\left[\left(B_o - R_s B_g\right)_n^{n+1} C_{op\,n} + B_{w\;n}^{n+1} C_{wp\,n} + B_{g\;n}^{n+1} C_{gp\,n} \right] p_{o\,n}^{n} \\
&- \left[\left(B_o - R_s B_g\right)_n^{n+1} q_{osc\,n}^{n} + B_{w\;n}^{n+1} q_{wsc\,n}^{n} + B_{g\;n}^{n+1} q_{gsc\,n}^{n} \right] + \sum_{m\in\psi_n} B_{w\;n}^{n+1} T_{w\,n,m}^{n} \left(P_{cow\,m}^{n} - P_{cow\,n}^{n} \right) \\
&- \sum_{m\in\psi_n} B_{g\;n}^{n+1} T_{g\,n,m}^{n} \left(P_{cgo\,m}^{n} - P_{cgo\,n}^{n} \right) + \sum_{m\in\psi_n} \left\{ \begin{array}{l} \left(B_o - R_s B_g\right)_n^{n+1} T_{o\,n,m}^{n} \bar{\gamma}_{o\,n,m}^{n} + B_{w\;n}^{n+1} T_{w\,n,m}^{n} \bar{\gamma}_{w\,n,m}^{n} \\ + B_{g\;n}^{n+1} \left[T_{g\,n,m}^{n} \bar{\gamma}_{g\,n,m}^{n} + \left(T_o R_s\right)_{n,m}^{n} \bar{\gamma}_{o\,n,m}^{n} \right] \end{array} \right\} \left(Z_m - Z_n\right)
\end{aligned}$$

..... (3.47)

Formulated into the matrix form,

$$\begin{vmatrix} b_1 & c_1 & 0 & 0 & 0 \\ a_2 & b_2 & c_2 & 0 & 0 \\ 0 & \dots & \dots & \dots & 0 \\ 0 & 0 & a_{n-1} & b_{n-1} & c_{n-1} \\ 0 & 0 & 0 & a_n & b_n \end{vmatrix} \begin{vmatrix} p_1^{n+1} \\ p_2^{n+1} \\ \dots \\ p_{n-1}^{n+1} \\ p_n^{n+1} \end{vmatrix} = \begin{vmatrix} d_1^n \\ d_2^n \\ \dots \\ d_{n-1}^n \\ d_n^n \end{vmatrix}$$

……..……..... (4.23)

For closed outer boundary, with the assumptions of no capillary pressure, and no gravity potential, the d_n is reduced to,

$$d_n = -\left[\left(B_o - R_s B_g\right)_n^{n+1} C_{op_n} + B_{w\ n}^{n+1} C_{wp_n} + B_{g\ n}^{n+1} C_{gp_n}\right] p_{o\ n}^n$$

……..……..... (4.24)

If the fluid compressibility is assumed to be zero (all C's are zero), then,

$$d_n = 0$$ ……..……..... (4.25)

In this boundary condition configuration, no flow rates are in consideration except at the inner boundary, so all the rest of d_i's are zero. The linear equation is reduced to this matrix form,

$$\begin{vmatrix} b_1 & c_1 & 0 & 0 & 0 \\ a_2 & b_2 & c_2 & 0 & 0 \\ 0 & \dots & \dots & \dots & 0 \\ 0 & 0 & a_{n-1} & b_{n-1} & c_{n-1} \\ 0 & 0 & 0 & a_n & b_n \end{vmatrix} \begin{vmatrix} p_1^{n+1} \\ p_2^{n+1} \\ \dots \\ p_{n-1}^{n+1} \\ p_n^{n+1} \end{vmatrix} = \begin{vmatrix} d_1^n \\ 0 \\ \dots \\ 0 \\ 0 \end{vmatrix}$$

……..……..... (4.26)

Specified pressure gradient at the outer boundary

At the outer boundary, we assume the pressure gradient is known, which means,

$$\frac{dp^{n}_{n-1,n}}{dx_{n-1,n}} = \frac{p^{n}_{n} - p^{n}_{n-1}}{\left(x_n + x_{n-1}\right)/2}$$

Let,

$$d_n = \frac{dp^{n}_{n-1,n}}{dx_{n-1,n}} = \frac{p^{n}_{n} - p^{n}_{n-1}}{\left(x_n + x_{n-1}\right)/2}$$

……...……..... (4.27)

Studying the linear equation at the inner boundary while ignoring the accumulation term at the boundary to make $a_n = b_n$,

$$\left(B_o - R_s B_g\right)^{n+1}_{n} C_{op\,n} + B^{n+1}_{w\;n} C_{wp\,n} + B^{n+1}_{g\;n} C_{gp\,n} = 0$$

……...……..... (4.28)

$$\begin{aligned} b_i &= \left(\begin{array}{l} \left(B_o - R_s B_g\right)^{n+1}_{n} C_{op\,n} + B^{n+1}_{w\;n} C_{wp\,n} + B^{n+1}_{g\;n} C_{gp\,n} \\ + \left(B_o - R_s B_g\right)^{n+1}_{n} T^{n}_{o\;n,n-1} + B^{n+1}_{w\;n} T^{n}_{w\;n,n-1} + B^{n+1}_{g\;n} \left[T^{n}_{g\;n,n-1} + \left(T_o R_s\right)^{n}_{n,n-1} \right] \end{array} \right) \\ &= \left\{ \left(B_o - R_s B_g\right)^{n+1}_{n} T^{n}_{o\;n,n-1} + B^{n+1}_{w\;n} T^{n}_{w\;n,n-1} + B^{n+1}_{g\;n} \left[T^{n}_{g\;n,n-1} + \left(T_o R_s\right)^{n}_{n,n-1} \right] \right\} \\ &= a_n \end{aligned}$$

……...……..... (4.29)

An example is given to calculate the pressure at time $n+1$ for an n gridblocks 1D reservoir ignoring the accumulation term at the outer boundary. Because we know the constant production rate at the inner boundary, we put the formulated equation into matrix form,

$$\begin{vmatrix} b_1 & c_1 & 0 & 0 & 0 \\ a_2 & b_2 & c_2 & 0 & 0 \\ 0 & ... & ... & ... & 0 \\ 0 & 0 & a_{n-1} & b_{n-1} & c_{n-1} \\ 0 & 0 & 0 & -a_n & a_n \end{vmatrix} \begin{vmatrix} p_1^{n+1} \\ p_2^{n+1} \\ ... \\ p_{n-1}^{n+1} \\ p_n^{n+1} \end{vmatrix} = \begin{vmatrix} d_1^n \\ d_2^n \\ ... \\ d_{n-1}^n \\ \dfrac{dp_{n-1,n}^n}{dx_{n-1,n}} \end{vmatrix}$$

……...……..... (4.30)

With the same assumption as the previous discussion, if the fluid compressibility is assumed to be zero (all *C*'s are zero), no capillary pressure, and the gravity potential is zero, the d_i is reduced to,

$$d_i = -\left[\left(B_o - R_s B_g\right)_n^{n+1} q_{osc\,n}^n + B_{w\ n}^{n+1} q_{wsc\,n}^n + B_{g\ n}^{n+1} q_{gsc\,n}^n\right]$$

……...……..... (4.31)

In this boundary condition configuration, no flow rates are in consideration, so all the d_i's are zero, except at the boundaries. The linear equation is reduced to,

$$\begin{vmatrix} b_1 & c_1 & 0 & 0 & 0 \\ a_2 & b_2 & c_2 & 0 & 0 \\ 0 & ... & ... & ... & 0 \\ 0 & 0 & a_{n-1} & b_{n-1} & c_{n-1} \\ 0 & 0 & 0 & -a_n & a_n \end{vmatrix} \begin{vmatrix} p_1^{n+1} \\ p_2^{n+1} \\ ... \\ p_{n-1}^{n+1} \\ p_n^{n+1} \end{vmatrix} = \begin{vmatrix} d_1^n \\ 0 \\ ... \\ 0 \\ \dfrac{dp_{n-1,n}^n}{dx_{n-1,n}} \end{vmatrix}$$

……...……..... (4.32)

Neglecting the accumulation term at the inner boundary, the final formulated linear equation is derived at these boundary conditions.

Summary

This chapter introduces the theoretical basis on the mass conservation and the transportation law (Darcy's equation), and obtains the multiphase difference equations. IMPES modeling implicitly solves a single pressure equation for each grid block by combining all the flow equations for different phases and calculates the saturation explicitly. Identification of the boundary conditions is extremely important and corresponds to different matrix forms for the solver. All the possible combinations of different inner and outer boundaries are summarized in **Fig. 4.1**.

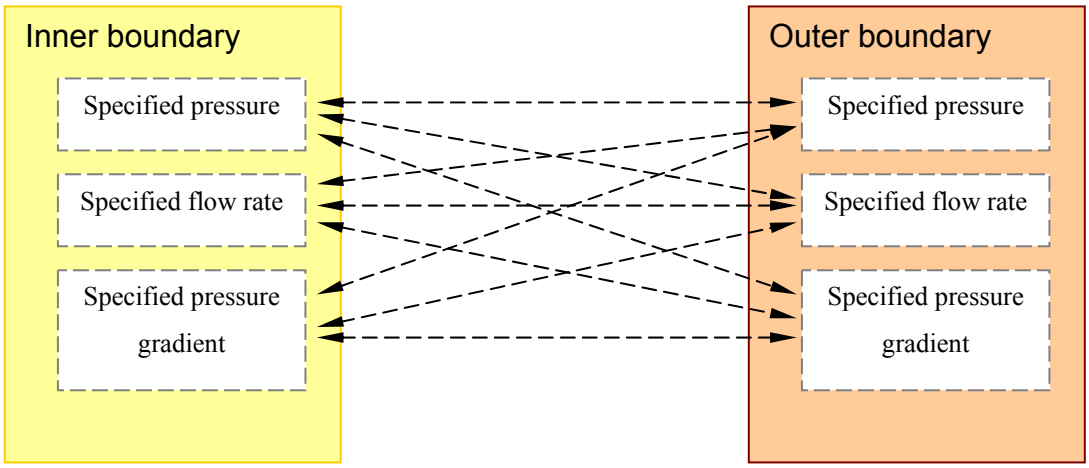

Fig.4.1—All the possible combinations of the different boundary conditions.

Summarizing the equations in matrix form under different boundary conditions

Case 1: Specified pressure at both inner and outer boundaries

$$\begin{vmatrix} b_2 & c_2 & 0 & 0 & 0 \\ a_3 & b_3 & c_3 & 0 & 0 \\ 0 & ... & ... & ... & 0 \\ 0 & 0 & a_{n-2} & b_{n-2} & c_{n-2} \\ 0 & 0 & 0 & a_{n-1} & b_{n-1} \end{vmatrix} \begin{vmatrix} p_2^{n+1} \\ p_3^{n+1} \\ ... \\ p_{n-2}^{n+1} \\ p_{n-1}^{n+1} \end{vmatrix} = \begin{vmatrix} d_2^n - a_2 p_1^{n+1} \\ d_3^n \\ ... \\ d_{n-2}^n \\ d_{n-1}^n - c_{n-1} p_n^{n+1} \end{vmatrix}$$

……..……..... (4.33)

Case 2: Specified pressure at inner boundary and specified flow rate at outer boundary

$$\begin{vmatrix} b_2 & c_2 & 0 & 0 & 0 \\ a_3 & b_3 & c_3 & 0 & 0 \\ 0 & ... & ... & ... & 0 \\ 0 & 0 & a_{n-1} & b_{n-1} & c_{n-1} \\ 0 & 0 & 0 & a_n & b_n \end{vmatrix} \begin{vmatrix} p_2^{n+1} \\ p_3^{n+1} \\ ... \\ p_{n-1}^{n+1} \\ p_n^{n+1} \end{vmatrix} = \begin{vmatrix} d_2^n - a_2 p_1^{n+1} \\ d_3^n \\ ... \\ d_{n-1}^n \\ d_n^n \end{vmatrix}$$

……..……..... (4.34)

Case 3: Specified pressure at inner boundary and specified pressure gradient at outer boundary

$$\begin{vmatrix} b_2 & c_2 & 0 & 0 & 0 \\ a_3 & b_3 & c_3 & 0 & 0 \\ 0 & ... & ... & ... & 0 \\ 0 & 0 & a_{n-1} & b_{n-1} & c_{n-1} \\ 0 & 0 & 0 & -a_n & a_n \end{vmatrix} \begin{vmatrix} p_2^{n+1} \\ p_3^{n+1} \\ ... \\ p_{n-1}^{n+1} \\ p_n^{n+1} \end{vmatrix} = \begin{vmatrix} d_2^n - a_2 p_1^{n+1} \\ d_3^n \\ ... \\ d_{n-1}^n \\ \frac{dp_{n-1,n}^n}{dx_{n-1,n}} \end{vmatrix}$$

……..……..... (4.35)

Case 4: Specified flow rate at inner boundary and specified pressure at outer boundary

$$\begin{vmatrix} b_1 & c_1 & 0 & 0 & 0 \\ a_2 & b_2 & c_2 & 0 & 0 \\ 0 & ... & ... & ... & 0 \\ 0 & 0 & a_{n-2} & b_{n-2} & c_{n-2} \\ 0 & 0 & 0 & a_{n-1} & b_{n-1} \end{vmatrix} \begin{vmatrix} p_1^{n+1} \\ p_2^{n+1} \\ ... \\ p_{n-2}^{n+1} \\ p_{n-1}^{n+1} \end{vmatrix} = \begin{vmatrix} d_1^n \\ d_2^n \\ ... \\ d_{n-2}^n \\ d_{n-1}^n - c_{n-1} p_n^{n+1} \end{vmatrix}$$

……...……..... (4.36)

Case 5: Specified flow rate at both inner and outer boundaries

$$\begin{vmatrix} b_1 & c_1 & 0 & 0 & 0 \\ a_2 & b_2 & c_2 & 0 & 0 \\ 0 & ... & ... & ... & 0 \\ 0 & 0 & a_{n-1} & b_{n-1} & c_{n-1} \\ 0 & 0 & 0 & a_n & b_n \end{vmatrix} \begin{vmatrix} p_1^{n+1} \\ p_2^{n+1} \\ ... \\ p_{n-1}^{n+1} \\ p_n^{n+1} \end{vmatrix} = \begin{vmatrix} d_1^n \\ d_2^n \\ ... \\ d_{n-1}^n \\ d_n^n \end{vmatrix}$$

……...……..... (4.37)

Case 6: Specified flow rate at inner boundary and specified pressure gradient at outer boundary

$$\begin{vmatrix} b_1 & c_1 & 0 & 0 & 0 \\ a_2 & b_2 & c_2 & 0 & 0 \\ 0 & ... & ... & ... & 0 \\ 0 & 0 & a_{n-1} & b_{n-1} & c_{n-1} \\ 0 & 0 & 0 & -a_n & a_n \end{vmatrix} \begin{vmatrix} p_1^{n+1} \\ p_2^{n+1} \\ ... \\ p_{n-1}^{n+1} \\ p_n^{n+1} \end{vmatrix} = \begin{vmatrix} d_1^n \\ d_2^n \\ ... \\ d_{n-1}^n \\ \dfrac{dp_{n-1,n}^n}{dx_{n-1,n}} \end{vmatrix}$$

……...……..... (4.38)

Case 7: Specified pressure gradient at inner boundary and specified pressure at outer boundary

$$\begin{vmatrix} -c_1 & c_1 & 0 & 0 & 0 \\ a_2 & b_2 & c_2 & 0 & 0 \\ 0 & ... & ... & ... & 0 \\ 0 & 0 & a_{n-2} & b_{n-2} & c_{n-2} \\ 0 & 0 & 0 & a_{n-1} & b_{n-1} \end{vmatrix} \begin{vmatrix} p_1^{n+1} \\ p_2^{n+1} \\ ... \\ p_{n-2}^{n+1} \\ p_{n-1}^{n+1} \end{vmatrix} = \begin{vmatrix} \frac{dp_{1,2}^n}{dx_{1,2}} \\ d_2^n \\ ... \\ d_{n-2}^n \\ d_{n-1}^n - c_{n-1} p_n^{n+1} \end{vmatrix}$$

……...……..... (4.39)

Case 8: Specified pressure gradient at inner boundary and specified flow rate at outer boundary

$$\begin{vmatrix} -c_1 & c_1 & 0 & 0 & 0 \\ a_2 & b_2 & c_2 & 0 & 0 \\ 0 & ... & ... & ... & 0 \\ 0 & 0 & a_{n-1} & b_{n-1} & c_{n-1} \\ 0 & 0 & 0 & a_n & b_n \end{vmatrix} \begin{vmatrix} p_1^{n+1} \\ p_2^{n+1} \\ ... \\ p_n^{n+1} \\ p_n^{n+1} \end{vmatrix} = \begin{vmatrix} \frac{dp_{1,2}^n}{dx_{1,2}} \\ d_2^n \\ ... \\ d_{n-1}^n \\ d_n^n \end{vmatrix}$$

……...……..... (4.40)

Case 9: Specified pressure gradient at both inner and outer boundaries

$$\begin{vmatrix} -c_1 & c_1 & 0 & 0 & 0 \\ a_2 & b_2 & c_2 & 0 & 0 \\ 0 & ... & ... & ... & 0 \\ 0 & 0 & a_{n-1} & b_{n-1} & c_{n-1} \\ 0 & 0 & 0 & -a_n & a_n \end{vmatrix} \begin{vmatrix} p_1^{n+1} \\ p_2^{n+1} \\ ... \\ p_{n-1}^{n+1} \\ p_n^{n+1} \end{vmatrix} = \begin{vmatrix} \frac{dp_{1,2}^n}{dx_{1,2}} \\ d_2^n \\ ... \\ d_{n-1}^n \\ \frac{dp_{n-1,n}^n}{dx_{n-1,n}} \end{vmatrix}$$

……...……..... (4.41)

CHAPTER V

BLACKOIL RESERVOIR SIMULATOR

Followed by the previously discussed IMPES model, a multiphase 1D simulator is built in FORTRAN with black oil PVT correlations. The literature-based PVT correlations are summarized in **APPENDIX B**. The software is built in Intel® Visual Fortran Compiler Integration (version 11.1.038), and the structure can be found in **APPENDIX C**.

Theory behind ECLIPSE

This self-built software must be validated by well-accepted commercial software before use. Although the goal of this work is to model the multiphase flow under transient conditions, this FORTRAN simulator must be able to repeat the identical results in large scale and with larger timesteps.

Eclipse 100, developed by Schlumberger, is one of the most popular and accepted commercial softwares in industry. It is also a blackoil simulator with the capacity of using the IMPES method; thus, Eclipse 100 is chosen to validate this FORTRAN simulator.

In Chapter 22 of the ECLIPSE User Manual (v. 2008.2), the non-linear residual, R_{fl}, for each fluid component in each grid block at each timestep is:

$$R_{fl} = \frac{M_{t+dt} - M_t}{dt} + F\left(P_{t+dt}, S_t\right) + Q\left(P_{t+dt}, S_t\right) \quad \text{(5.1)}$$

where M represents the mass term, per unit surface density, accumulated during the current timestep, dt, F is the net flow rate into neighboring grid blocks, and Q is the net flow rate into wells during the timestep.

The flow rate into cell *i* from a neighboring cell *n*, F_{ni}, is

$$F_{ni} = T_{ni}\begin{bmatrix} \frac{k_{ro}}{B_o\mu_o} & 0 & \frac{R_v k_{rg}}{B_g\mu_g} \\ 0 & \frac{k_{rw}}{B_w\mu_w} & 0 \\ \frac{R_s k_{ro}}{B_o\mu_o} & 0 & \frac{k_{rg}}{B_g\mu_g} \end{bmatrix}_u \times \begin{bmatrix} dP_{oni} \\ dP_{wni} \\ dP_{gni} \end{bmatrix}$$

……...…….…….…..... (5.2)

The Jacobian, $J = \frac{dR}{dX}$, where

$$\sum_i (R_o)_i = \sum_i \left(\frac{dM_o}{dt}\right)_i + \sum_i (Q_o)_i$$

$$\sum_i (R_w)_i = \sum_i \left(\frac{dM_w}{dt}\right)_i + \sum_i (Q_w)_i$$

$$\sum_i (R_g)_i = \sum_i \left(\frac{dM_g}{dt}\right)_i + \sum_i (Q_g)_i$$

$$X = \begin{vmatrix} p_o \\ S_w \\ S_g \ or \ R_S \ or \ R_v \end{vmatrix}$$

……...…….…….…..... (5.3)

Eclipse uses Newton iteration to solve the IMPES equations till all the residuals have been reduced to a sufficiently small value. IMPES method eliminates the non-linearities from relative permeabilities that remain fixed throughout the timestep. Eclipse calculates the maximum saturation normalized residuals, which are considered to have converged if they are all less than 0.001. However, no further information is available on how to control the converging problem after this point.

The flow rate into a production well from cell *i* is,

$$Q_i = -T_{wi}(P_{oi} - H_{iw} - P_{bh}) \begin{bmatrix} \frac{k_{ro}}{B_o \mu_o} + \frac{R_v k_{rg}}{B_g \mu_g} \\ \frac{k_{rw}}{B_w \mu_w} \\ \frac{k_{rg}}{B_g \mu_g} + \frac{R_s k_{ro}}{B_o \mu_o} \end{bmatrix}_i$$

……...…….……..…..... (5.4)

where T_{wi} is the transmissibility factor, H is the hydrostatic head correction, and p_{bh} is the bottomhole pressure.

Another interesting statement adopted from the ECLIPSE User Manual is,

> *The net flow rate from cell i into neighboring cells is obtained by summing over the neighboring cells,* $F_i = \sum_n F_{ni}$.

So from the above quote, it seems Eclipse does not consider the accumulation term when it calculates the internal flow rates between the adjacent gridblocks.

Validating this Self-Built Simulator

As discussed previously, this self-built software must be validated before the appropriate use.

Validating with a textbook example

The first validation is made with the *Example 9.26* of the SPE textbook, *Basic Applied Reservoir Simulation* (Ertekin, 1998).

Case Description

Example 9.26. A homogeneous, 1D horizontal oil reservoir is 1,000 ft long with a cross-sectional area of 10,000 sq ft. It is discretized into four equal gridblocks. Initially, $S_{wi} = S_{iw} = 0.160$ and $p_i = 1{,}000$ psi everywhere. Water is injected at x=0 at a rate of 75.96 B/D at standard conditions, and oil is produced at x =1,000 ft at the same rate. The gridblock dimensions and properties are $\Delta x = 250$ ft, $k_x = 300md$, $A_x = 10{,}000\,ft^2$, and $\phi = 0.20$. The reservoir fluid are incompressible with $B_w = B_o = 1RB/STB$ and $\mu_o = \mu_w = 1cp$. The oil/water capillary pressure is zero… Using the IMPES solution method, find the pressure and saturation distributions at 100 and 300 days.

Upon this configuration, the simulation results from this FORTRAN simulator are identical to the textbook solutions for 100 and 300 days (**Fig. 5.1**).

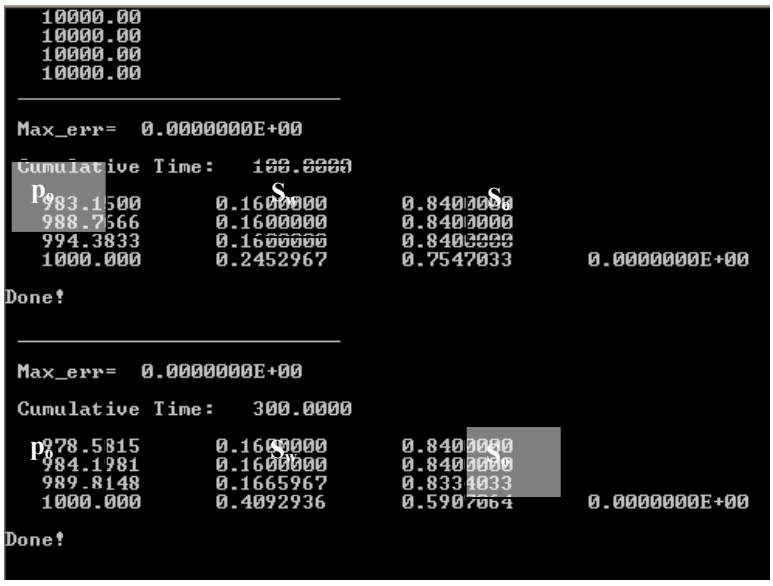

Fig. 5.1—A snapshot: the simulation results from the FORTRAN simulator.

Validating with Eclipse 100

Next, this FORTRAN simulator was validated with the commercial software ECLIPSE 100. This simulator was tested with different boundary conditions, and compared the results with Eclipse properly.

Case Description

A homogeneous, 1D horizontal oil reservoir is 1,000 ft long with a cross-sectional area of 10,000 sq ft. It is discretized into 20 unequal gridblocks. The size of the first nine gridblocks is 10 ft, and for the remaining gridblocks, the size is listed in **Table 5.1**. Initially, $S_{wi} = S_{iw} = 0.160$ and $p_i = 7{,}880$ psi everywhere. The reservoir fluids are characterized by black oil correlations from the literature (Appendix B), and the same PVT tables were extracted and imported to Eclipse. The gridblock properties are: $k_x = 300\ md$, $A_x = 10{,}000\ ft^2$, and $\phi = 0.20$, except $\phi = 1$ for the cell at the outer boundary to maintain the reservoir pressure for the initial timesteps. The oil/water capillary pressure is neglected in this case study. The curve for relative permeability is shown (**Fig. 5.2**). Simulated pressure and saturation distributions at 0.005 days, 0.5 days, 5 days, and 50days.

Table 5.1—LOGARITHMIC GRIDDING METHOD

Grid No.	10	11	12	13	14	15	16	17	18	19	20
Size, ft	22	27	34	42	53	66	82	102	127	158	197

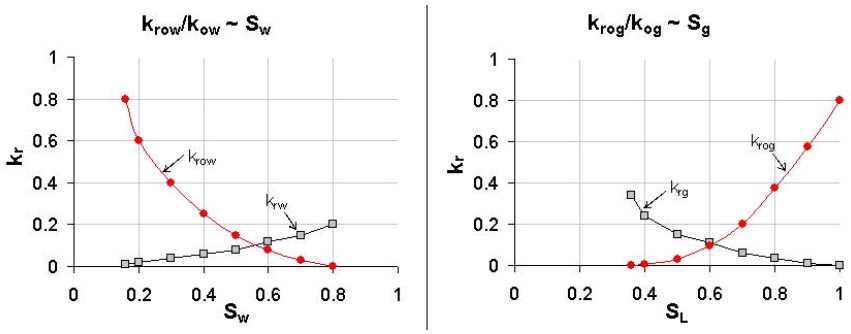

Fig. 5.2—Relative permeability vs. wetting phase saturation.

Closed outer boundary, and oil is produced at 1,000 STB/D at the inner boundary

After running the simulator for 0.005 days, the deeper part of the reservoir (farther than 400 ft from the wellbore) has no feeling from the production well. The material balance check is OK. The FORTRAN simulator just turned out the identical results as Eclipse (**Fig. 5.3**), the maximum relative difference is about 0.3%, which might be caused by the convergence criterion or discontinuous PVT table in Eclipse.

Radius	FORTRAN	ECL	Rel. Error
10.09	7851.83	7854.922	0.04%
20.09	7852.1	7855.251	0.04%
30.09	7852.36	7855.577	0.04%
40.09	7852.62	7855.899	0.04%
50.09	7852.88	7856.219	0.04%
60.09	7853.13	7856.536	0.04%
70.09	7853.38	7856.85	0.04%
80.09	7853.63	7857.161	0.04%
90.09	7853.87	7857.469	0.05%
112.13	7854.4	7857.959	0.05%
139.55	7855.03	7858.698	0.05%
173.69	7855.79	7859.595	0.05%
216.17	7856.69	7860.675	0.05%
269.05	7857.74	7861.966	0.05%
334.85	7858.92	7863.489	0.06%
416.76	7860.21	7865.259	0.06%
518.7	7861.53	7867.279	0.07%
645.57	7862.75	7869.525	0.09%
803.47	7863.59	7871.949	0.11%
1000	7863.59	7874.467	0.14%

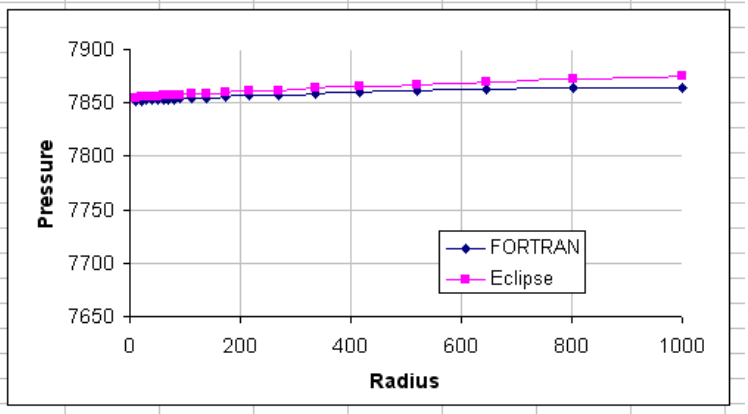

Fig. 5.3—The comparison of the simulation results between the FORTRAN simulator with Eclipse 100 after 0.005 day.

Simulation results for the pressure and saturation distributions at 0.5 day, 1 day, 3 days, 5 days, 7 days and 10 days, shown in **Fig. 5.4, to 5.9**.

Radius	FORTRAN	ECL	Rel. Error
10.09	7851.83	7854.922	0.04%
20.09	7852.1	7855.251	0.04%
30.09	7852.36	7855.577	0.04%
40.09	7852.62	7855.899	0.04%
50.09	7852.88	7856.219	0.04%
60.09	7853.13	7856.536	0.04%
70.09	7853.38	7856.85	0.04%
80.09	7853.63	7857.161	0.04%
90.09	7853.87	7857.469	0.05%
112.13	7854.4	7857.959	0.05%
139.55	7855.03	7858.698	0.05%
173.69	7855.79	7859.595	0.05%
216.17	7856.69	7860.675	0.05%
269.05	7857.74	7861.966	0.05%
334.85	7858.92	7863.489	0.06%
416.76	7860.21	7865.259	0.06%
518.7	7861.53	7867.279	0.07%
645.57	7862.75	7869.525	0.09%
803.47	7863.59	7871.949	0.11%
1000	7863.59	7874.467	0.14%

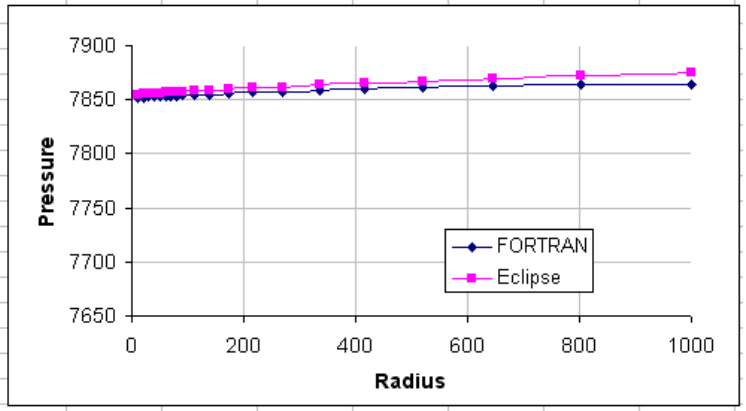

Fig. 5.4—The comparison of the simulation results between the FORTRAN simulator with Eclipse 100 after 0.5 day.

Radius	FORTRAN	ECL	Rel. Error
10.09	7831.72	7844.222	0.16%
20.09	7831.99	7844.551	0.16%
30.09	7832.25	7844.878	0.16%
40.09	7832.51	7845.203	0.16%
50.09	7832.77	7845.525	0.16%
60.09	7833.02	7845.846	0.16%
70.09	7833.27	7846.164	0.16%
80.09	7833.52	7846.48	0.17%
90.09	7833.76	7846.794	0.17%
112.13	7834.29	7847.293	0.17%
139.55	7834.93	7848.051	0.17%
173.69	7835.69	7848.976	0.17%
216.17	7836.59	7850.099	0.17%
269.05	7837.63	7851.453	0.18%
334.85	7838.82	7853.071	0.18%
416.76	7840.11	7854.982	0.19%
518.7	7841.44	7857.206	0.20%
645.57	7842.65	7859.743	0.22%
803.47	7843.49	7862.559	0.24%
1000	7843.49	7865.557	0.28%

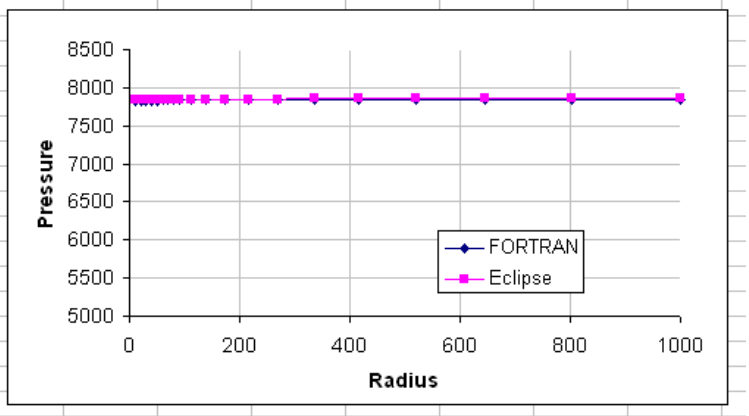

Fig. 5.5—The comparison of the simulation results between the FORTRAN simulator with Eclipse 100 after 1 day.

Radius	FORTRAN	ECL	Rel. Error
10.09	7751.75	7798.528	0.60%
20.09	7752.02	7798.857	0.60%
30.09	7752.28	7799.184	0.60%
40.09	7752.54	7799.509	0.60%
50.09	7752.79	7799.832	0.60%
60.09	7753.05	7800.153	0.60%
70.09	7753.3	7800.473	0.60%
80.09	7753.54	7800.79	0.61%
90.09	7753.78	7801.106	0.61%
112.13	7754.31	7801.609	0.61%
139.55	7754.95	7802.375	0.61%
173.69	7755.71	7803.314	0.61%
216.17	7756.61	7804.457	0.61%
269.05	7757.65	7805.843	0.62%
334.85	7758.82	7807.51	0.62%
416.76	7760.11	7809.495	0.63%
518.7	7761.43	7811.826	0.65%
645.57	7762.64	7814.512	0.66%
803.47	7763.48	7817.521	0.69%
1000	7763.48	7820.747	0.73%

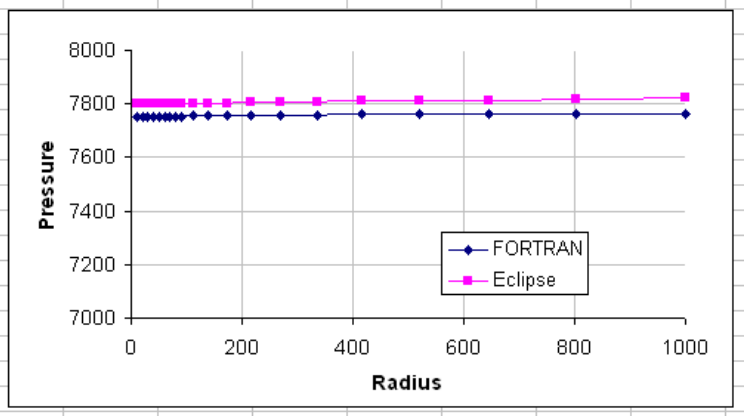

Fig. 5.6—The comparison of the simulation results between the FORTRAN simulator with Eclipse 100 after 3 days.

Radius	FORTRAN	ECL	Rel. Error
10.09	7671.99	7726.816	0.71%
20.09	7672.26	7727.144	0.71%
30.09	7672.52	7727.469	0.71%
40.09	7672.78	7727.793	0.71%
50.09	7673.03	7728.115	0.71%
60.09	7673.28	7728.435	0.71%
70.09	7673.53	7728.753	0.71%
80.09	7673.78	7729.069	0.72%
90.09	7674.02	7729.384	0.72%
112.13	7674.54	7729.885	0.72%
139.55	7675.18	7730.648	0.72%
173.69	7675.93	7731.583	0.72%
216.17	7676.83	7732.722	0.72%
269.05	7677.86	7734.102	0.73%
334.85	7679.03	7735.762	0.73%
416.76	7680.31	7737.74	0.74%
518.7	7681.63	7740.062	0.75%
645.57	7682.83	7742.738	0.77%
803.47	7683.66	7745.735	0.80%
1000	7683.66	7748.95	0.84%

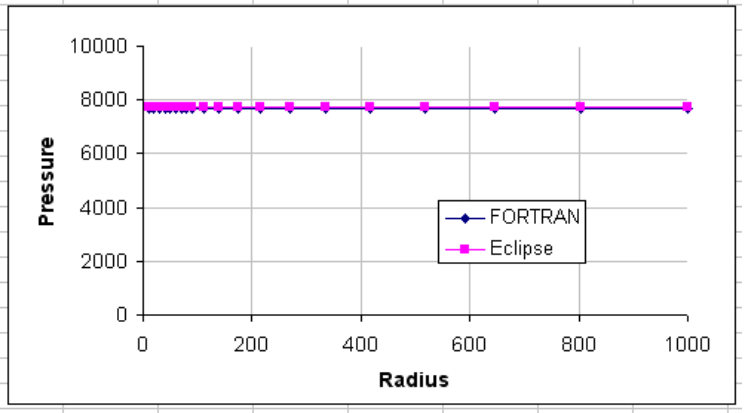

Fig. 5.7—The comparison of the simulation results between the FORTRAN simulator with Eclipse 100 after 5 days.

Radius	FORTRAN	ECL	Rel. Error
10.09	7599.92	7602.786	0.04%
20.09	7600.05	7603.09	0.04%
30.09	7600.19	7603.393	0.04%
40.09	7600.32	7603.694	0.04%
50.09	7600.44	7603.993	0.05%
60.09	7600.57	7604.292	0.05%
70.09	7600.7	7604.588	0.05%
80.09	7600.82	7604.882	0.05%
90.09	7600.95	7605.176	0.06%
112.13	7601.22	7605.643	0.06%
139.55	7601.52	7606.356	0.06%
173.69	7601.87	7607.23	0.07%
216.17	7602.26	7608.297	0.08%
269.05	7602.74	7609.593	0.09%
334.85	7603.29	7611.154	0.10%
416.76	7603.93	7613.019	0.12%
518.7	7604.63	7615.215	0.14%
645.57	7605.31	7617.752	0.16%
803.47	7605.79	7620.603	0.19%
1000	7605.79	7623.666	0.23%

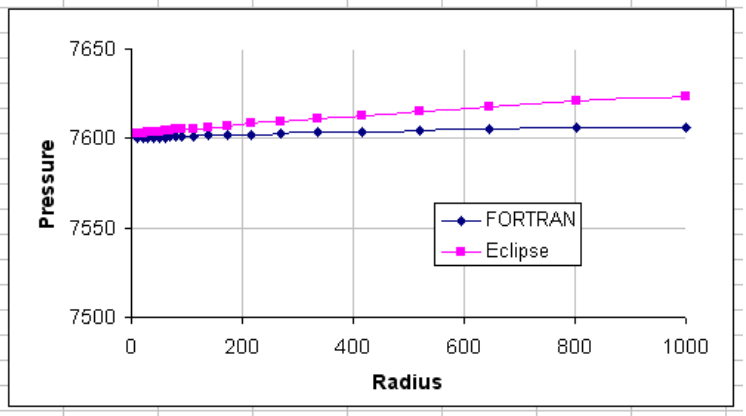

Fig. 5.8—The comparison of the simulation results between the FORTRAN simulator with Eclipse 100 after 7 days.

Radius	FORTRAN	ECL	Rel. Error
10.09	7599.92	7600.086	0.00%
20.09	7599.93	7600.096	0.00%
30.09	7599.95	7600.106	0.00%
40.09	7599.97	7600.115	0.00%
50.09	7599.98	7600.125	0.00%
60.09	7600	7600.134	0.00%
70.09	7600.02	7600.144	0.00%
80.09	7600.03	7600.153	0.00%
90.09	7600.05	7600.162	0.00%
112.13	7600.09	7600.177	0.00%
139.55	7600.13	7600.201	0.00%
173.69	7600.19	7600.229	0.00%
216.17	7600.25	7600.265	0.00%
269.05	7600.33	7600.309	0.00%
334.85	7600.43	7600.362	0.00%
416.76	7600.55	7600.427	0.00%
518.7	7600.69	7600.506	0.00%
645.57	7600.81	7600.599	0.00%
803.47	7600.89	7600.706	0.00%
1000	7600.89	7600.823	0.00%

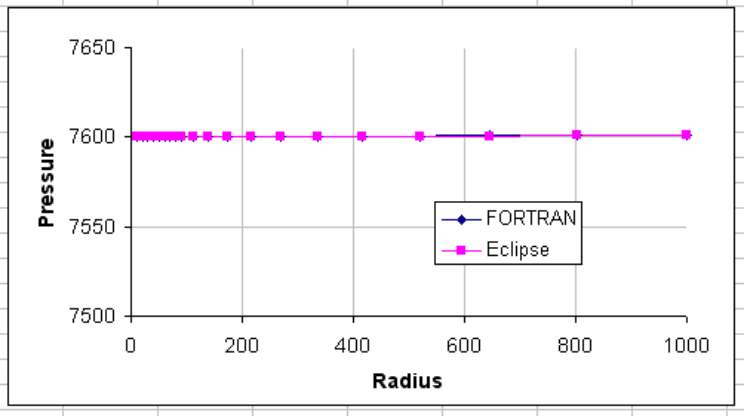

Fig. 5.9—The comparison of the simulation results between the FORTRAN simulator with Eclipse 100 after 10 days.

The commercial software Eclipse 100 is not well designed for users to test different boundary configurations. In this case study, the outer boundary is closed, which means no mass transfer and the pressure drops as depleting by time. But the inner boundary configurations are changed from constant production rate control to fixed bottomhole pressure control.

The boundary combinations are *Case 2* and *Case 5* as discussed before. For the remaining cases, Eclipse does not allow users to set different boundary conditions, as confirmed by ECLIPSE custom support.

However, from the current approaches, this FORTRAN simulator is verified by the commercial software ECLIPSE 100. The little discrepancy between the two simulators might be created by the discrete format of the PVT data, the different convergence criteria required by the IMPES model, or the way to update the explicit variables (Eclipse might use Generalized Newton Raphson method).

CHAPTER VI

VALIDATION OF THE U-SHAPED PRESSURE PROFILE IN THE NEAR-WELLBORE REGION

Objectives

Such is the importance of liquid loading that the industry has devoted a lot of attention to the alleviation of the problem using various measures. However, the fundamental understanding of the associated phenomena is still surprisingly weak. This applies not only to the flows in the wells, but also to the ways in which these flows interact with those in the reservoir. The classical way of dealing with these interactions is through inflow performance relationships (IPRs) where the inflow from the reservoir is related to the pressure at the bottom of the well, which is related to the multiphase flow behavior in the well (and in the rest of the production system, if appropriate). The latter is also usually calculated from steady-state relationships (though these often lack a fundamental basis). However, a transition from an acceptable liquid loading regime to an unacceptable one may occur over a relatively short time. Flow at the surface will remain in mist or annular flow regime till the conditions change sufficiently to exhibit characteristics of the phenomena of transitional flow. At this point, the well production becomes somewhat erratic, progressing to slug and churn flow, while following an overall decreasing trend. As a result, the liquids start to dynamically accumulate in the wellbore, causing downhole pressure fluctuations. The increasing liquid holdup augments the backpressure on the formation, which ultimately accounts for the well's death.

The conventional pressure profile in the near wellbore region of a flowing reservoir (**Fig. 6.1a**) is not suitable to characterize the transient phenomena that take place during liquid

loading. The wellbore phase redistribution that occurs during liquid loading changes the bottomhole pressure with time. The frequency and amplitude of these changes vary with the magnitude of the liquid loading occurrence. If the reservoir were capable of providing an instantaneous response to the bottomhole pressure fluctuations, the pressure profile in the near wellbore would quickly re-adjust to the new wellbore conditions (**Fig. 6.1b**). However, due to a combination of inertia and compressibility effects, the reservoir response is not instantaneous and can be particularly slow for tight formations. A sequence of conventional pressure profiles (from **a** to **b** in **Fig. 6.1**) could be assumed, but this would imply a temporary discontinuity of the pressure function at the wellbore, which is unphysical. Thus, in this paper, a U-shaped pressure profile is proposed (**Fig. 6.1c**), which could also explain the possibility of reinjection of the heavier phase into the reservoir.

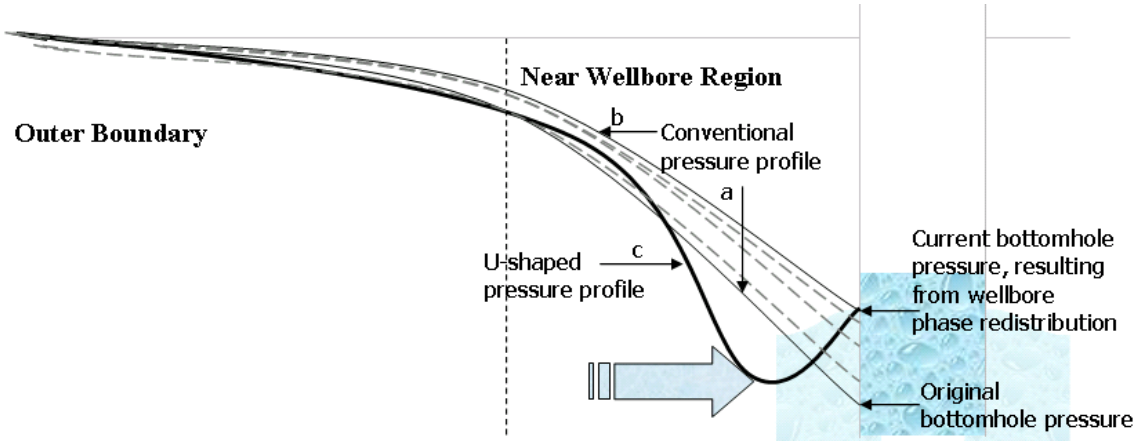

Fig. 6.1—U-shaped pressure profile in the near-wellbore region.
The fat arrow points to the minimum pressure existing in the near-wellbore region, where the pressure profile is actually a U-shaped curve (Zhang, 2009).

This work captures the transient U-shaped pressure profile that responds to bottomhole pressure oscillations. As a result of the simulations described in what follows, we

calculated the backflow rates from the wellbore into the reservoir, and from grid block to grid block within the reservoir for two synthetic field cases.

The strategy of this modeling work consisted of starting from the simplest, yet fundamental, case: single-phase compressible gas radial flow, and homogeneous porous medium. Later, a similar procedure was followed for a dry gas/water two-phase system and an oil/water/gas three-phase system reservoir. The water and oil phases are slightly compressible, but after the reservoir pressure dropped below the bubblepoint pressure, the compressible free gas was introduced into the system. As the inner-boundary pressure fluctuated up and down, corresponding to a trigonometric function with time, the U-shaped curve was again obtained in the near-wellbore region. The backflow rates were calculated for each phase in every single gridblock.

A sensitivity analysis was performed to evaluate the length of the "disturbed" distance from the wellbore under multiphase flow conditions. High frequency of the bottomhole pressure oscillation, large fluid compressibility, and low reservoir permeability will lead to a shorter length of the U-shaped pressure profile. The fluctuating amplitude shows no significant effect on the penetration distance of the U-shape.

Methodology

This work is based on conventional numerical reservoir modeling techniques and uses them in a way that accommodates transient pressure and rate boundary conditions at the wellbore and also along the distance from the well.

Implicit pressure explicit saturation (IMPES) approach

Numerical reservoir modeling is based on the solution of the diffusivity equation, which combines mass conservation equations (differential mass balance), PVT fluid characterization, and a transport law (Darcy's equation) in a multiphase flow system.

When using the IMPES approach, the diffusivity equation is solved implicitly for pressure and explicitly for phase saturation, as summarized in Eq. 6. 1. This formulation is also explained in Chapter IV in detail.

$$\sum_{m\in\psi_n}\left\{\left(B_o-R_sB_g\right)_n^{n+1}T_{o\,n,m}^{n}+B_{w\;n}^{n+1}T_{w\,n,m}^{n}+B_{g\;n}^{n+1}\left[T_{g\,n,m}^{n}+\left(T_oR_s\right)_{n,m}^{n}\right]\right\}p_{o\;m}^{n+1}$$
$$-\left(\left(B_o-R_sB_g\right)_n^{n+1}C_{op\,n}+B_{w\;n}^{n+1}C_{wp\,n}+B_{g\;n}^{n+1}C_{gp\,n}+\sum_{m\in\psi_n}\left\{\begin{matrix}\left(B_o-R_sB_g\right)_n^{n+1}T_{o\,n,m}^{n}\\+B_{w\;n}^{n+1}T_{w\,n,m}^{n}+B_{g\;n}^{n+1}\left[T_{g\,n,m}^{n}+\left(T_oR_s\right)_{n,m}^{n}\right]\end{matrix}\right\}\right)p_{o\;n}^{n+1}$$
$$=-\left[\left(B_o-R_sB_g\right)_n^{n+1}C_{op\,n}+B_{w\;n}^{n+1}C_{wp\,n}+B_{g\;n}^{n+1}C_{gp\,n}\right]p_{o\,n}^{n}-\left[\left(B_o-R_sB_g\right)_n^{n+1}q_{osc\,n}+B_{w\;n}^{n+1}q_{wsc\,n}^{n}+B_{g\;n}^{n+1}q_{gsc\,n}\right]$$
$$+\sum_{m\in\psi_n}B_{w\;n}^{n+1}T_{w\,n,m}^{n}\left(P_{cow\,m}^{n}-P_{cow\,n}^{n}\right)-\sum_{m\in\psi_n}B_{g\;n}^{n+1}T_{g\,n,m}^{n}\left(P_{cgo\,m}^{n}-P_{cgo\,n}^{n}\right)$$
$$+\sum_{m\in\psi_n}\left\{\left(B_o-R_sB_g\right)_n^{n+1}T_{o\,n,m}^{n}\bar{\gamma}_{o\,n,m}^{n}+B_{w\;n}^{n+1}T_{w\,n,m}^{n}\bar{\gamma}_{w\,n,m}^{n}+B_{g\;n}^{n+1}\left[T_{g\,n,m}^{n}\bar{\gamma}_{g\,n,m}^{n}+\left(T_oR_s\right)_{n,m}^{n}\bar{\gamma}_{o\,n,m}^{n}\right]\right\}\left(Z_m-Z_n\right)$$

…… (6.1)

The reservoir simulator generated for this study is sensitive to the pressure fluctuating under transient conditions. Proper configurations of the fluid PVT properties, the grid refinement in the near-wellbore region, and the ratio of the pressure oscillation period to the timestep are extremely critical.

Peaceman (1977) revealed that the IMPES method is only stable when

$$\frac{\Delta t}{\Delta x^2}<6.23\times10^{-5}\,. \qquad \text{…… (6.2)}$$

where the timestep is in days and the minimum gridding block length is in feet.

Fluid PVT characterization

For this transient modeling work, fluid PVT properties were carefully selected to provide the necessary system compressibility and allow sufficient mass storage. The black oil correlations were chosen (**Fig. 6.2**).

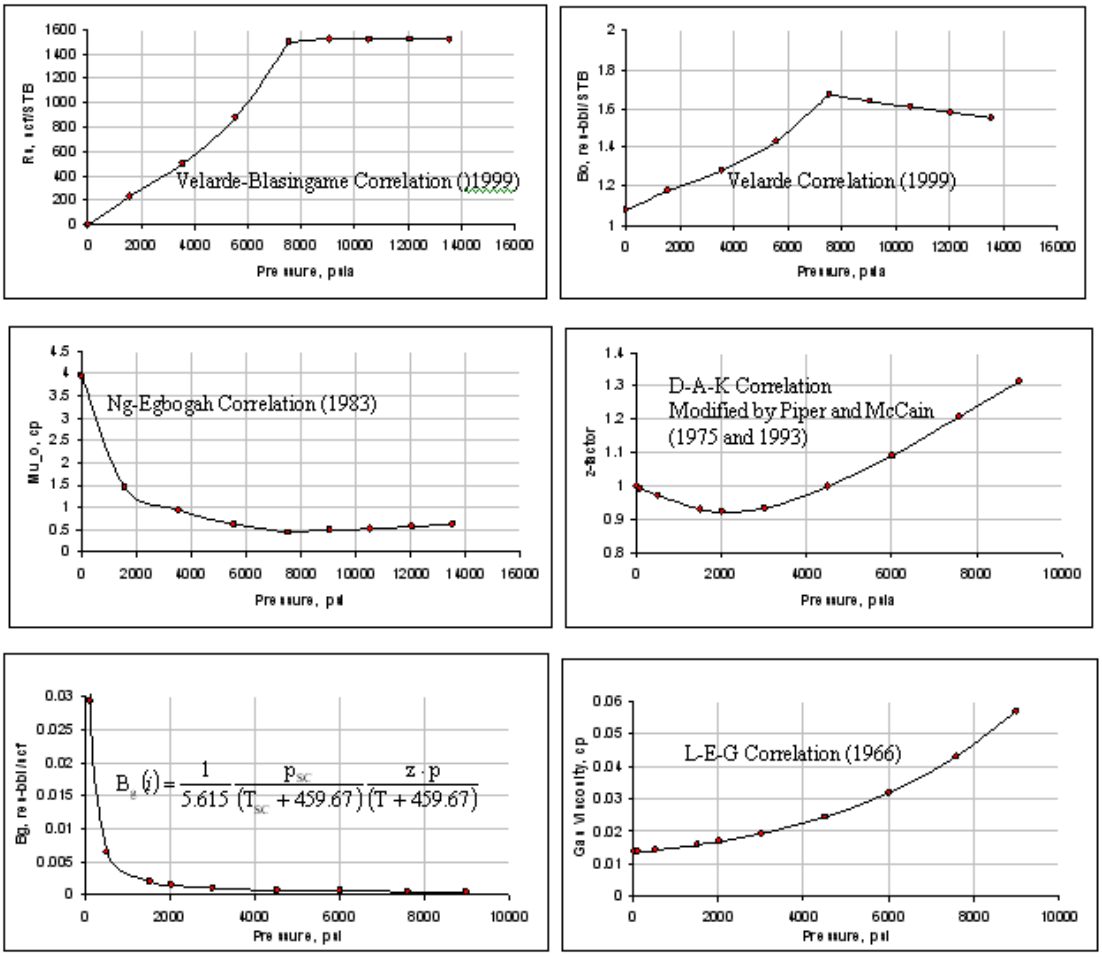

Fig. 6.2—Realistic fabricated PVT data lay out the correct trends upon pressure and create appropriate fluid compressibility for pressure oscillation in the near-wellbore region.

Grid refinement

Grid refinement is essential in the near-wellbore region because the pressure disturbance can only be sustained at a comparatively short distance from the wellbore. However, the depth of the disturbance zone into the reservoir is not known a priori and varies with the frequency of the pressure fluctuations. To achieve this gridding refinement, the logarithmic gridding method (Eq. 6.3) is employed.

$$r_j = r_w \left(\frac{r_e}{r_w} \right)^{\frac{j-1}{Nx}} \quad \text{..... (6.3)}$$

where j is the gridblock number and Nx is the total number of grids in the 1D direction. The smallest gridblock is adjacent to the wellbore, and this size decides the maximum timestep by Eq. 2.

Pressure oscillation

To numerically generate the U-shaped pressure profile, a simplified pressure oscillation at the wellbore was imposed to represent the actual oscillations that would be dictated by phase distribution effects in the wellbore, combined with the inertia opposed by the reservoir. For the preliminary studies, a sinusoidal wellbore pressure oscillation was assumed:

$$p_{BH} = p_1 + \Delta p \sin\left(i \times \frac{\pi}{c} \right) \quad \text{..... (6.4)}$$

where Δp is the oscillation amplitude, i is an integer representing the current cumulative time and c is a constant integer determining the trigonometric function period.
The period, P, will be

$$P = 2c\Delta t \, . \quad \text{..... (6.5)}$$

Correspondingly, the frequency of the sine function is

$$f = \frac{\pi}{c\Delta t} \quad \text{(6.6)}$$

As previously mentioned, proper PVT data lead to correct calculations of the fluid compressibility, which provide the potential for pressure collisions. The grid refinement techniques achieve a balance of zooming in on the near-wellbore region and determining the maximum timestep to obtain stable IMPES solutions. Moreover, the pressure oscillation frequency is dynamically linked with the timestep, which ensures the numerical simulation is capable of capturing any rapid pressure inconstancy in the refined near-wellbore region. All these prerequisites help constitute the U-shaped curve pressure profile.

Single Gas Phase System

The reservoir is assumed to contain dry gas that is produced from a single well under radial flow conditions with a constant initial pressure. This study is regarded as a pilot test for the proposed methodology, so it used a very simplified diffusivity equation.

Diffusivity equation

The verification of the U-shaped pressure profile started with a single-gas phase 1D model on the premise of a homogeneous porous medium. In terms of pseudopressure integral, the simplified diffusivity equation in radial geometry is:

$$\frac{\partial^2 m(p)}{\partial r^2} + \frac{1}{r}\frac{\partial m(p)}{\partial r} = \frac{\phi\mu c_t}{k}\frac{\partial m(p)}{\partial t} \quad \text{(6.7)}$$

This equation neglects the production term.

Reservoir petrophysical parameters and gas PVT data

Reservoir petrophysical parameters and gas PVT data have been theoretically assumed (**Table 6.1**).

Table 6.1—SYNTHETIC PETROPHYSICAL AND FLUID PROPERTIES FOR CASE 1(*)

Reservoir drainage, (r_e), ft	Constant reservoir pseudopressure, (p_e), psia^2/cp	Reservoir porosity	Total compressibility, Pa^{-1}	Reservoir permeability, mD	Gas viscosity, cp
328	2.1×10^{-8}	0.21	5.87×10^{-7}	8.56×10^{-5}	0.0137

(*) All the fluid properties listed are assumed to be constant

Reservoir gridding

The wellbore radius is 0.3 ft (0.091 m), and this synthetic gas reservoir contains 10 gridblocks in logarithmic scale (Eq. 6.3). The minimum gridblock size is around 1.9 ft (0.58 m), so the maximum timestep is around 0.2 seconds, regardless of the real field requirements. This approach zoomed in on the near-wellbore region. The timestep was arbitrarily taken as 0.2 seconds.

Pressure oscillation function

The initial bottomhole pseudopressure is set at 2.1×10^{-8} psia^2/cp, to cast a conventional profile in the near wellbore. The pseudopressure oscillation starts in the form of Eq. 4 by setting p_1 as 5 psia^2/cp, Δp as 4 psia^2/cp and c as 2, which implies that the period of the sine function will take five time steps, that is around 1 second. The pseudopressure at the outer boundary is set constant at 2.1×10^{-7} psia^2/cp.

Results and discussions

Fig. 6.3 shows the U-shaped pseudopressure profile in the near-wellbore region using logarithmic scale for the radial distance from the center of the well. At the third timestep, it clearly shows the generated U-shaped pressure distribution.

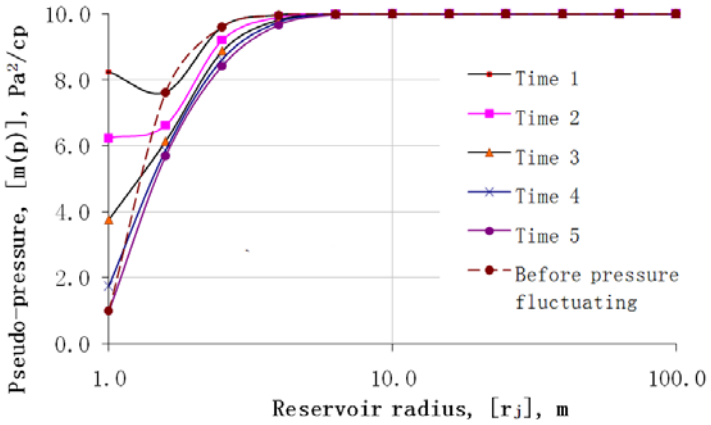

Fig. 6.3—Case Study 1 successfully obtained the "distorted" pseudopressure profile.

Two Phases Dry Gas and Water System

Encouraged by the previous successful results, this study is closer to the real field conditions. Similarly to the previous approach for a single dry gas reservoir, as the inner boundary pressure fluctuated up and down, corresponding to a trigonometric function with time, the U-shaped curve was again obtained in the near-wellbore region. The backflow rates were calculated for each phase in every single gridblock.

Diffusivity equation

This case study was performed with a 1D multiphase simulator according to Eq. 6.8, which is a simplified formation of Eq. 6.1. Neglecting the capillary pressure, the pressure of water phase is equal to the gas phase.

$$\sum_{m\in\psi_n}\left\{\left(B_o-R_sB_g\right)_n^{n+1}T_{o\,n,m}^{n}+B_{w\ n}^{n+1}T_{w\,n,m}^{n}+B_{g\ n}^{n+1}\left[T_{g\,n,m}^{n}+\left(T_oR_s\right)_{n,m}^{n}\right]\right\}p_{g\ m}^{n+1}$$

$$-\left(\left(B_o-R_sB_g\right)_n^{n+1}C_{op_n}+B_{w\ n}^{n+1}C_{wp_n}+B_{g\ n}^{n+1}C_{gp_n}+\sum_{m\in\psi_n}\left\{\begin{matrix}\left(B_o-R_sB_g\right)_n^{n+1}T_{o\,n,m}^{n}\\+B_{w\ n}^{n+1}T_{w\,n,m}^{n}+B_{g\ n}^{n+1}\left[T_{g\,n,m}^{n}+\left(T_oR_s\right)_{n,m}^{n}\right]\end{matrix}\right\}\right)p_{g\ n}^{n+1}$$

$$=-\left[\left(B_o-R_sB_g\right)_n^{n+1}C_{op_n}+B_{w\ n}^{n+1}C_{wp_n}+B_{g\ n}^{n+1}C_{gp_n}\right]p_{g_n}^{n}-\left[\left(B_o-R_sB_g\right)_n^{n+1}q_{osc_n}+B_{w\ n}^{n+1}q_{wsc_n}^{n}+B_{g\ n}^{n+1}q_{gsc_n}\right]$$

$$+\sum_{m\in\psi_n}\left\{\left(B_o-R_sB_g\right)_n^{n+1}T_{o\,n,m}^{n}\bar{\gamma}_{on,m}^{-n}+B_{w\ n}^{n+1}T_{w\,n,m}^{n}\bar{\gamma}_{wn,m}^{-n}+B_{g\ n}^{n+1}\left[T_{g\,n,m}^{n}\bar{\gamma}_{g_{n,m}}^{-n}+\left(T_oR_s\right)_{n,m}^{n}\bar{\gamma}_{on,m}^{-n}\right]\right\}\left(Z_m-Z_n\right)$$

…….. (6.8)

Reservoir PVT and petrophysical parameters

The same PVT Characterization as Fig. 6.2 was used based on synthetic data. The input dataset for the multiphase system is summarized in **Table 6.2**. The PVT behavior is depicted in **Fig. 2**. The petrophysical parameters are as summarized in **Table 6.3**.

Table 6.2—PARAMETERS AVAILABLE IN FIELD THAT ARE USED FOR PVT CHARACTERIZATION THROUGH LITERATURE CORRELATIONS

Reservoir temperature (T_R), °F	Separator gas specific gravity (γ_{gSP})	Separator Temperature (T_{sep}), °F	Separator Pressure (p_{sep}), psia
220.0	0.63	60.0	114.7

Table 6.3—SYNTHETIC PETROPHYSICAL USED FOR CASE STUDY 2

Initial reservoir pressure, (p_i), psi	Reservoir porosity	Initial water saturation, (S_{wi})	Total compressibility, Pa^{-1}	Reservoir permeability, (k), md
7880	0.20	0.36	$5.87x10^{-7}$	300

Reservoir rock is water-wet compared to the gas phase, the relative permeability curves shown in **Fig. 6.4**. Where water replaces gas, it is an inhibition process; on the other hand, where the free gas replaces oil, it is a drainage process.

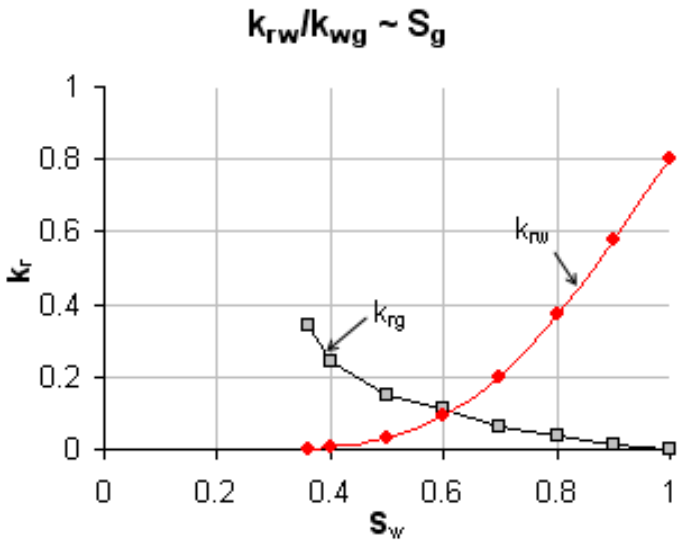

Fig. 6.4—Relative permeability vs. wetting phase saturation.

Reservoir gridding

The logarithmic method automatically refines the near-wellbore region; however, the first (smallest) gridblock size is only 0.23 ft. From Eq. 6.2, the maximum timestep is about 3.29×10^{-6} days (0.28 seconds) to ensure stable IMPES solutions. This small timestep is against any practical application, and further refinement of the gridblocks is required.

Thus, the reservoir was divided into 20 gridblocks in 1D. The first 10 cells have the uniform size of 10 ft and the rest of the reservoir follows the logarithmic gridding method. After recalculation, a maximum timestep of 0.006 days (518 seconds) was obtained and considered acceptable. This work adopted 0.005 days as an appropriate timestep.

Pressure oscillation function

The pressure oscillation is described in the form of the Eq. 6.4. The amplitude, Δp, is assumed as 50 psia, and the oscillation period is 864 seconds, or approximately 14.4 minutes. p_1 is equal to 7,848 psi.

Results and discussions

The pressure and oil saturation profiles were initialized assuming constant production rate at the inner boundary and constant reservoir pressure at the outer boundary. After the first four days of production, a conventional pressure profile was cast in **Fig. 6.5**.

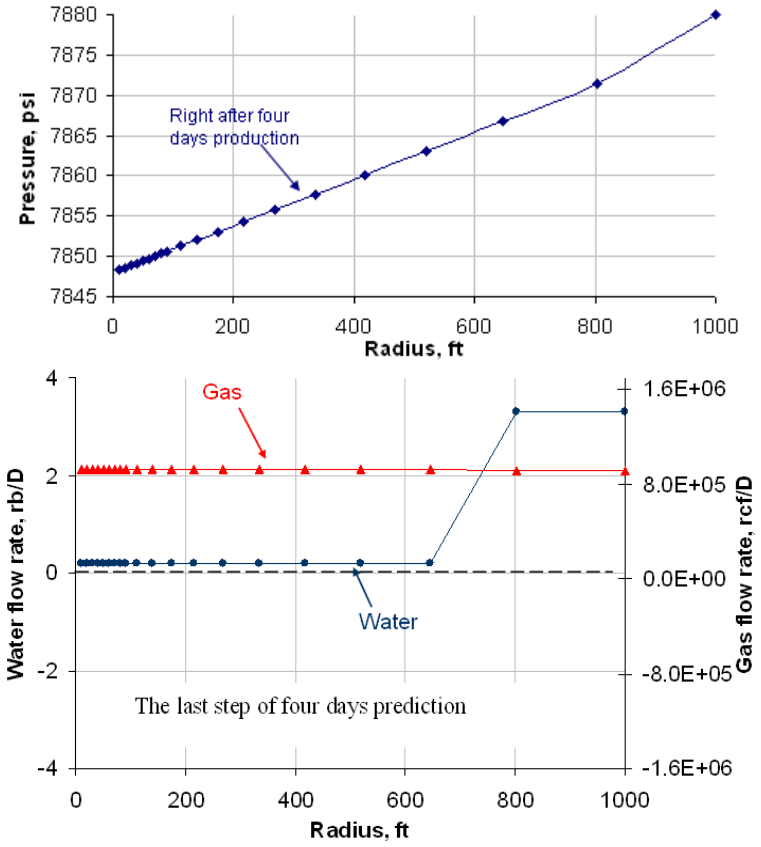

Fig. 6.5—Plots for the pressure and saturation of the three phases along the distance. Water encroachment stops around 700 ft from the wellbore after four days production.

Applying the pressure oscillation function at the inner boundary generates the U-shaped pressure profile in **Fig. 6.6**. The affected distance is around 450 ft. The transient backflow rate at the first timestep is also calculated and illustrated in **Fig. 6.7** after bottomhole pressure started to fluctuate (14.4 minutes). Simulation results show the backflow rate is suddenly increased over 10 times at the wellbore, and the U-shaped pressure profile is evident in **Fig. 6.8**. This result supports the hypotheses of possible fluid reinjection from the wellbore to the reservoir in certain transient situations.

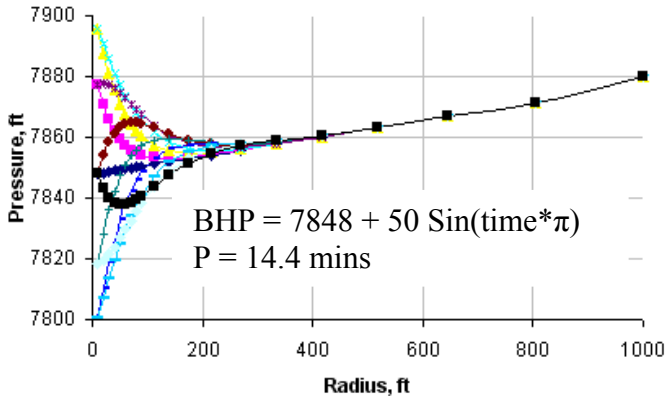

Fig. 6.6—The combined distorted pressure profile for one period. Beyond 300 ft from the wellbore, the pressure profile keeps an identical shape without feeling the bottomhole pressure oscillation. *P* means the period of the oscillation.

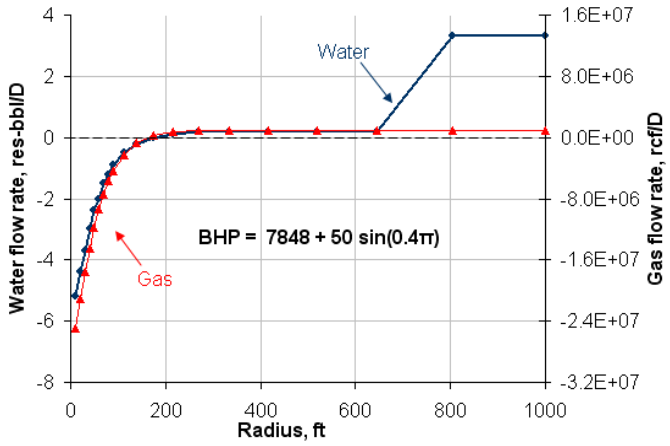

Fig. 6.7—The flow rates distribution between each pair of adjacent gridblocks after bottomhole pressure oscillation started (14.4 minutes). Negative rates mean backflow rates.

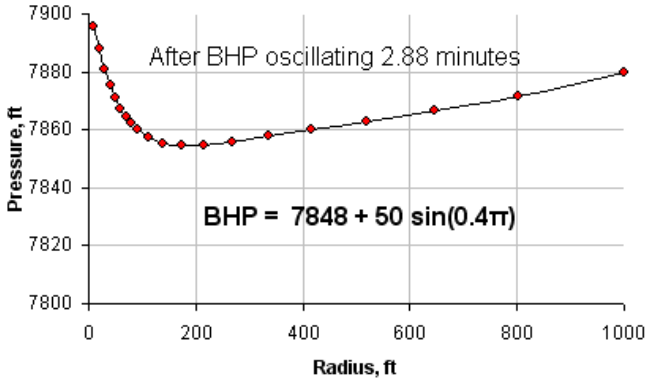

Fig. 6.8—The evident U-shaped pressure profile for the first timestep after BHP oscillation started (14.4 minutes).

Sensitivity analysis on the affected distance from wellbore

A sensitivity analysis was carried out on the affected distance from the wellbore regarding the pressure oscillation frequency, oscillation amplitude, Δp, various fluid compressibility, and rock properties.

The same reservoir gridding settings were kept, but the timestep was set to 0.001 days (86.4 seconds). The pressure oscillation function keeps the form of Eq. 6.4, and p_1 is set as 7,880 psi.

Varying the oscillation frequency

The analysis was carried out for one time period of the trigonometric function. Different *c* values were chosen (**Table 6.4**). The remaining model configurations are the same as in Case Study 2. The U-shaped curves in an individual period time are illustrated in **Fig. 6.9**.

Table 6.4—AFFECTED RADIUS UNDER DIFFERENT PRESSURE OSCILLATION FREQUENCY FOR DRY GAS/WATER TWO-PHASE RESERVOIR

One Period	8.64 s	8.64 min	7.2 min	14.4 min	1.2 hour
Affected radius, ft	50	220	300	450	650

As both the figure and table reveal, a lower frequency pressure fluctuation causes a longer disturbed distance from the wellbore for a single period. As *c* is equal to one, the wellbore pressure is a constant 7,880 psia. If the pressure oscillation at the wellbore is long enough, its effect will always reach the outer reservoir boundary.

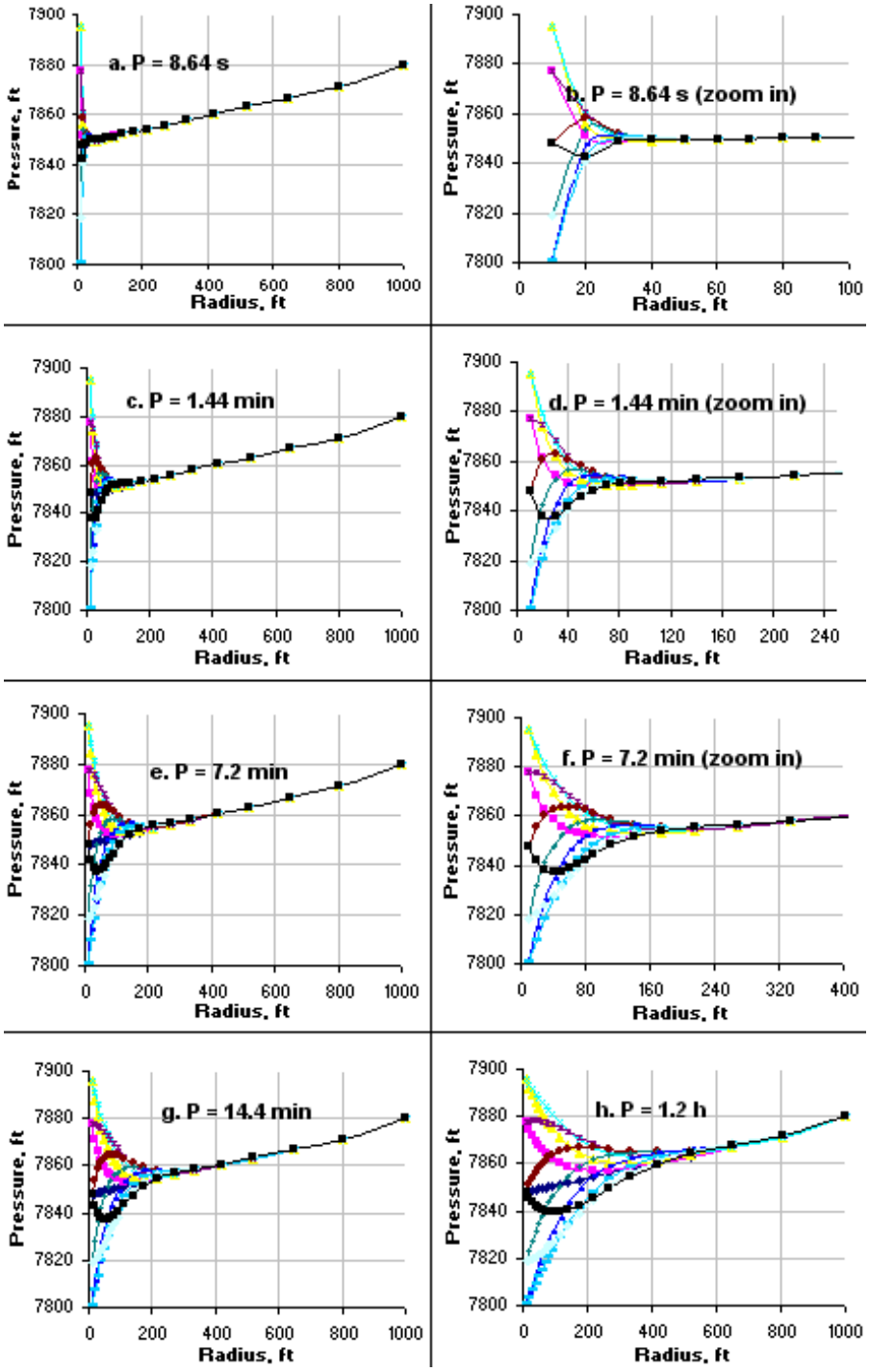

Fig. 6.9—A sensitivity analysis by different oscillation frequencies (2-phase). It showed that lower frequency leads to a longer affected length. In an extreme case, the bottomhole pressure was taken as the reservoir pressure in the last plot. Each line in any plot is a snapshot of the pressure profile at a given timestep. *P* represents the oscillation period.

Varying the oscillation amplitude

Different amplitudes were chosen (**Table 6.5**). The oscillation period was set to 14.4 minutes. All the remaining parameters kept the same values. The U-shaped curves in an individual time period are illustrated in **Fig. 6.10**. Both the table and figure clearly show that the affected distance is practically independent of the oscillation amplitude; however, a stronger pressure fluctuation is observed in the near-wellbore region for the greater oscillation amplitude cases.

Table 6.5—AFFECTED RADIUS UNDER DIFFERENT PRESSURE OSCILLATION AMPLITUDE FOR DRT GAS/WATER TWO-PHASE RESERVOIR

Amplitude, Δp	10	50	100	200	500
Affected radius, ft	450	450	450	450	450

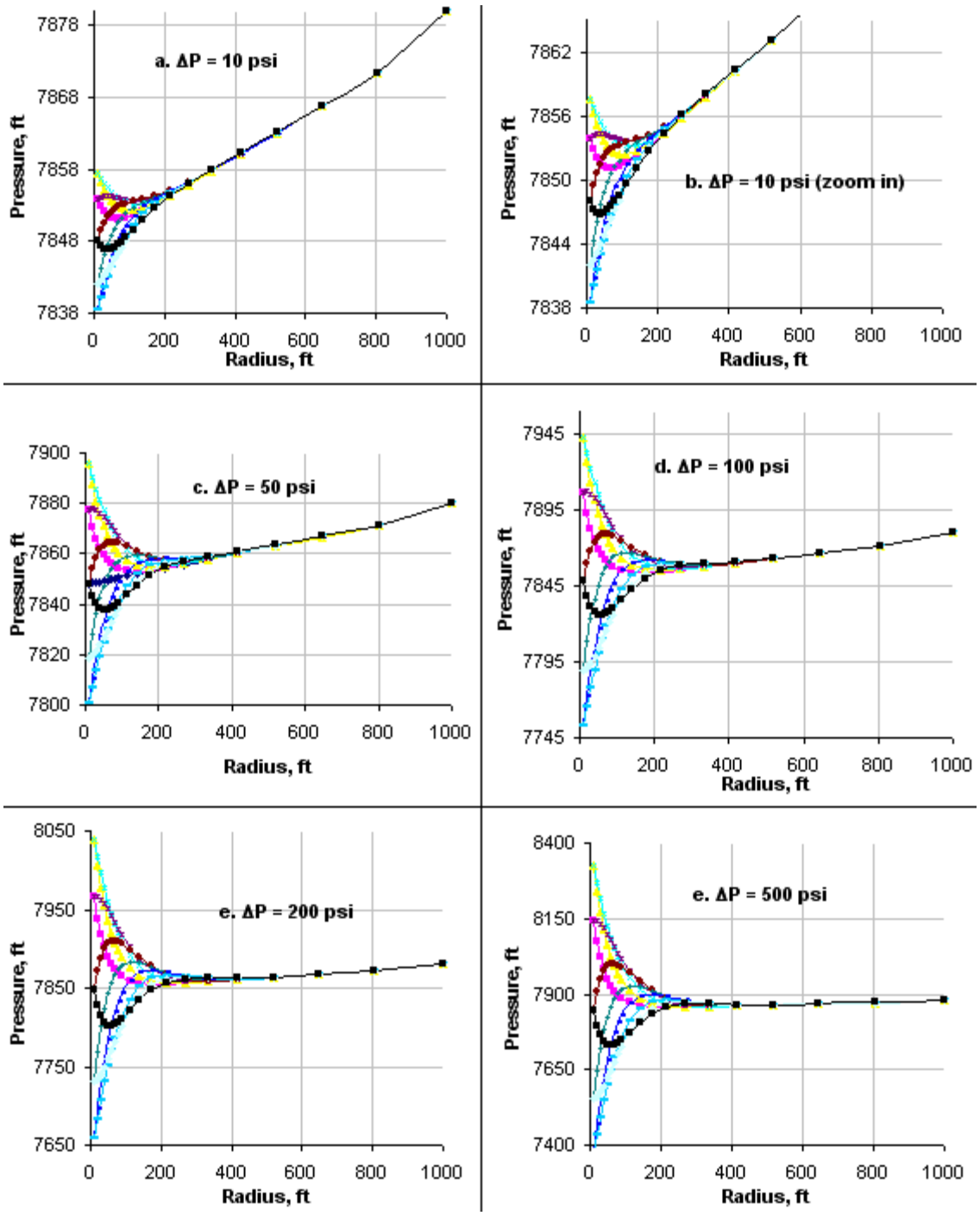

Fig. 6.10—A sensitivity analysis by different oscillation amplitudes (2-phase). The affected distance is about 800 ft and is insensitive to oscillation amplitude. Each line is a snapshot of the pressure profile at a certain timestep.

Varying the reservoir permeability

Different reservoir permeability values were selected (**Table 6.6**). The oscillation period was set to 14.4 minutes. All other parameters kept the same values, and the starting pressure profile was imaged after 4 days of production. Snapshots of the U-shaped curves during an individual time period are presented in **Fig. 6.11**. The results show a longer affected distance with higher permeability. In the extreme case of 10 darcys, the pressure at the outer boundary "felt" the oscillations almost instantly. The less permeable of the formation, the more profound the U-shaped curve and the effects were presented by this work become.

Table 6.6—AFFECTED RADIUS UNDER DIFFERENT RESERVOIR PERMEABILITY FOR DRY GAS/WATER TWO-PHASE RESERVOIR

Permeability, md	3	30	300	1000	3000	10000
Affected radius, ft	30	100	450	700	950	Almost instant response

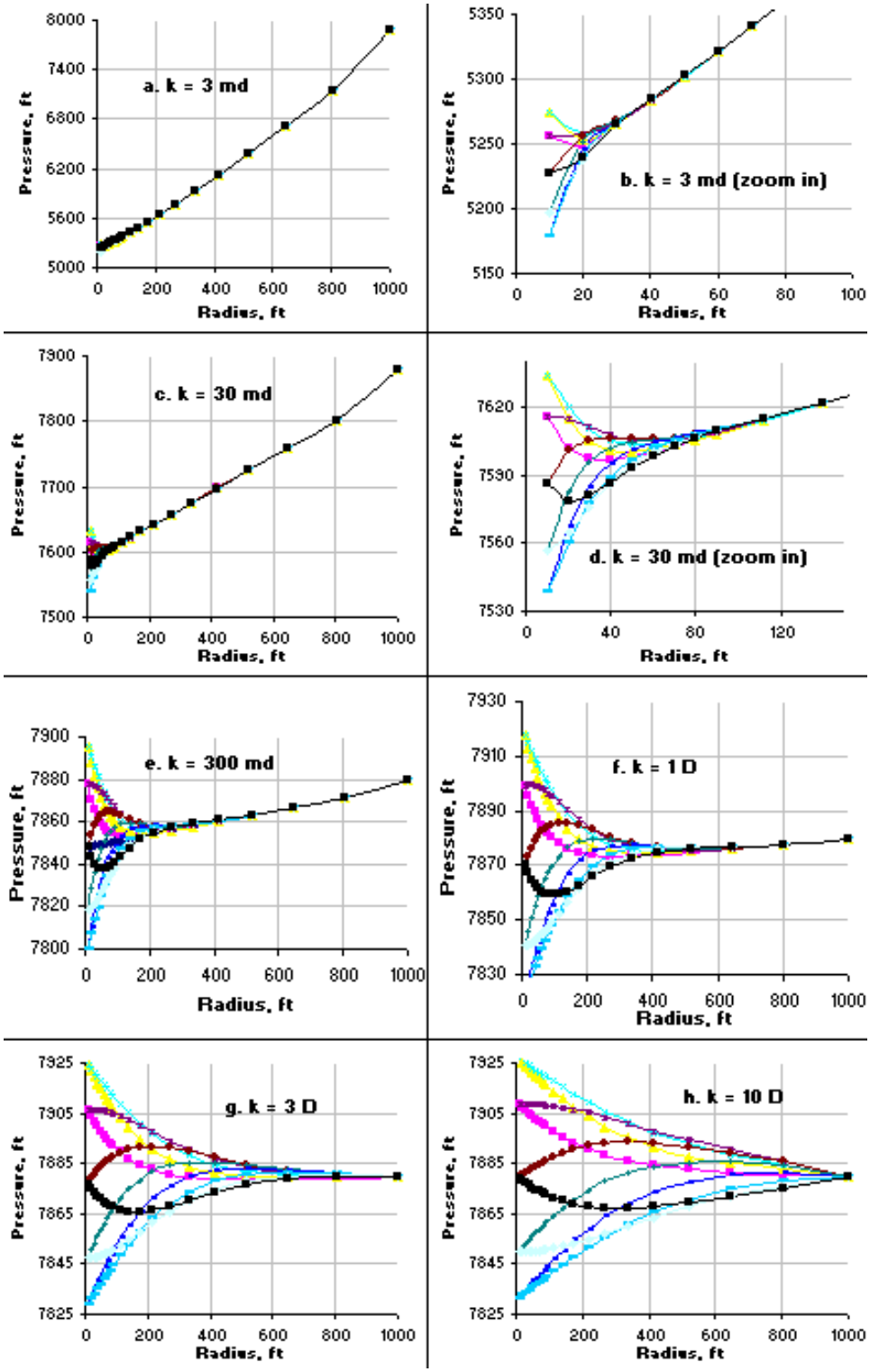

Fig. 6.11—A sensitivity analysis by different permeability values (2-phase). It showed the tighter reservoir leads to a shorter affected length. Each line is a snapshot of the pressure profile at certain timestep.

Varying the fluid compressibility

The oil compressibility is directly related to the oil coefficients of $\Delta_t p_o$ in the expansion of oil accumulation, C_{gp} in Eq. 6.1. Different multipliers on this parameter were considered to investigate the compressibility effect on the U-shaped radius (**Table 6.7**). The oscillation period was set to 14.4 minutes. All other parameters sustained the same values. The U-shaped curves within an individual period of time are shown in **Fig. 6.12**.

A higher compressibility fluid can better absorb the pressure oscillations coming from the wellbore. In the first two columns of the table, the affected radius changed significantly with respect to the multiplier magnitude on gas coefficients, C_{gp}. This unrealistic multiplier has made the gas phase behave like a less-compressible liquid. The higher compressibility affiliated to gas absorbs most of the pressure oscillation in the near-wellbore region, and results in the U-shaped pressure profile.

Table 6.7—THE AFFECTED RADIUS UNDER DIFFERENT OIL COEFFICIENT C_{OP} FOR DRY GAS/WATER TWO-PHASE RESERVOIR

Multiplier (xC_{gp})	0.01	0.1	1	10	50
C_{op} in the 1st grid, STB/D-psia	2.18 E3	2.18 E4	2.18 E5	2.18 E6	1.09 E7
Affected radius, ft	Almost instant response	900	600	180	70

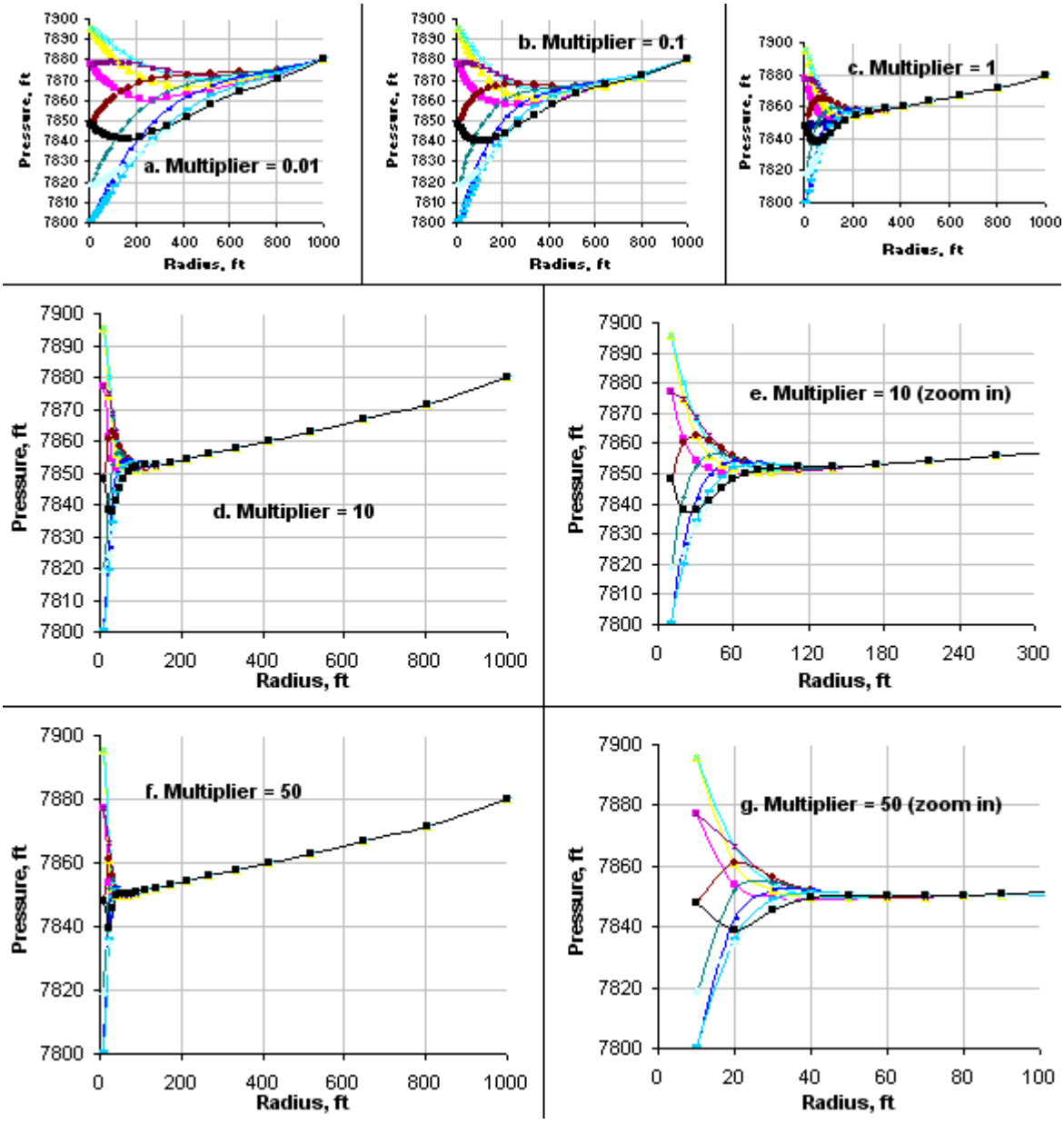

Fig. 6.12—A sensitivity analysis by different fluid compressibility (2-phase).
It showed that lower compressibility leads to a longer affected length;
however, if the multiphase fluid is incompressible,
the rigid system failed to give a U-shaped curve.
Each line is a snapshot of the pressure profile at a certain timestep.

Three Phases System

This study was performed for a synthetic oil/solution-gas/water three-phase reservoir, and it is more complicated and closer to real field conditions. Similarly to the previous approaches, as the inner-boundary pressure fluctuated up and down, corresponding to a trigonometric function with time, the U-shaped curve was again obtained in the near-wellbore region. The backflow rates were calculated for each phase in every single gridblock.

Diffusivity equation

This case study was performed with a 1D multiphase simulator according to Eq. 6.1. Neglecting the capillary pressure, the pressure of the water and gas phases is equal to the oil phase.

Reservoir PVT and petrophysical parameters

The PVT Characterization was carried out based on synthetic data. The input dataset for the multiphase system is summarized in **Table 6.8**. The oil bubblepoint pressure and the related PVT parameters were obtained from correlations (Valko and McCain, 2003). The PVT behavior is depicted in Appendix A. The calculated bubblepoint pressure is 7,602 psia and the solution-gas/oil ratio is 1,519.5 scf/STB. The petrophysical parameters are as summarized in **Table 6.9**.

Table 6.8—PARAMETERS AVAILABLE IN FIELD THAT ARE USED FOR PVT CHARACTERIZATION THROUGH LITERATURE CORRELATIONS

Stock-tank oil gravity (API), °API	Separator solution gas/oil ratio (R_{SP}), scf/STB	Reservoir temperature (T_R), °F	Separator gas specific gravity (γ_{gSP})	Separator Temperature (T_{sep}), °F	Separator Pressure (p_{sep}), psia
28.0	1500.0	220.0	0.63	60.0	114.7

Table 6.9—SYNTHETIC PETROPHYSICAL USED FOR CASE STUDY 2				
Initial reservoir pressure, (p_i), psi	Reservoir porosity	Initial water saturation, (S_{wi})	Total compressibility, Pa^{-1}	Reservoir permeability, (k), md
7880	0.20	0.16	5.87×10^{-7}	300

Assuming the reservoir rock is water-wet, the relative permeability curves shown in **Fig. 6.13** represent a typical scenario. Where water replaces oil, it is an inhibition process; on the other hand, where the free gas replaces oil, it is a drainage process. The Stone's Method II (Eq. 6.9) is used to calculate the relative permeability,

$$k_{ro} = k_{rocw}\left(\frac{k_{row}}{k_{rocw}} + \frac{k_{rw}}{k_{rocw}}\right)\left(\frac{k_{rog}}{k_{rocw}} + \frac{k_{rg}}{k_{rocw}}\right) - \left(k_{rw} + k_{rg}\right). \quad \ldots\ldots\ldots\ldots\ldots\ldots\ldots\ldots (6.9)$$

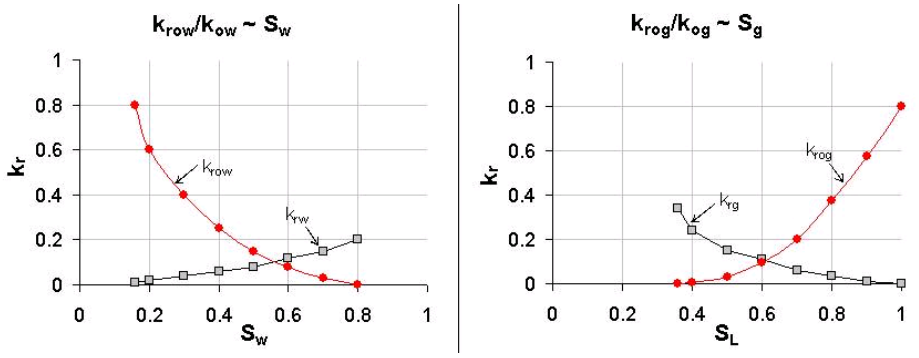

Fig. 6.13—Relative permeability vs. wetting phase saturation.

Reservoir gridding

A similar half-logarithmic method was used as in the previous two-phase simulation work. Thus, the reservoir was divided into 20 gridblocks in 1D. The first 10 cells have the uniform size of 10 ft and the rest of the reservoir follows the logarithmic gridding method. After re-calculation, this work adopted 0.005 days as an appropriate timestep.

Pressure oscillation function

The pressure oscillation is described in the form of the Eq. 6.4. The amplitude, Δp, is assumed as 500 psia, and the constant c is 5, with an oscillation period of $10\Delta t$, that is 5,184 seconds, or approximately 86 minutes.

Results and discussions

The pressure and oil saturation profiles were calculated first assuming constant production rate at the inner boundary. After the first four days of production, a conventional pressure profile was cast in **Fig. 6.14**.

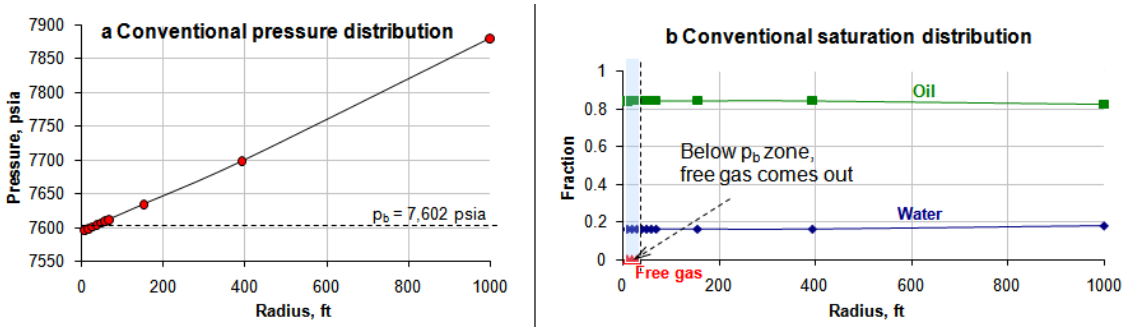

Fig. 6.14—Plots for the pressure and saturation of the three phases along the distance. Free gas exists as the pressure is below the bubblepoint pressure

Applying the pressure oscillation function at the inner boundary generates the U-shaped pressure profile in **Fig. 6.15**. The affected distance is around 800 ft. The transient backflow rate at the first timestep is also calculated and illustrated in **Fig. 6.16**. Simulation results show the backflow rate is suddenly increased over 10 times at the wellbore, and the U-shaped pressure profile is evident in **Fig. 6.17**. This result again supports the hypotheses of possible fluid reinjection from the wellbore to the reservoir in certain transient situations.

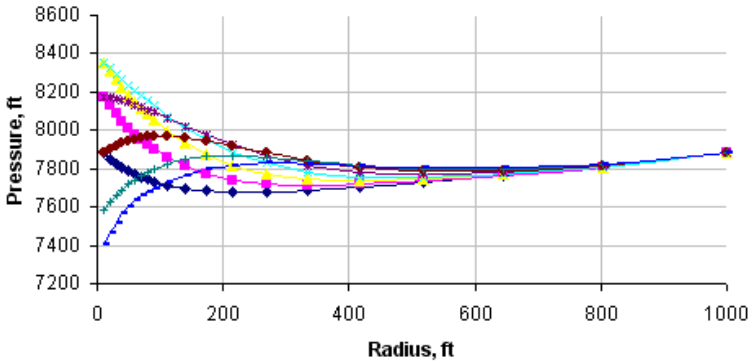

Fig. 6.15—The combined distorted pressure profile for one hour. Beyond 800 ft from the wellbore, the pressure profile keeps an identical shape without feeling the bottomhole pressure oscillation.

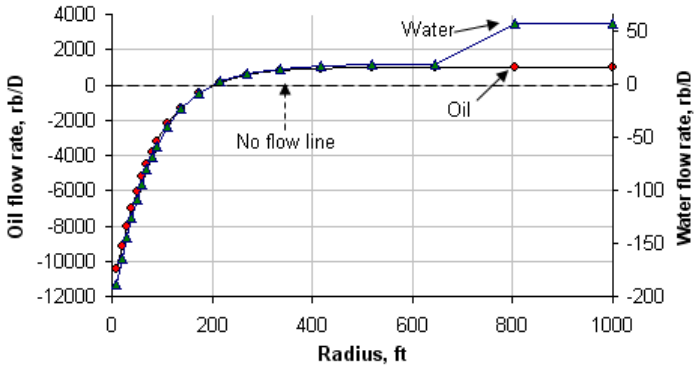

Fig. 6.16—The flow rates distribution between each pair of adjacent gridblocks. Negative rates mean backflow rates.

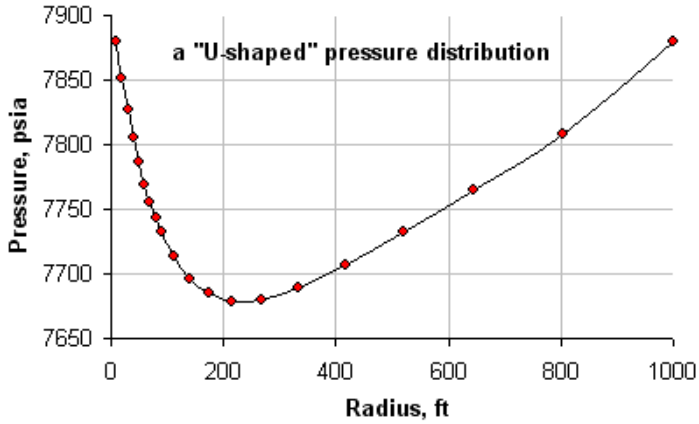

Fig. 6.17—Another evident U-shaped pressure profile after the BHP oscillation started (8.6 minutes).

Sensitivity analysis on the affected distance from wellbore

A sensitivity analysis was carried out on the affected distance from the wellbore regarding the pressure oscillation frequency, oscillation amplitude, Δp, various fluid compressibility, and rock properties.

The same reservoir gridding settings were kept, but the timestep was set to 0.001 days (86.4 seconds). The pressure oscillation function keeps the form of Eq. 6.4, and p_1 is set as 7,880 psi.

Varying the oscillation frequency

The analysis was carried out for one time period of the trigonometric function. Different c values were chosen (**Table 6.10**). The remaining model configurations were kept the same. The U-shaped curves in an individual period time are illustrated in **Fig. 6.18**.

Table 6.10—AFFECTED RADIUS UNDER DIFFERENT PRESSURE OSCILLATION FREQUENCY

Timestep, D	0.00001	0.0006	0.005	0.005	0.005	0.005
One Period	8.64 s	8.64 min	14.4 min	0.48 hour	2.4 hour	0
Frequency	0.73 s^{-1}	0.73 min^{-1}	0.44 min^{-1}	13.09 $hour^{-1}$	2.62 $hour^{-1}$	N/A
Affected radius, ft	75	380	550	800	950	1000

As both the figure and table reveal, a lower frequency pressure fluctuation causes a longer disturbed distance from the wellbore for a single period. As c is equal to one, the wellbore pressure is a constant 7,880 psia. If the pressure oscillation at the wellbore is long enough, its effect will always reach the outer reservoir boundary.

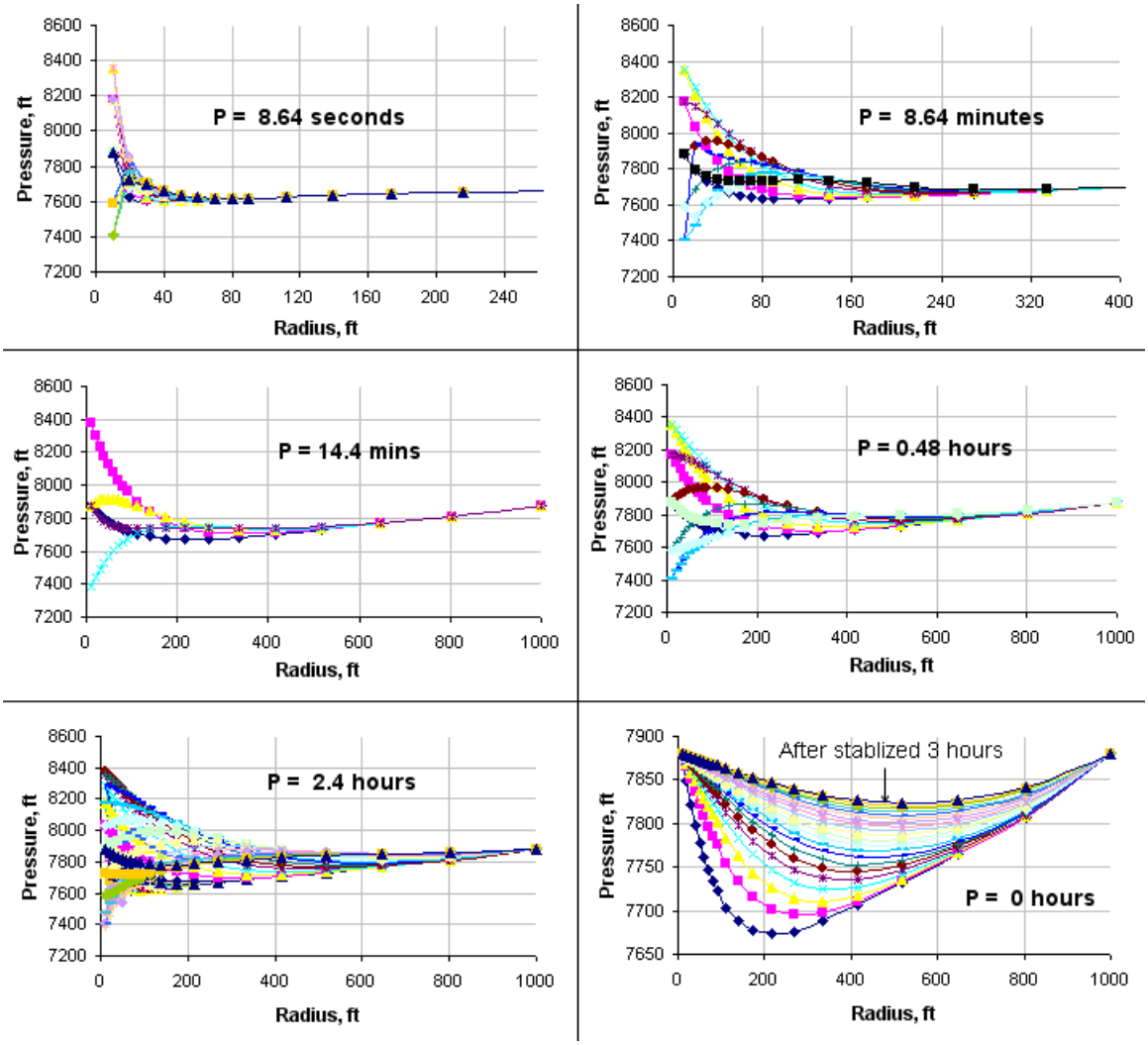

Fig. 6.18—A sensitivity analysis by different oscillation frequencies (3-phase).
It showed that lower frequency leads to a longer affected length.
In an extreme case, the BHP was taken as the reservoir pressure in the last plot.
Each line in any plot is a snapshot of the pressure profile at a given timestep.
***P* represents the oscillation period.**

Varying the oscillation amplitude

Different amplitudes were chosen (**Table 6.11**). The oscillation period was set to 0.48 hours. All the remaining parameters kept the same values. The U-shaped curves in an individual time period are illustrated in **Fig. 6.19**. The IMPES solution failed to converge for the case where the amplitude was 10% of the reservoir pressure. Both the table and figure clearly show that the affected distance is practically independent of the oscillation amplitude; however, a stronger pressure fluctuation is observed in the near-wellbore region for the greater oscillation amplitude cases, when the affected distance from the wellbore is 800 ft.

Table 6.11—AFFECTED RADIUS UNDER DIFFERENT PRESSURE OSCILLATION AMPLITUDE

Amplitude, Δp	10	100	500	750	800
Affected radius, ft	800	800	800	800	Convergence failed

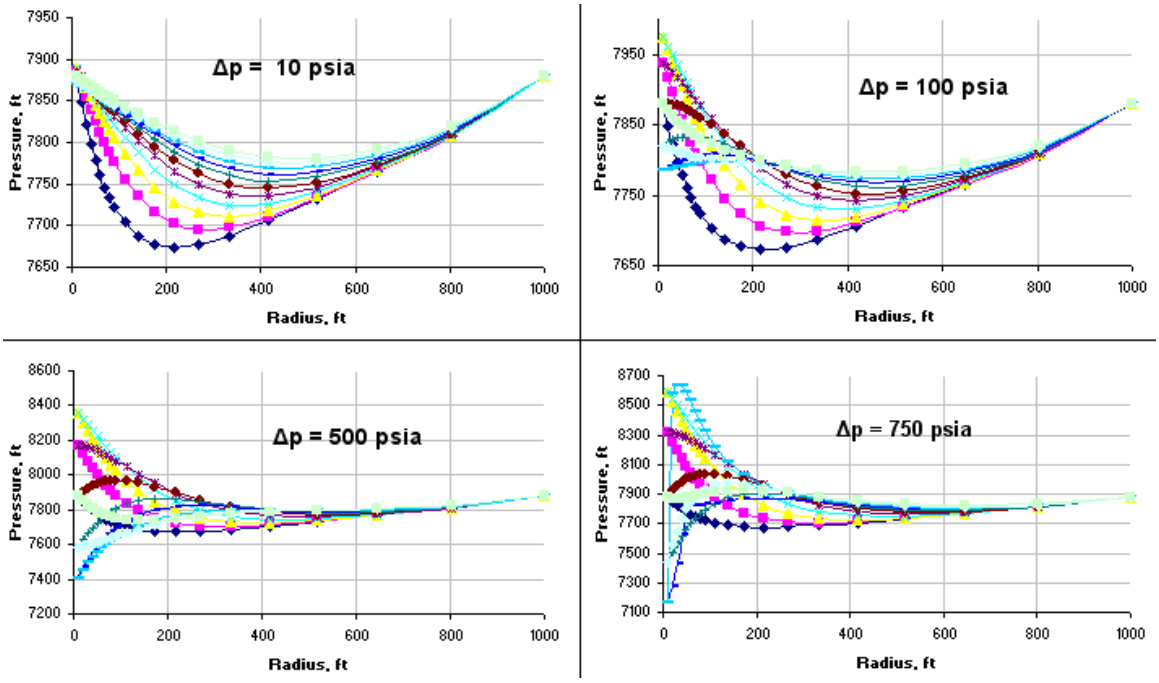

Fig. 6.19—A sensitivity analysis by different oscillation amplitudes (3-phase). The affected distance is about 800 ft and is insensitive to oscillation amplitude. Each line is a snapshot of the pressure profile at a certain timestep.

Varying the reservoir permeability

Different reservoir permeability values were selected (**Table 6.12**). The oscillation period was set to 0.48 hours. All other parameters kept the same values as in Case Study 2, and the starting pressure profile was imaged after 4 days of production. Snapshots of the U-shaped curves during an individual time period are presented in **Fig. 6.20**. The results show a longer affected distance with higher permeability. In the extreme case of 3 darcys, the pressure at the outer boundary can "feel" the oscillations instantly, and no U-shaped profile can be observed. The less permeable of the formation, the more profound U-shaped curve and the effects described by this work become.

Table 6.12—AFFECTED RADIUS UNDER DIFFERENT RESERVOIR PERMEABILITY

Permeability, md	0.03	0.3	3	30	1000	3000
Affected radius, ft	30	80	350	800	1000	Instant response

Varying the fluid compressibility

The oil compressibility is directly related to the oil coefficients of $\Delta_t p_o$ in the expansion of oil accumulation, C_{op} in Eq. 6.1. Different multipliers on this parameter were considered to investigate the compressibility effect on the U-shaped radius (**Table 6.13**). The oscillation period was set to 0.48 hours. All other parameters sustained the same values as in Case Study 2. The U-shaped curves within an individual period of time are shown in **Fig. 6.21**.

A higher compressibility fluid can better absorb the pressure oscillations coming from the wellbore. Moreover, free gas plays a dominant role. In the first two columns of the table, the affected radius does not change significantly with respect to the multiplier magnitude on liquid coefficients, C_{op} and C_{wp}. However, if this multiplier is applied to the gas coefficient, C_{gp}, the behavior of the reservoir becomes "rigid" and responds to the bottomhole pressure fluctuation instantly. The higher compressibility affiliated to gas absorbs most of the pressure oscillation in the near-wellbore region, and results in the U-shaped pressure profile.

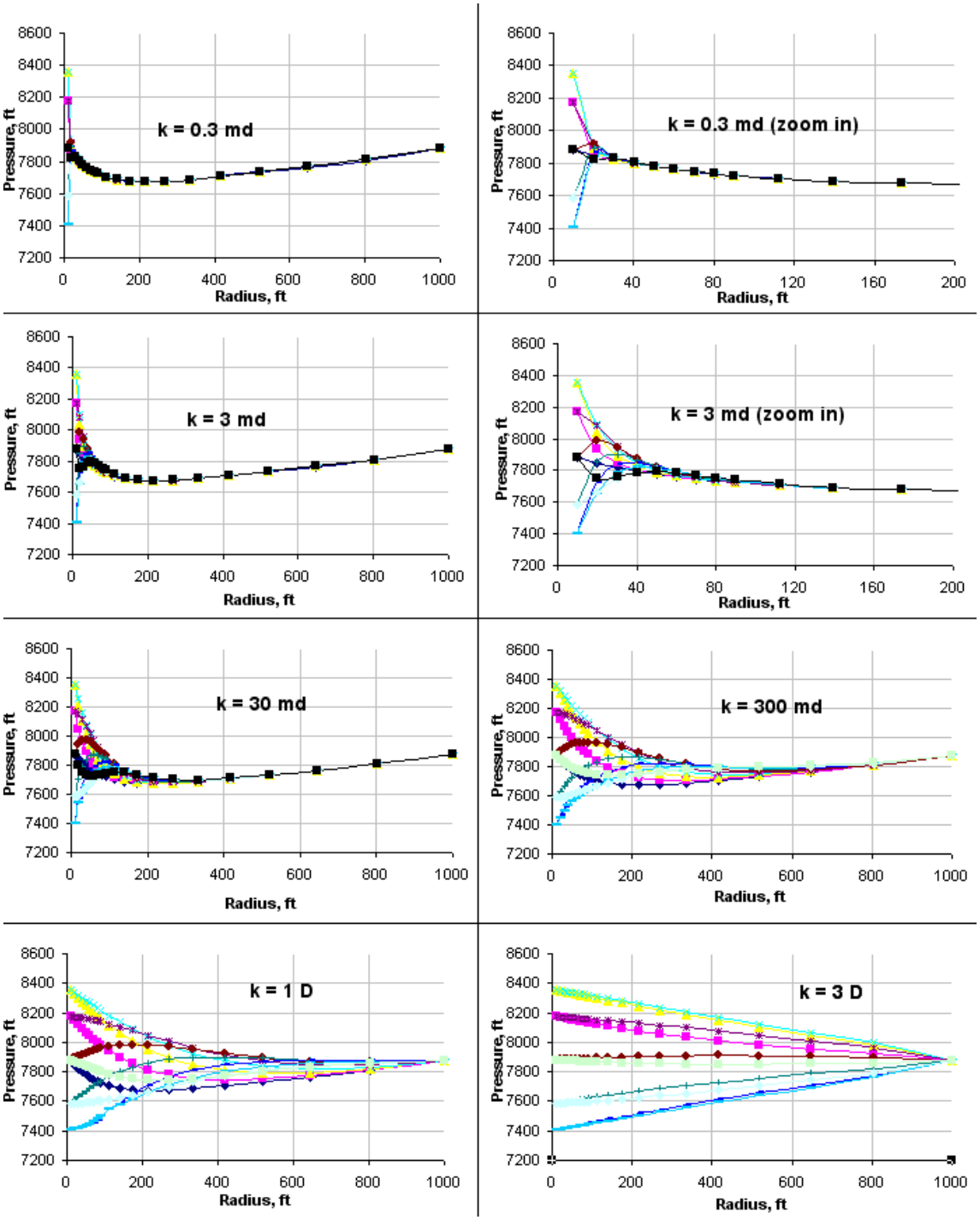

Fig. 6.20—A sensitivity analysis by different permeability values (3-phase). It showed the tighter reservoir leads to a shorter affected length. Each line is a snapshot of the pressure profile at certain timestep.

Table 6.13—THE AFFECTED RADIUS UNDER DIFFERENT OIL COEFFICIENT C_{OP}							
Multiplier	0.01xC_{op}	0.01x(C_{op},C_{wp})	0.01x(C_{op},C_{wp},C_{gp})	0.1	1	10	20
C_{op} in the 1st grid, STB/D-psia	0.0499	0.0499	0.0499	0.5	5	50	100
Affected radius, ft	950	950	Instant response	900	800	450	300

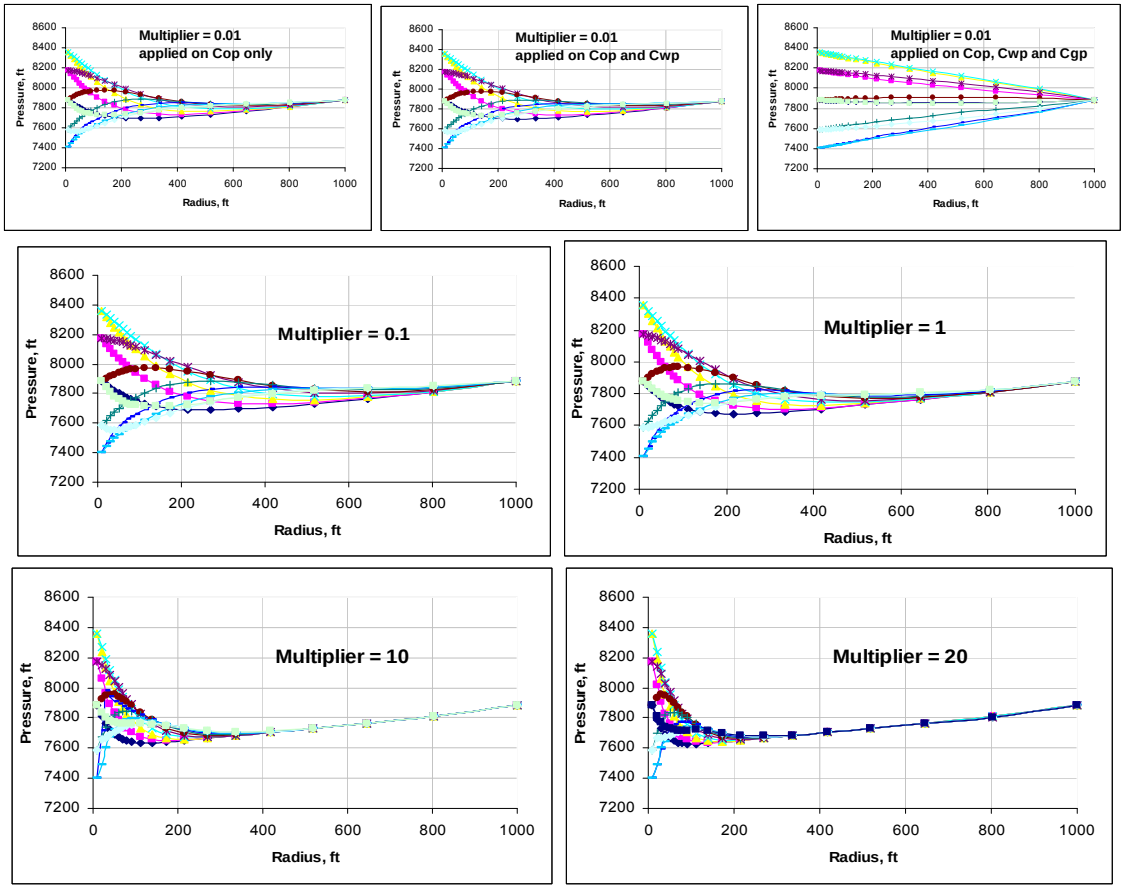

Fig. 6.21—A sensitivity analysis by different fluid compressibility (3-phase). It showed that lower compressibility leads to a longer affected length; however, if the multiphase fluid is incompressible, the rigid system failed to give a U-shaped curve. Each line is a snapshot of the pressure profile at a certain timestep.

The Failure of the Approach in ECLIPSE

The well-accepted commercial software Eclipse at the current version (2008.2) is not capable of generating this kind of U-shaped pressure distribution.

To configure a similar simulation case, in the ".data" file, the keyword "WCONINJE" is redefined two times in the "SCHEDULE" section with totally different target bottomhole pressures (**Fig. 6.22**).

```
WCONPROD
   'P1' 'OPEN' 'Orat' 1000 4*  6000 /
  /

TSTEP
  0.005 /

TSTEP
--  40*0.005
  2*0.5
/

WCONPROD
   'P1' 'OPEN' 'BHP' 1* 4*  7800 /
  /

TSTEP
 20*0.005 /

TSTEP
 2*0.5  /
```

Fig. 6.22—One typical approach to configure Eclipse with the goal to change the bottomhole pressure sharply in the ".data" file.

All the remaining configurations are exactly the same as in the relative part of validating the FORTRAN simulator with Eclipse in Chapter V. This black oil reservoir has a closed outer boundary and constant production rate inner boundary before the bottomhole pressure drops below the preset value. After 24 hours, the initialized pressure

distribution profile is obtained in the yellow line (**Fig. 6.23**).The first timestep was set as 7.2 minutes. However, because the keyword "WCONINJE" can only set a target BHP instead of the specified BHP, it failed to simulate the backflow, which does happen in the field. The timestep was further decreased till 4.32 seconds, and ECLIPSE still couldn't generate the same U-shaped pressure profile (**Fig. 6.24**).

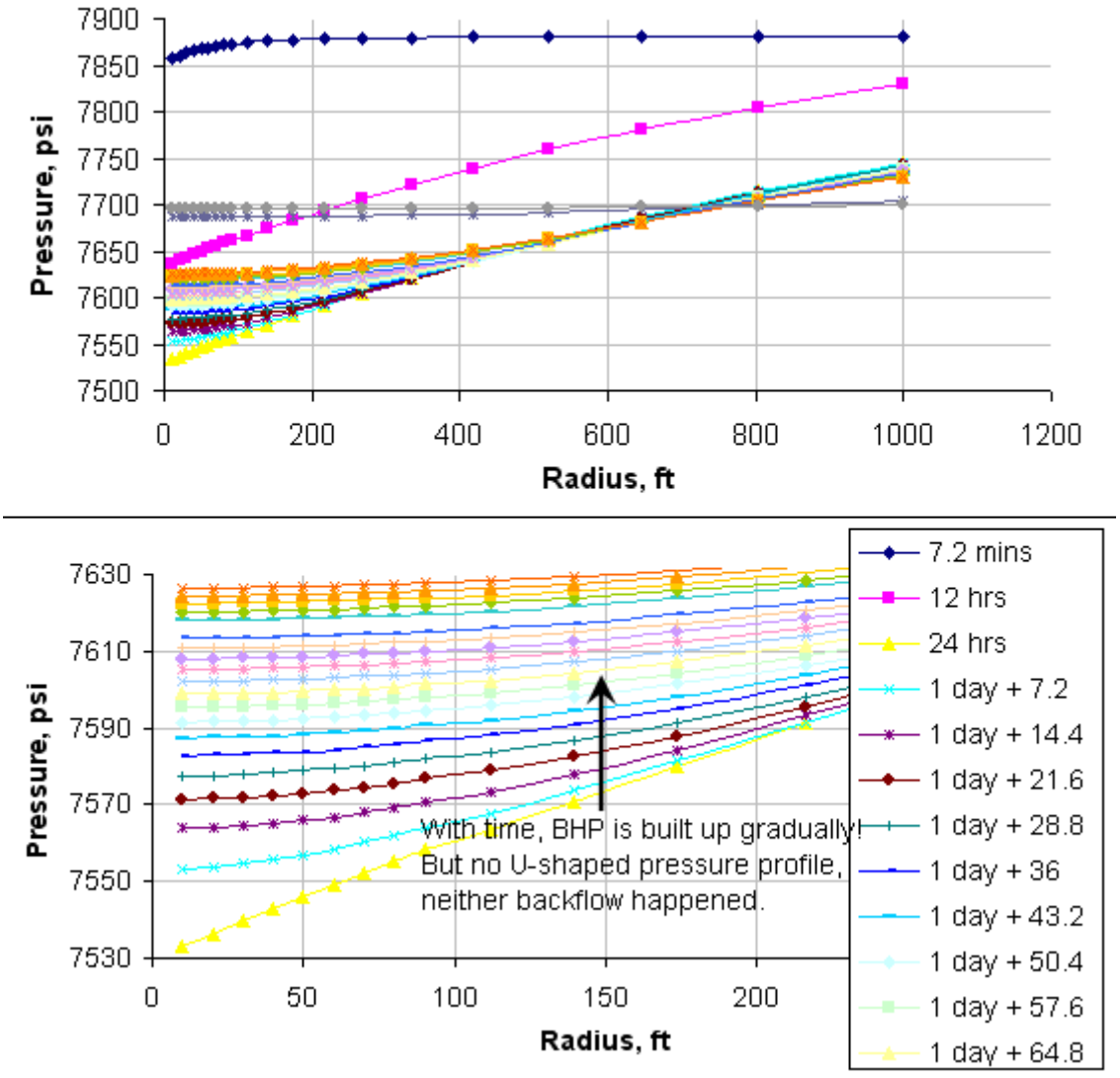

Fig. 6.23—The BHP gradual build-up process with the timestep of 7.2 minutes.

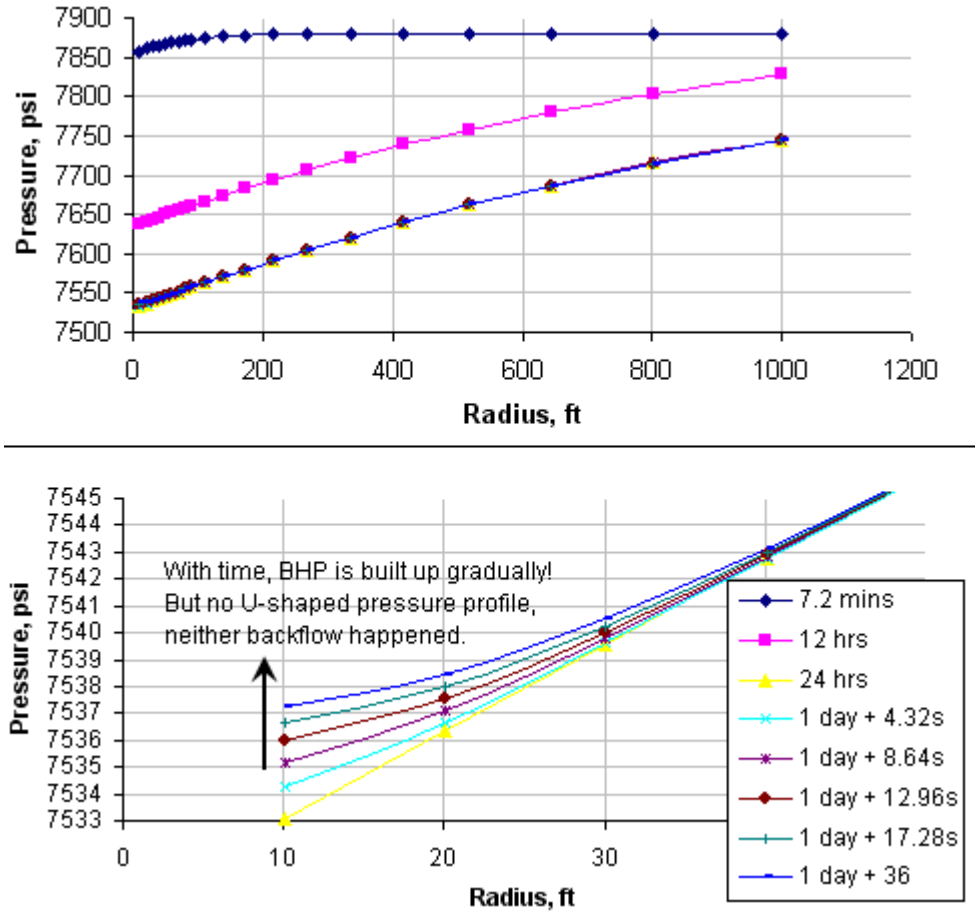

Fig. 6.24—The BHP gradual build-up process with the timestep of 4.32 seconds.

This section clearly showed the well-accepted commercial software, ECLISPE, is not capable of simulating the fully transient conditions. It could not generate the U-shaped pressure profile in the near-wellbore region as BHP oscillating; neither can calculate the backflow rates.

Summary

This work presents the existing U-shaped pressure distribution in the near-wellbore region under fully transient conditions.

- This FORTRAN simulator is more sensitive to the inner-boundary pressure oscillation than the conventional modeling approaches. The work suggests the existence of a U-shaped pressure profile in the near-wellbore region.

- High frequency of the bottomhole pressure oscillation, large fluid compressibility, and low permeability will cause a shorter length of the U-shaped pressure profile. The fluctuating amplitude has no effect on the U-shaped distance. This conclusion is consistent with the two-phase dry gas reservoir and three-phase black oil reservoir.

- This study successfully simulated that liquid can be reinjected to the formation and gas will be produced.

- The results add to the current understanding of dynamic interactions between reservoir and wellbore in situations when wellbore phase redistribution effects can temporarily prevail over the inertia of the reservoir.

- One of the most popular softwares used in industry, ECLIPSE, is not capable of generating the same results under fully transient conditions.

CHAPTER VII
USE OF HYSTERESIS IN SATURATION FUNCTIONS

Introduction

Both wetting- and nonwetting-phase relative permeability may exhibit hysteresis. Nonwetting relative permeabilities show considerable reduction when compared with the associated drainage functions at the same saturation because of the "trapping off" of the nonwetting phase by the advancing wetting phase (**Fig. 7.1**). The nonwetting phase is entrapped by the wetting phase in a discontinuous, immobile state. A greater amount of the entrapment leads to a greater reduction in the nonwetting relative permeability.

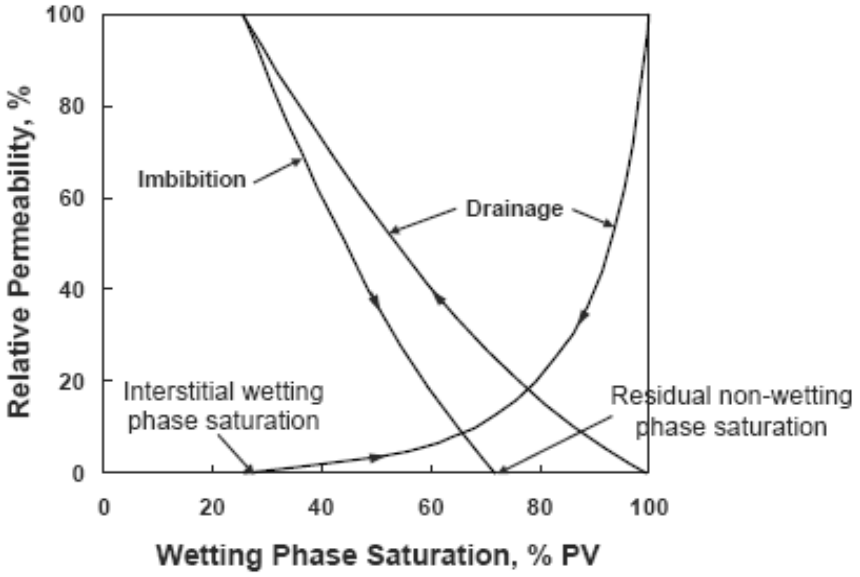

Fig. 7.1—Imbibition and drainage relative permeability curve. Normally the wetting phase is water (McCain, 2008).

Imbibition relative permeabilities exhibit a more or less reversible nature. As an imbibition process has begun, imbibition relative permeabilities will be used, even in drainage processes, until the historical maximum nonwetting saturation has been attained. But if the nonwetting saturation is greater than the maximum, nonwetting relative permeability will follow the drainage function (**Fig. 7.2**).

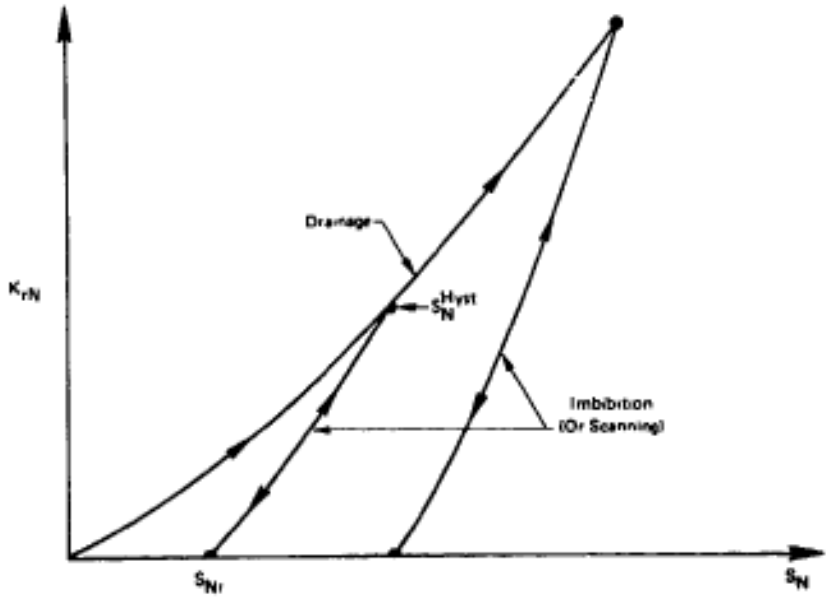

Fig. 7.2—Hysteresis relative permeability curves for nonwetting phase (Killough, 1976).

The wetting-phase relative permeabilities exhibit a far smaller dependence on the trapped nonwetting saturation; however, a greater trapped saturation results in a greater imbibition wetting-phase relative permeability than the value in the drainage process upon the same saturation (**Fig. 7.3**). Also, the imbibition wetting-phase relative permeability exhibits a somewhat reversible nature. Imbibition relative permeability thus falls in the range of the historical maximum nonwetting saturation and the trapped or residual saturation.

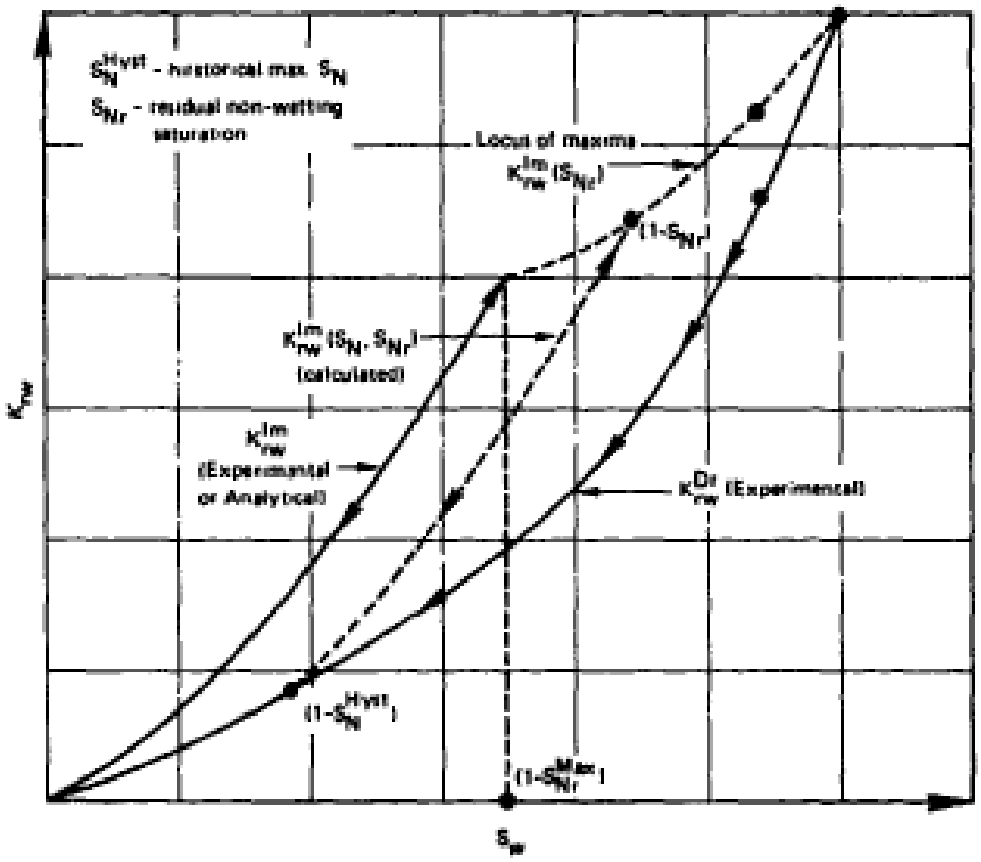

Fig. 7.3—Hysteresis relative permeability curves for wetting phase (Killough, *1976*).

As previous study indicates, the use of hysteresis in saturation functions shows results significantly different from those obtained by conventional methods. Smooth transitions of both relative permeabilities from *drainage-to-imbibition* or *imbibition-to-drainage* states are allowed. In addition, the effect of trapped gas or oil saturations on relative permeabilities must be accounted for.

Approach Description

The drainage relative permeability data needs to be given first, and then the calculation follows the steps:

1. Trapped nonwetting saturations are calculated using the semi-empirical expression derived by Land (Eq. 7.1).

$$S_{Nr} = \frac{S_N^{Hyst}}{1 + C * S_N^{Hyst}} \quad \text{..... (7.1)}$$

where

S_{Nr} is the residual or trapped nonwetting saturation.

S_N^{Hyst} is the maximum historical nonwetting saturation.

$C = \frac{1}{S_{Nr}^{Max}} - \frac{1}{S_N^{Max}}$.

S_{Nr}^{Max} is the maximum possible residual or trapped nonwetting saturation.

S_N^{Max} is the maximum possible nonwetting saturation.

2. The relative permeability for the nonwetting phase is calculated by interpolating between the drainage relative permeability at the historical maximum nonwetting saturation and zero relative permeability at the trapped saturation. The method of parametric curve is used in this work (Eq. 7.2).

$$k_{rN}^{\mathrm{Im}}\left(S_N\right) = k_{rN}^{Dr}\left(S_N^{Hyst}\right) \cdot \left(\frac{S_N - S_{Nr}}{S_N^{Hyst} - S_{Nr}}\right)^{\lambda} \quad \text{..... (7.2)}$$

where

$k_{rN}^{\mathrm{Im}}\left(S_N\right)$ is the imbibition nonwetting-phase relative permeability at the current nonwetting-phase saturation.

$k_{rN}^{Dr}\left(S_N^{Hyst}\right)$ is the drainage nonwetting-phase relative permeability at the maximum historical nonwetting saturation.

S_N is the current nonwetting-phase saturation.

λ is a given parameter.

From the above equation, the relative permeability for the nonwetting phase is zero at the trapped saturation, and is equal to the value in the drainage process at the maximum historical nonwetting saturation, as the intermediate scanning curve shown in Fig. 7.2.

3. As long as nonwetting-phase saturations increase, drainage functions are used. However, a decrease in S_N results in a scanning imbibition relative permeability curve for the wetting phase that falls between the relative permeability for the wetting-phase in the drainage process at the maximum historical nonwetting saturation, $k_{rw}^{Dr}\left(S_N^{Hyst}\right)$, and a maximum relative permeability for the wetting phase in the imbibition process, $k_{rw}^{\mathrm{Im}}\left(S_{Nr}\right)$. The S_{Nr} is a given value, which is approximately 50% in Fig. 7.3. The calculation for the maximum relative permeability of the wetting phase, $k_{rw}^{\mathrm{Im}}\left(S_{Nr}\right)$, is followed by Eq. 7.3.

$$k_{rw}^{\mathrm{Im}}\left(S_{Nr}\right)=k_{rw}^{Dr}\left(1-S_{Nr}\right)+\Delta k_{rw}\cdot\left(\frac{S_{Nr}}{S_{Nr}^{Max}}\right)^{a_2} \quad \text{.....} \quad (7.3)$$

where

$\Delta k_{rw}=k_{rw}^{*\mathrm{Im}}\left(1-S_{Nr}^{Max}\right)-k_{rw}^{Dr}\left(1-S_{Nr}^{Max}\right)$.

$k_{rw}^{*\mathrm{Im}}\left(1-S_{Nr}^{Max}\right)$ is the relative permeability for wetting-phase in the imbibition process, but it is an analytical or experimental curve (solid line for imbibition curve in Fig. 7.3).

α_2 is the exponent for interpolation of imbibition wetting-phase relative permeabilities.

In the next step, the imbibition k_{rw} for a given trapped S_N is calculated using Eq. 7.4.

$$k_{rw}^{\mathrm{Im}}\left(S_N\right)=k_{rw}^{Dr}\left(1-S_{Nr}^{Hyst}\right)+\left[\frac{k_{rw}^{*\mathrm{Im}}\left(S_N^{Norm}\right)-k_{rw}^{*\mathrm{Im}}\left(S_N^{Max}\right)}{k_{rw}^{*\mathrm{Im}}\left(S_{Nr}^{Max}\right)-k_{rw}^{*\mathrm{Im}}\left(S_N^{Max}\right)}\right]\cdot\left[k_{rw}^{\mathrm{Im}}\left(S_{Nr}\right)-k_{rw}^{Dr}\left(1-S_{Nr}^{Hyst}\right)\right]$$

…….. (7.4)

where $S_N^{Norm}=\left[\frac{\left(S_N-S_{Nr}\right)\cdot\left(S_N^{Max}-S_{Nr}^{Max}\right)}{\left(S_N^{Hyst}-S_{Nr}\right)}\right]+S_{Nr}^{Max}$

4. Both wetting and nonwetting relative permeabilities are allowed to follow imbibition curves as long as the saturation of the nonwetting phase does not exceed the historical maximum. As this scenario happens, the relative permeability will begin to follow the bounding drainage function until another reversal process in the direction of saturation change occurs.

Many attempts have been made to investigate the magnitude of hysteresis in relative permeability relations, which have shown that the wetting-phase imbibition and drainage relative permeabilities show little deviation from each other, while considerable differences have been observed for the nonwetting-phase relative permeabilities (Furati, 1997, 1998). The deviation depends on the trapped saturation, and the greater the trapped saturation, the greater the imbibition wetting-phase relative permeability. So this work neglects the deviation of the relative permeability for the wetting-phase water.

Simulation Results

This work is performed based on the configuration for a tight gas reservoir in the Chapter VII; however, the relative permeability curves for gas and water are changed and consider the imbibition and drainage processes (**Fig. 7.4** and **Fig. 7.5**). In this fully synthetic case study, the wetting-phase of the water and the corresponding history-dependence effects are neglected.

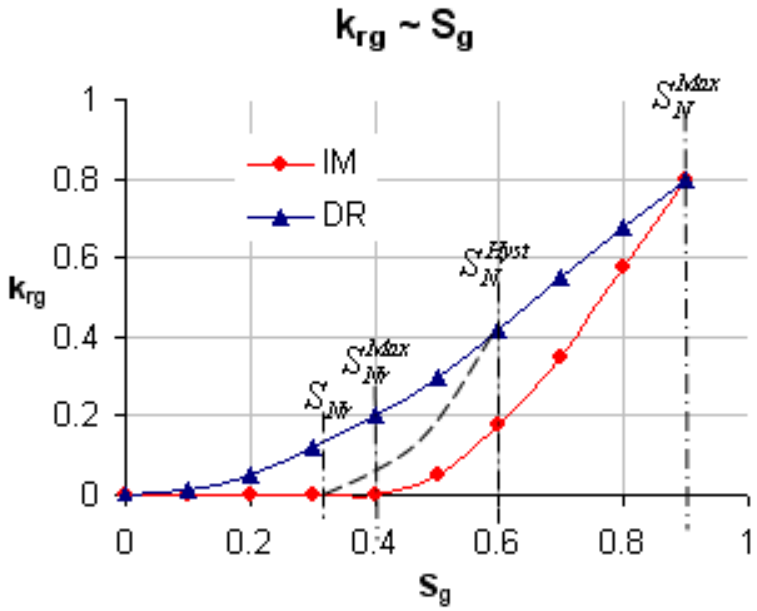

Fig. 7.4—The relative permeability curves for nonwetting-phase gas.
The dashed line is an example hysteresis curve and the difference magnitude is obvious.

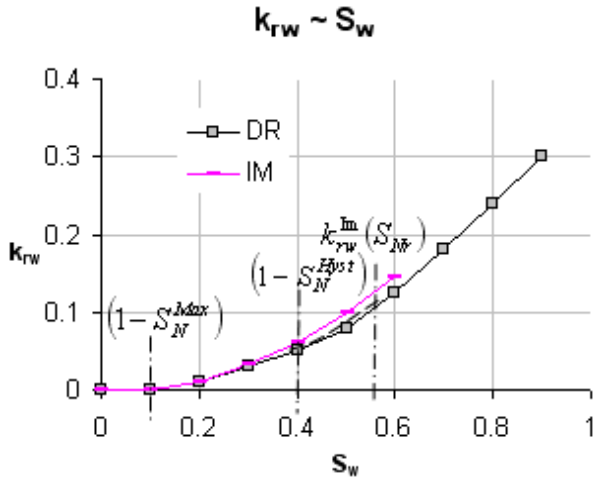

Fig. 7.5—The relative permeability curves for wetting-phase water.
The dashed line is an example hysteresis curve and the difference magnitude could be neglected.

In this case study, the hysteresis starts while the wetting phase is 0.6, and the corresponding relative permeability is 0.3 at the imbibition process.

1. Trapped nonwetting saturations are calculated using the semi-empirical expression derived by Land (Eq. 7.1).

$$S_N^{Hyst} = 0.6 \ ;$$

$$C = \frac{1}{S_{Nr}^{Max}} - \frac{1}{S_N^{Max}} = \frac{1}{0.4} - \frac{1}{0.9} = 1.39 \ ;$$

$$S_{Nr}^{Max} = 0.4 \ ;$$

$$S_N^{Max} = 0.9 \ .$$

So

$$S_{Nr} = \frac{S_N^{Hyst}}{1 + C * S_N^{Hyst}}$$

$$S_{Nr} = \frac{S_N^{Hyst}}{1 + C * S_N^{Hyst}} = \frac{0.6}{1 + 1.39 * 0.6} = 0.327 \quad \ldots\ldots\ldots\ldots\ldots\ldots\ldots\ldots\ldots\ldots (7.5)$$

2. The relative permeability for the nonwetting-phase is calculated by interpolating between the drainage relative permeability at the historical maximum nonwetting saturation and zero relative permeability at the trapped saturation. The method of parametric curve is used in this work (Eq. 7.2).

$$k_{rN}^{\mathrm{Im}}\left(S_N\right)=k_{rN}^{Dr}\left(S_N^{Hyst}\right)\cdot\left(\frac{S_N-S_{Nr}}{S_N^{Hyst}-S_{Nr}}\right)^{\lambda}$$

$$k_{rN}^{\mathrm{Im}}\left(S_N\right)=0.42\cdot\left(\frac{S_N-0.327}{0.6-0.327}\right)^{\lambda}=0.42\cdot\left(\frac{S_N-0.327}{0.273}\right)^{\lambda} \quad \text{…...……...…..} \quad (7.6)$$

Now, the given parameter λ is determined by sensitivity analysis shown in **Table 7.1**, **Fig. 7.6**., and **Fig. 7.7**.

Table 7.1—THE SENSITIVITY ANALYSIS TO DETERMINE THE PARAMETER λ

S_N	Value of the given parameter, λ							
	0.01	0.1	0.2	0.5	1	2	5	10
0.327	0.000	0.000	0.000	0.000	0.000	0.000	0.000	0.000
0.355	0.410	0.334	0.265	0.420	0.042	0.004	0.000	0.000
0.382	0.413	0.358	0.304	0.214	0.084	0.017	0.000	0.000
0.409	0.415	0.372	0.330	0.325	0.126	0.038	0.001	0.000
0.436	0.416	0.383	0.350	0.312	0.168	0.067	0.004	0.000
0.464	0.417	0.392	0.366	0.338	0.210	0.105	0.013	0.000
0.491	0.418	0.399	0.379	0.353	0.252	0.151	0.033	0.003
0.518	0.419	0.405	0.391	0.370	0.294	0.206	0.071	0.012
0.545	0.419	0.411	0.402	0.387	0.336	0.269	0.138	0.045
0.573	0.420	0.416	0.411	0.403	0.378	0.340	0.248	0.146
0.600	0.420	0.420	0.420	0.420	0.420	0.420	0.420	0.420

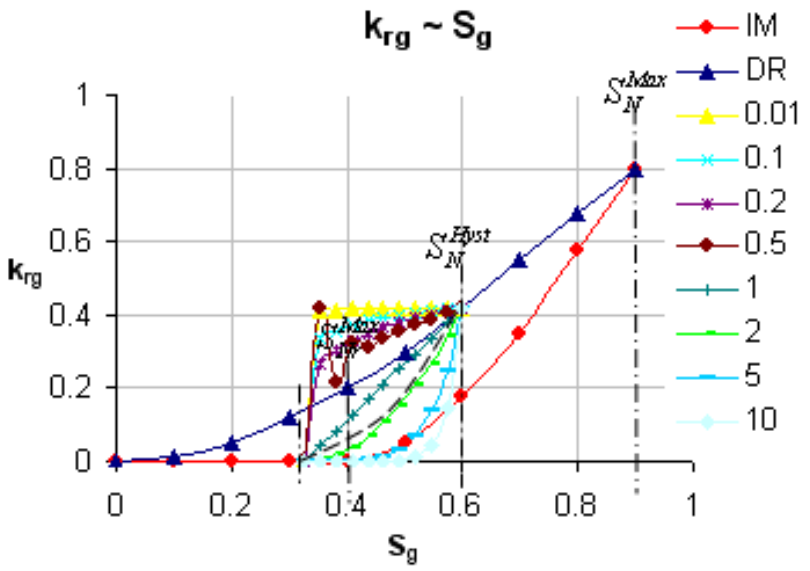

Fig. 7.6—Sensitivity analysis to determine the best fit parameter.

λ is in the range from 0.01 to 10.

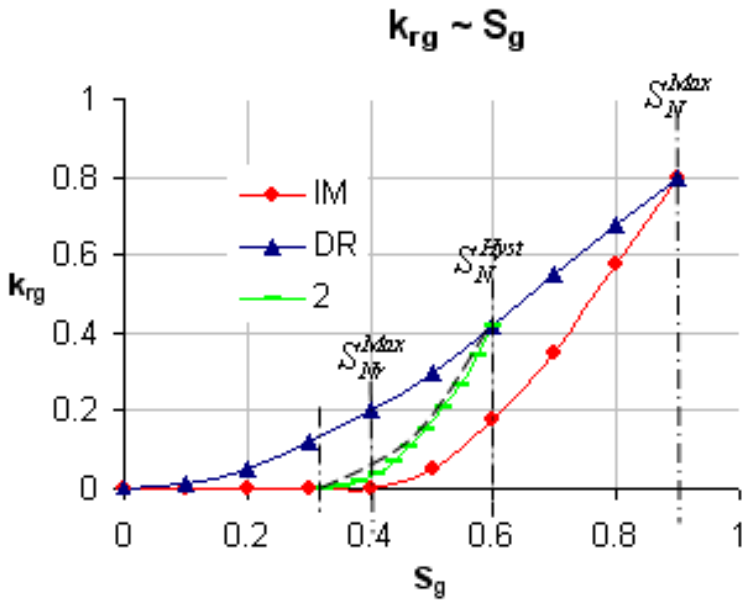

Fig. 7.7—The best fit with the proposed dashed line (experimental) as parameter $\lambda = 2$.

Now the given parameter λ is chosen as 2 by the above results, so Eq. 7.6 is further developed as Eq. 7.7.

$$k_{rN}^{\mathrm{Im}}(S_N) = 0.42\left(\frac{S_N - 0.327}{0.273}\right)^2 \quad \text{..... (7.7)}$$

3. Because the relative difference is rather small in Fig. 7.4, this step is skipped, which is also well accepted (Furati, 1997, 1998).

4. Both wetting and nonwetting relative permeabilities are allowed to follow imbibition curves as long as the saturation of the nonwetting phase does not exceed the historical maximum. As this scenario happens, the relative permeability will begin to follow the bounding drainage function until another reversal process in the direction of saturation change occurs.

The corresponding FORTRAN code is as follows:

```
If (Sg_func<0.6) then
        FindkrgHys = 0.42*((sg_func-0.327)/0.327)**2.0
Else
        FindkrgHys = Findkrg(Sg_func)
End if
```

The next step is to implement this hysteresis study into the FORTAN simulator.

Case description

The synthetic dry gas reservoir is 1,000 ft long with a cross-sectional area of 10,000 ft^2. The wellbore radius, r_w, is specified as 0.09144 ft. An active aquifer exists at the outer

boundary and water is encroaching, so the outer boundary could sustain the reservoir pressure as 7,880 psi. The target dry gas production rate is the equivalent pore volume (PV) of 1,000 STB/D. The initial water saturation in the reservoir is 40% and dry gas saturation is 60%. The irreducible water and gas saturation is 10% and 40% (in the acceptable range, S. Karine, 2001). We assume it is a homogeneous reservoir. The permeability is 3 md and the porosity is 0.15. Capillary pressure between gas and water phases is not negligible. The input dataset for gas PVT Characterization is the same as previous studies in **Table 7.2**, and the petrophysical parameters are as summarized in **Table 7.3**.

Table 7.2—PARAMETERS AVAILABLE IN FIELD THAT ARE USED FOR PVT CHARACTERIZATION THROUGH LITERATURE CORRELATIONS

Reservoir temperature (T_R), °F	Separator gas specific gravity (γ_{gSP})	Separator Temperature (T_{sep}), °F	Separator Pressure (p_{sep}), psia
220.0	0.63	60.0	114.7

Table 7.3—SYNTHETIC PETROPHYSICAL PARAMETERS

Initial reservoir pressure, (p_i), psi	Reservoir porosity	Initial water saturation, (S_{wi})	Reservoir permeability, (k), md
7880	0.15	0.40	3

Implicit pressure explicit saturation (IMPES) approach

Numerical reservoir modeling is based on the solution of the diffusivity equation, which combines mass conservation equations (differential mass balance), PVT fluid characterization and a transport law (Darcy equation) in a multiphase flow system. When using the IMPES approach, the diffusivity equation is solved implicitly for pressure and explicitly for phase saturation. Because the capillary pressure between oil and water phases is negligible, the water pressure is identical to oil pressure, as summarized in Eq. 7.8.

$$\sum_{m\in\psi_n}\left\{\left(B_o-R_sB_g\right)_n^{n+1}T^{\,n}_{o\,n,m}+B_{w\;n}^{n+1}T^{\,n}_{w\,n,m}+B_{g\;n}^{n+1}\left[T^{\,n}_{g\,n,m}+\left(T_oR_s\right)^n_{n,m}\right]\right\}p_{w\;m}^{n+1}$$
$$-\left(\begin{array}{l}\left(B_o-R_sB_g\right)_n^{n+1}C_{op\,n}+B_{w\;n}^{n+1}C_{wp\,n}+B_{g\;n}^{n+1}C_{gp\,n}\\+\sum_{m\in\psi_n}\left\{\left(B_o-R_sB_g\right)_n^{n+1}T^{\,n}_{o\,n,m}+B_{w\;n}^{n+1}T^{\,n}_{w\,n,m}+B_{g\;n}^{n+1}\left[T^{\,n}_{g\,n,m}+\left(T_oR_s\right)^n_{n,m}\right]\right\}\end{array}\right)p_{w\;n}^{n+1}$$
$$=-\left[\left(B_o-R_sB_g\right)_n^{n+1}C_{op\,n}+B_{w\;n}^{n+1}C_{wp\,n}+B_{g\;n}^{n+1}C_{gp\,n}\right]p^n_{wn}-\left[\left(B_o-R_sB_g\right)_n^{n+1}q_{osc\,n}+B_{w\;n}^{n+1}q^n_{wsc\,n}+B_{g\;n}^{n+1}q_{gsc\,n}\right]$$
$$\sum_{m\in\psi_n}B_{g\;n}^{n+1}T^{\,n}_{g\,n,m}\left(P^n_{cgw\,m}-P^n_{cgw\,n}\right)+\sum_{m\in\psi_n}\left\{\begin{array}{l}\left(B_o-R_sB_g\right)_n^{n+1}T^{\,n}_{o\,n,m}\bar{\gamma}^{\,n}_{o\,n,m}+B_{w\;n}^{n+1}T^{\,n}_{w\,n,m}\bar{\gamma}^{\,n}_{w\,n,m}\\+B_{g\;n}^{n+1}\left[T^{\,n}_{g\,n,m}\bar{\gamma}^{\,n}_{g\,n,m}+\left(T_oR_s\right)^n_{n,m}\bar{\gamma}^{\,n}_{o\,n,m}\right]\end{array}\right\}\left(Z_m-Z_n\right)$$

…… (7.8)

The gas pressure is calculated by Eq. 7.9:

$$p_g=p_w+P_{cgw} \quad \text{…….} \quad (7.9)$$

The reservoir simulator generated for this study is sensitive to the pressure fluctuating under transient conditions. Proper configurations of the fluid PVT properties, the grid refinement in the near-wellbore region, and the ratio of the pressure oscillation period to the timestep are extremely critical.

Fluid PVT characterization

For this transient modeling work, fluid PVT properties were carefully selected to provide the necessary system compressibility and allow sufficient mass storage. The PVT behavior is depicted by the blackoil correlations in Appendix A (**Fig. 7.8**).

Reservoir rock is water-wet compared to the gas phase; the relative permeability curves are shown in **Fig. 7.9**. Where water replaces gas, it is an inhibition process; on the other hand, where the free gas replaces oil, it is a drainage process. The connate water

saturation is 10%. The hysteresis curve for relative permeability is studied for the nonwetting-phase in the imbibition process.

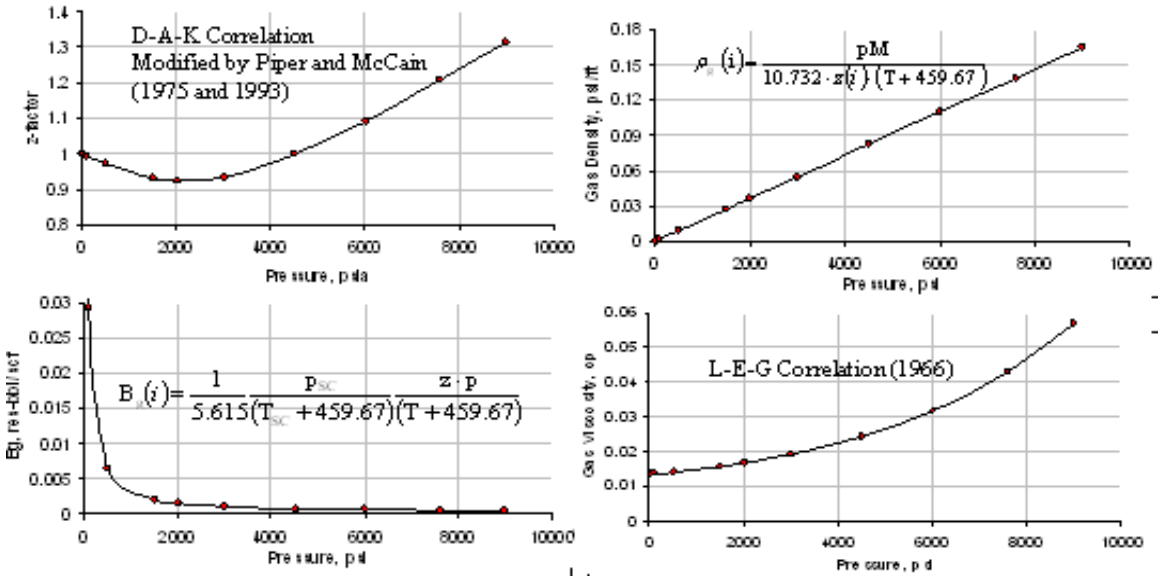

Fig. 7.8—Realistic fabricated PVT data lay out the correct trends upon pressure and create appropriate fluid compressibility for pressure oscillation in the near-wellbore region.

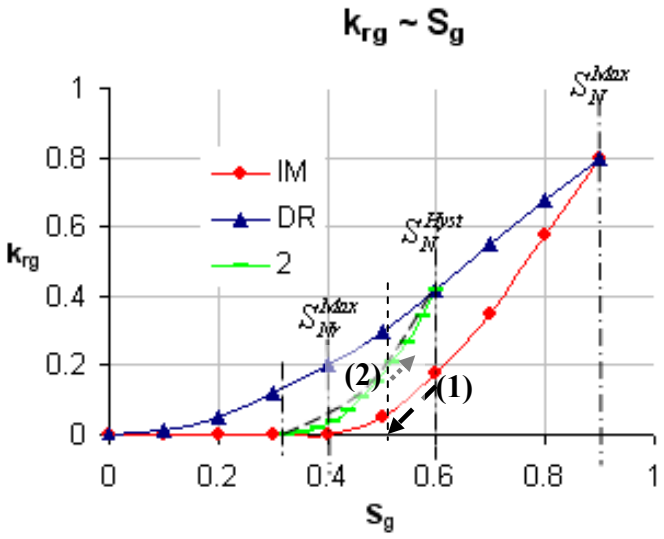

Fig. 7.9—Imbibition process happens first and the relative permeability for gas as the dashed arrow (1); then the drainage process follows as the dashed arrow (2). The green line represents the lambda is set to 2.

Grid refinement

Grid refinement is essential in the near-wellbore region because the pressure disturbance can only be sustained at a comparatively short distance from the wellbore. However, the depth of the disturbance zone into the reservoir is not known a priori and varies with the frequency of the pressure fluctuations. To achieve this gridding refinement, the logarithmic gridding method is employed.

The logarithmic method automatically refines the near-wellbore region; however, the first (smallest) gridblock size is only 0.23 ft. The smallest gridblock is adjacent to the wellbore, and this size decides the maximum timestep, which is about 3.29×10^{-6} days (0.28 seconds) to ensure stable IMPES solutions. This small timestep is against any practical application, and further refinement of the gridblocks is required. Thus, the reservoir was divided into 20 gridblocks in 1D. The first 10 cells have the uniform size of 10 ft and the rest of the reservoir follows the logarithmic gridding method. After recalculation, a maximum timestep of 0.006 days (518 seconds) was obtained and considered acceptable.

Investigation procedure

We can run the forward prediction for 12 days with constant reservoir pressure and constant production rates, 930 Mscf/D. The stabilized pressure distribution profile is shown in **Fig. 7.10.** Then the comparison was made between with the hysteresis and non-hysteresis of the relative permeability cases.

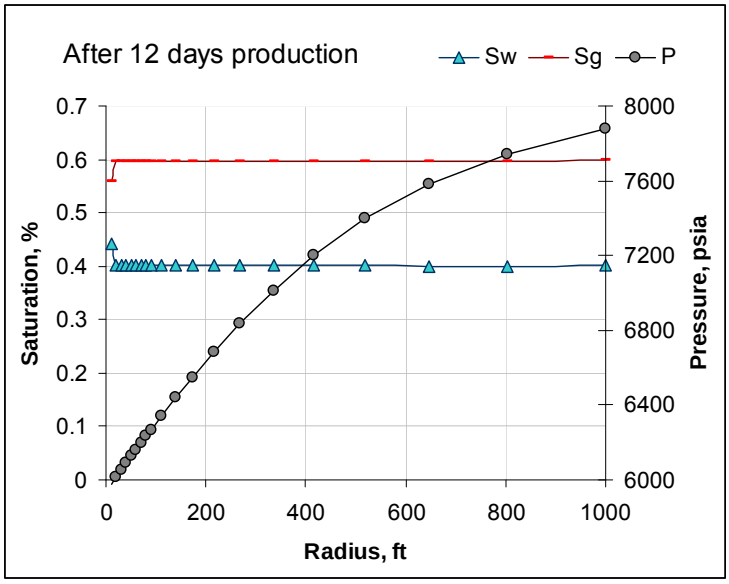

Fig. 7.10—The stabilized pressure profile after 12 days constant rate production. Water has started to accumulated in the near wellbore region.

Comparison 1

In this comparison, the bottomhole pressure is fixed as 6,500 psia, and we checked the process of the pressure buildup in the near-wellbore region. **Fig. 7.11** illustrates the simulation results after 12, 24, 36, and 48 hours respectively. In the left column, the plots capture the whole pressure distribution through the reservoir, and in the right column, the plots zoom in on the near-wellbore region corresponding to the left one. The difference between using a hysteresis curve for relative permeability and not using it is obvious.

However, the difference is not cumulative as investigating the maximum relative error at different timesteps shows in **Table 7.4**. At the last investigation timestep, after buildup for 12 hours, the maximum relative error is reduced to 0.23%, because the pressure in the near-wellbore region is close to the preset 6,500 psia.

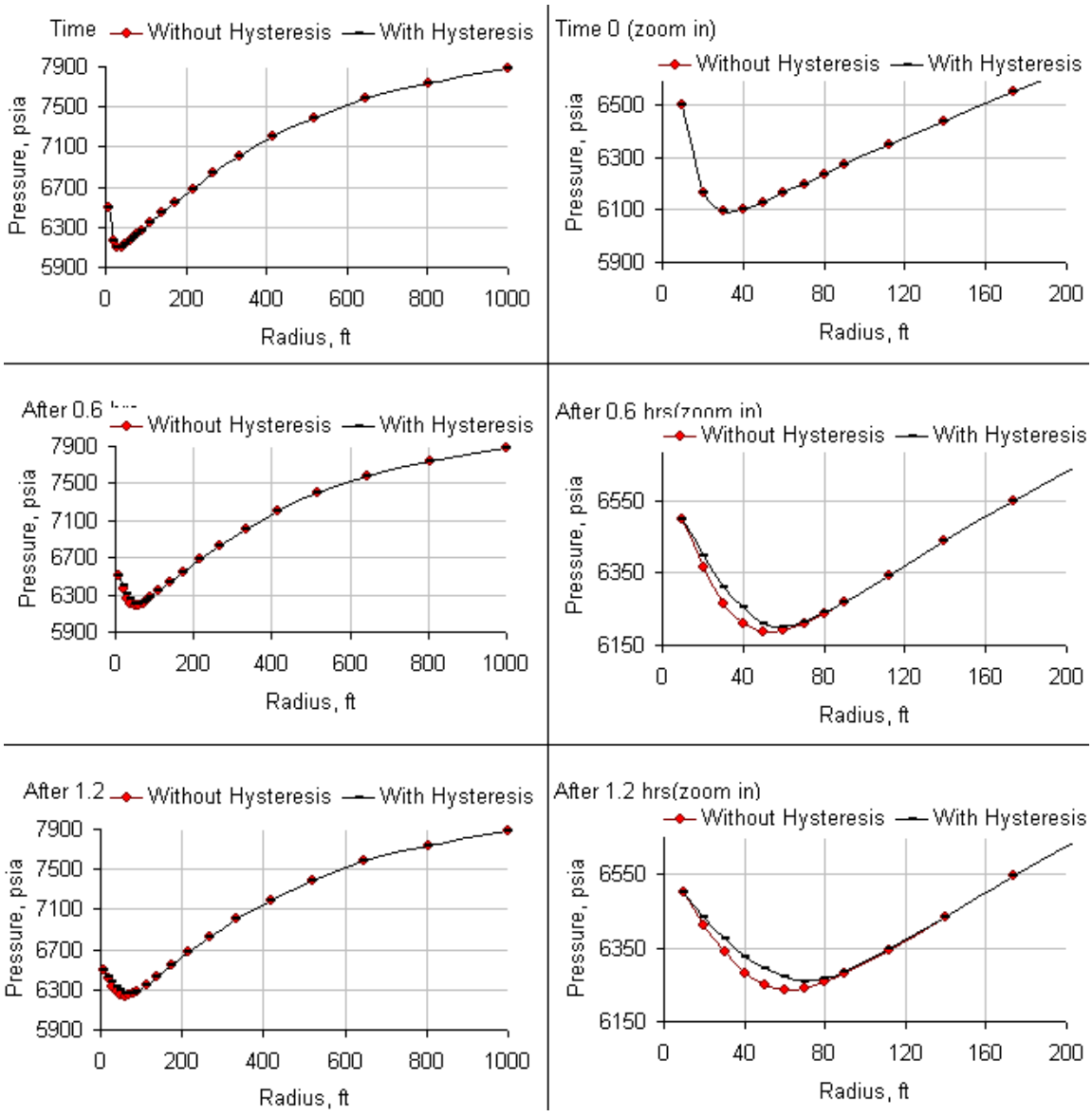

Fig. 7.11—The difference between using hysteresis of relative permeability and not. The red line is the case without the hysteresis curve, and the black line is the case with it.

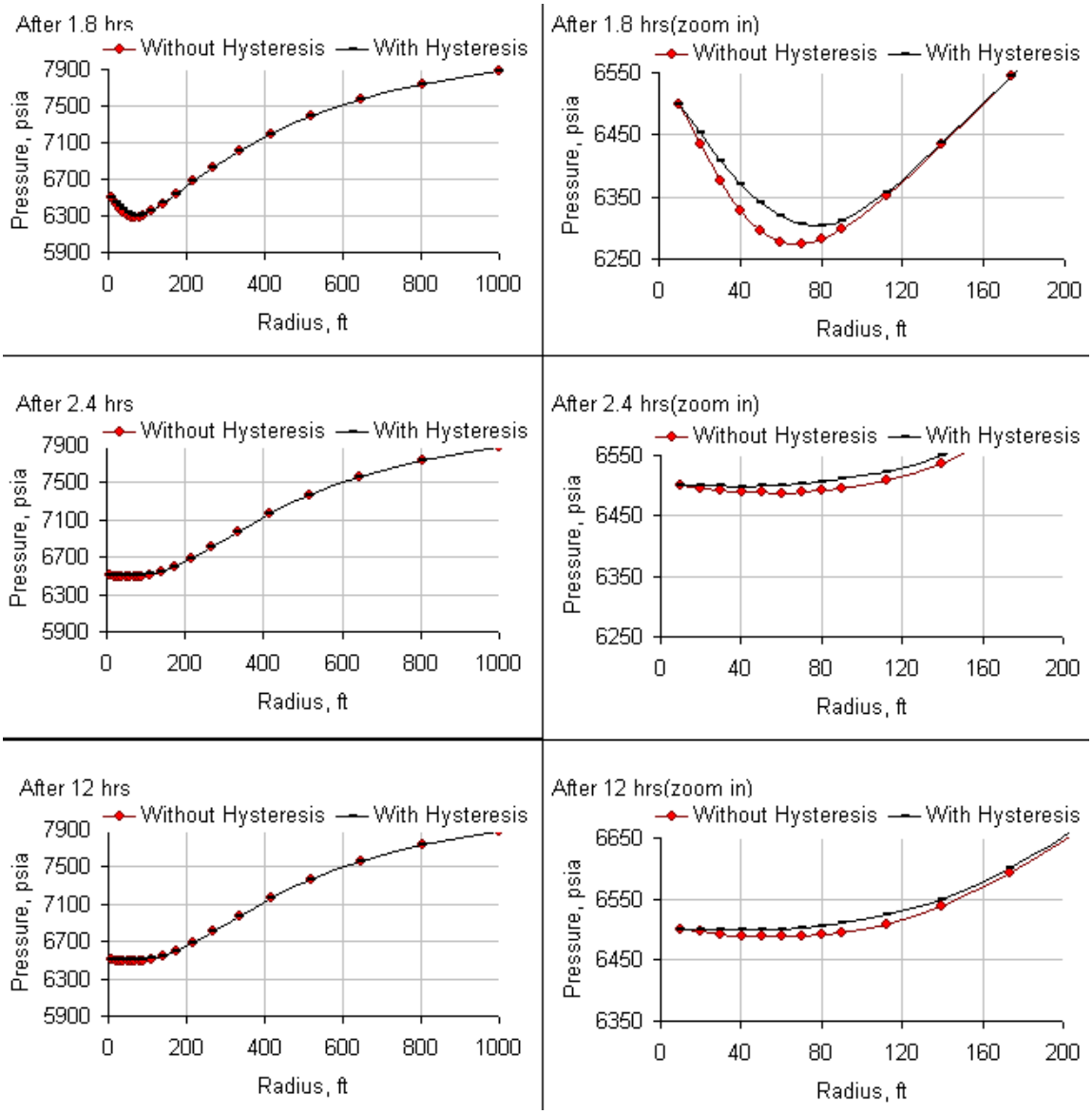

(Fig.7.11 Continued)

Table 7.4—THE MAXIMUM RELATIVE ERROR BETWEEN USING HYSTERESIS OF RELATIVE PERMEABILITY AND NOT AT EACH POINT OF INTEREST AFTER THE BOTTOMHOLE PRESSURE INCREASED					
Build Up Time, hrs	0.12	0.24	0.36	0.48	0.6
Max relative error, %	0.61%	0.58%	0.64%	0.69%	0.72%
Build Up Time, hrs	0.72	0.84	0.96	1.08	1.2
Max relative error, %	0.71%	0.72%	0.73%	0.72%	0.71%
Build Up Time, hrs	1.32	1.44	1.56	1.68	1.8
Max relative error, %	0.70%	0.71%	0.71%	0.72%	0.71%
Build Up Time, hrs	1.92	2.04	2.16	2.28	2.4
Max relative error, %	0.70%	0.69%	0.69%	0.68%	0.68%

As the results show, when using the hysteresis curve for the nonwetting phase during imbibition process, the pressure drop will be less than not using it. The reason is that the hysteresis curve favors the nonwetting-phase relative permeability, and meanwhile it does not decrease much of the relative permeability for the wetting phase (in this study, the identical relative permeability was used). So the total permeability is increased, and the pressure drop will be less, which is why the pressure distribution in the black line is over the red line in Fig. 7.11.

Comparison 2

In this comparison, the bottomhole pressure oscillates in as a sine function. This is a similar study as pervious case studies. The oscillation period is about 1.2 hours. **Fig. 7.12** illustrates the simulation results after 4.8, 9.6, 14.4, and 19.2 hours respectively. In the left column, the plots capture the whole pressure distribution through the reservoir, and in the right column, the plots zoom in on the near-wellbore region corresponding to

the left one. The difference between using a hysteresis curve for relative permeability and not using one is not obvious.

As the results show, in this case the hysteresis function will not play an important role. The periodical fluctuation cancels the hysteresis effect.

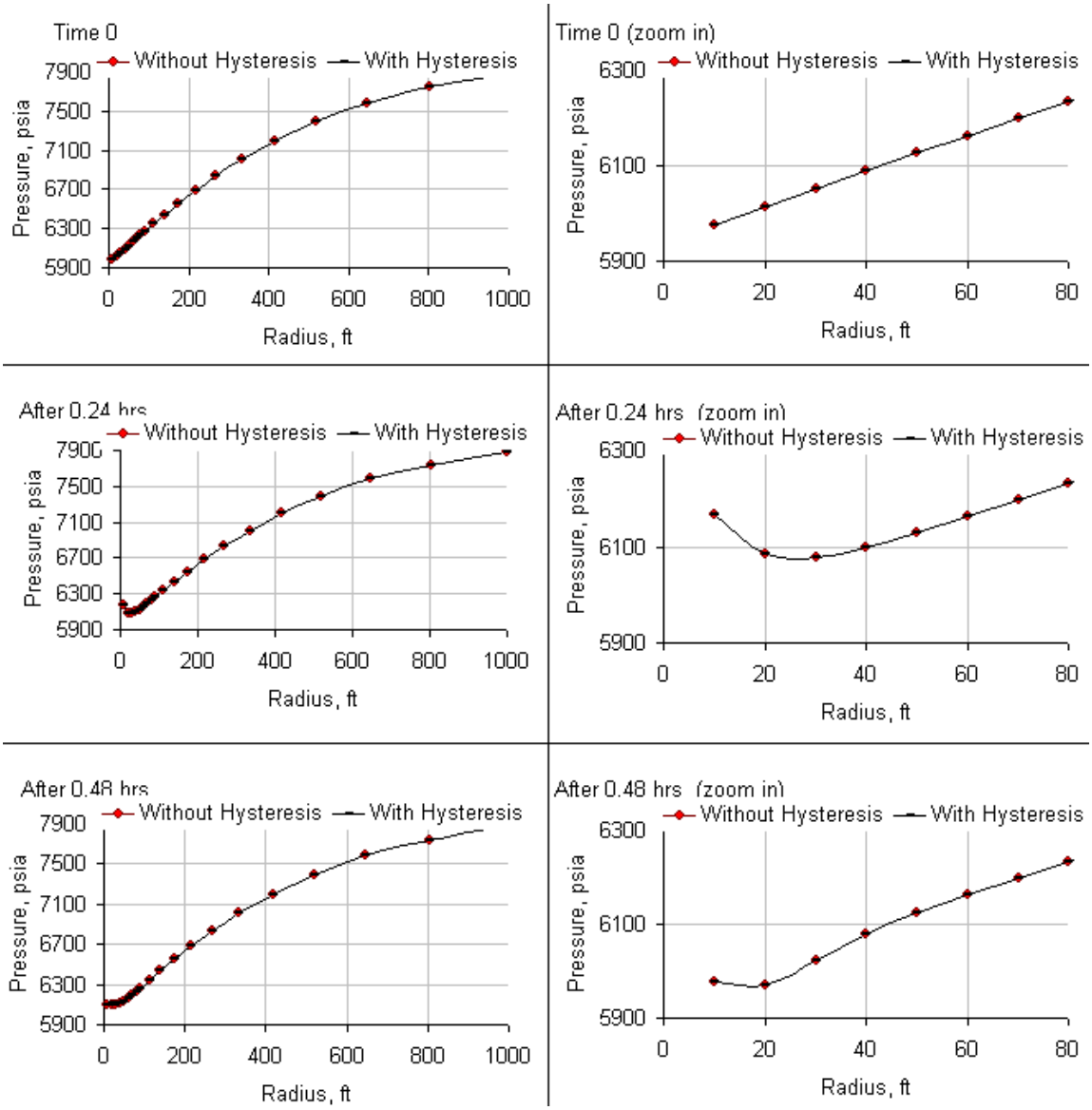

Fig.7.12—The difference between using hysteresis of relative permeability and not in the case of bottomhole pressure oscillating in sine function style.

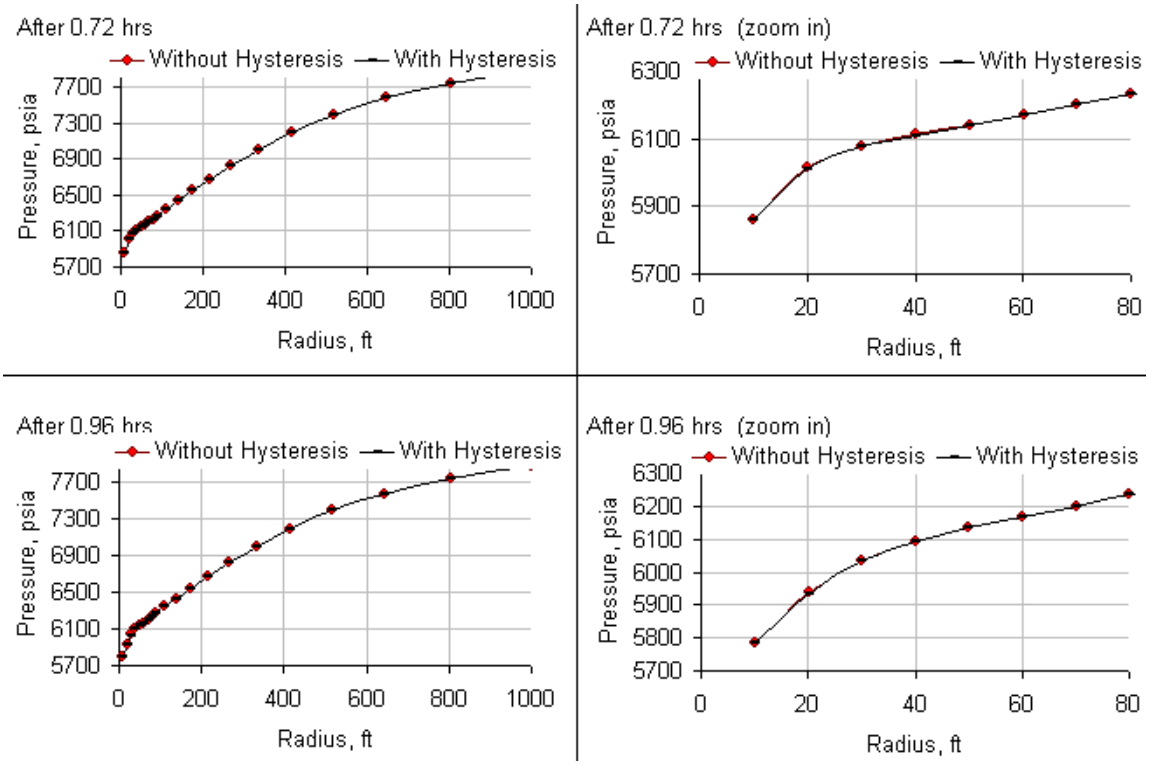

(Fig.7.12 Continued)

Summary

This study focuses on the hysteresis effects of the relative permeability. This effect will lead to less pressure drop, and no significant difference in saturation distribution is observed. However, if the frequency of the fluid reinjection is high, the effect is negligible.

CHAPTER VII
SIMULATION OF THE COUNTER-CURRENT FLOW IN THE NEAR-WELLBORE REGION

In the previous Chapter VI, the modeling efforts did not consider the capillary pressure. However, counter-current flow is observed in field, and capillary pressure must take responsibility for that scenario. This chapter successfully simulated the possible existing counter-current flow under fully transient conditions for a gas reservoir; further, capillary pressure is identified to be responsible.

Approach Description

This work was performed based on the blackoil FORTRAN simulator used before, and reached its the solution by the IMPES method. Although this work is based on conventional numerical reservoir modeling techniques, we use them in a way that accommodates transient pressure and rate boundary conditions at the wellbore and also along the distance from the well.

Reservoir model description

The synthetic dry gas reservoir has permeability of 1 md, porosity is 12.15%, the water saturation is 12%, and gas saturation is 88%; capillary effects were considered and constructed by the Leverett J-function (**Fig. 8.1**); and the relative permeability curve is constructed by the Coery correlation (**Fig. 8.2**). Where water replaces gas, it is an inhibition process; on the other hand, where the free gas replaces oil, it is a drainage process. Forward predictions were carried out for 20 days. A similar case study was performed with Eclipse for comparison purpose. The final results from the FORTRAN code and ECLIPSE are similar up to this point (**Fig. 8.3**). The BHP then starts oscillating. We proposed a step function (**Fig. 8.4**) to simulate the effects of slug flow in

the wellbore. The BHP builds up at a constant rate of 1 psia every 2 minutes. After every 10 minutes, one liquid slug is lifted to the surface; consequently, the pressure drops by 25 psia, and the cycle starts again. In Fig. 8.4, the labels beginning with a letter *t* represent the different simulation timesteps, each is two minutes.

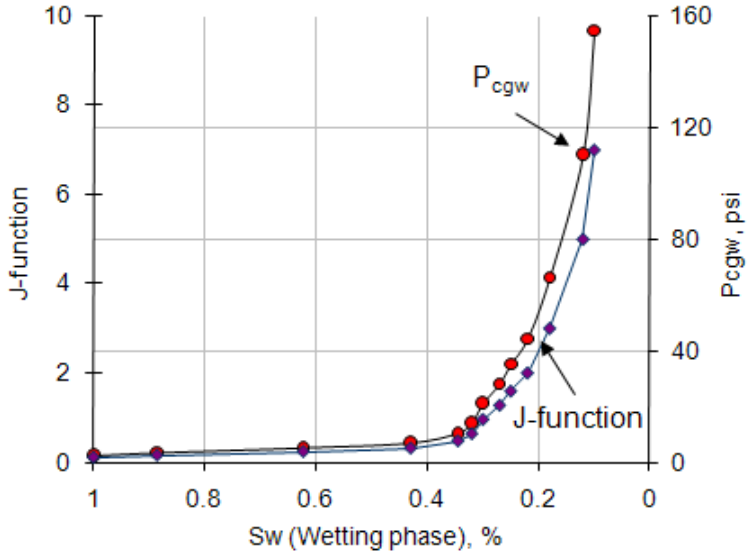

Fig. 8.1—J-Function and calculated gas-water capillary pressure versus water saturation. The maximum capillary pressure is about 160 psi.

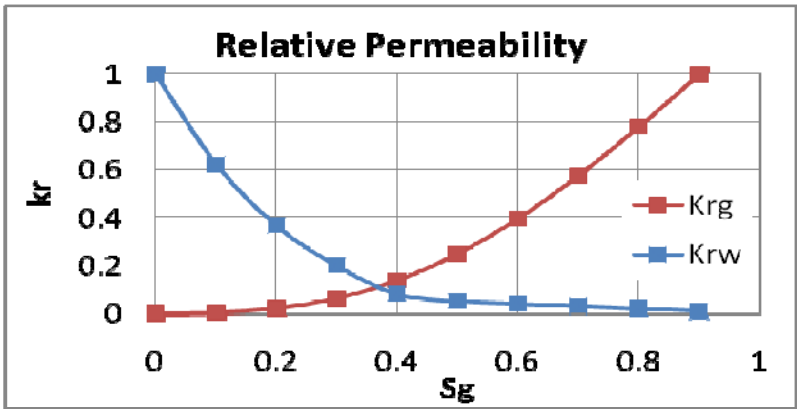

Fig. 8.2—The relative permeability with gas saturation. This curve is calculated by the Corey's correlation.

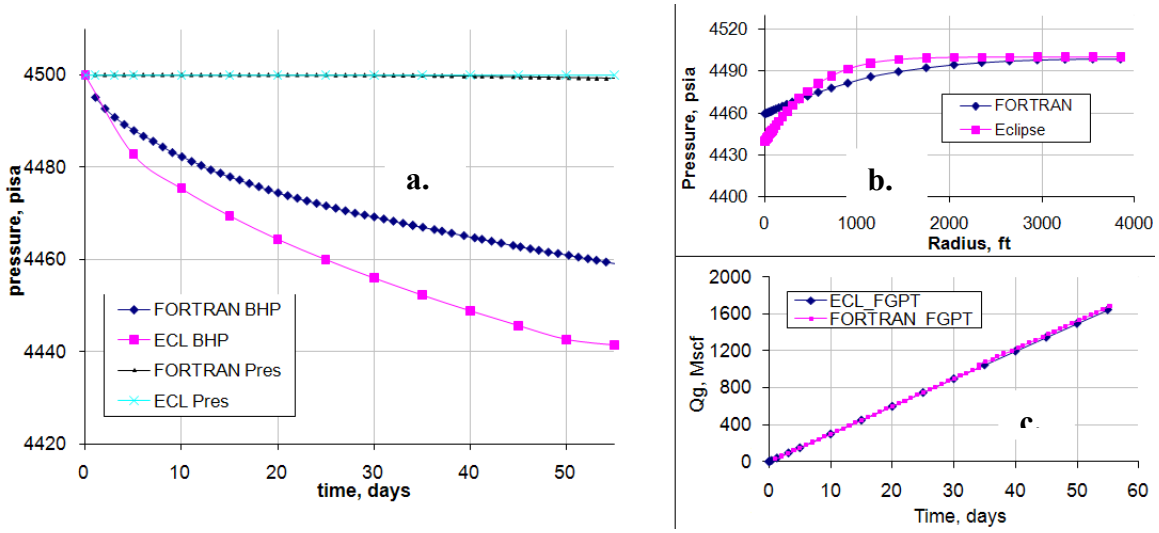

Fig.8.3—Comparison by time between Eclipse and the research code.
a is the comparison for the BHP (water phase) and reservoir pressure at the outer boundary;
b is the comparison for the water phase pressure distribution;
c is the comparison for the field cumulative gas production.

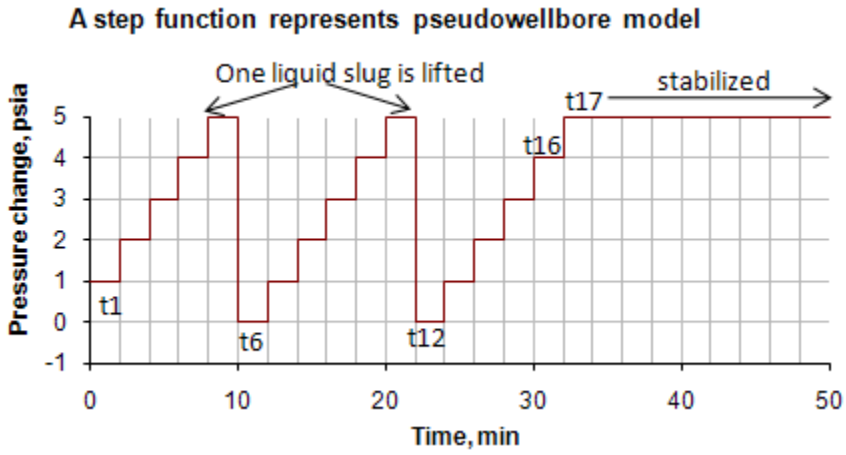

Fig.8.4—A step function to represent the pattern of BHP oscillation.
When the BHP is built up to the maximum, one liquid slug is lifted.
After three buildup cycles, the BHP is fixed as 4465 psia in FORTRAN and stabilized for 5 days.

As in the previous discussion in Chapter VI, proper PVT data lead to correct calculations of the fluid compressibility, which provides the potential for pressure collisions. The

grid refinement techniques achieve a balance of zooming in on the near-wellbore region and determining the maximum timestep to obtain stable IMPES solutions. All these prerequisites help constitute the U-shaped curve pressure profile.

Implicit pressure explicit saturation (IMPES) approach

Numerical reservoir modeling is based on the solution of the diffusivity equation, which combines mass conservation equations (differential mass balance), PVT fluid characterization, and a transport law in a multiphase flow system. When using the IMPES approach, the diffusivity equation is solved implicitly for pressure and explicitly for phase saturation. Because the capillary pressure between oil and water phases is negligible, the water pressure is identical to oil pressure as summarized in Eq. 3.48.

$$\sum_{m\in\psi_n}\left\{B_{w\,n}^{n+1}T_{w\,n,m}^{n}+B_{g\,n}^{n+1}\left[T_{g\,n,m}^{n}\right]\right\}p_{w\,m}^{n+1}-\left(B_{w\,n}^{n+1}C_{wp\,n}+B_{g\,n}^{n+1}C_{gp\,n}+\sum_{m\in\psi_n}\left\{B_{w\,n}^{n+1}T_{w\,n,m}^{n}+B_{g\,n}^{n+1}\left[T_{g\,n,m}^{n}\right]\right\}\right)p_{w\,n}^{n+1}$$
$$=-\left[B_{w\,n}^{n+1}C_{wp\,n}+B_{g\,n}^{n+1}C_{gp\,n}\right]p_{w\,n}^{n}-\left[B_{w\,n}^{n+1}q_{wsc\,n}^{n}+B_{g\,n}^{n+1}q_{gsc\,n}\right]-\sum_{m\in\psi_n}B_{g\,n}^{n+1}T_{g\,n,m}^{n}\left(P_{cgo\,m}^{n}-P_{cgo\,n}^{n}\right)$$

…… (3.48 *or* 8.1)

The gas pressure is calculated by Eq. 8.2,

$$p_g = p_w + P_{cgw} \quad \text{……} \quad (8.2)$$

The reservoir simulator generated for this study is sensitive to the pressure fluctuating under transient conditions. Proper configurations of the fluid PVT properties, the grid refinement in the near-wellbore region, and the ratio of the pressure oscillation period to the timestep are extremely critical.

Fluid PVT characterization

For this transient modeling work, the fluid PVT properties were defined on the basis of blackoil correlations available in the literature, and they provide the practical systems compressibility that allow sufficient mass storage. The PVT behavior is depicted by the blackoil correlations in Appendix B (**Fig. 8.5**).

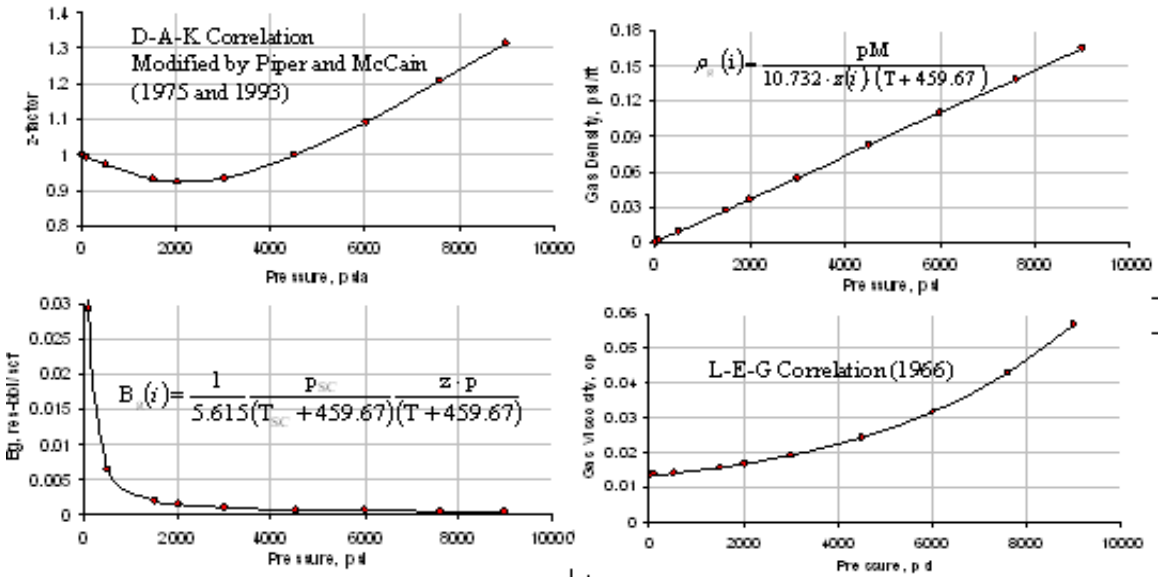

Fig. 8.5—Realistic fabricated PVT data lay out the correct trends upon pressure and create appropriate fluid compressibility for pressure oscillation in the near-wellbore region.

Grid refinement

Grid refinement is essential in the near-wellbore region because the pressure disturbance can only be sustained at a comparatively short distance from the wellbore. However, the

depth of the disturbance zone into the reservoir is not known a priori and varies with the frequency of the pressure fluctuations. In this study, logarithmic gridding was employed.

Definition of the Pressure Oscillation at the Wellbore

During liquid loading in gas wells, the BHP fluctuates as a result of wellbore phase redistribution effects, combined with the inertia opposed by the reservoir. In our preliminary investigations, sinusoidal wellbore pressure oscillations or step function (as in this present work) are assumed.

Gas/water capillary pressure calculation

Because of the variation of properties affecting capillary pressures in a reservoir, a universal capillary pressure curve is impossible to generate, so the Leverett J-function method was used to convert all capillary pressure data to a universal curve as in Eq. (8.3).

$$P_c = \frac{J(S_w)\cdot \sigma \ \cos\theta \sqrt{\frac{\phi}{k}}}{0.22} \quad \text{..... (8.3)}$$

where $J(S_w)$ is the Leverett J-function, σ is interfacial tenstion.

θ is the contact angle.

In this work, the tension is set as 4.7 dynes/cm and the contact angle is 30^o. Our later case study was based on different Leverett J-function curves upon water saturation.

Simulation Results and Discussions

Under this fully transient condition, our code captures the transient pressure distribution in the near-wellbore region and the backflow rates. The U-shaped curve for water and gas pressure distribution is shown in **Figs. 8.6** and **8.7**.

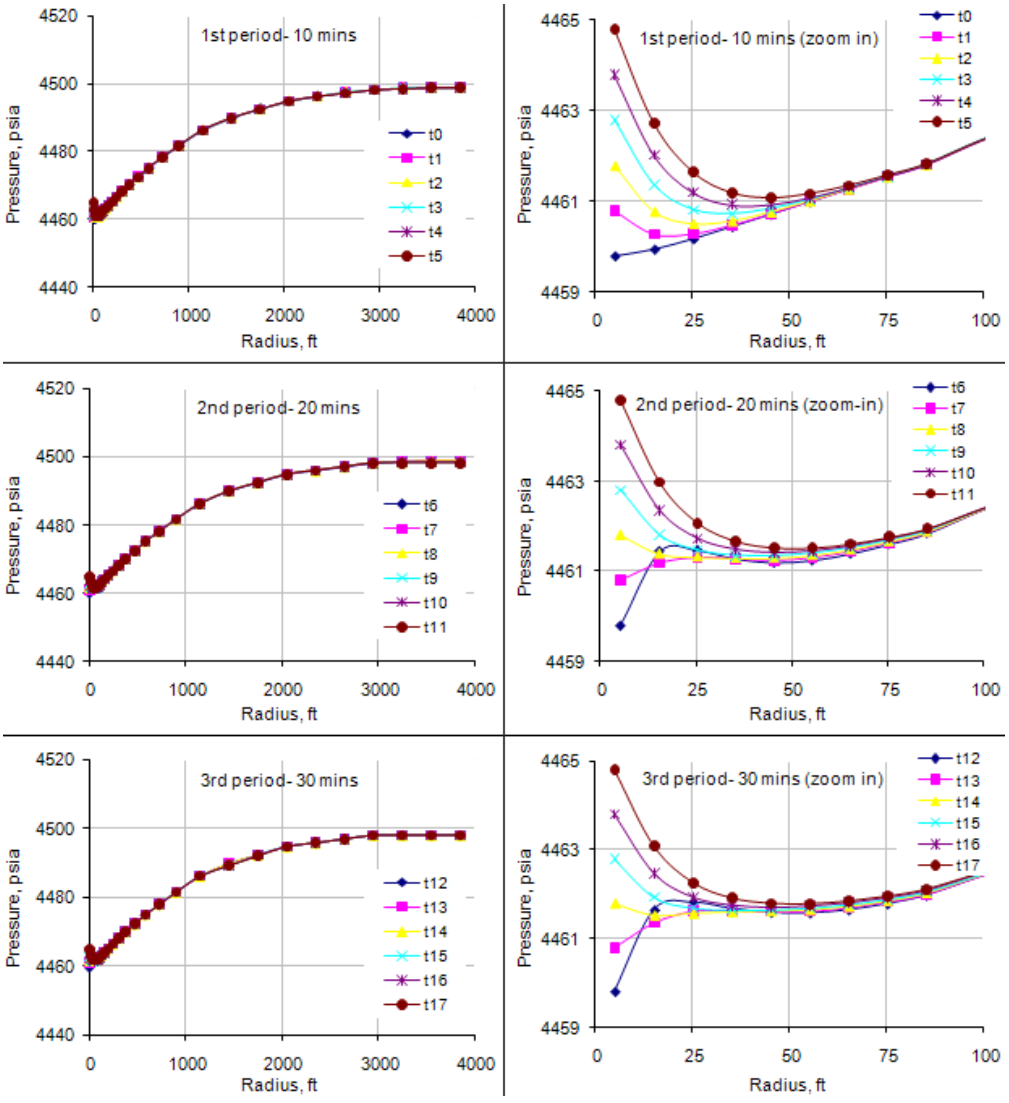

Fig.8.6—The water phase pressure distribution upon radius in the three buildup cycles. Similar U-shaped curves are observed.

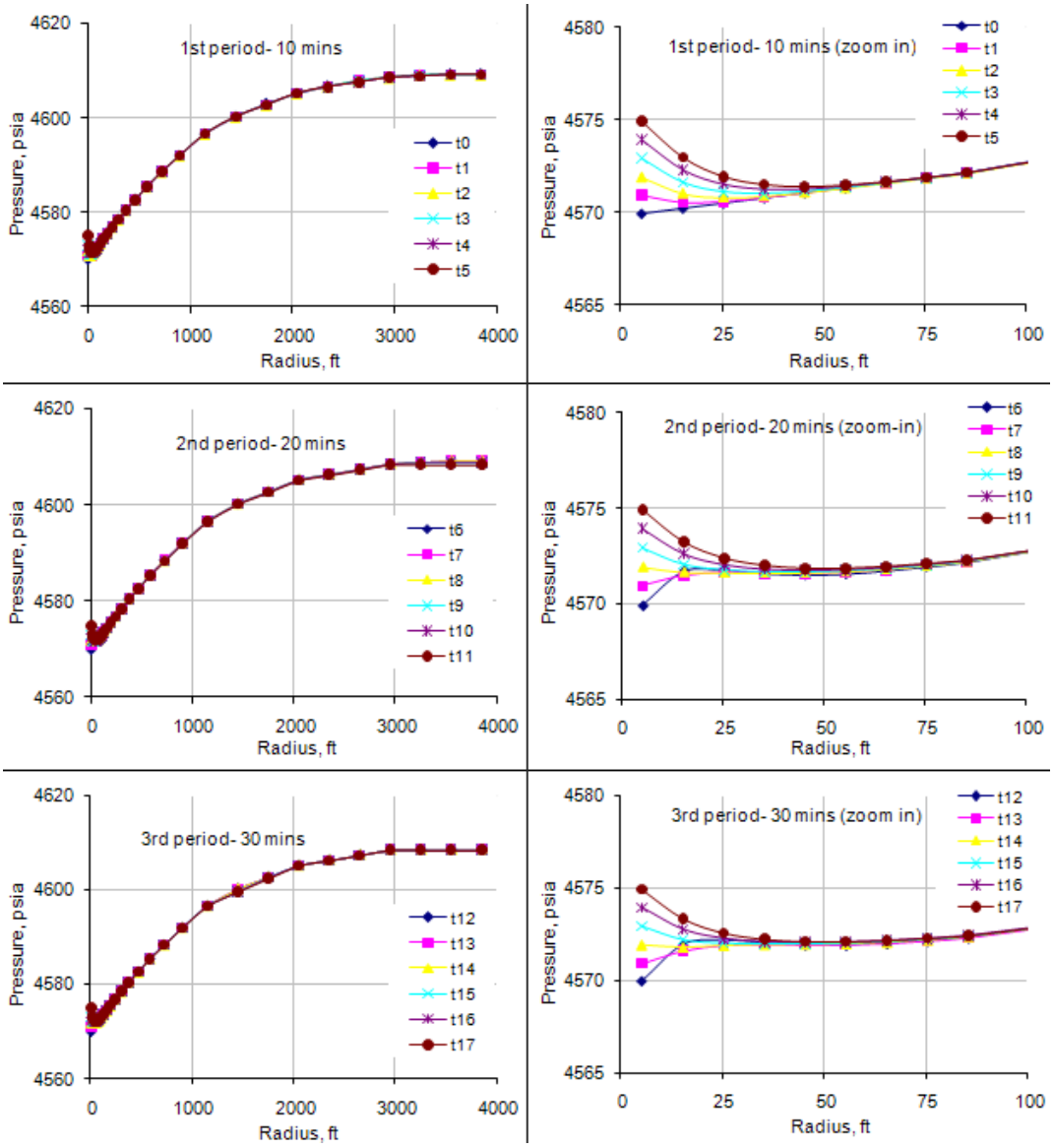

Fig.8.7—The gas phase pressure distribution upon radius in the three buildup cycles. Similar U-shaped curves are observed.

However, beginning from the same point at 20 days from production start-up, ECLIPSE does not seem to describe the same transient scenarios in **Figs. 8.8** and **8.9**.

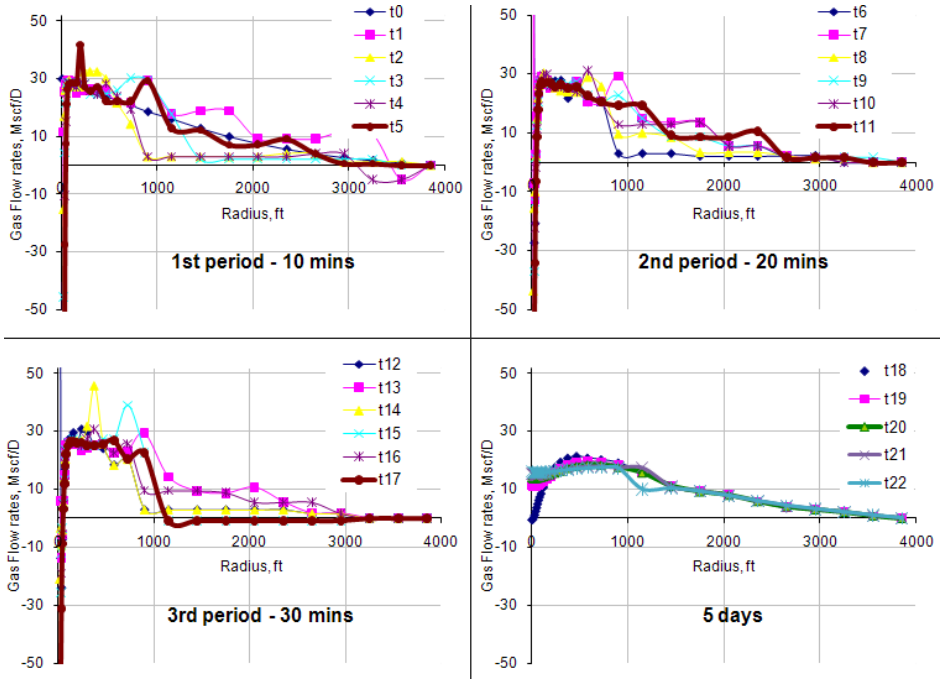

Fig.8.8—The inter-gridblock gas flow rates upon three periods.
Negative values mean the backflow rates. After some stabilization time, the backflow disappeared.

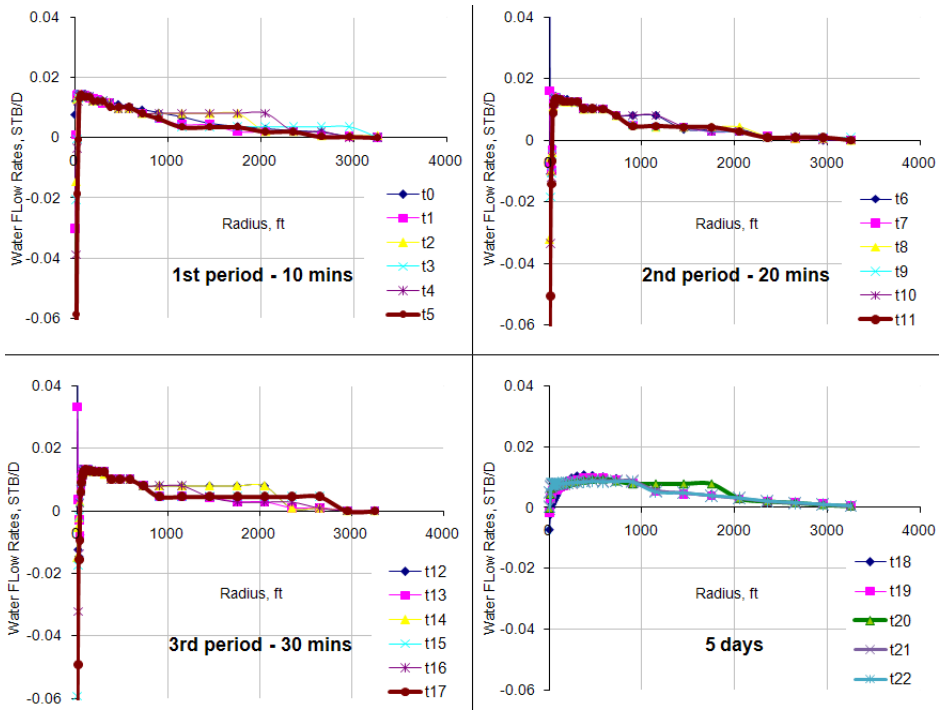

Fig.8.9—The inter-gridblock water flow rates upon three periods.
Negative values mean the backflow rates. After some stabilization time, the backflow disappeared.

In our code, after three oscillation cycles, the BHP is sustained with an increase of 5 psia for 5 days. Both simulators gave close results again as expected (**Fig. 8.10)**. The similar results for late time also support the validation of this FORTRAN simulator, as well as the U-shaped pressure distribution in the near-wellbore region.

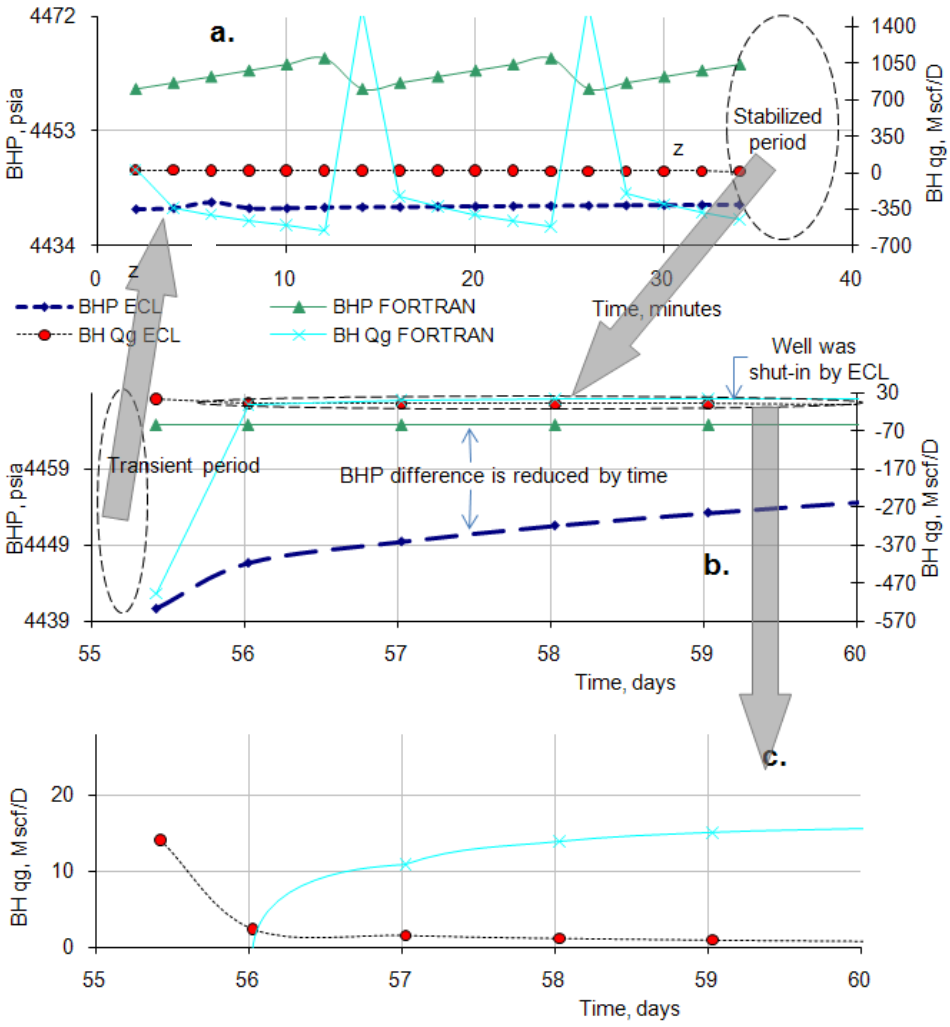

Fig.8.10—The comparison of the BHP fluctuating and bottomhole inter-gridblock gas flow rates with time.
The top figure (a) shows the initial transient reservoir response;
the middle figure (b) shows the reservoir response in the later stabilized period;
the bottom figure (c) zooms in on the flowrate distribution in stabilization time.
The well was shut in in ECL simulation results; meanwhile FORTRAN still produces at a reduced rate.
Negative values mean backflow rates.
After tabilizing the reservoir for 5 days, the backflow disappeared in FORTRAN results.

Counter-current flow is observed even for this 1D simulation case in **Fig. 8.11** to **8.14**. In the stabilization time, as long as the BHP can be sustained at a high value while assuming an infinite source from the wellbore, the liquid keeps being reinjected to the formation; meanwhile, because of the increasing water saturation in the very near-wellbore region, the capillary pressure is reduced, leaving a conventional pressure distribution profile for the gas phase. The U-shaped curve disappears for the gas phase. Previous researchers (Dousi et al. 2005) did an analog phase reinjection study, but on the basis of an upper producing gas zone and a lower reinjection water zone. Our 1D model is based on the same data, and also finds this counter-current flow. As a conclusion, capillary pressure is responsible for the counter-current flow in the stabilization period.

Further, during the approaching for this work, an opposite counter-current flow was also identified when the BHP oscillation first started; the liquid phase flowed to the wellbore, and the gas phase flowed back to the formation. This is because the large compressibility for the gas phase absorbs the BHP oscillation effects most, so the pressure profile responds to the BHP oscillation quicker than the liquid phase. As a consequence, this kind of counter-current scenario only exists in the very beginning and for a short time period right after the oscillation starts, so it is less important for production engineers.

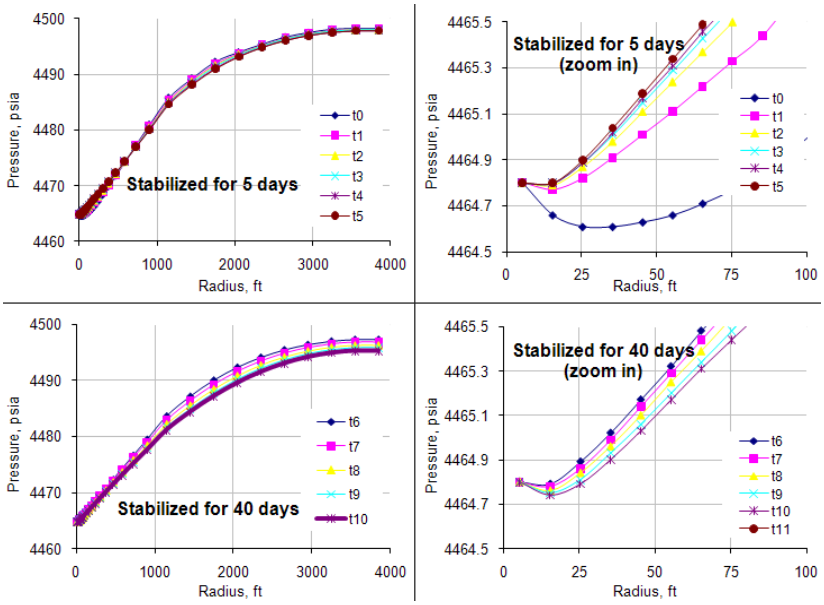

Fig.8.11—After long enough stabilization time, the pressure profile of the water phase still showed the U curve in the near-wellbore region, and introduced a backflow.

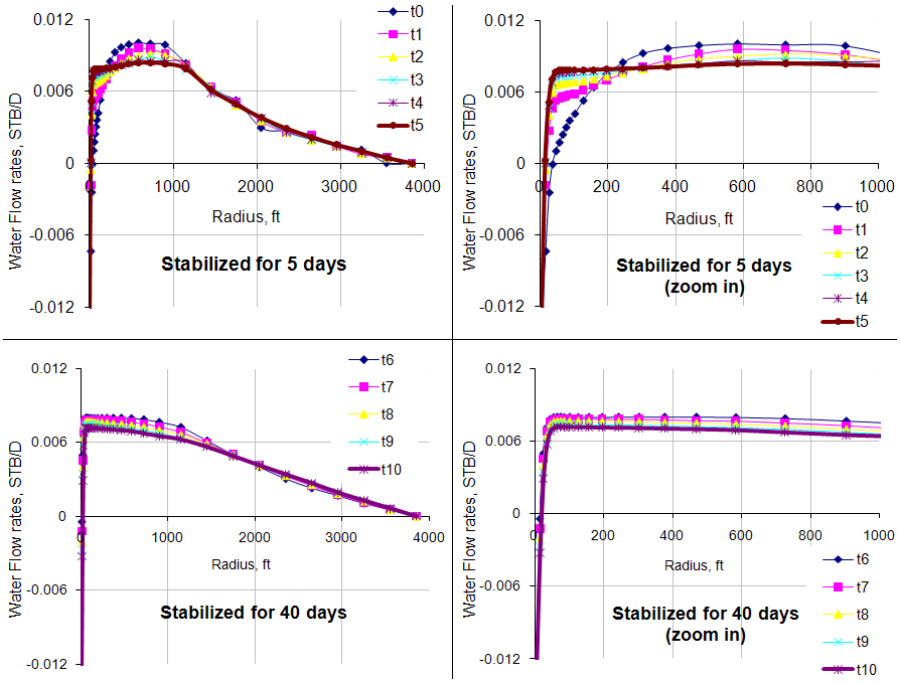

Fig.8.12—The backflow happened in the U-shaped pressure profile area, although the water backflow rates are small.

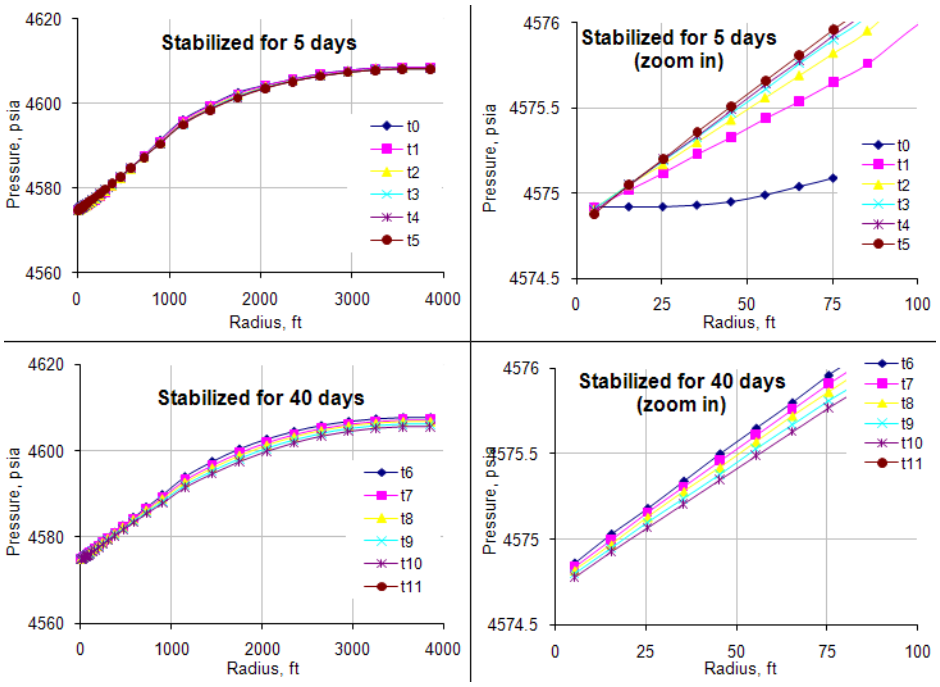

Fig.8.13—After long enough stabilization time, as the water saturation increased in the near-wellbore region, the capillary pressure is decreased, so the U-shaped pressure profile of the gas phase disappeared.

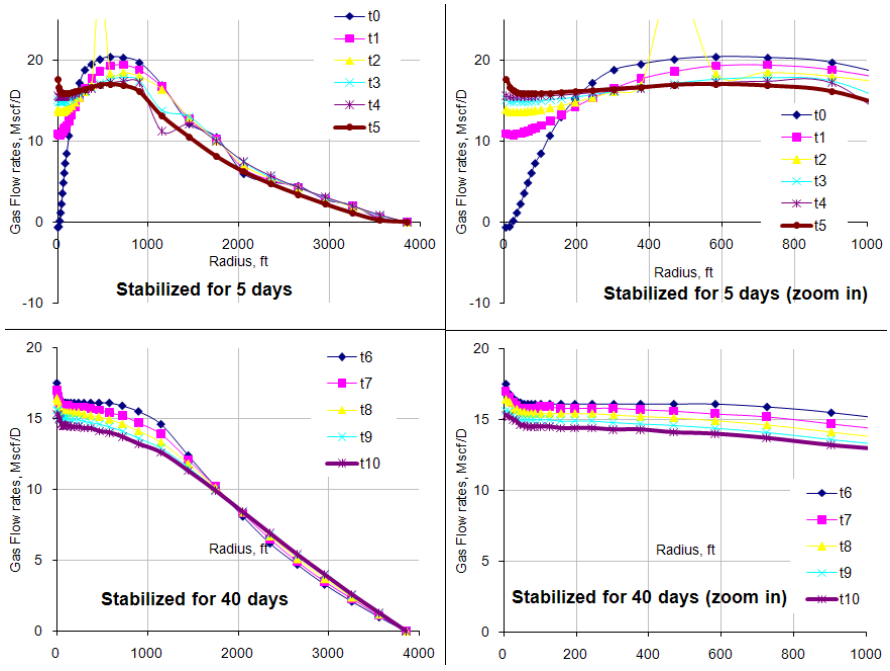

Fig.8.14—Positive gas flow rates mean the reinjection disappeared; however, the rates have been dramatically decreased from the previous 30 Mscf/D by sustaining the higher BHP.

Summary

The investigation of liquid loading in gas wells requires the understanding of the dynamic interactions between reservoir and wellbore. The conventional pressure profile in the near-wellbore region of a flowing reservoir is not suitable to characterize the transient phenomena that take place during liquid loading. Due to a combination of inertia and compressibility effects, the reservoir response to wellbore phase redistribution effects is not instantaneous. In this paper, a U-shaped pressure profile is proposed to characterize the transient response of the near-wellbore region to liquid loading in the wellbore. Such pressure profile could also explain the possibility of reinjection of the heavier phase into the reservoir.

This chapter presents the results of a comparison between a state-of-the-art commercial reservoir simulator and the research FORTRAN code for a synthetic, low-permeability gas reservoir under oscillating BHP conditions typical of a liquid-loaded well. The results show that the commercial software is unable to capture a transient pressure profile in the near-wellbore region and the associated reinjection of the liquid into the formation. This is because of the difference in the way the boundary conditions are defined at the wellbore. The commercial simulator defines the perturbed BHP as a target, not as a fixed constraint, and so introduces a gradual pressure buildup process. Also, when defining a wellbore, the user has to specify a priori if it is going to be a producer or an injector, and the well will not be allowed to automatically switch mode unless the user states so in a subsequent production schedule. This means that backflow rates cannot be detected with a conventional numerical simulator. On the other hand, our code captures the transient phase profiles of both the gas and the liquid phase; it also simulates counter-current flow due to capillary pressure effects, without considering gravitational effects, and models liquid reinjection into the formation.

CHAPTER IX
A FULLY-IMPLICIT METHOD
TO COUPLE THE WELLBORE AND RESERVOIR MODEL

An explicit coupling procedure was proposed for a single dry gas-phase reservoir by Faclone (2005) in Chapter II. The coupling method includes a five-step iteration loop. In the third step, the proposed method translates the flow rate at the bottom hole to a pressure gradient as the inner boundary for reservoir simulator. The set of algorithms for the reservoir and wellbore were well described in Chapter III and APPENDIX D respectively.

Five Steps

Although this model was not validated, the raw work evoked the right way to couple wellbore/reservoir models under fully transient conditions. A general procedure is given with some modifications (**Fig. 9.1**):

1. Guess one BHP or flow rate.
2. Solve the multiphase well equations and obtain the flow rate or BHP.
3. In various ways, transfer the results from wellbore model to the inner boundary for the reservoir simulator; for example, the specified pressure, flow rate or bottomhole pressure gradient.
4. Using the IMPES method to solve the multiphase diffusivity equation, obtain the pressure profile in the reservoir and update the corresponding values in step 1 (bottomhole pressure or flow rate).
5. Go back to Step 2 to re-do the procedures until it converges.

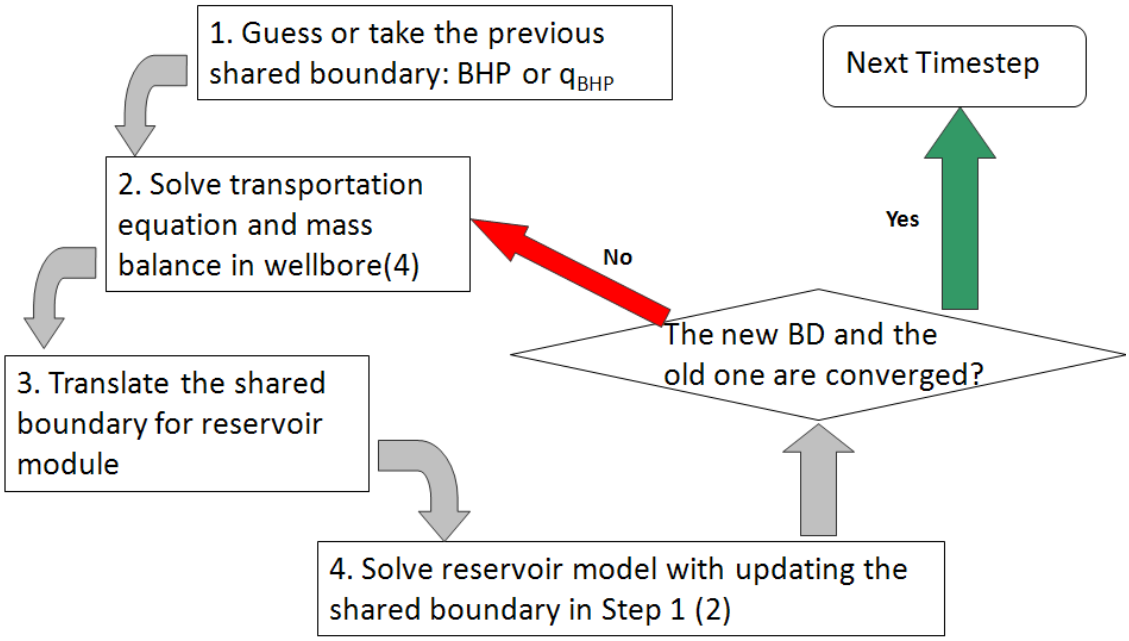

Fig.9.1—A diagram to illustrate the five-step explicit coupling approach.

Test of Coupling the Reservoir Model with a Pseudowellbore Model

The FORTRAN reservoir simulator is successfully built and validated through our previous work. To test if the proposed method is appropriate, an assumed pseudowellbore is implicitly coupled with this IMPES model.

An example of the integrated wellbore/reservoir model

The case study is based on a synthetic black oil reservoir. Again, it is a 1D IMPES model with single black oil phase. The grid block is distributed in a logarithmic method for 1,000 ft. The outer boundary reservoir pressure is constant at 1,000 psi. Reservoir permeability and PVT data are homogeneous and constant. In this single well model, the production rate is 75.96 STB/D. Water is reinjected from the outer boundary at the same

rate to satisfy the mass balance. The reservoir was initialized by the forward prediction for 1,000 days and reached a steady-state condition. This configuration is adopted from the validating case with a textbook example in Chapter V. Detailed information can be found *it Example 9.26* of the SPE textbook, *Basic Applied Reservoir Simulation* (Ertekin, 1998).

Starting from this initialized configuration, the reservoir simulation was coupled with an assumed linear VLP curve (Eq. 9.1) at the inner boundary–the straight line in **Fig. 9.2**.

$$q_{o,BH} = 0.248 p_{o,BH} \quad \text{.....} \quad (9.1)$$

Following the five-step method proposed before, we

1. Arbitrarily took the current BHP.
2. Brought this "current" BHP to Eq. 9.1 and obtain a "new" production.
3. Used the "new" production rate as the outer boundary of the reservoir module.
4. Through IMPES method, solved the pressure profile for a "new" BHP and updated the corresponding BHP in step 1.
5. Went back to Step 2 to re-do the procedures until it converged.

After six iteration steps, results converged, and the production rate was increased from 75.92 bbl/D to 130.86 bbl/D, while the BHP was reduced from 910.94 psi to 527.55 psi. Fig. 9.2a shows the convergent process of the six iterations, and Fig. 9.2b is the zooming in of the last three iteration results, which clearly confirmed the validity of the proposed five-step method.

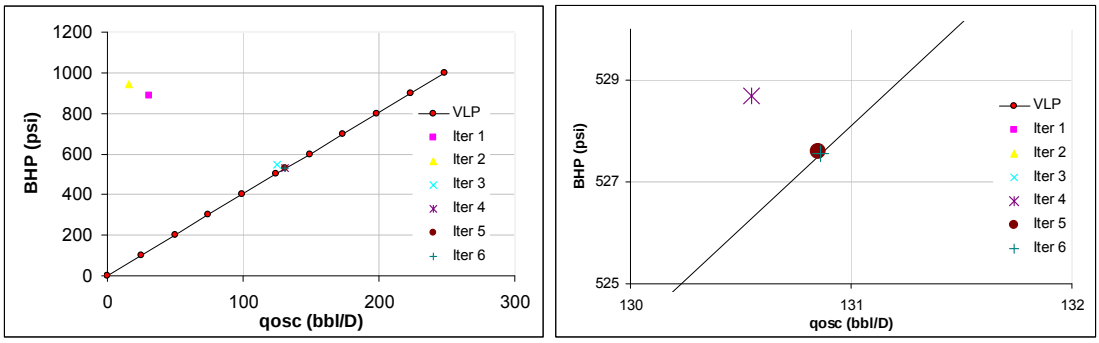

Fig. 9.2—The successful integration example of the self-developed reservoir simulator with a pseudowellbore model was performed with the theory of Five Steps.

When we couple this reservoir with our wellbore module, timestep adjustments are very important. The timestep required by reservoir side is much larger than the wellbore side. If we always use the tiny timestep required by the wellbore module, a several-years-long simulation task can be extremely time-consuming and impractical.

Initially the simulator always picks up a large timestep to run, followed by a material balance check (MB check). If the MB check is satisfied, the current solution is considered to be a stable one and proceeds to the next timestep; however, if the solution is failed with the allowed Newton-Raphson iterations, a diverging problem occurs, and the simulator just stops the forward prediction and recovers the integrated system to the last stable configurations. Then the simulator divides the current timestep by 2, 2^2, 2^3, 2^4, 2^5, 2^6, …, and runs the results based on these different timesteps from large to tiny ones. At the end, it selects the best solution according to the MB check results, granting it as the most stable solution.

A possible time sequence of the simulation is like that: first, it runs with a large timestep, but that leads to a bad MB check result; then it runs several tiny timesteps to stabilize the integrated system until it gets good MB check results. This method simply speeds up the simulation time cost, but it sacrifices the accuracy. However, this is a novel numerical method to couple a fully transient reservoir and pipe models.

Summary

The idea of this modified “five-step” method works for single oil phase under transient conditions. The self-developed simulator is ready to implement, with the wellbore model with replacing the pseudowellbore model.

CHAPTER X

INVESTIGATION ON TRANSIENT PERMEABILITY

Permeability is usually assumed to be a constant value, a function of the rock. However, in the framework of developing a transient reservoir simulator, it is important to consider the possibility of a transient permeability, a function of the fluid pressure. Literature review (Fournie, 2008, Baggio, 2009) shows that some studies of transient permeability are tailored to tight formations and involve measurements under transient conditions, mostly due to the very long time otherwise required reaching steady-state flow prior to conventional measurement of absolute rock permeability. Our review highlighted the lack of dedicated investigations on backpressure waves' effects on pore fluid pressure and, in turn, on permeability.

A study was therefore carried out to identify key parameters for an ideal experiment that would assess the existence of a transient, pore-pressure-dependent permeability. To this aim, preliminary laboratory experiments with a modified Hassler cell were performed at Clausthal University of Technology, Germany, to mimic the effect of oscillating downhole pressure on the gas flow in the near-wellbore region of a reservoir. Such oscillations could be triggered by wellbore phase redistribution. Pressure gauges were installed along the core to monitor the pressure profile.

Experiment Description

This experiment was designed and conducted at TU Clausthal by Dr. Catalin Teodoriu and Youping Wang, PhD student. It consists of a modified Hassler cell containing a low-permeability core specimen, through which air is circulated (from left to right in **Fig. 10.1**).

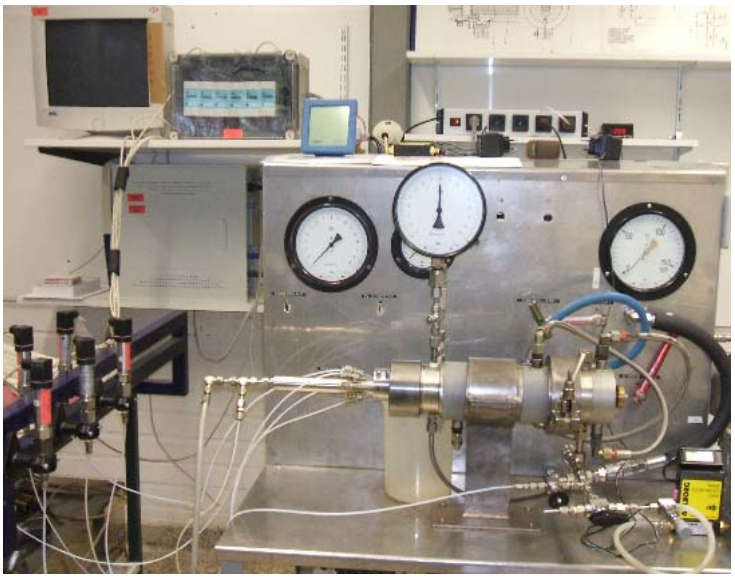

Fig.10.1—Experimental setup (Teodoriu, 2009).

The maximum confinement pressure supported by the Hassler cell is 16 bar (232 psia) and the maximum allowed inlet pressure is half of this value, i.e. 8 bar (116 psia) to avoid any boundary leaks. Experiments are run with a confinement pressure of 9 bar; inlet pressures vary from 1.5 to 6 bar, and the outlet is left at atmospheric pressure. Flow rate is measured at the level of the outlet valve (yellow device at the bottom right in Fig. 10.1); pressures are measured through six pressure gauges located at different points of the cell (**Fig 10.2**).

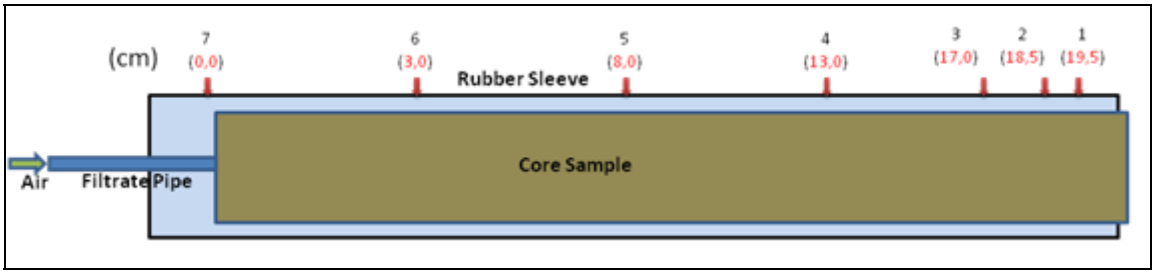

Fig.10.2—Schematic longitudinal section of the Hassler cell shows the location of pressure gauges.

In the first stage, the air flows at imposed inlet and outlet pressures until the flow is stabilized, which indicates the steady-state condition is reached. Inlet and outlet pressures, along with the outlet flow rate at the outlet are recorded, and the sample permeability is evaluated by Darcy's law for compressible gas in Eq. 10.1,

$$k = \frac{2q_{out}\mu p_{out}L}{A\left(p_{in}^2 - p_{out}^2\right)} \quad \text{..... (10.1)}$$

In the second stage, the outlet valve is suddenly closed, and pressure is sampled simultaneously at all measuring points via a LabVIEW program, at every small time period.

All the available parameters of the fluid and rock used in the experiments are summarized in **Table 10.1** (Baggio, 2009).

Table 10.1—ROCK SAMPLE	
Porosity	**17-18%**
Diameter	**0.00554 sq-ft**
Length	**0.68 ft**
Fluid	
Nature	**air**
Viscosity	**0.0184 cp**
Specific gravity	**1**
Experimental parameters	
Temperature	**71.42 degF**
Confinement pressure	**130 psia**
Inlet pressure	**22-87 psia**
Outlet pressure	**14.7 psia**
Perturbation	**total/partial valve closure**
Test duration	**10-15 min**

All the experiments have been run using exactly the same settings, except for the outlet valve, which was only partially closed.

Performed Simulation

We conducted simulations with the commercial software ECLIPSE and the developed FORTRAN simulator. The same input parameters were used as the actual experiment.

Results and Discussions

The results under the steady-state condition are shown in **Fig. 10.3**, and both of the simulation results matched the experimental data very well. **Fig. 10.4** shows the results under transient conditions–the outlet valve was closed, and the inlet pressure was maintained constant while initiating a transient pressure buildup at the core outlet. Then the experiment started to sample the pressure data along the core every 30 seconds. The results show the consistent pressure profile in both of the simulators, but the buildup process is much slower from the experiments. A few more comparisons were performed according to different outlet disturbances or slightly different inlet pressures, but the similar discrepancy between experiments and simulations always appeared (Baggio, 2009).

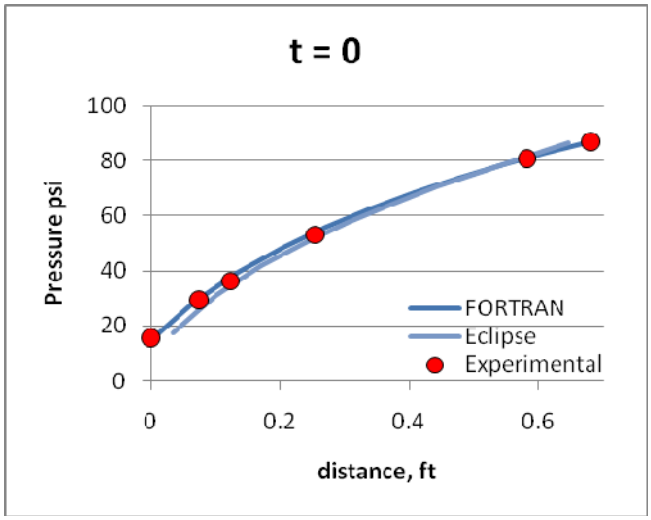

Fig.10.3—Comparison between simulations and experimental data under steady-state conditions; all curves are almost superimposed.

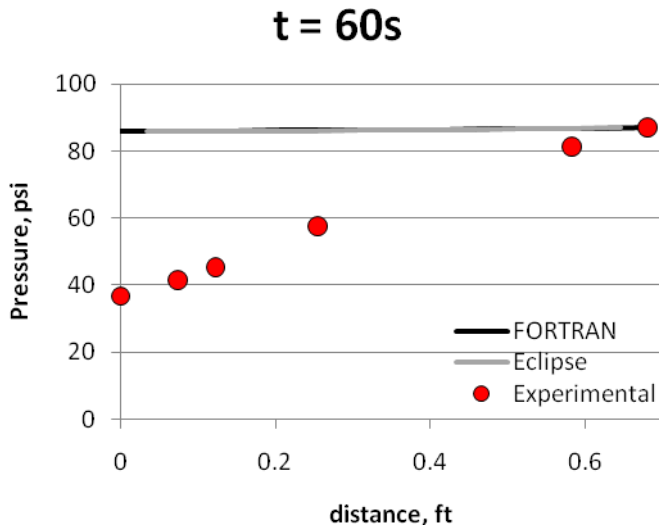

Fig.10.4—Comparison between simulations and experimental data under transient condition; simulation curves are almost superimposed between the two simulators, but far away from the experimental data.

These results suggest a possible pressure-dependent permeability, and need the support form more experimental data.

CHAPTER XI

CONCLUSIONS

This work presents a 1D dry gas and water two-phase reservoir simulator, coupled with a pseudowellbore model. The results of this study support the possible existence of a U-shaped pressure profile in the near wellbore, combined with reinjection rates into the formation, and counter-current flow.

- This FORTRAN simulator is more sensitive to the inner boundary pressure oscillation than the conventional modeling approaches. The work suggests the existence of a U-shaped pressure profile in the near-wellbore region.

- High frequency of the bottomhole pressure oscillation, large fluid compressibility, and low permeability will cause a shorter length of the U-shaped pressure profile. The fluctuating amplitude has no effect on the U-shaped distance. This conclusion is consistent with the two-phase dry gas reservoir and three-phase black oil reservoir.

- This study successfully mimics liquid reinjection into the formation while gas continues being produced.

- This near-wellbore model was coupled with a pseudowellbore model experiencing slug flow, and the simulation results reveal the gas well dying procedure.

- Capillary effect plays an important role in the near-wellbore region and is responsible for counter-current backflow rate without considering gravity effects.

- The work has prepared the future integration of a fully transient wellbore model with this fully transient near-wellbore model.

- This work will help production engineers identify or predict the onset of the liquid loading problem, help determine the best remedy to save liquid-loaded wells, and save liquid-loaded wells while generating profits for industry. The results add to the current understanding of dynamic interactions between reservoir and wellbore in situations when liquid loading occurs.

The modeling efforts have successfully developed representative solutions for the transient flow in the near-wellbore region. It has many applications in the field; for example:

- It is capable of working under fully transient condition to avoid setting aggressive producing rates and preventing liquid loading.

- It is capable of forcasting a threatening disturbed pressure profile due to bottomhole shut-in to estimate the potential damage to downhole equipments.

- It is capable of optimizing the injection spots for gas lift design. To design an artificial lift project, field engineers need to determine the effective injection points along the wellbore. For a fixed flowing wellhead pressure, the required BHP can be calculated to carry out all the liquid from the wellbore, which is the H_{inj} in Eq. 11.1. This calculation is clearly related to the BHP oscillation characterization. An integrated wellbore and reservoir modeling approach (our work) is highly encouraged to estimate the pressure collision in the near-wellbore region. An accurate average BHP by a fully transient model will ensure a successful project.

$$p_{wf} = p_{tf} + H_{inj}\left(\frac{dp}{dz}\right)_a + \left(H - H_{inj}\right)\left(\frac{dp}{dz}\right)_b \qquad \text{……………………………….. (11.1)}$$

– It is capable of predicting the transient flow in fractures, especially for shale gas reservoirs.

REFERENCES

Ali, A.M., Falcone, G., Hewitt, G.F., Bozorgzadeh, M. and Gringarten, A.C. 2005. Experimental Investigation of Wellbore Phase Redistribution Effects on Pressure-Transient Data. Paper SPE 96587 presented by an SPE Program Committee following review of information contained in a proposal by the authors. SPE-96587-MS DOI: 10.2118/96587-MS.

Al-Darmaki, S., Falcone, G., Hale, C.P. and Hewitt, G. F. 2006. Experimental Investigation and Modeling of the Effects of Rising Gas Bubbles in a Closed Pipe. Paper SPE 103129 presented at the 2006 SPE Annual Technical Conference and Exhibition, San Antonio, Texas, 24-27 September. SPE-103129-PA DOI: 10.2118/103129-PA.

Baggio, S. 2009. Investigation on the Concept of Transient Permeability in the Case of Liquid Loading in Gas Wells, Part II. MEng project report. Texas A&M University, College Station, TX.

Cazenave, T. and Dickstein, F. 1996. On the Initial Value Problem for a Linear Model of Well-reservoir Coupling. *Nonlinear World*, **3:** 567-587.

Chupin, G., Hu, B., Haugset, T. and Claudel, M. Integrated Wellbore/Reservoir Model Predicts Flow Transient in Liquid-Loading Gas Wells. Paper SPE 110461 presented at the SPE Annual Technical Conference and Exhibition, Anaheim, California, 11-14 November. SPE-110461-MS DOI: 10.2118/110461-MS.

Coleman, S.B., Clay, H.B., McCurdy, D.G., and Norris, H.L. Ill "A New Look at Predicting Gas-Well Load Up," *J. of Pet.Tech.*, **43**(3): 329-333. DOI: 10.2118/20280-PA.

Corey, A,T. The Interrelation Between Gas and OiI Relative Permeabilities. *Producers Monthly*, Nov. 1954 38-41.

Coats, B.K., Fleming, G.C., Watts, J.W., Rame, M. and Shiralkar, G.S. 2003. A Generalized Wellbore and Surface Facility Model, Fully Coupled to a Reservoir Simulator. Paper SPE 79704 presented at the SPE Reservoir Simulation Symposium, Houston, Texas, 3-5 February. SPE-79704-MS DOI: 10.2118/79704-MS.

Dousi, N., Veeken, C.A.M. and Currie, P. K. 2005. Numerical and Analytical Modeling of the Gas-Well Liquid-Loading Process. Paper SPE 95282 presented at the 2005 SPE Offshore Europe Aberdeen, 6-9 September. SPE -95282-MS. DOI 10.2118/95282-MS.

Dranchuk, P.M. and Abou-Kassem, J.H. 1975. Calculation of z Factor for Natural Gas Using Equations of State. J. of Cdn. Pet. Tech. **14**(3): 34-36. DOI: 10.2118/75-03-03.

Economides, M.J., Hill, D.A. and Ehlig-Economides, C. 1994. *Petroleum Production Systems.* Prentice Hall, Upper Saddle River, New Jersey.

Ertekin, T., Abou-Kassem, J. H., and King, G. R. 2001. *Basic Applied Reservoir Simulation*, Textbook Series, SPE, Richardson, Texas 7: 218-271.

Falcone, G. 2006. Modeling of Flows in Vertical Pipes and its Application to Multiphase Flow Metering at High Gas Content and to the Prediction of Well Performance. PhD dissertation. Imperial College, London, UK.

Fanchi, R.J. 2006. Petroleum Engineering Handbook, SPE Richardson, Texas.

Filho, C.O.C. and Bordalo, S.N. 2005. Assessment of Intermittent Gas Lift Performance Through Simulations and Coupled Dynamic Simulation. Paper SPE 94946 presented at the SPE Latin American and Caribbean Petroleum Engineering Conference, Rio de Janeiro, Brazil, 20-23 June. SPE-94946-MS DOI: 10.2118/94946-MS.

Fournie, J.-C. 2008. On the Track of the Concept of Transient Permeability. MEng project report. Texas A&M University, College Station, TX.

Gessner, T.R. and Barbosa, J.R. 2008. Numerical Solution of A Shock Tube: A Comparison Between Formulations Based on the Split Coeffeicient Matrix Method. Paper presented at 12th Brazilian Congress of Thermal Engineering and Sciences, Belo Horizonte, MG, Brazil, 10-14 November.

Hadgu, T, Zimmerman, R.W. and Bodvarsson, G.S. 1995. Coupled Reservoir-wellbore Simulation of Geothermal Reservoir Behavior. *Geothermics* **24**(2): 145-166.

Izgec, B., Kabir, C.S., Zhu, D., and Hasan, A.R. 2007. Transient Fluid and Heat Flow Modeling in Coupled Wellbore/Reservoir Systems. Paper SPE 102070 presented at the 2006 SPE Annual Technical Conference and Exhibition, San Antonio, Texas, 24-27 November. SPE-102070-PA DOI: 10.2118/102070-PA.

Lea, J., Nickens, H., and Wells, M. R. 2003. Gas Well Deliquification, Solutions to Gas Well Liquid Loading Problems, Houston, Texas: Gulf Professional Publishing.

Lee, A. L., Gonzalez, M. H., and Eakin, B. E. 1966. The Viscosity of Natural Gases. *JPT* **18**(8): 997-1000. SPE-1340-PA. DOI 10.2118/1340-PA.

Mach, J,, Pmano, E., and Brown, K.E. 1979. A Nodal Approach for Applying Systems Analysis to the Flowing and Artificial Lift Oil or Gas Well. unsolicited paper SPE 8025, available at SPE eLibrary.

Madray, R., Coll, C., Veitch, G., Butter, M., Bahri, S., Yaich, B. and Saada, T. 2008. Integrated Field Modelling of the Miskar Field. Paper SPE 113873 presented at the SPE Europec/EAGE Annual Conference and Exhibition, Rome, Italy, 9-12 June. SPE-113873-MS DOI: 10.2118/113873-MS.

McCain, W.D. Jr. 1993. *The Properties of Petroleum Fluids*, Tulsa, Oklahoma: PennWell Publishing Co.

McCain, W.D. Jr. 2008. Classnote of *PETE 665 Reservoir Engineering* offered at Dept. of Petroleum Engineering, Texas A&M Univeristy.

Morris, R.L., and Biggs W.P. 1967. Using Log-Derived Values of Water Saturation and Porosity. Paper SPWLA 1967-X presented at the SPWLA 8th Annual Logging Symposium, Society of Petrophysicists & Well Log Analysts. Paper X, 26p.

Nennie, E.D., Alberts, G.J.N., Belfroid, S.P.C., Peters, E., and Joosten, G.J.P. An Investigation Into the Need of a Dynamic Coupled Well-Reservoir Simulator. Paper SPE 110316 presented at the SPE Annual Conference and Exhibition, Anaheim, California, 11-14 November. SPE-110316-MS DOI: 10.2118/110316-MS.

Ng, J.T.H. and Egbogah, E.O. 1983. An Improved Temperature-Viscosity Correlation for Crude Oil Systems. *J. Cdn. Pet. Tech.* 22(2): 32-32. Society of CIM 83-34-32.

Peaceman, D.W. 1977. *Fundamentals of Numerical Reservoir Simulation*, Amsterdam, New York: Elsevier Scientific Pub. Co.

Piper, L.D., McCain, W.D. Jr., and Corredor, J.H. 1993. Compressibility Factors for Naturally Occurring Petroleum Gases. Paper SPE 26668 presented at the SPE Annual Technical Conference and Exhibition, Houston, Texas, 3-6 October. SPE-26668-MS DOI 0.2118/26668-MS.

Sagen, J., Sira, T. and Ek, A. 2007. A Coupled Dynamic Reservoir and Pipeline Model – Development and Initial Experience. Paper presented at the 13th International Conference on Multiphase Production Technology 07, Edinburg, UK, 13-15 June 2007.

Schlumberger. 2008. ECLIPSE Technical Description, v2008.2.

Solomon, F.A., Falcone, G., and Teodoriu, C. 2008. Critical Review of Existing Solutions To Predict and Model Liquid Loading in Gas Wells. Paper SPE 115933 presented at the SPE Annual Technical Conference and Exhibition, Denver, Colorado, 21-24 September. SPE 115933-MS DOI 10.2118/115933-MS.

Spivey, J.P., Valko, P.P., and McCain, W.D. 2005. Application of the Coefficient of Isothermal Compressibility to Various Reservoir Situations With New Correlations for Each Situation. Paper SPE 96415 presented at the SPE Annual Technical Conference and Exhibition, Dallas, Texas, 9-12 October. SPE-96415-MS DOI 10.2118/96415-MS.

Sturm, W.L., Belfroid, S.P.C., Van Wolfswinkel, O., Peters, M.C.A.M. and Verhelst, F.J.P.C.M.G. 2004. Dynamic Reservoir Well Interaction. Paper SPE 90108 presented at the SPE Annual Technical Conference and Exhibition, Houston, 26-29 September. SPE-90108-MS. DOI 10.2118/90108-MS.

Turner, R. G., Hubbard, M. G., and Dukler, A. E. 1969. Analysis and Prediction of Minimum Flow Rate for the Continuous Removal of Liquids from Gas Wells. *J. of Pet. Tech* (**21**)11: 1475-1482. DOI: 10.2118/2198-PA

Valko, P.P. and McCain, W.D. Jr. 2003. Reservoir Oil Bubblepoint Pressures Revisited; Solution-gas/oil Ratio and Surface Gas Specific Gravities. *J. Pet. Sci. & Eng.* **37**(2003): 153-169. DOI 10.1016/S0920-4105(02)00319-4.

Velarde, J., Balsingame, T.A., and McCain, W.D. 1997. Correlation of Black Oil Properties at Pressure Below Bubblepoint Pressure — A new Approach. Paper presented at the 48th Annual Technical Meeting of the Petroleum Society, Calgary, Alberta, 8-11 June. DOI: 10.2118/97-93.

Vicente, R., Sarica, C., and Ertekin, T. 2000. A Numerical Model Coupling Reservoir and Horizontal Well-Flow Dynamics: Transient Behavior of Single-Phase Liquid and Gas Flow. Paper presented at the 2000 SPE/Petroleum Society of CIM International Conference on Horizontal Well Technology held in Calgary, Alberta, Canada, 6-8 November. DOI: 10.2118/65508-MS.

Witte, T.W., Jr. 1987. The Development of a Correlation for Determing Oil Density in High Temperature Reservoirs. M.S.Thesis. Texas A&M University, College Station, Texas.

Zhang, H., Falcone, G., Valko, P., and Teodoriu, C. 2009. Numerical Modeling of Fully transient Flow in the Near-Wellbore Region During Liquid Loading in Gas Wells. Paper SPE 122785 presented at the SPE Latin American and Caribbean Petroleum Engineering Conference, Cartagena, Colombia, 31 May–3 June. SPE 122785-MS DOI 10.2118/122785-MS.

APPENDIX A

GAS-WATER TWO PHASE FLOW IMPES ALGORITHMS

Conservation Equation

Combining mass-conservation equations (differential mass balance), EoS, and transport equation-Darcy's law in a multiphase flow system to develop the PDE.

$$(m_i)_c - (m_o)_c + s_c = (m_a)_c$$

where

$$(m_i)_c = \left[\left(\dot{m}_{cx}A_x\right)_{x-\Delta x/2} + \left(\dot{m}_{cy}A_y\right)_{y-\Delta y/2} + \left(\dot{m}_{cz}A_z\right)_{z-\Delta z/2}\right]\Delta t$$

$$(m_o)_c = \left[\left(\dot{m}_{cx}A_x\right)_{x+\Delta x/2} + \left(\dot{m}_{cy}A_y\right)_{y+\Delta y/2} + \left(\dot{m}_{cz}A_z\right)_{z+\Delta z/2}\right]\Delta t$$

$$s_c = \left(q_{mt_c} + q_{m_c}\right)\Delta t$$

$$(m_a)_c = V_b\left[(m_{vc})_{t+\Delta t} - (m_{vc})_t\right]$$

Bringing the definitions into the above equation, we have

$$\left[\left(\dot{m}_{cx}A_x\right)_{x-\Delta x/2} + \left(\dot{m}_{cy}A_y\right)_{y-\Delta y/2} + \left(\dot{m}_{cz}A_z\right)_{z-\Delta z/2}\right]\Delta t$$
$$-\left[\left(\dot{m}_{cx}A_x\right)_{x+\Delta x/2} + \left(\dot{m}_{cy}A_y\right)_{y+\Delta y/2} + \left(\dot{m}_{cz}A_z\right)_{z+\Delta z/2}\right]\Delta t + \left(q_{mt_c} + q_{m_c}\right)\Delta t = V_b\left[(m_{vc})_{t+\Delta t} - (m_{vc})_t\right]$$
$$-\left[\left(\dot{m}_{cx}A_x\right)_{x+\Delta x/2} - \left(\dot{m}_{cx}A_x\right)_{x-\Delta x/2}\right] - \left[\left(\dot{m}_{cy}A_y\right)_{y+\Delta y/2} - \left(\dot{m}_{cy}A_y\right)_{y-\Delta y/2}\right]$$
$$-\left[\left(\dot{m}_{cz}A_z\right)_{z+\Delta z/2} - \left(\dot{m}_{cz}A_z\right)_{z-\Delta z/2}\right] = \frac{V_b}{\Delta t}\left[(m_{vc})_{t+\Delta t} - (m_{vc})_t\right] - \left(q_{mt_c} + q_{m_c}\right)$$
$$-\left[\frac{\left(\dot{m}_{cx}A_x\right)_{x+\Delta x/2} - \left(\dot{m}_{cx}A_x\right)_{x-\Delta x/2}}{\Delta x}\right]\Delta x - \left[\frac{\left(\dot{m}_{cy}A_y\right)_{y+\Delta y/2} - \left(\dot{m}_{cy}A_y\right)_{y-\Delta y/2}}{\Delta y}\right]\Delta y$$
$$-\left[\frac{\left(\dot{m}_{cz}A_z\right)_{z+\Delta z/2} - \left(\dot{m}_{cz}A_z\right)_{z-\Delta z/2}}{\Delta z}\right]\Delta z = \frac{V_b}{\Delta t}\left[(m_{vc})_{t+\Delta t} - (m_{vc})_t\right] - \left(q_{mt_c} + q_{m_c}\right)$$

In a differential expression,

$$-\frac{\partial}{\partial x}\left(\dot{m}_{cx}A_x\right)\Delta x-\frac{\partial}{\partial y}\left(\dot{m}_{cy}A_y\right)\Delta y-\frac{\partial}{\partial z}\left(\dot{m}_{cz}A_z\right)\Delta z=V_b\frac{\partial}{\partial t}\left(m_{v_c}\right)-\left(q_{mt_c}+q_{m_c}\right)$$

While "*c*" means component (= *w, g*)

By the definitions of $B_c=\frac{\rho_{\mathrm{csc}}}{\rho_c}=\frac{q_c}{q_{sc}}$, $m_{v_c}=\frac{\phi\cdot S_c}{B_c}$ and $\dot{m}_c=\alpha_c\rho_c u_c$, this derives as

Water: $$-\frac{\partial}{\partial x}\left(\frac{A_x}{B_w}u_{wx}\right)\Delta x-\frac{\partial}{\partial y}\left(\frac{A_y}{B_w}u_{wy}\right)\Delta y-\frac{\partial}{\partial z}\left(\frac{A_z}{B_w}u_{wz}\right)\Delta z=\frac{V_b}{\alpha_c}\frac{\partial}{\partial t}\left(\frac{\phi S_w}{B_w}\right)-q_{wsc}$$

Gas: $$-\frac{\partial}{\partial x}\left(\frac{A_x}{B_g}u_{fgx}\right)\Delta x-\frac{\partial}{\partial y}\left(\frac{A_y}{B_g}u_{fgy}\right)\Delta y-\frac{\partial}{\partial z}\left(\frac{A_z}{B_g}u_{fgz}\right)\Delta z=\frac{V_b}{\alpha_c}\frac{\partial}{\partial t}\left(\frac{\phi S_g}{B_g}\right)-\left(q_{fgsc}\right)$$

Bringing Darcy's law into the above three equations for each phase

$$\vec{u}_l=-\beta_c\frac{kk_{rl}}{\mu_l}\left(\vec{\nabla}p_l-\gamma_l\vec{\nabla}Z\right)$$

Water: $$\frac{\partial}{\partial x}\left(\beta_c\frac{A_x}{B_w}\frac{k_xk_{rw}}{\mu_w}\left(\frac{\partial p_w}{\partial x}-\gamma_w\frac{\partial Z}{\partial x}\right)\right)\Delta x+\frac{\partial}{\partial y}\left(\beta_c\frac{A_y}{B_w}\frac{k_yk_{rw}}{\mu_w}\left(\frac{\partial p_w}{\partial y}-\gamma_w\frac{\partial Z}{\partial y}\right)\right)\Delta y$$
$$+\frac{\partial}{\partial z}\left(\beta_c\frac{A_z}{B_w}\frac{k_zk_{rw}}{\mu_w}\left(\frac{\partial p_w}{\partial z}-\gamma_w\frac{\partial Z}{\partial z}\right)\right)\Delta z=\frac{V_b}{\alpha_c}\frac{\partial}{\partial t}\left(\frac{\phi S_w}{B_w}\right)-q_{wsc}$$

Gas:

$$\frac{\partial}{\partial x}\left(\beta_c \frac{A_x}{B_g}\frac{k_x k_{rg}}{\mu_g}\left(\frac{\partial p_g}{\partial x}-\gamma_g\frac{\partial Z}{\partial x}\right)\right)\Delta x + \frac{\partial}{\partial y}\left(\beta_c \frac{A_y}{B_g}\frac{k_y k_{rg}}{\mu_g}\left(\frac{\partial p_g}{\partial y}-\gamma_g\frac{\partial Z}{\partial y}\right)\right)\Delta y + \frac{\partial}{\partial z}\left(\beta_c \frac{A_z}{B_g}\frac{k_z k_{rg}}{\mu_g}\left(\frac{\partial p_g}{\partial z}-\gamma_g\frac{\partial Z}{\partial z}\right)+\right)\Delta z = \frac{V_b}{\alpha_c}\frac{\partial}{\partial t}\left(\frac{\phi S_g}{B_g}\right)-\left(q_{fgsc}\right)$$

We have four unknowns in the above three equations, which are p_w p_g S_w S_g.

Now consider the two constraints:

1. Phase-saturation constraint.
2. Capillary pressures as function of phase saturation.

$$S_w + S_g = 1$$

Usually water is the wetting phase, oil is the intermediate-wetting phase, and gas is the nonwetting phase, so we have

$$p_g = p_w + P_{cgw}(S_w)$$

Then we can reduce the six unknowns to three:

Water:

$$\frac{\partial}{\partial x}\left(\beta_c \frac{A_x}{B_w}\frac{k_x k_{rw}}{\mu_w}\left(\frac{\partial p_g}{\partial x}-\frac{\partial P_{cgw}(S_g)}{\partial x}-\gamma_w\frac{\partial Z}{\partial x}\right)\right)\Delta x + \frac{\partial}{\partial y}\left(\beta_c \frac{A_y}{B_w}\frac{k_y k_{rw}}{\mu_w}\left(\frac{\partial p_o}{\partial y}-\frac{\partial P_{cow}}{\partial y}-\gamma_w\frac{\partial Z}{\partial y}\right)\right)\Delta y + \frac{\partial}{\partial z}\left(\beta_c \frac{A_z}{B_w}\frac{k_z k_{rw}}{\mu_w}\left(\frac{\partial p_o}{\partial z}-\frac{\partial P_{cow}}{\partial z}-\gamma_w\frac{\partial Z}{\partial z}\right)\right)\Delta z = \frac{V_b}{\alpha_c}\frac{\partial}{\partial t}\left(\frac{\phi S_w}{B_w}\right)-q_{wsc}$$

Gas: $$\frac{\partial}{\partial x}\left(\beta_c \frac{A_x}{B_g}\frac{k_x k_{rg}}{\mu_g}\left(\frac{\partial p_g}{\partial x}-\gamma_g\frac{\partial Z}{\partial x}\right)\right)\Delta x$$

$$+\frac{\partial}{\partial y}\left(\beta_c \frac{A_y}{B_g}\frac{k_y k_{rg}}{\mu_g}\left(\frac{\partial p_g}{\partial x}-\gamma_g\frac{\partial Z}{\partial x}\right)\right)\Delta y$$

$$+\frac{\partial}{\partial z}\left(\beta_c \frac{A_z}{B_g}\frac{k_z k_{rg}}{\mu_g}\left(\frac{\partial p_g}{\partial x}-\gamma_g\frac{\partial Z}{\partial x}\right)\right)\Delta z=\frac{V_b}{\alpha_c}\frac{\partial}{\partial t}\left(\frac{\phi S_g}{B_g}\right)-\left(q_{fgsc}\right)$$

Now, for any basic flow models, the equations can be expressed in terms of oil pressure and fluid saturations in the $\left(p_o - S_w - S_g\right)$formation.

Discretization of the Multiphase-Flow Equations by a set of FDE's

Assume $T_{lx}=\beta_c\frac{k_x A_x}{\Delta x}\frac{k_{rl}}{\mu_l B_l}$ $T_{ly}=\beta_c\frac{k_y A_y}{\Delta y}\frac{k_{rl}}{\mu_l B_l}$ $T_{lz}=\beta_c\frac{k_z A_z}{\Delta z}\frac{k_{rl}}{\mu_l B_l}$

Meanwhile, remember the finite-difference approximation of the second-order partial derivatives in the x, y, and z directions are,

$$\frac{\partial f}{\partial x}\Delta x\approx\Delta_x f \qquad \frac{\partial f}{\partial y}\Delta y\approx\Delta_y f \qquad \frac{\partial f}{\partial z}\Delta z\approx\Delta_z f$$

So the above three equations can be simplified for each gridblock (*i,j,k*) as

Water: $$\Delta\left[T_w\left(\Delta p_w-\gamma_w\Delta Z\right)\right]=\frac{V_b}{\alpha_c\Delta t}\Delta_t\left(\frac{\phi S_w}{B_w}\right)-q_{wsc}$$

Gas: $$\Delta\left[T_g\left(\Delta p_g-\gamma_g\Delta Z\right)\right]=\frac{V_b}{\alpha_c\Delta t}\Delta_t\left(\frac{\phi\left(1-S_w-S_o\right)}{B_g}\right)-q_{gsc}$$

Discretization in Time

Explicit finite-difference equations for all components in the black-oil model my now be written in a compact form,

$$\text{Water: } \Delta\left[T_w\left(\Delta p_w - \gamma_w \Delta Z\right)\right]^n = \frac{V_b}{\alpha_c \Delta t}\left(\left[\frac{\phi S_w}{B_w}\right]^{n+1} - \left[\frac{\phi S_w}{B_w}\right]^n\right) - q_{wsc}^n$$

$$\text{Gas: } \Delta\left[T_g\left(\Delta p_g - \gamma_g \Delta Z\right)\right]^n = \frac{V_b}{\alpha_c \Delta t}\left(\left[\frac{\phi(1-S_w)}{B_g}\right]^{n+1} - \left[\frac{\phi(1-S_w)}{B_g}\right]^n\right) - \left(q_{fgsc}\right)^n$$

Implicit finite-difference equations for all components in the black-oil model my now be written in a compact form,

$$\text{Water: } \Delta\left[T_w\left(\Delta p_w - \gamma_w \Delta Z\right)\right]^{n+1} = \frac{V_b}{\alpha_c \Delta t}\left(\left[\frac{\phi S_w}{B_w}\right]^{n+1} - \left[\frac{\phi S_w}{B_w}\right]^n\right) - q_{wsc}^{n+1}$$

$$\text{Gas: } \Delta\left[T_g\left(\Delta p_g - \gamma_g \Delta Z\right)\right]^{n+1} = \frac{V_b}{\alpha_c \Delta t}\left(\left[\frac{\phi(1-S_w)}{B_g}\right]^{n+1} - \left[\frac{\phi(1-S_w)}{B_g}\right]^n\right) - \left(q_{fgsc}\right)^{n+1}$$

Implicit FDE's are unconditionally stable. Hence the implicit, backward-in-time discretization is used almost exclusively in modeling black-oil reservoirs.

Expansion of Accumulation Terms

From the reference *Basic Applied Reservoir Simulation* (Ertekin, 2001), page 234 , Example 9.9, we have,

$$\Delta_t f = f^{n+1} - f^n$$

where f is the time accumulation term.

Convert it to

$$\Delta_t(UVXY) = (UVXY)^{n+1} - (UVXY)^n$$

Where $U \equiv \phi\ V \equiv \frac{1}{B_l}\ X \equiv R_s\ Y \equiv S_l$

The derived conservative expansion formula is,

$$\Delta_t(UVXY) = (VXY)^n \Delta_t U + U^{n+1}(XY)^n \Delta_t V + (UV)^{n+1} Y^n \Delta_t X + (UVX)^{n+1} \Delta_t Y$$

$$\Delta_t U = \Delta_t \phi = \phi' \Delta_t p_o$$

$$\Delta_t V = \Delta_t \left(\frac{1}{B_l}\right) = \left(\frac{1}{B_l}\right)' \Delta_t p_o$$

$$\Delta_t X = \Delta_t R_s = R_s' \Delta_t p_o$$

$$\Delta_t Y = \Delta_t S_l = S_l' \Delta_t p_o$$

For a three-variable function,

$$\Delta_t\left[\frac{\phi S_l}{B_l}\right] = (UY)^n \Delta_t U + U^{n+1}(Y)^n \Delta_t V + (UV)^{n+1} \Delta_t Y$$

$$= \left(\frac{1}{B_l} S_l\right)^n \Delta_t \phi + \phi^{n+1}(S_l)^n \Delta_t \left(\frac{1}{B_l}\right) + \left(\phi \frac{1}{B_l}\right)^{n+1} \Delta_t S_l$$

$$= \left(\frac{1}{B_l} S_l\right)^n \phi' \Delta_t p_o + \phi^{n+1}(S_l)^n \left(\frac{1}{B_l}\right)' \Delta_t p_o + \left(\frac{\phi}{B_l}\right)^{n+1} \Delta_t S_l$$

$$= \left[\frac{\phi'}{B_l^n} + \phi^{n+1}\left(\frac{1}{B_l}\right)'\right] S_l{}^n \Delta_t p_o + \left(\frac{\phi}{B_l}\right)^{n+1} \Delta_t S_l$$

Now we can present the implicit (backward) finite-difference equations as:.

$$\Delta\left[T_w\left(\Delta p_w - \gamma_w \Delta Z\right)\right]^{n+1} = \frac{V_b}{\alpha_c \Delta t}\left(\left[\frac{\phi'}{B_w^n} + \phi^{n+1}\left(\frac{1}{B_w}\right)'\right] S_w{}^n \Delta_t p_o + \left(\frac{\phi}{B_w}\right)^{n+1} \Delta_t S_w\right) - q_{wsc}^{n+1}$$

$$\Delta\left[T_w\left(\Delta p_w - \gamma_w \Delta Z\right)\right]^{n+1} = \frac{V_b}{\alpha_c \Delta t}\left[\frac{\phi'}{B_w^n} + \phi^{n+1}\left(\frac{1}{B_w}\right)'\right] S_w{}^n \Delta_t p_o + \frac{V_b}{\alpha_c \Delta t}\left(\frac{\phi}{B_w}\right)^{n+1} \Delta_t S_w - q_{wsc}^{n+1}$$

$$\Delta\left[T_w\left(\Delta p_w - \gamma_w \Delta Z\right)\right]^{n+1} = C_{wp}\Delta_t p_w + C_{ww}\Delta_t S_w - q_{wsc}^{n+1}$$

where $C_{wp} = \frac{V_b}{\alpha_c \Delta t}\left[\frac{\phi'}{B_w^n} + \phi^{n+1}\left(\frac{1}{B_w}\right)'\right] S_w{}^n$

$$C_{ww} = \frac{V_b}{\alpha_c \Delta t}\left(\frac{\phi}{B_w}\right)^{n+1}$$

Gas:

$$\Delta\left[T_g\left(\Delta p_g - \gamma_g \Delta Z\right)\right]^{n+1} = \frac{V_b}{\alpha_c \Delta t}\left(\left[\frac{\phi(1-S_w)}{B_g}\right]^{n+1} - \left[\frac{\phi(1-S_w)}{B_g}\right]^{n}\right) - \left(q_{fgsc}\right)^{n+1}$$

$$\Delta\left[T_g\left(\Delta p_g - \gamma_g \Delta Z\right)\right]^{n+1} = \frac{V_b}{\alpha_c \Delta t}\left(\left[\frac{\phi(1-S_w)}{B_g}\right]^{n+1} - \left[\frac{\phi(1-S_w)}{B_g}\right]^{n}\right) - \left(q_{fgsc}\right)^{n+1}$$

$$\Delta\left[T_g\left(\Delta p_g - \gamma_g \Delta Z\right)\right]^{n+1} = \frac{V_b}{\alpha_c \Delta t}\left(\left[\frac{\phi'}{B_g^n} + \phi^{n+1}\left(\frac{1}{B_g}\right)'\right] S_g^n \Delta_t p_g + \left(\frac{\phi}{B_g}\right)^{n+1} \Delta_t S_g\right) - \left(q_{fgsc}\right)^{n+1}$$

$$\Delta\left[T_g\left(\Delta p_w + \Delta P_{cgo} - \gamma_g \Delta Z\right)\right]^{n+1} = C_{gp}\Delta_t p_w + C_{gg}\Delta_t S_g - q_{gsc}^{n+1}$$

where $C_{gp} = \frac{V_b}{\alpha_c \Delta t}\left(\frac{\phi'}{B_g^n} + \phi^{n+1}\left(\frac{1}{B_g}\right)'\right)(1-S_w)^n$

$$C_{gg} = \frac{V_b}{\alpha_c \Delta t}\left(\frac{\phi}{B_g}\right)^{n+1}$$

$$q_{gsc}^{n+1} = \left(q_{fgsc}\right)^{n+1}$$

IMPES Method

The objective of the IMPES method is to obtain a single pressure equation for each grid block by combining all flow equations to eliminate the saturation unknowns. By this method, capillary pressure, and transmissibilities will be evaluated explicitly (at time level *n*).

$$\Delta\left[T_w\left(\Delta p_w - \gamma_w \Delta Z\right)\right]^{n+1} = C_{wp}\Delta_t p_o + C_{ww}\Delta_t S_w - q_{wsc}^{n+1}$$

$$\frac{\Delta\left[T_w\left(\Delta p_w - \gamma_w \Delta Z\right)\right]^{n+1} - C_{wp}\Delta_t p_o + q_{wsc}^{n+1}}{C_{ww}} = \Delta_t S_w \quad \text{..... (A1)}$$

$$\Delta\left[T_g\left(\Delta p_w + \Delta P_{cgo} - \gamma_g \Delta Z\right)\right]^{n+1} = C_{gp}\Delta_t p_w + C_{gg}\Delta_t S_g - q_{gsc}^{n+1}$$

$$\frac{\Delta\left[T_g\left(\Delta p_w + \Delta P_{cgo} - \gamma_g \Delta Z\right)\right]^{n+1} - C_{gp}\Delta_t p_o + q_{gsc}^{n+1}}{C_{gg}} = \Delta_t S_g = -\Delta_t S_w \quad \text{..... (A2)}$$

Combining Eq. A1 and A2,

$$\frac{\Delta\left[T_w\left(\Delta p_w - \gamma_w \Delta Z\right)\right]^{n+1} - C_{wp}\Delta_t p_w + q_{wsc}^{n+1}}{C_{ww}} = -\frac{\Delta\left[T_g\left(\Delta p_w + \Delta P_{cgo} - \gamma_g \Delta Z\right)\right]^{n+1} - C_{gp}\Delta_t p_w + q_{gsc}^{n+1}}{C_{gg}}$$

$$B_w^{n+1}\left(\Delta\left[T_w\left(\Delta p_w - \gamma_w \Delta Z\right)\right]^{n+1} - C_{wp}\Delta_t p_w + q_{wsc}^{n+1}\right)$$

$$= -B_g^{n+1}\left(\Delta\left[T_g\left(\Delta p_w + \Delta P_{cgo} - \gamma_g \Delta Z\right)\right]^{n+1} - C_{gp}\Delta_t p_w + q_{gsc}^{n+1}\right)$$

$$\left(B_w^{n+1}\Delta\left[T_w\left(\Delta p_w - \gamma_w \Delta Z\right)\right]^{n+1} - B_w^{n+1}C_{wp}\Delta_t p_w + B_w^{n+1}q_{wsc}^{n+1}\right)$$

$$+\left(B_g^{n+1}\Delta\left[T_g\left(\Delta p_w + \Delta P_{cgo} - \gamma_g \Delta Z\right)\right]^{n+1} - B_g^{n+1}C_{gp}\Delta_t p_w + B_g^{n+1}q_{gsc}^{n+1}\right) = 0$$

$$B_w^{n+1}\Delta\left[T_w\left(\Delta p_w - \gamma_w \Delta Z\right)\right]^{n+1} + B_g^{n+1}\Delta\left[T_g\left(\Delta p_w + \Delta P_{cgo} - \gamma_g \Delta Z\right)\right]^{n+1}$$

$$= B_w^{n+1}C_{wp}\Delta_t p_w + B_g^{n+1}C_{gp}\Delta_t p_w - \left(B_w^{n+1}q_{wsc}^{n+1} + B_g^{n+1}q_{gsc}^{n+1}\right)$$

We now apply the CVFD method (CVFD is used for the expansion of the spatial-difference operator at a given gridblock-ordering scheme) and rearrange it. In a simple case, a water/gas system, assuming no gradational change,

$$\sum_{m\in\psi_n}\left\{B_{w\ n}^{n+1}T_{w\ n,m}^{n}+B_{g\ n}^{n+1}\left[T_{g\ n,m}^{n}\right]\right\}p_{w\ m}^{n+1}-\left(B_{w\ n}^{n+1}C_{wp_n}+B_{g\ n}^{n+1}C_{gp_n}+\sum_{m\in\psi_n}\left\{B_{w\ n}^{n+1}T_{w\ n,m}^{n}+B_{g\ n}^{n+1}\left[T_{g\ n,m}^{n}\right]\right\}\right)p_{w\ n}^{n+1}$$
$$=-\left[B_{w\ n}^{n+1}C_{wp_n}+B_{g\ n}^{n+1}C_{gp_n}\right]p_{w\ n}^{n}-\left[B_{w\ n}^{n+1}q_{wsc\ n}^{n}+B_{g\ n}^{n+1}q_{gsc_n}\right]-\sum_{m\in\psi_n}B_{g\ n}^{n+1}T_{g\ n,m}^{n}\left(P_{cgo\ m}^{n}-P_{cgo_n}^{n}\right)$$

Subscripts:

m is the neighboring gridblock to gridblock n

n is the study gridblock

Superscripts:

n is the old timestep

n+1 is the current timestep

$m\in\psi_n$ is the study matrix, in a simplified case, is only the x-direction

To calculate the water and gas saturation explicitly:

$$S_{w\ n}^{n+1}=S_{w_n}^{n}+\frac{1}{C_{ww_n}}\left\{\Delta\left[T_w\left(\Delta p_w-\gamma_w\Delta Z\right)\right]^{n+1}-C_{wp}\Delta_t p_w+q_{wsc}^{n+1}\right\}$$

$$S_{g\ n}^{n+1}=S_{g_n}^{n}+\frac{1}{C_{gg_n}}\left\{\Delta\left[T_g\left(\Delta p_w+\Delta P_{cgo}-\gamma_g\Delta Z\right)\right]^{n+1}-C_{gp}\Delta_t p_w+q_{gsc}^{n+1}\right\}$$

or $S_{g\ n}^{n+1}=1-S_{w\ n}^{n+1}$

To calculate the water and gas flow rates explicitly:

$$q_{wsc}^{n+1}=C_{wp}\Delta_t p_o+C_{ww}\Delta_t S_w-\Delta\left[T_w\left(\Delta p_w-\gamma_w\Delta Z\right)\right]^{n+1}$$

$$q_{gsc}^{n+1}=C_{gp}\Delta_t p_w+C_{gg}\Delta_t S_g-\Delta\left[T_g\left(\Delta p_w+\Delta P_{cgo}-\gamma_g\Delta Z\right)\right]^{n+1}$$

APPENDIX B

BLACK OIL PVT CHARACTERIZATION

A set of PVT data for oil FVF, gas/oil ratio, and oil viscosity were generated to support the multiphase black oil simulation. All the correlations were obtained in the past literature (McCain, 1993 et al.).

A case study is illustrated to get the full PVT tables

In the field, normally we can have the API for stock-tank oil gravity, solution-gas/oil ratio in the separator, reservoir temperature, separator gas specific gravity, separator temperature, and pressure as follow:

Table B1—PARAMETERS OBTAINED IN FIELD

Stock-tank oil gravity (API), ^{o}API	Separator solution-gas/oil ratio (R_{SP}), scf/STB	Reservoir temperature (T_R), ^{o}F	Separator gas specific gravity (γ_{gSP})	Separator Temperature (T_{sep}), ^{o}F	Separator Pressure (p_{sep}), psia
28.0	1500.0	220.0	0.63	60.0	114.7

Part I Solution-gas/oil PVT data evaluation

STEP 1 Calculate stock-tank solution-gas/oil ratio, R_{ST}

Define $z_n = C0_n + C1_n VAR_n + C2_n VAR_N^2$;

all the coefficients are given in Table B2.

Table B2—COEFFICIENTS USED TO CALCULATE Z_N FOR R_{ST}					
n	VAR	C0	C1	C2	z_n
1	ln p_{SP}	-8.005	2.7	-0.161	1.178
2	ln T_{SP}	1.224	-0.5	0	-0.823
3	API	-1.587	0.0441	-1.29×10^{-5}	-1.440

$$z = \sum_{n=1}^{3} z_n = -1.085$$

$$\ln R_{ST} = 3.955 + 0.83z - 0.024z^2 + 0.075z^3 = 2.970$$

$$R_{ST} = 19.498 \text{ scf/STB}$$

STEP 2 Calculate the solution-gas/oil ratio at bubblepoint pressure R_{Sb}

$$R_{sb} = R_{ST} + R_{SP} = 1519.499 \text{ scf/STB}$$

STEP 3 Calculate the stock-tank gas gravity, γ_{gST}

$$z_n = C0_n + C1_n VAR_n + C2_n VAR_N^2 + C3_n VAR_N^3 + C4_n VAR_N^4$$

Table B3—COEFFICIENTS USED TO CALCULATE γ_{gST}							
n	VAR	C0	C1	C2	C3	C4	z_n
1	ln p_{sp}	-17.275	7.9597	-1.1013	2.7735×10^{-2}	3.2287×10^{-3}	0.296
2	ln R_{SP}	-0.3354	-0.3346	0.1956	-3.4374×10^{-2}	2.08×10^{-3}	0.184
3	API	3.705	-0.4273	-1.818×10^{-2}	-3.459×10^{-4}	2.505×10^{-6}	-5.976×10^{-2}
4	γ_{gSP}	-155.52	629.61	-957.38	647.57	-163.26	-2.645
5	ln T_{sp}	2.085	-7.097×10^{-2}	9.859×10^{-4}	-6.312×10^{-6}	1.4×10^{-8}	1.811

$$z = \sum_{n=1}^{3} z_n = \text{-}0.415$$

$$\gamma_{gST} = 1.219 + 0.198z + 0.0845z^2 + 0.03z^3 + 0.003z^4 = 1.149$$

STEP 4 Calculate the weight average gas gravity, γ_g

$$\gamma_g = \frac{\gamma_{gSP} R_{SP} + \gamma_{gST} R_{ST}}{R_{SP} + R_{ST}} = 0.6367$$

STEP 5 Calculate the bubble-point pressure[1]

$$z_n = C0_n + C1_n VAR_n + C2_n VAR_N^2 + C3_n VAR_N^3$$

$$z = \sum_{n=1}^{3} z_n = 2.007$$

$$\ln p_b = 7.475 + 0.713z + 0.0075z^2 = 8.936$$

Table B4—COEFFICIENTS USED TO CALCULATE P_B

n	VAR	C0	C1	C2	C3	z_n
1	ln R_{sb}	-5.48	-0.0378	0.281	-0.0206	1.225
2	API	1.27	-0.0449	4.36×10^{-4}	-4.76×10^{-6}	0.250
3	γ_{gSP}	4.51	-10.84	8.39	-2.34	0.426
4	T_R	-0.7835	6.23×10^{-3}	-1.22×10^{-5}	1.03×10^{-8}	0.106

$p_b = 7602.001$ psia

STEP 6 Calculate the oil density at the bubble-point pressure, ρ_{oRb}

Table B5—INPUT PARAMETERS TO CALCULATE ρ_{oRb}				
Stock-tank oil gravity (API), °API	Separator gas specific gravity (γ_{gSP})	Reservoir temperature (T_R), °F	Bubblepoint pressure (p_b), psia	Solution-gas/oil ratio at p_b (R_{Sb}), scf/STB
28.0	0.63	220.0	7602.001	1519.499

$$p_a = 38.52\times10^{-0.00326\,API} + (94.75 - 33.93\log API)\log\gamma_{gSP} = 22.058\,lb/cuft$$

$$\gamma_{STO} = \frac{141.5}{API + 131.5} = 0.887$$

$$\rho_{po} = \frac{R_{sb}\gamma_{gSP} + 4600\,\gamma_{STO}}{73.71 + R_{sb}\gamma_{gSP}/\rho_a} = 43.022\,lb/cuft$$

$$\Delta\rho_p = \left(0.167 + 16.181\times10^{-0.0425\rho_{po}}\right)\left(\frac{p_b}{1000}\right) - 0.01\left(0.299 + 263\times10^{-0.0603\rho_{po}}\right)\left(\frac{p_b}{1000}\right)^2$$
$$= 2.536\,lb/cuft$$

$$\rho_{bs} = \rho_{po} + \Delta\rho_p = 45.558\,lb/cuft$$

$$\Delta\rho_T = \left(0.00302 + 1.505\rho_{bs}^{-0.951}\right)(T_R - 60) - \left(0.0216 - 0.0233\times10^{-0.0161\rho_{bs}}\right)(T_R - 60)^{0.475}$$
$$= 4.813\,lb/cuft$$

$$\rho_{oRb} = \rho_{bs} - \Delta\rho_T = 40.745\,lb/cuft$$

STEP 7 Calculate the oil FVF at the bubblepoint pressure, B_{ob}

Table B6—INPUT PARAMETERS TO CALCULATE B_{OB}			
Stock-tank oil gravity (API), °API	Solution-gas/oil ratio at p_b (R_{Sb}), scf/STB	Weighted average gas specific gravity (γ_g)	oil density at p_b (ρ_{oRb}), lb/cu-ft
28.0	1519.499	0.6367	40.745

$$\gamma_{STO} = \frac{141.5}{API + 131.5} = 0.887$$

$$\rho_{STO} = 62.368\gamma_{STO} = 55.330 lb/cuft$$

$$Bob = \frac{\rho_{STO} + 0.01357 R_{Sb}\gamma_g}{\rho_{oRb}} = 1.680 \frac{resbbl}{STB}$$

STEP 8 Calculate the oil viscosity at the bubble-point pressure, μ_{ob}[4]

Table B7—INPUT PARAMETERS TO CALCULATE μ_{ob}			
Stock-tank oil gravity (API), °API	Reservoir temperature (T_R), °F	Solution-gas/oil ratio at p_b (R_{Sb}), scf/STB	Bubblepoint pressure (p_b), psia
28.0	220.0	1519.499	7602.001

$$A = 10.715\left(R_{Sb} + 100\right)^{-0.515} = 0.238$$

$$B = 5.44\left(R_{Sb} + 150\right)^{-0.338} = 0.443$$

$$\log\log(\mu_{oD} + 1) = 1.8653 - 0.025086 API - 0.5644 \log T_R = -0.159$$

$$\mu_{oD} = 3.933$$

$$\mu_{ob} = A \times \mu_{oD}{}^{B} = 0.437 cp$$

STEP 9 Calculate the solution oil-gas ratio at interest point, R_S

Table B8—INPUT PARAMETERS TO CALCULATE R_S					
Solution-gas/oil ratio at p_b (R_{Sb}), scf/STB	Stock-tank oil gravity (API), °API	Separator gas specific gravity (γ_{gSP})	Reservoir temperature (T_R), °F	Bubblepoint pressure (p_b), psia	Pressure interested, psi
1519.499	28.0	0.63	220.0	7602.001	p(i)

If the pressure at the interest point is below the bubblepoint pressure, the solution-gas/oil ratio is as same as the solution-gas/oil ratio at the bubble-point pressure; otherwise, the calculation is performed as the following by the *Velarde et.al.* method (1999).

$$z_n = A\gamma_{gSP}^{B} API^{C} T_R^{D} \left(p_b - 14.7\right)^{E}$$

Table B9—COEFFICIENTS USED TO CALCULATE R_S

n	A	B	C	D	E
1	9.73×10^{-7}	1.672608	0.929870	0.247235	1.056052
2	0.022339	-1.00475	0.337711	0.132795	0.302065
3	0.725167	-1.48548	-0.164741	-0.091330	0.047094

$$p_r = \frac{p(i) - 14.7}{p_b - 14.7}$$

$$R_{Sr} = z_1 p_r^{\,z_2} + \left(1 - z_1\right) p_r^{\,z_3}$$

$$R_S(i) = R_{Sb} \cdot R_{Sr}$$

Study the solution-gas/oil ratio corresponding to the pressure range from 14.7 to 14000 psia, and the "Rs vs. p" plot is shown in **Fig. B1**.

STEP 10 Calculate the oil FVF at interest point, B_o

Table B10—INPUT PARAMETERS TO CALCULATE B_o

Stock-tank oil gravity (API), °API	Weighted avg. gas SG (γ_g)	Reservoir temperature (T_R), °F	Bubble-point pressure (p_b), psia	Oil FVF at p_b (B_{ob}), res-bbl/STB	Solution-gas/oil ratio at p_b (R_{Sb}), scf/STB	Separator gas specific gravity (γ_{gSP})
28.0	0.6367	220.0	7602.001	1.680	1519.5	0.63

If the pressure at the interest point is above the bubblepoint pressure,

$$B_o(i) = B_{ob} \times EXP\left[c_{ofb}\left(p_b - p\right)\right]$$

C_{ofb} can be obtained following Spivey et al. method[6].

Table B11—COEFFICIENTS USED TO CALCULATE C_{ofb}

n	x	$C_{0,n}$	$C_{1,n}$	$C_{2,n}$
1	ln °API	3.011	-2.6254	0.497
2	ln γ_{gSP}	-0.0835	-0.259	0.382
3	ln p_b	3.51	-0.0289	-0.0584
4	ln p/p_b	0.327	-0.608	0.0911
5	ln R_{Sb}	-1.918	-0.642	0.154
6	ln T_R	2.52	-2.73	0.429

$$z_n = C_{0,n} + C_{1,n}x_n + C_{2,n}x_n^2$$

$$z = \sum_{n=1}^{6} z_n$$

$$\ln\left(c_{ofb}(i)\times 10^6\right) = 2.434 + 0.475z + 0.048z^2$$

$$c_{ofb}(i) = EXP\left(2.434 + 0.475z + 0.048z^2\right)\times 10^{-6}$$

Now, the oil FVF above the bubblepoint can be calculated.

If the pressure at the interest point is below the bubblepoint pressure, the first step is to calculate the ρ_{oRb} following the similar procedures in Step 6, and the second step is to calculate oil FVF following the similar procedures in Step 7.

Calculate the $\rho_{oRb}(i)$ at the pressure of interest:

$$p_a = 38.52\times 10^{-0.00326\,API} + \left(94.75 - 33.93\log API\right)\log\gamma_{gSP}$$

$$\gamma_{STO} = \frac{141.5}{API + 131.5} = 0.887$$

$$\rho_{po} = \frac{R_{sb}\gamma_{gSP} + 4600\gamma_{STO}}{73.71 + R_{sb}\gamma_{gSP}/\rho_a} = 43.022 lb/cuft$$

$$\Delta\rho_p = \left(0.167 + 16.181\times10^{-0.0425\rho_{po}}\right)\left(\frac{p}{1000}\right) - 0.01\left(0.299 + 263\times10^{-0.0603\rho_{po}}\right)\left(\frac{p}{1000}\right)^2$$

$$\rho_{bs} = \rho_{po} + \Delta\rho_p$$

$$\Delta\rho_T = \left(0.00302 + 1.505\rho_{bs}^{-0.951}\right)\left(T_R - 60\right) - \left(0.0216 - 0.0233\times10^{-0.0161\rho_{bs}}\right)\left(T_R - 60\right)^{0.475}$$

$$\rho_{oRb}(i) = \rho_{bs} - \Delta\rho_T / cuft$$

Calculate the B_o at pressure of interest:

$$B_o(i) = \frac{\rho_{STO} + 0.01357 R_{Sb}\gamma_g}{\rho_{oRb}(i)}$$

From the oil FVF corresponding to the pressure range from 14.7 to 14,000 psia, the "B_o vs. p" plot is shown in **Fig. B2**. Also, from the oil density corresponding to the pressure range from 14.7 to 14,000 psia, the "ρ_o vs. p" plot is shown in **Fig. B3**. Also, from the oil compressibility corresponding to the pressure range from 14.7 to 14,000 psia, the "c_o vs. p" plot is shown in **Fig. B4**.

STEP 11 Calculate the oil viscosity at interest point, μ_o

Table B12—INPUT PARAMETERS TO CALCULATE μ_o

Stock-tank oil gravity (API), °API	Reservoir temperature (T_R), °F	Solution-gas/oil ratio at p_b (R_{Sb}), scf/STB	Bubblepoint pressure (p_b), psia	Oil Viscosity at p_b (μ_o), cp
28.0	220.0	1519.499	7602.001	0.437

If the pressure at the interest point is above the bubblepoint pressure,

$$D = 2.6 p^{1.187} EXP\left(-11.513 - 8.98 \times 10^{-5} p\right)$$

$$\mu_o(i) = \mu_{ob} \left(p / p_b\right)^D$$

If the pressure at the interest point is below the bubblepoint pressure, the oil viscosity can be calcualted following the same procedure as STEP 8.

$$A = 10.715\left(R_S + 100\right)^{-0.515}$$

$$B = 5.44\left(R_S + 150\right)^{-0.338}$$

$$\log\log(\mu_{oD} + 1) = 1.8653 - 0.025086 API - 0.5644 \log T_R$$

$$\mu_{oD} = EXP\left(EXP\left(1.8653 - 0.025086 API - 0.5644 \log T_R\right)\right) - 1$$

$$\mu_o(i) = A \times {\mu_{oD}}^B$$

From the oil FVF corresponding to the pressure range from 14.7 to 14,000 psia, the "B_o vs. p" plot is shown in **Fig. B5**.

PART II Gas PVT data evaluation

STEP 12 Calculate the gas compressibility z-factor at interest point, z (Piper et al. 1993) In this study, as the hydrocarbon composition of the reservoir gas is unknown, the SBV parameters *J* and *K* are obtained based on the non-hydrocarbon mole percentage in the gas. γ_g is obtained in the previous Step 4.

$$J = \alpha_o + \sum_{i=1}^{3} \alpha_i y_i \left(\frac{T_C}{p_C} \right)_i + \alpha_4 \gamma_g + \alpha_5 \gamma_g^2$$

$$K = \alpha_o + \sum_{i=1}^{3} \beta_i y_i \left(\frac{T_C}{\sqrt{p_C}} \right)_i + \beta_4 \gamma_g + \beta_5 \gamma_g^2$$

Table B13—COEFFICIENTS USED TO CALCULATE SBV PARAMETERS *J* AND *K*

i	Non-hydrocarbon Components	α_i	β_i
0	————	0.11582	3.8216
1	H_2S	-0.45820	-0.065340
2	CO_2	-0.90348	-0.42113
3	N_2	-0.66025	-0.91249
4	————	0.70729	17.438
5	————	-0.099397	-3.2191

$$T_{pc} = \frac{K^2}{J} \qquad P_{pc} = \frac{K^2}{J^2}$$

$$T_{pr} = \frac{T}{T_{pc}} \text{ (unit: }^{o}\text{R)} \qquad p_{pr} = \frac{p}{p_{pc}} \text{ (unit: psia)}$$

$$\rho_{pr} = \frac{0.27\, p_{pr}}{z(i) \cdot T_{pr}}$$

As illustrated, the above equation also includes z-factor, so it is an iteration process.

$$z(i) = 1 + \left(0.3265 - 1.0700/T_{pr} - 0.5339/T_{pr}^3 + 0.01569/T_{pr}^4 - 0.05165/T_{pr}^5\right)\rho_{pr}$$
$$+ \left(0.5475 - 0.7361/T_{pr} + 0.1844/T_{pr}^2\right)\rho_{pr}^2 - 0.1056\left(-0.7361/T_{pr} + 0.1844/T_{pr}^2\right)\rho_{pr}^5$$
$$+ 0.6134\left(1 + 0.7210\rho_{pr}^2\right)\left(\rho_{pr}^2/T_{pr}^3\right)EXP\left(-0.7210\rho_{pr}^2\right)$$

From the gas z-factor corresponding to the pressure range from 14.7 to 9,000 psia, the "*z*-factor vs. *p*" plot is shown in **Fig. B6**.

STEP 13 Calculate the gas formation volume factor at interest point, B_g

$$B_g(i) = \frac{1}{5.615}\frac{p_{SC}}{(T_{SC} + 459.67)}\frac{z(i) \cdot p}{(T + 459.67)}$$

Where p_{SC} = 14.65 psia and T_{SC} = 60.0 ^{o}F.

B_g is in the unit of res-bbl/scf.

From the gas z-factor corresponding to the pressure range from 14.7 to 9000 psia, and the "B_g vs. p" plot is shown in **Fig. B7**.

STEP 14 Calculate the gas viscosity at interest point, μ_g.

Since γ_g is obtained in the previous Step 4, the gas average molecular weight is,

$$M = 29\gamma_g$$

The gas density is calculated as

$$\rho_g(\mathrm{i}) = \frac{\mathrm{pM}}{10.732 \cdot z(i) \cdot (\mathrm{T} + 459.67)}$$

Then the viscosity at the interest point is calculated following the LGE method. The required unit for temperature is Rankine and for density is gram/cubic-centimeter.

$$\mu_g(i) = 10^{-4} A \times EXP\left(B \cdot \rho_g^C\right)$$

Where

$$A = \frac{(9.379 + 0.01607M)(T + 459.67)^{1.5}}{209.2 + 19.26M + (T + 459.67)}$$

$$B = 3.448 + \frac{986.4}{(T + 459.67)} + 0.01009M$$

$$C = 2.447 - 0.2224B$$

ρ_g is converted from pound/cu-ft to gram/cubic-centimeter.

$$\frac{lb}{cu - fu} \frac{1}{62.42796} = \frac{g}{cc}$$

From the gas viscosity corresponding to the pressure range from 14.7 to 9,000 psia, the "ρ_g vs. p" plot is shown in **Fig. B8**. From the gas viscosity corresponding to the pressure range from 14.7 to 9,000 psia, the "μ_g vs. p" plot is shown in **Fig. B9**.

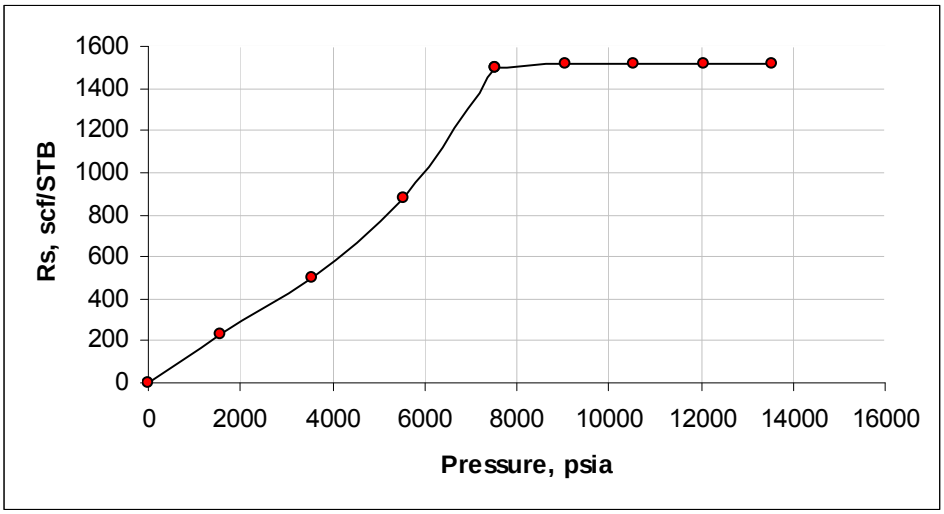

Fig. B1— Rs vs. p.

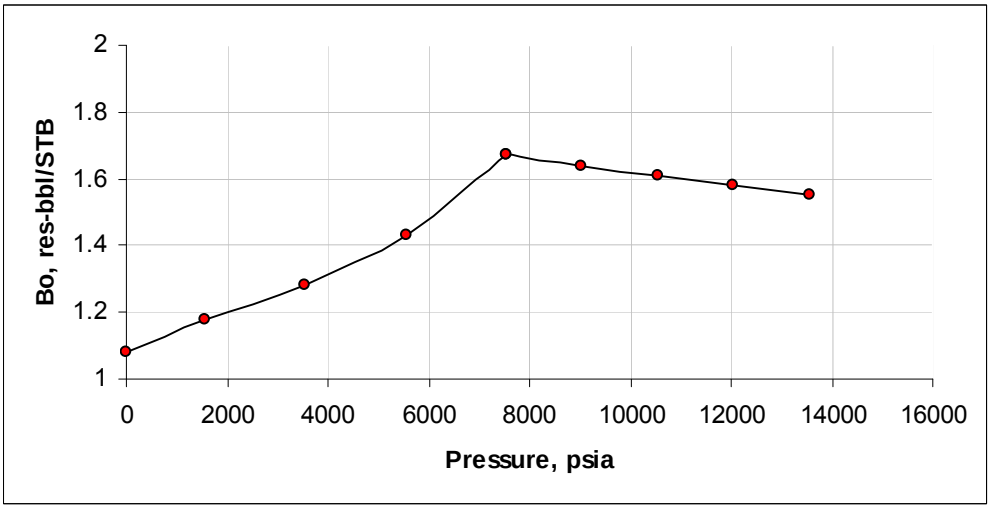

Fig. B2— Oil FVF vs. p.

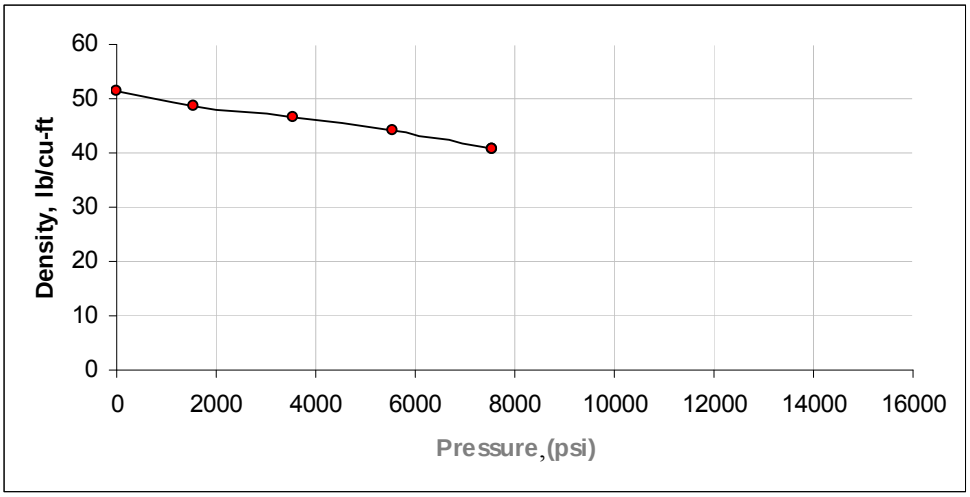

Fig. B3— Oil density vs. p

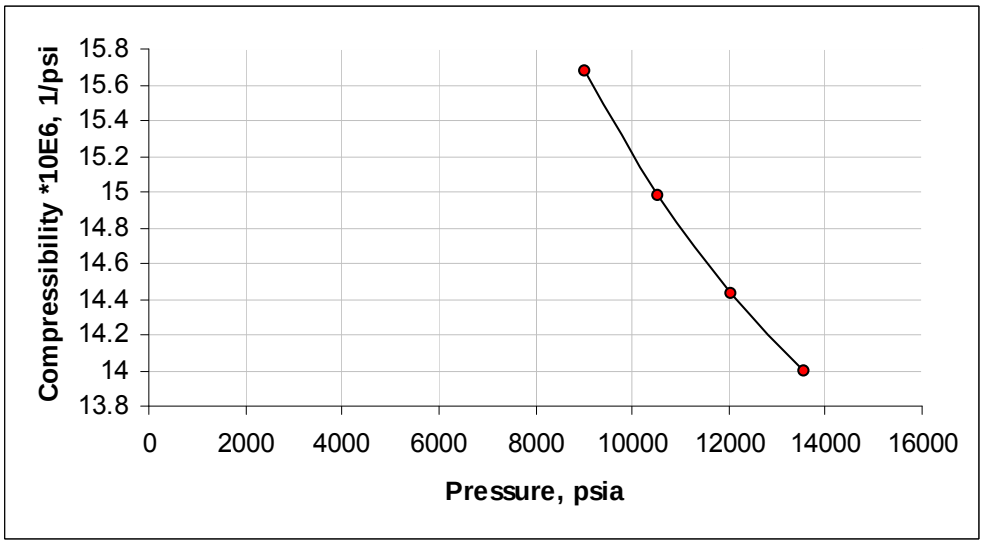

Fig. B4— Oil Compressibility vs. p.

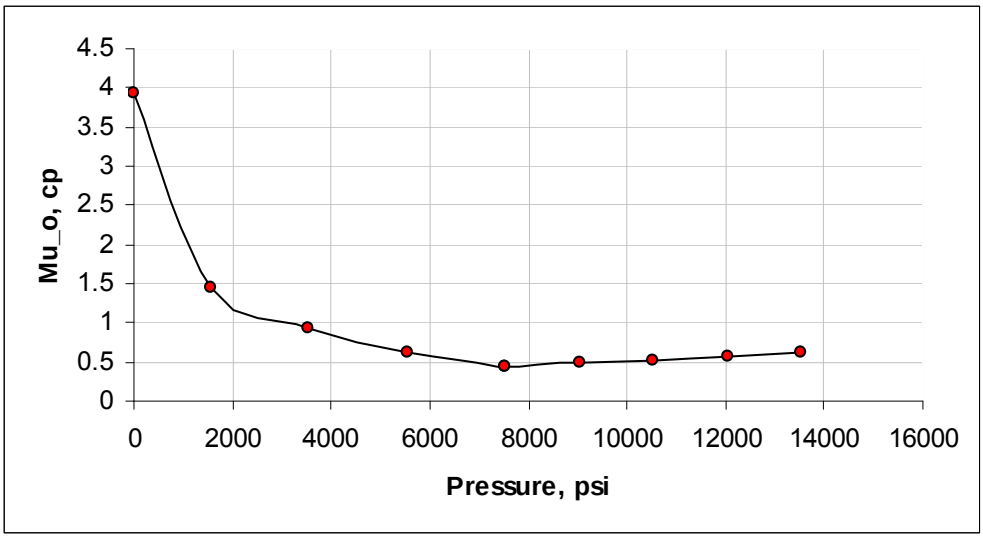

Fig. B5— Oil viscosity vs. p.

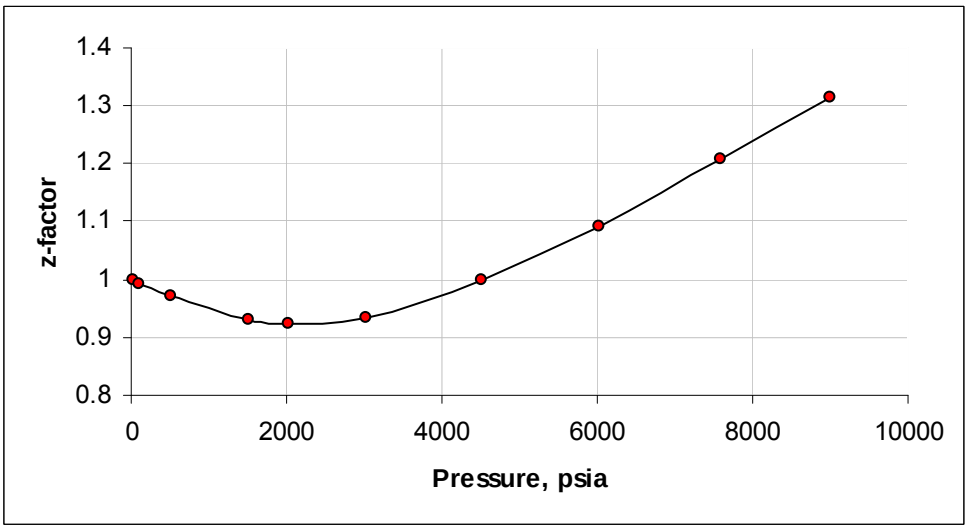

Fig. B6— z-factor vs. p.

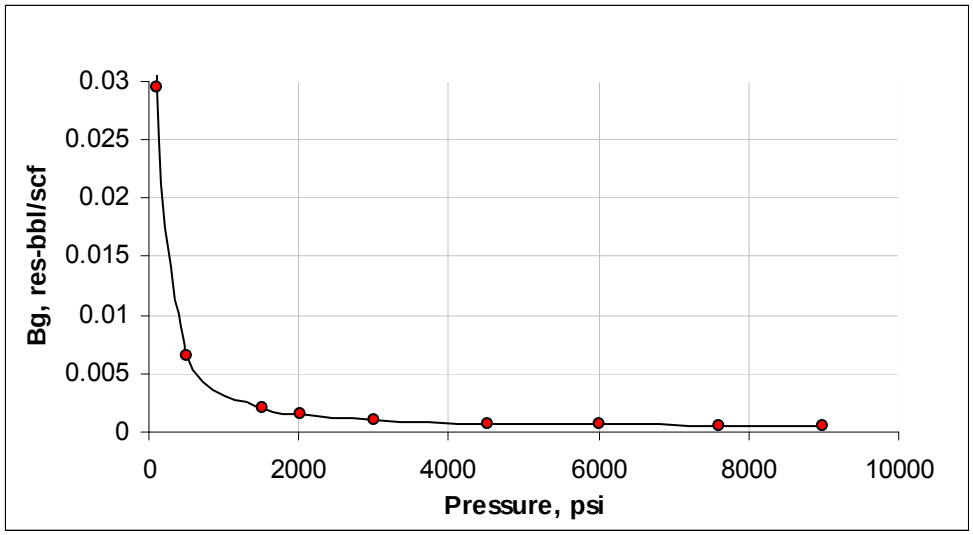

Fig. B7—Gas FVF vs. p.

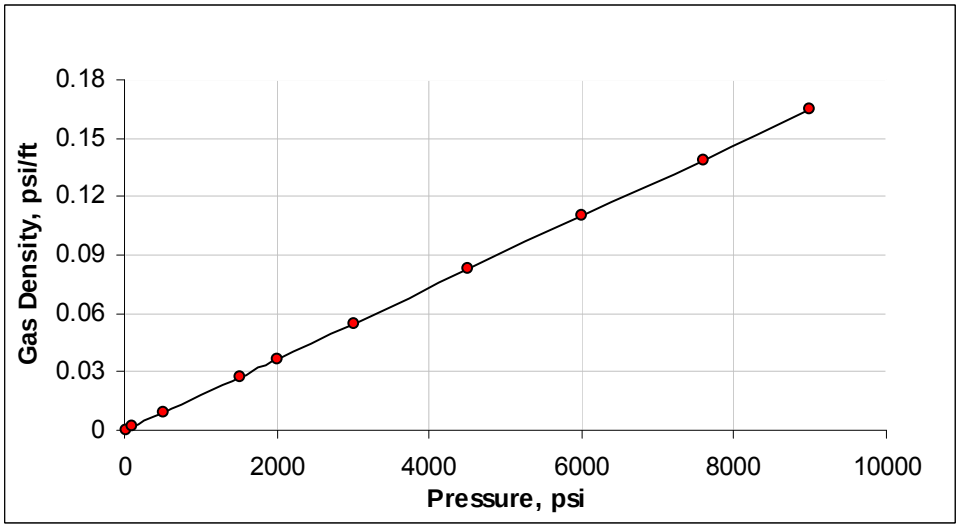

Fig. B8— Gas density vs. p.

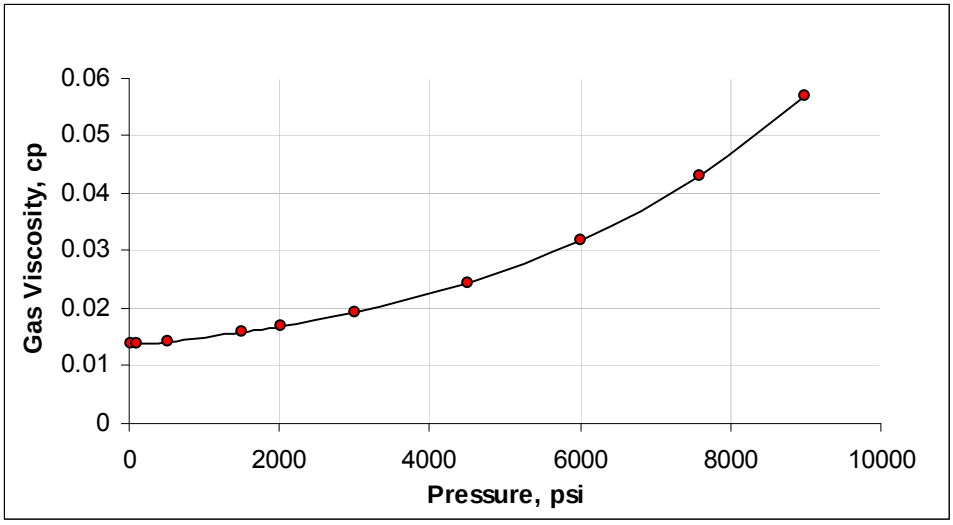

Fig. B9— Gas viscosity vs. p.

APPENDIX C

SOFTWARE STRUCTURE

Currently this simulator includes these files:

- GSSimulator.F90 – main program
- Input.F90 – defines case dimension, initial flow rate, connate water saturation and some constants etc.
- Sched.F90 – the dynamic simulation schedule
- FORMAT.FI – the output standards
- Memory_Allocate.F90 – allocate memories for the required variables
- GBAND.for – solve the linear equation
- IMPES_Newton.F90 – IMPES (forward) module
- Init.F90 – initializes petrophysical parameters, like porosity, permeability, define gridblocks etc.
- MB_chk.F90 – material balance check module
- Pipe.F90 – wellbore module (forwarded from Tobias and Barbosa at UFSC, Brazil)
- Print_Screen.F90 – outputs on screen
- PVT_BO.F90 – blackoil PVT Characterization
- PVT_updates.F90 – PVT explicitly updates module
- Recover.F90 - records the last stabilized solution in the previous timestep. If the current timestep is too large to get a stabilized IMPES solution, the program will adjust the timestep and running simulation from this point.
- Sat_rate_updates.F90 – updates the saturation and rates explicitly (out of the Newton iteration).
- Solver.F90 – identifies the different boundary conditions and formulates the linear equation.

- Stab_sol.F90 – saves the last stabilized solution in the previous timestep. If the current timestep is too large to get a stabilized IMPES solution, the program adjusts the timestep and running simulation from this point.
- Utils.F90 – various utility functions
- Readme.txt – self-introduction

Fig. C1 illustrates the software structure in debugging model.

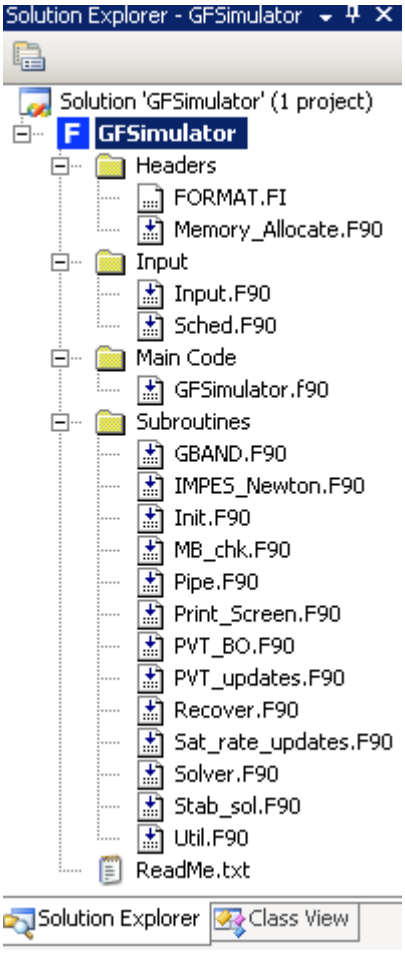

Fig.C1 – Software structure view in Visual Studio (Version Dec. 2009)

APPENDIX D

HOMOGENEOUS FLOW IN THE WELLBORE

Although this work mainly focused on modeling multiphase flow in the near-wellbore region, a mechanistic model for modeling homogeneous flow in the wellbore was also built in VBA as a parallel study.

Homogeneous flow means the velocities of the two phases are identical, and this implies

$$u_G = u_L = u_H , \quad \text{.....(D.1)}$$

$$S = \frac{u_G}{u_L} = 1, \quad \text{.....(D.2)}$$

$$\varepsilon_G = \frac{W_G}{W_G + W_L} = \frac{x}{x + (1-x)\rho_G / \rho_L} \quad \text{.....(D.3)}$$

where W is the volumetric flow rate, m^3 / s, and x is the quality.

$$\rho_{TP} = \rho_H = \frac{\rho_G \rho_L}{x\rho_L + (1-x)\rho_G}, \quad \text{.....(D.4)}$$

where ρ_{TP} is the two-phase density and ρ_H is the homogeneous density.

Conservation Equations

Conservation of Mass

The derivations for the diffusivity equation are consistently in SI units through this chapter. Each intermediate equation will be verified by the unit check.

We start with the mass balance equation as the rate of mass creation equal to the outflow rate minus the inflow rate, and plus the storage rate, in Eq. D.5.

$$0=\left[j\rho_H A+\delta z\frac{\partial}{\partial z}\left(j\rho_H A\right)\right]-j\rho_H A+A\delta z\frac{\partial \rho_H}{\partial t} \quad \text{.....} \quad \text{(D.5)}$$

where j is the total volume flux, given by $j=\frac{W_G+W_L}{A}=U_G+U_L$, in the unit of $\frac{m^3}{m^2\cdot s}$ or m/s equally.

We rearrange Eq. D.5,

$$\delta z\frac{\partial}{\partial z}\left(j\rho_H A\right)+A\delta z\frac{\partial \rho_H}{\partial t}=0 \quad \text{.....(D.6)}$$

The right-hand-side (RHS) has dimensionless units, and the left-hand-side (LHS) has two terms. We perform the unit check successfully.

$$m\frac{\frac{m^3}{m^2\cdot s}\frac{kg}{m^3}m^2}{m}+m^2 m\frac{\frac{kg}{m^3}}{s}\Rightarrow\frac{kg}{s}+\frac{kg}{s} \quad \text{.....(D.7)}$$

Conservation of Momentum

Momentum is the effect of motion; the SI unit is

$$kg \cdot \frac{m}{s} = \frac{N}{\frac{m}{s^2}} \frac{m}{s} = N \cdot s \,. \quad \text{.....(D.8)}$$

So the SI unit for momentum rate is Newton, *N*.

The momentum term in the center portion is equal to the sum of forces acting on the study object. For momentum conservation, the sum of forces acting on a control volume is equal to the momentum outflow rate minus the momentum inflow rate, and plus the momentum storage rate, as in Eq. D.9.

$$GjA + \delta z \frac{\partial}{\partial z}(GjA) - \dot{m}jA + \frac{\partial}{\partial t}(GA\delta z) = p \cdot A - \left(p + \delta z \frac{\partial p}{\partial z} \right) \cdot A - \rho_H g A \delta z \cdot \sin\alpha - \tau_0 \delta z P$$

..... (D.9)

where G is the mass flux in the unit of $\frac{kg}{m^2 \cdot s}$; j is the total volume flux in the unit of $\frac{m^3}{m^2 \cdot s}$; A is the channel cross-section area in the unit of m^2; and P is the channel perimeter in the unit of m .

We perform the unit check successfully.

$$LHS: \frac{kg}{m^2 \cdot s} \frac{m^3}{m^2 \cdot s} m^2 + m \frac{\frac{kg}{m^2 \cdot s} \frac{m^3}{m^2 \cdot s} m^2}{m} - \frac{kg}{m^2 \cdot s} \frac{m^3}{m^2 \cdot s} m^2 + \frac{\frac{kg}{m^2 \cdot s} m^2 \cdot m}{s}$$

$$= \frac{kg \cdot m}{s^2} + \frac{kg \cdot m}{s^2} - \frac{kg \cdot m}{s^2} + \frac{kg \cdot m}{s^2} = N + N - N + N$$

.....(D.10)

$$RHS: Pa \cdot m^2 - \left(Pa + m \cdot \frac{Pa}{m} \right) \cdot m^2 - \frac{kg}{m^3} \frac{m}{s^2} m^2 \cdot m - \frac{N}{m^2} m \cdot m$$

$$= N - (N + N) - kg \frac{m}{s^2} - N = N - (N + N) - N - N$$

…… (D.11)

Using G to represent $\dot{m}$, Eq. D.9 can be simplified as,

$$\delta z \frac{\partial (GjA)}{\partial z} + \frac{\partial (GA\delta z)}{\partial t} = -\left(\delta z A \frac{\partial p}{\partial z} \right) - \rho_H g A \delta z \cdot \sin\alpha - \tau_0 \delta z P \, .$$

……..(D.12)

Bringing $G = \rho_H j \Rightarrow j = \frac{G}{\rho_H}$ into Eq. D.12,

$$\delta z \frac{\partial \left(\frac{G^2}{\rho_H} A \right)}{\partial z} + \frac{\partial (GA\delta z)}{\partial t} = -\left(\delta z A \frac{\partial p}{\partial z} \right) - \rho_H g A \delta z \cdot \sin\alpha - \tau_0 \delta z P$$

$$\delta z \frac{\partial \left(\frac{G^2}{\rho_H} A \right)}{\partial z} + \delta z \frac{\partial (GA)}{\partial t} + GA \frac{\partial (\delta z)}{\partial t} = -\left(\delta z A \frac{\partial p}{\partial z} \right) - \rho_H g A \delta z \cdot \sin\alpha - \tau_0 \delta z P$$

……(D.13)

Assuming $\frac{\partial (\delta z)}{\partial t}$ is negligible, and we remove the terms including this second derivative,

$$\delta z \frac{\partial \left(\frac{G^2}{\rho_H} A \right)}{\partial z} + \delta z \frac{\partial (GA)}{\partial t} = -\left(\delta z A \frac{\partial p}{\partial z} \right) - \rho_H g A \delta z \cdot \sin\alpha - \tau_0 \delta z P$$

……..(D.14)

divide it by δz,

$$\frac{\partial\left(\frac{G^2}{\rho_H}A\right)}{\partial z}+\frac{\partial(GA)}{\partial t}=-\left(A\frac{\partial p}{\partial z}\right)-\rho_H gA\cdot\sin\alpha-\tau_0 P \quad \text{.....(D.15)}$$

and take out the constant cross-section area, A,

$$\frac{1}{A}\frac{\partial\left(G\frac{G}{\rho_H}A\right)}{\partial z}+\frac{1}{A}\frac{\partial(GA)}{\partial t}=-\left(\frac{\partial p}{\partial z}\right)-\rho_H g\cdot\sin\alpha-\frac{\tau_0 P}{A} \quad \text{.....(D.16)}$$

because in the "no-slip" model,

$$G=\frac{W}{A}, \quad \text{.....(D.17)}$$

where W is constant along the wellbore.

Now Eq. D.16 can be converted to Eq. D.18,

$$\frac{1}{A}\frac{\partial\left(W\frac{G}{\rho_H}\right)}{\partial z}+\frac{1}{A}\frac{\partial(GA)}{\partial t}=-\left(\frac{\partial p}{\partial z}\right)-\rho_H g\cdot\sin\alpha-\frac{\tau_0 P}{A} \quad \text{.....(D.18)}$$

More, we define the mixture velocity v_M, in the unit of m/s,

$$v_M=\frac{G}{\rho_H} \quad \text{.....(D.19)}$$

Eq. D.18 can be derived and rearranged as,

$$\frac{W}{A}\frac{\partial v_M}{\partial z}+\frac{1}{A}\frac{\partial(GA)}{\partial t}=-\left(\frac{\partial p}{\partial z}\right)-\rho_H g\cdot\sin\alpha-\frac{\tau_0 P}{A}$$

$$\left(\frac{\partial p}{\partial z}\right)=-\left[\frac{W}{A}\frac{\partial v_M}{\partial z}+\frac{1}{A}\frac{\partial(GA)}{\partial t}\right]-\rho_H g\cdot\sin\alpha-\frac{\tau_0 P}{A} \quad \text{……(D.20)}$$

For steady-state flow, $\frac{\partial(GA)}{\partial t}$ is zero, and Eq. D.20 is further reduced to,

$$-\left(\frac{\partial p}{\partial z}\right)=\frac{W}{A}\frac{\partial v_M}{\partial z}+\rho_H g\cdot\sin\alpha+\frac{\tau_0 P}{A}. \quad \text{……(D.21)}$$

By convention, a minus sign is used for pressure drop terms,

$$-\left(\frac{dp}{dz}\right)=-\frac{dp_a}{dz}-\frac{dp_g}{dz}-\frac{dp_F}{dz}. \quad \text{……(D.22)}$$

Diffusivity Equations for the Single Gas Flow in Wellbore

From the mass balance Eq. D.6,

$$\delta z\frac{\partial}{\partial z}(j\rho_H A)+A\delta z\frac{\partial\rho_H}{\partial t}=0 \quad \text{……(D.6)}$$

Assuming δz and cross-section ducts, A, are constants, Eq. D.5 can be simplified as,

$$\frac{\partial}{\partial z}(j\rho_H)+\frac{\partial\rho_H}{\partial t}=0 \quad \text{……(D.23)}$$

Bringing $G = \rho_H j \Rightarrow j = \dfrac{G}{\rho_H}$ into Eq. D.23,

$$\frac{\partial}{\partial z}\left(\frac{G}{\rho_H}\rho_H\right) + \frac{\partial \rho_H}{\partial t} = 0$$

$$\frac{\partial G}{\partial z} + \frac{\partial \dfrac{\overline{m}}{\overline{V}}}{\partial t} = 0 \Rightarrow \frac{\partial G}{\partial z} + \frac{\partial \dfrac{1}{\dfrac{zRT}{p}}}{\partial t} = 0 \quad \text{.....(D.24)}$$

Assuming unit volume and ideal gas $\overline{m} = 1$ and $\overline{V} = \dfrac{zRT}{p}$ obtains

$$\frac{1}{ZRT}\frac{\partial p}{\partial t} + \frac{\partial G}{\partial z} = 0 \quad \text{.....(D.25)}$$

Unit Check:

$$\frac{1}{Pa \cdot m^3}\frac{Pa \cdot kg}{s} + \frac{\dfrac{kg}{m^2 \cdot s}}{m} = \frac{kg}{m^3 \cdot s} + \frac{kg}{m^3 \cdot s} \quad \text{.....(D.26)}$$

Replacing $\dot{m}$ with G, the first diffusivity equation is obtained,

$$\frac{1}{ZRT}\frac{\partial p}{\partial t} + \frac{\partial G}{\partial z} = 0 \quad \text{.....(D.27)}$$

From conservation of momentum under unsteady-state conditions, Eq. D.21,

$$\left(\frac{\partial p}{\partial z}\right) = -\left[\frac{W}{A}\frac{\partial v_M}{\partial z} + \frac{1}{A}\frac{\partial (GA)}{\partial t}\right] - \rho_H g \cdot \sin\alpha - \frac{\tau_0 P}{A} \quad \text{.....(D.21)}$$

The acceleration pressure-gradient term under steady-state flow is zero.

$$\frac{\partial(GA)}{\partial t} = 0 \quad \text{.....(D.28)}$$

So Eq. D.21 is further derived as Eq. D.29,

$$-\left(\frac{\partial p}{\partial z}\right) = \frac{W}{A}\frac{\partial v_M}{\partial z} + \rho_H g \cdot \sin\alpha + \frac{\tau_0 P}{A} \quad \text{.....(D.29)}$$

Considering the term of acceleration pressure drop, $-\frac{dp_a}{dz}$,

$$-\frac{dp_a}{dz} = G\frac{\partial v_M}{\partial z} = G\frac{\partial\left(\frac{W}{A\rho}\right)}{\partial z} = GW\frac{\partial\left(\frac{1}{A\rho}\right)}{\partial z} = G^2 A\frac{\partial\left(\frac{1}{A\rho}\right)}{\partial z} = G^2 A\frac{1}{A}\frac{\partial\left(\frac{1}{\rho}\right)}{\partial z} + G^2 A\frac{1}{\rho}\frac{\partial\left(\frac{1}{A}\right)}{\partial z}$$

$$= G^2\frac{\partial\left(\frac{1}{\rho}\right)}{\partial z} + G^2 A\frac{1}{\rho}\left[-\left(\frac{1}{A}\right)^2\right]\frac{\partial A}{\partial z} = G^2\frac{\partial}{\partial z}\left(\frac{1}{\rho}\right) - \frac{G^2}{\rho}\frac{1}{A}\frac{\partial A}{\partial z} \quad \text{..... (D.30)}$$

From the very beginning, the fluid density at the wellhead is,

$$\rho_{TP} = \rho_H = \frac{\rho_G \rho_L}{x\rho_L + (1-x)\rho_G} \quad \text{.....(D.4)}$$

Rearranging Eq. D.4,

$$\frac{1}{\rho_H} = \frac{x}{\rho_G} + \frac{1-x}{\rho_L} = xv_G + (1-x)v_L \quad \text{..... (D.31)}$$

So the derivative of Eq. D.31 is,

$$\frac{\partial}{\partial z}\left(\frac{1}{\rho}\right)=\frac{\partial}{\partial z}\left[xv_G+(1-x)v_L\right]=v_G\frac{\partial x}{\partial z}+x\frac{\partial v_G}{\partial z}+(1-x)\frac{\partial v_L}{\partial z} \quad \text{……..……(D.32)}$$

Because the two phases are treated as compressible fluids, $v_G=v_G(p)$ and $v_L=v_L(p)$,

$$\frac{\partial}{\partial z}\left(\frac{1}{\rho}\right)=\frac{\partial}{\partial z}\left[xv_G+(1-x)v_L\right]=v_G\frac{\partial x}{\partial z}+\frac{\partial p}{\partial z}\left[x\frac{\partial v_G}{\partial p}+(1-x)\frac{\partial v_L}{\partial p}\right] \quad \text{…..…….(D.33)}$$

As a summary, the second diffusivity equation for a steady-state condition is

$$-\frac{dp_a}{dz}=G^2\left\{v_G\frac{\partial x}{\partial z}+\frac{\partial p}{\partial z}\left[x\frac{\partial v_G}{\partial p}+(1-x)\frac{\partial v_L}{\partial p}\right]\right\}-\frac{G^2}{\rho}\frac{1}{A}\frac{\partial A}{\partial z} \quad \text{. …...……... (D.34)}$$

The equation for an unsteady-state condition is

$$-\frac{dp_a}{dz}=G^2\left\{v_G\frac{\partial x}{\partial z}+\frac{\partial p}{\partial z}\left[x\frac{\partial v_G}{\partial p}+(1-x)\frac{\partial v_L}{\partial p}\right]\right\}-\frac{G^2}{\rho}\frac{1}{A}\frac{\partial A}{\partial z}+\frac{1}{A}\frac{\partial(GA)}{\partial t}$$

…….... (D.35)

The total pressure drop under transient condition along the wellbore is

$$-\left(\frac{\partial p}{\partial z}\right)=\left\{G^2\left\{v_G\frac{\partial x}{\partial z}+\frac{\partial p}{\partial z}\left[x\frac{\partial v_G}{\partial p}+(1-x)\frac{\partial v_L}{\partial p}\right]\right\}-\frac{G^2}{\rho}\frac{1}{A}\frac{\partial A}{\partial z}+\frac{1}{A}\frac{\partial(GA)}{\partial t}\right\}+\rho_H g\cdot\sin\alpha+\frac{\tau_0 P}{A}$$

…….. (D.36)

Assuming that:

- constant cross-sectional area: $A = \text{const.} \Rightarrow \dfrac{\partial A}{\partial z} = 0$
- No phase change: $x = \text{const.} \Rightarrow \dfrac{\partial x}{\partial z} = 0\,\text{s}$
- Incompressible liquid: $v_L = \text{const.} \Rightarrow \dfrac{\partial v_L}{\partial p} = 0$
- Further, consider single-phase gas only: $x = \text{ const.} = 1$

Then the total pressure drop along the wellbore is reduced to

$$-\left(\frac{\partial p}{\partial z}\right) = \left\{G^2\left[\frac{\partial p}{\partial z}\left(\frac{\partial v_G}{\partial p}\right)\right] + \frac{\partial G}{\partial t}\right\} + \rho_H g \cdot \sin\alpha + \frac{\tau_0 P}{A}$$

$$\left(\frac{\partial p}{\partial z}\right) + \left\{G^2\left[\frac{\partial p}{\partial z}\left(\frac{\partial v_G}{\partial p}\right)\right] + \frac{\partial G}{\partial t}\right\} = -\rho_H g \cdot \sin\alpha - \frac{\tau_0 P}{A} \quad \text{..... (D.37)}$$

Assuming that the fluid is ideal gas, $PV = nZRT$, then we have,

$$\rho_G = \frac{p\overline{m}}{ZRT} \text{ or } v_G = \frac{ZRT}{p\overline{m}}, \text{ .....(D.38)}$$

So, $$\frac{\partial(v_G)}{\partial p} = \frac{\partial\left(\dfrac{ZRT}{p\overline{m}}\right)}{\partial p} = -\frac{ZRT}{p^2\overline{m}}. \text{ ..... (D.39)}$$

Bringing Eq. D.39 back into Eq. D.37,

$$\left(\frac{\partial p}{\partial z}\right) + G^2\left(\frac{\partial v_G}{\partial p}\right)\left(\frac{\partial p}{\partial z}\right) + \frac{\partial G}{\partial t} = -\rho_H g \cdot \sin\alpha - \frac{\tau_0 P}{A}$$

$$\left(\frac{\partial p}{\partial z}\right) - G^2 \frac{ZRT}{p^2 \overline{m}}\left(\frac{\partial p}{\partial z}\right) + \frac{\partial G}{\partial t} = -\rho_H g \cdot \sin\alpha - \frac{\tau_0 P}{A}$$

$$\because \rho_G = \frac{p\overline{m}}{ZRT} \Rightarrow p = \frac{ZRT\rho_G}{\overline{m}}$$

$$\left(\frac{\partial p}{\partial z}\right) - G^2 \frac{ZRT}{\left(\frac{ZRT\rho_G}{\overline{m}}\right)^2 \overline{m}}\left(\frac{\partial p}{\partial z}\right) + \frac{\partial G}{\partial t} = -\rho_H g \cdot \sin\alpha - \frac{\tau_0 P}{A}$$

$$\left(\frac{\partial p}{\partial z}\right) - G^2 \frac{\overline{m}}{ZRT\rho_G^2}\left(\frac{\partial p}{\partial z}\right) + \frac{\partial G}{\partial t} = -\rho_H g \cdot \sin\alpha - \frac{\tau_0 P}{A}$$

$$\left(1 - \frac{G^2 \overline{m}}{\rho_G^2 ZRT}\right)\left(\frac{\partial p}{\partial z}\right) + \frac{\partial G}{\partial t} = -\rho_H g \cdot \sin\alpha - \frac{\tau_0 P}{A} \quad \text{..... (D.40)}$$

Now bringing the equations of perimeter $P = 2\pi r$ and $A = \pi r^2$ into the above equation

$$\left(1 - \frac{G^2 \overline{m}}{\rho_G^2 ZRT}\right)\left(\frac{\partial p}{\partial z}\right) + \frac{\partial G}{\partial t} = -\rho_H g - \frac{\tau_0 (2\pi r)}{(\pi r^2)}$$

$$\left(1 - \frac{G^2 \overline{m}}{\rho_G^2 ZRT}\right)\left(\frac{\partial p}{\partial z}\right) + \frac{\partial G}{\partial t} = -\rho_H g - \frac{4\tau_0}{(2r)}$$

$$\left(1 - \frac{G^2 \overline{m}}{\rho_G^2 ZRT}\right)\left(\frac{\partial p}{\partial z}\right) + \frac{\partial G}{\partial t} = -\rho_H g - \frac{4\tau_0}{d_T} \quad \text{.....(D.41)}$$

Because the unit value, $\overline{m}$ is *1*, the final second equation for the conservation of momentum under the above assumptions is,

$$\left(1 - \frac{G^2}{\rho^2 ZRT}\right)\frac{\partial p}{\partial z} + \frac{\partial G}{\partial t} + \frac{2G}{\rho}\frac{\partial G}{\partial z} = -\rho g - \frac{4}{d_T}\tau_w \quad \text{..(D.42)}$$

We perform unit check, and put back multiplier $\overline{m}$ for the second term in the bracket,

$$\left(1-\frac{G^2}{\rho^2 ZRT}\cdot\overline{m}\right)\frac{\partial p}{\partial z}+\frac{\partial G}{\partial t}+\frac{2G}{\rho}\frac{\partial G}{\partial z}=-\rho g-\frac{4}{d_T}\tau_w \quad \text{..... (D.43)}$$

$$LHS:\left(\frac{\left(\frac{kg}{m^2\cdot s}\right)^2 kg}{\left(\frac{kg}{m^3}\right)^2 Pa\cdot m^3}\right)\frac{Pa}{m}+\frac{\frac{kg}{m^2\cdot s}}{\partial t}+\frac{\frac{kg}{m^2\cdot s}}{\frac{kg}{m^3}}\frac{\frac{kg}{m^2\cdot s}}{m}$$

$$=\left(\frac{kg^2}{m^4\cdot s^2}\right)\left(\frac{m^6}{kg^2}\right)\frac{kg}{Pa\cdot m^3}\frac{Pa}{m}+\frac{kg}{m^2\cdot s}\frac{m^3}{kg}\frac{1}{m}\frac{kg}{m^2\cdot s} \quad \text{..... (D.44)}$$

$$=\frac{kg}{m^2 s^2}+\frac{kg}{m^2 s^2}$$

$$RHS:\frac{kg}{m^3}\frac{m}{s^2}+\frac{\frac{N}{m^2}}{m}=\frac{kg}{m^2\cdot s^2}+\frac{kg\frac{m}{s^2}}{m^3}=\frac{kg}{m^2\cdot s^2}+\frac{kg}{m^2\cdot s^2} \quad \text{..... (D.45)}$$

An Example to Build the Linear Equation for Mechanistic Wellbore Model

Now that the two PDF equations have been derived, we can provide a simulation example. The wellbore is divided into five blocks (**Fig. D1**).

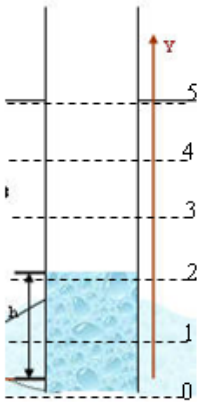

Fig.D1 – The wellbore is divided into five blocks

At time zero, assume we know the BHP ($p_0^t = p_B^t$)

The case of $j = 0$ is special because p_B is known,

$$-\frac{C_{12}}{\Delta z}G_0^1 + \frac{1}{\Delta t}p_1^1 + \frac{C_{12}}{\Delta z}G_1^1 = \frac{1}{\Delta t}p_1^0 \quad \text{..... (D.46)}$$

$$-\frac{C_{22}}{\Delta z}G_0^1 + \frac{C_{21}}{\Delta z}p_1^1 + \left(\frac{1}{\Delta t} + \frac{C_{22}}{\Delta z}\right)G_1^1 = \bar{R} + \frac{1}{\Delta t}G_1^0 + \frac{C_{21}}{\Delta z}p_0^1 \quad \text{..... (D.47)}$$

At $j = 1$,

$$-\frac{C_{12}}{\Delta z}G_1^1 + \frac{1}{\Delta t}p_2^1 + \frac{C_{12}}{\Delta z}G_2^1 = \frac{1}{\Delta t}p_2^0 \text{ ..... (D.48)}$$

$$-\frac{C_{21}}{\Delta z}p_1^1 - \frac{C_{22}}{\Delta z}G_1^1 + \frac{C_{21}}{\Delta z}p_2^1 + \left(\frac{1}{\Delta t} + \frac{C_{22}}{\Delta z}\right)G_2^1 = \bar{R} + \frac{1}{\Delta t}G_2^0 \quad \text{..... (D.49)}$$

At $j = 2$,

$$-\frac{C_{12}}{\Delta z}G_2^1 + \frac{1}{\Delta t}p_3^1 + \frac{C_{12}}{\Delta z}G_3^1 = \frac{1}{\Delta t}p_3^0 \quad \text{..... (D.50)}$$

$$-\frac{C_{21}}{\Delta z}p_2^1 - \frac{C_{22}}{\Delta z}G_2^1 + \frac{C_{21}}{\Delta z}p_3^1 + \left(\frac{1}{\Delta t} + \frac{C_{22}}{\Delta z}\right)G_3^1 = \bar{R} + \frac{1}{\Delta t}G_3^0 \quad \text{..... (D.51)}$$

At $j = 3$,

$$-\frac{C_{12}}{\Delta z}G_3^1 + \frac{1}{\Delta t}p_4^1 + \frac{C_{12}}{\Delta z}G_4^1 = \frac{1}{\Delta t}p_3^0 \quad \text{..... (D.52)}$$

$$-\frac{C_{21}}{\Delta z}p_3^1 - \frac{C_{22}}{\Delta z}G_3^1 + \frac{C_{21}}{\Delta z}p_4^1 + \left(\frac{1}{\Delta t} + \frac{C_{22}}{\Delta z}\right)G_4^1 = \bar{R} + \frac{1}{\Delta t}G_4^0 \quad \text{..... (D.53)}$$

At $j = 4$, the case is special again since G_H (G_5) is given,

$$-\frac{C_{12}}{\Delta z}G_4^1 + \frac{1}{\Delta t}p_5^1 = \frac{1}{\Delta t}p_4^0 - \frac{C_{12}}{\Delta z}G_5^1 \quad \text{(D.54)}$$

$$-\frac{C_{21}}{\Delta z}p_4^1 - \frac{C_{22}}{\Delta z}G_4^1 + \frac{C_{21}}{\Delta z}p_5^1 = \bar{R} + \frac{1}{\Delta t}G_5^0 - \left(\frac{1}{\Delta t} + \frac{C_{22}}{\Delta z}\right)G_5^1 \quad \text{(D.55)}$$

To obtain the elements of C_{21} and C_{22}, we define two functions depending on the G values at the same space step but at the previous timestep.

$$C_{21,j} = f_{21}(G_j^n) = 1 - \frac{\left(G_j^n\right)^2}{\rho^2 zRT} \quad \text{(D.56)}$$

$$C_{22,j} = f_{22}(G_j^n) = \frac{2\left(G_j^n\right)}{\rho} \quad \text{(D.57)}$$

We formulate all the equations from Eq. D.46 to D.55 in matrix form of **Fig. D2**.

$$\begin{vmatrix}
-\frac{C_{12,j=0}}{\Delta z} & \frac{1}{\Delta t} & \frac{C_{12,j=0}}{\Delta z} & 0 & 0 & 0 & 0 & 0 & 0 & 0 \\
-\frac{C_{22,j=0}}{\Delta z} & \frac{C_{21,j=0}}{\Delta z} & \left(\frac{1}{\Delta t}+\frac{C_{22,j=0}}{\Delta z}\right) & 0 & 0 & 0 & 0 & 0 & 0 & 0 \\
0 & 0 & -\frac{C_{12,j=1}}{\Delta z} & \frac{1}{\Delta t} & \frac{C_{12,j=1}}{\Delta z} & 0 & 0 & 0 & 0 & 0 \\
0 & -\frac{C_{21,j=1}}{\Delta z} & -\frac{C_{22,j=1}}{\Delta z} & \frac{C_{21,j=1}}{\Delta z} & \left(\frac{1}{\Delta t}+\frac{C_{22,j=1}}{\Delta z}\right) & 0 & 0 & 0 & 0 & 0 \\
0 & 0 & 0 & 0 & -\frac{C_{12,j=2}}{\Delta z} & \frac{1}{\Delta t} & \frac{C_{12,j=2}}{\Delta z} & 0 & 0 & 0 \\
0 & 0 & 0 & -\frac{C_{21,j=2}}{\Delta z} & -\frac{C_{22,j=2}}{\Delta z} & \frac{C_{21,j=2}}{\Delta z} & \left(\frac{1}{\Delta t}+\frac{C_{22,j=2}}{\Delta z}\right) & 0 & 0 & 0 \\
0 & 0 & 0 & 0 & 0 & 0 & -\frac{C_{12,j=3}}{\Delta z} & \frac{1}{\Delta t} & \frac{C_{12,j=3}}{\Delta z} & 0 \\
0 & 0 & 0 & 0 & 0 & -\frac{C_{21,j=3}}{\Delta z} & -\frac{C_{22,j=3}}{\Delta z} & \frac{C_{21,j=3}}{\Delta z} & \left(\frac{1}{\Delta t}+\frac{C_{22,j=3}}{\Delta z}\right) & 0 \\
0 & 0 & 0 & 0 & 0 & 0 & 0 & -\frac{C_{12,j=4}}{\Delta x} & \frac{1}{\Delta t} & \\
0 & 0 & 0 & 0 & 0 & 0 & 0 & -\frac{C_{21,j=4}}{\Delta z} & -\frac{C_{22,j=4}}{\Delta z} & \frac{C_{21,j=4}}{\Delta z}
\end{vmatrix}
\times
\begin{vmatrix}
G_0^1 \\ p_1^1 \\ G_1^1 \\ p_2^1 \\ G_2^1 \\ p_3^1 \\ G_3^1 \\ p_4^1 \\ G_4^1 \\ p_5^1
\end{vmatrix}
=
\begin{vmatrix}
\frac{1}{\Delta t}p_0^0 \\
\bar{R} + \frac{1}{\Delta t}G_1^0 + \frac{C_{21}}{\Delta x}p_0^1 \\
\frac{1}{\Delta t}p_2^0 \\
\bar{R} + \frac{1}{\Delta t}G_2^0 \\
\frac{1}{\Delta t}p_3^0 \\
\bar{R} + \frac{1}{\Delta t}G_3^0 \\
\frac{1}{\Delta t}p_3^0 \\
\bar{R} + \frac{1}{\Delta t}G_4^0 \\
\frac{1}{\Delta t}p_4^0 - \frac{C_{12}}{\Delta x}G_5^1 \\
\bar{R} + \frac{1}{\Delta t}G_5^0 - \left(\frac{1}{\Delta t} + \frac{C_{22}}{\Delta x}\right)G_5^1
\end{vmatrix}$$

Fig. D2 –Illustration of the linear equation combined by two PDFs in matrix form.

Numerical Simulation by VBA Approach

A wellbore mechanistic simulator is built in VBA. A synthetic case was tested and compared with a steady-state simulator, Petroleum Production Systems model (PPS, 1995). The input data for study is in SI units, illustrated by the snapshot of the user interface (**Fig. D3**).

Parameters	Values	SI Unit	Values	Field Unit
p_b (Guessed)	1.72E+07	Pa	2494.65	psi
ρ@res	39.27	kg/m³	0.33	lb/Gallon
r_w	0.09144	m	0.30	ft
d_T	0.1524	m	0.50	ft
t_w	100	Pa	0.01	psi
T @FBHP	377.6	K	220.00	°F
T @tf	338.7	K	150.00	°F
T @Res	377.6	K	220.00	°F
Roughness	0.0006		0.0006	
Slant Angle	90	°	90.00	°
Δz	100	m	328.08	ft
Δr	152.4	m	500	ft
Δt	10000	s	10000	s
z	0.96		0.96	
R	8.3145	J/(mol K)	1.99	cal/(mol K)
g	9.81	m/s²		
Π	3.14		3.14	
k	8.45E-13	m²	0.845	Darcy
h	18.288	m	60.00	ft
phi	0.21		0.21	
c_t	5.87E-07	1/Pa	0.00405	1/psi
μ	1.37E-05	kg/(m·s)	0.0137	cp
Bg	1		1	
Bo	1		1	
$p_{.....i}$	2.48E+07	Pa	3600	psi
Skin_total	0		0	
eta	2.00		1.38E-05	

Fig.D3 –The summary of input data for running this example.
Temperature gradient is 0.007 ºC/ft. Users can change the input values in the "Main" worksheet.

The same configuration was set for the steady-state simulator, PPS, and we just performed the comparison between the two simulators at the first timestep from shut-in to production. The maximum relative error for the pressure along the wellbore is about 14.5%, and the flow rates are constant in the steady-state correlations (**Fig. D4, Table D1**). In transient conditions, the mechanistic model is exceptionally required, and the relative error of the steady-state or pseudosteady-state models is not tolerated.

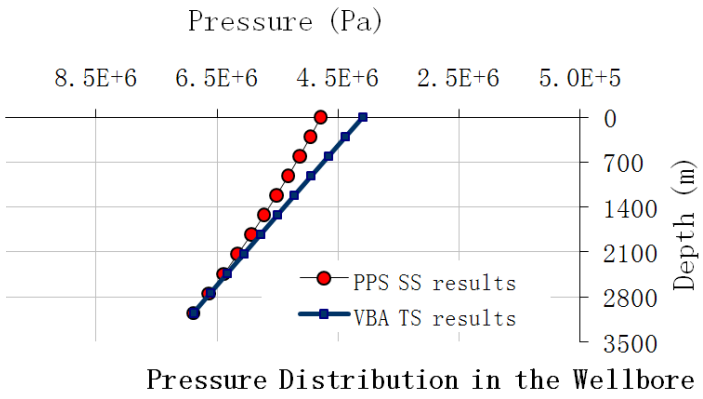

Fig.D4 –The comparison of the simulation results for the first timestep between a mechanistic model and the steady-state model PPS.

Table D1 -Comparson between the steady-state and transient wellbore models.					
Steady-state Model		Transient Model		Relative difference	
Mass flow rate ($kg/m^2/s$)	Current Pressure (kPa)	Mass flow rate ($kg/m^2/s$)	Current Pressure (kPa)	mass	Pressure
651.16	6894.74	556.83	6890.00	16.94%	0.07%
651.16	6638.26	557.42	6614.94	16.82%	0.35%
651.16	6390.74	558.75	6339.03	16.54%	0.82%
651.16	6162.52	561.38	6062.17	15.99%	1.66%
651.16	5939.13	565.49	5784.37	15.15%	2.68%
651.16	5726.09	571.43	5505.52	13.95%	4.01%
651.16	5522.00	579.54	5225.57	12.36%	5.67%
651.16	5326.88	590.17	4944.44	10.34%	7.73%
651.16	5139.34	603.64	4662.07	7.87%	10.24%
651.16	4960.08	620.32	4378.37	4.97%	13.29%
651.16	4787.71	651.16	4092.89	0.00%	16.98%

Summary

This appendix proposed a transient homogeneous wellbore model. The comparisons show the steady-state model is not appropriate for transient conditions. The parallel work led by Prof. Jader Barbosa's group at the Department of Mechanical Engineering, Federal University of Santa Catarina in Brazil is under the process to build a transient multiphase wellbore model in FORTRAN, which is used to couple with this transient reservoir model at Texas A&M.

VITA

He Zhang received his B.En. in computer application; B.S. in polymer chemistry, from University of Science and Technology of China in 2002 and 2003 respectively, and obtained his M.S. in chemistry from University of New Orleans in 2006. He entered the Petroleum Engineering program at Texas A&M University and received his Doctor of Philosophy degree in May 2010. His research interests include modeling multiphase flow in porous media and pipe, coupling the wellbore/reservoir models under fully transient conditions, PVT Characterization, and numerical skills.

He Zhang may be reached at 3116 TAMU - 602 Richardson Building, College Station, TX 77843-3116. His Email is hezhang1980@gmail.com.